# Numerical simulation of gas-liquid Taylor flow with catalyzed heterogeneous reaction

Zur Erlangung des akademischen Grades eines
DOKTORS DER INGENIEURWISSENSCHAFTEN (Dr.-Ing.)

von der KIT-Fakultät für Maschinenbau des
Karlsruher Instituts für Technologie (KIT)
angenommene

DISSERTATION

von

M. Sc. Mino Woo

| | |
|---|---|
| Tag der mündlichen Prüfung: | 14. September 2017 |
| Hauptreferent: | Prof. Dr. Bettina Frohnapfel |
| Korreferent: | Prof. Dr. Olaf Deutschmann |
| Korreferent: | Prof. Dr. Yosuke Hasegawa |

# Acknowledgements

Firstly, I would like to thank my supervisor Dr. Martin Wörner. The completion of this doctoral research project would not have been successful without his vast knowledge, enthusiasm and patience. Martin has offered no end of help and advice, particularly in the numerical aspects of this research. I truly appreciate Prof. Olaf Deutschmann for giving me the opportunity to conduct this research with AKD members, and for constant encouragement. I am grateful to Prof. Bettina Frohnapfel for being my official supervisor at Department of Mechanical Engineering. I would also like to thank Prof. Yosuke Hasegawa for being delighted to be a co-examiner traveling from the opposite side of the world.

I would like to extend my thanks to AKD colleagues. I am extremely grateful to Dr. Steffen Tischer for all his support regarding DETCHEM$^{TM}$. I greatly appreciate Dr. Lubow Maier for her huge help to generate the detailed kinetic mechanism which is essential to verify the capability of this research. I would like to thank Dr. Matthias Hettel for giving me ideas of coupling CFD software and DETCHEM$^{TM}$. I also specially thank my office mates: Dr. Xuan Cai, Dipl.-Ing Carlos Falconi, M.Sc. Sercan Erdogan and M.Sc. Farshid Jamshidi. I am very grateful to them not only for sharing their scientific knowledge but also for advising me to settle down a foreign place. Besides AKD, I would like to thank Dr. Daniela Piccioni Koch (SCC) for supporting code development.

I acknowledge the funding by Helmholtz Energy Alliance "Energy Efficient Chemical Multiphase Processes" (HA-E-0004) and thank the Steinbeis GmbH for a cost-free license of DETCHEM$^{TM}$. I sincerely appreciate DAAD STIBET program for funding pre-graduation scholarship twice. I am truly grateful to Dipl.-Ing Carlos Falconi once again for giving me an opportunity to work at Automotive Simulation Center Stuttgart e.V. which allows me to have both financial aid and work experience in massive computation.

It was unforgettable moments when my daughter Jesin and my son Sersin came to the world. I wholeheartedly appreciate my wife Ahyoung Lee for her boundless support and patience to three of us. I would also like to thank Korean society in Karlsruhe and Dr. Seungchul Lee who is the only Korean friend at KIT, which save my family from nostalgia.

Finally, I would like to take this opportunity to express my gratitude again to those who have helped me achieve the doctoral degree.

# Abstract

A promising novel technology for multiphase reaction is a gas-liquid Taylor flow within a catalytic monolith reactor. Having this flow characteristic offers distinct benefits for the two-phase mass transfer by means of very thin liquid film between the bubble and the catalytic wall as well as the large interface-to-volume ratio. This doctoral study aims at the development of a numerical solver to tackle the hydrodynamic and reactive mass transport phenomena accompanied with the Taylor flow in such a monolith channel. For this purpose, two computer codes, TURBIT-VOF and DETCHEM$^{TM}$, have been successfully coupled by embedding subroutines of DETCHEM$^{TM}$ into TURBIT-VOF. In coupled solver, TURBIT-VOF computes the hydrodynamics of the gas-liquid flow and the mass transfer of dilute species in both phases, while DETCHEM$^{TM}$ calculates the chemical kinetics at the catalytic walls. For multispecies mass transfer, multicomponent diffusion model and effective diffusivity model have been implemented and validated with several test cases. Moreover, the solver has been further verified for hydrodynamics and reaction kinetics as well as a special numerical model to ensure the mass conservation across the interface.

Catalyzed hydrogenation of nitrobenzene to aniline is chosen as a reaction of interest in the present study, which is a part of the project 'Energy efficient chemical multiphase processes' funded by Helmholtz energy alliance. As a preliminary study, an artificial fluid system whose physical properties are more favorable to numerical simulations is employed in order to find the appropriate range of test conditions for real fluid system where gas hydrogen undergoes mass transfer into liquid nitrobenzene. Reynolds number and capillary number are the main parameters, and those ranges for numerically stable solutions are $Re<100$ and $0.01<Ca<1$. The corresponding channel height and bubble velocity are 100 μm and $0.5<u_B<1.2$ m/s, respectively. The fluid properties (density, viscosity, diffusivity and surface tension) are assumed constant during the calculation. In order to simulate mass transfer efficiently, the moving reference frame approach has been proposed. Once the velocity reaches to the quasi-steady state, the velocity and the void fraction are frozen, and only species conservation equations are further solved on the fixed flow field. Therefore, less computational effort is required without solving hydrodynamics of Taylor flows. One-step global reaction kinetics of pellet catalyst is applied to the reactive boundary condition. The reaction rate is converted from volumetric reaction to surface reaction via specific surface area of pellet catalyst. The mass transfer of gaseous species is most active in the rear part of the bubble where the liquid film is thinnest. With changing bubble velocity, the mass transfer is affected by the intensity of convective mass transfer (induced by the recirculating flow between bubbles) versus diffusive mass transfer (within the liquid film region). Furthermore, a detailed kinetic mechanism for hydrogenation of nitrobenzene is generated from the study of density functional theory. Feasibility test of the coupled solver has been performed with the generated detailed mechanism. To the best of authors' knowledge, this is the first study to analyze the behaviors of multiple bulk (4) and surface (10) species within a Taylor flow.

To account for the mass transfer with respect to the changing liquid composition during the reaction process, one-dimensional diffusion equation is computed with composition dependent mixture properties obtained (or estimated) from literature. Based on the variable diffusivity, solubility and film thickness, the mass transfer in liquid mixture makes a complicated relation of liquid composition and is not intuitively simple as for the gas phase mixture. Finally, the series of results comes up with the appropriate range of the bubble length for a certain extent of the saturation.

# Kurzfassung

Eine vielversprechende neue Technologie für mehrphasige reaktive Strömungen ist die Taylor-Strömung in Monolith-Reaktoren. Die Strömung von Taylorblasen in kleinen Kanälen kombiniert ein großes Verhältnis von Phasengrenzfläche zu Volumen mit einem dünnen Flüssigkeitsfilm zwischen Blase und Wand und ermöglicht so eine verbesserte Stoffübertragung. Gegenstand der vorliegenden Arbeit ist die Entwicklung eines Rechenprogramms für die Taylorströmung im Einzelkanal eines Monolith-Reaktors mit Oberflächenreaktionen. Zu diesem Zweck werden die Rechenprogramme TURBIT-VOF und DETCHEM$^{TM}$ gekoppelt, indem Unterprogramme von DETCHEM$^{TM}$ in TURBIT-VOF eingebunden werden. Im gekoppelten Code führt TURBIT-VOF die Direkt Numerische Simulation von Hydrodynamik und Stoffübertragung der Zweiphasenströmung aus, während DETCHEM$^{TM}$ die chemische Kinetik der heterogenen katalytischen Reaktionen behandelt. Zur Beschreibung der Diffusion im Mehrkomponentengemisch werden das Multikomponenten-Model und das Modell eines effektiven Diffusionskoeffizienten implementiert, und anhand von analytischen Lösungen und experimentellen Daten validiert. Außerdem werden die numerischen Ergebnisse von Hydrodynamik und Reaktionskinetik sowie eine spezielle numerische Behandlung der diskontinuierlichen Konzentrationsverteilung an der Phasengrenzfläche verifiziert.

Als Mehrphasenreaktion wird in der vorliegenden Arbeit mit der katalytischen Hydrierung von Nitrobenzol zu Anilin eine der beiden Modellsynthesen der Helmholtz Energie-Allianz "Energieeffiziente chemische Mehrphasenprozesse" untersucht. Vor der Betrachtung des praxisrelevanten Stoffsystems Wasserstoff (Gas) und Nitrobenzol (Flüssigkeit) werden zunächst Simulationen für ein artifizielles Stoffsystem durchgeführt, um so einen geeigneten Parameterbereich hinsichtlich Kapillar-Zahl ($Ca$) und Reynolds-Zahl ($Re$) zu identifizieren. Die so bestimmten Testbedingungen ($Re < 100$ und $0,01 < Ca < 1$) entsprechen bei einer Kanalhöhe von 100 μm Blasengeschwindigkeiten im Bereich $0,5 < u_B < 1,2$ m/s. Die Fluideigenschaften (Dichte, Viskosität, Diffusionskoeffizienten und Oberflächenspannung) werden während der Berechnung als konstant angenommen. Für eine effiziente Simulation der Stoffübertragung wird ein mit der Taylorblase mitbewegtes Referenzsystem verwendet, in dem das Geschwindigkeitsfeld und die Phasenverteilung eingefroren bleiben. Die Hydrierung von Nitrobenzol zu Anilin wird zunächst über eine einstufige globale Reaktionskinetik mit einer angepassten Reaktionsgeschwindigkeit als Randbedingung an der katalytischen Wand modelliert. Die numerischen Ergebnisse zeigen, dass der Stoffübergang von Wasserstoff im hinteren Bereich der Blase mit der dünnsten Filmdicke am höchsten ist. Bei einer Veränderung der Blasengeschwindigkeit wird der Stoffübergang sowohl durch die konvektive Zirkulation im Flüssigkeitspfropfen als auch durch Diffusionsvorgänge im Flüssigkeitsfilm beeinflusst. Für eine detaillierte Modellierung der chemischen Reaktion werden zusätzlich erstmals qualitative Rechnungen mit einem aus der Dichtefunktionaltheorie abgeleiteten Reaktionsmechanismus durchgeführt (bestehend aus vier Bulk-Spezies und zehn Oberflächenspezies) und damit die Möglichkeiten des gekoppelten Lösers demonstriert.

Zur Untersuchung der Abhängigkeit von der wechselnden Zusammensetzung der Flüssigkeit aufgrund der Reaktion, wird eine eindimensionale Diffusionsgleichung für die Stoffübertragung im Flüssigkeitsfilm der Taylorströmung betrachtet. Aufgrund variabler Diffusionsfähigkeit, Löslichkeit und Filmdicke bildet die Stoffübertragung im Flüssigkeitsgemisch eine komplizierte Funktion der Zusammensetzung. Als Ergebnis dieser Untersuchungen wird für einen gewünschten Sättigungsgrad des Flüssigkeitsfilms mit Wasserstoff ein geeigneter Bereich der Blasenlänge identifiziert.

# Contents

**Acknowledments** I

**Abstract** III

**Kurzfassung** V

**Table of contents** VII

**Chapter 1 Introduction** ........................................ **1**

1.1 Numerical simulation of gas-liquid Taylor flow in catalytic monolith reactor..... 3

1.2 Hydrogenation of nitrobenzene to aniline .................................. 4

1.3 Numerical methods .................................. 4

1.4 Multicomponent diffusion .................................. 7

1.5 Objectives .................................. 8

**Chapter 2 Mathematical description** ........................................ **11**

2.1 Equations for hydrodynamics .................................. 11

2.2 Numerical method for hydrodynamics .................................. 14

2.3 Equations for mass transfer .................................. 15

2.4 Numerical method for mass transfer .................................. 19

2.4.1 Discretization .................................. 19

2.4.2 Boundary conditions .................................. 20

2.4.3 Continuous concentration diffusivity model (CCDM) .................................. 21

2.4.4 Data exchange between TURBIT-VOF and DETCHEM$^{TM}$ .................................. 22

2.5 Modeling multicomponent diffusion .................................. 25

2.5.1 Generalized Fick's law .................................. 27

2.5.2 Maxwell-Stefan equation .................................. 28

2.5.3 Multicomponent model .................................. 29

2.5.4 Effective diffusivity model .......... 29

**Chapter 3 Validations .......... 31**

3.1 Hydrodynamics: Two-layer Poiseuille flow .......... 32

3.2 Multispecies mass transfer within a single phase .......... 37

3.2.1 Stefan diffusion for a ternary mixture .......... 38

3.2.2 Ternary diffusion with heterogeneous reaction .......... 41

3.3 Mass transfer across the interface between two phases .......... 46

3.3.1 Validation of CCDM for transient two-phase mass transfer .......... 46

3.3.2 Parametric study on the two-phase mass transfer .......... 49

3.4 Multispecies mass transfer across the phase interface .......... 52

3.5 Influence of dilution .......... 54

3.6 Validation of reaction kinetics for hydrogenation of nitrobenzene .......... 58

3.6.1 Simplified one-step kinetic model .......... 59

3.6.2 Reaction kinetics with gas-liquid mass transfer limitation .......... 62

**Chapter 4 Parametric studies on Taylor flow for artificial fluid systems .......... 67**

4.1 Characteristics of gas-liquid Taylor flow .......... 67

4.2 Influence of the gas density and gas viscosity .......... 76

4.3 Grid dependency test .......... 80

4.4 Moving reference frame approach for mass transfer .......... 85

**Chapter 5 Catalyzed hydrogenation of nitrobenzene within a Taylor flow .......... 93**

5.1 Physical properties .......... 94

5.1.1 Density and viscosity .......... 95

5.1.2 Diffusivity .......... 96

5.1.3 Solubility .......... 98

5.1.4 Surface tension ... 102

5.2 Hydrodynamics for Taylor flow of hydrogen in nitro-benzene ... 103

5.2.1 Determination of simulation parameters ... 104

5.2.2 Velocity field and bubble shape at quasi-steady state ... 105

5.3 Simulation of catalyzed hydrogenation of nitrobenzene within a Taylor flow. 107

5.3.1 Pure nitrobenzene ... 109

5.3.2 Nitrobenzene pre-saturated with hydrogen ... 117

5.3.3 Influence of recirculation and diffusion ... 120

5.3.4 Influence of reaction rate on mass transfer ... 123

5.4 Detailed reaction mechanism ... 125

5.4.1 Reaction in zero-dimensional problem (CSTR) ... 126

5.4.2 Detailed mechanism with pure nitrobenzene ... 127

5.4.3 Detailed mechanism with pre-saturated nitrobenzene ... 131

**Chapter 6 Influence of liquid composition on mass transfer in liquid film... 133**

6.1 Physical properties in binary liquid mixture ... 134

6.1.1 Density and viscosity of liquid mixture ... 134

6.1.2 Diffusivity of hydrogen in liquid mixture ... 137

6.1.3 Solubility of hydrogen in liquid mixture ... 139

6.1.4 Surface tension of liquid mixture ... 141

6.2 Mass transfer rate of hydrogen in liquid film ... 143

6.2.1 Fixed capillary number (*Ca*=0.01) ... 145

6.2.2 Variable capillary number ... 150

6.2.3 Estimation of a favorable bubble length ... 153

**Chapter 7 Summary and conclusions ... 157**

**Bibliography** ..... 163

**Publications related to the dissertation** ..... 171

**Nomenclature** ..... 173

**List of figures** ..... 177

**List of tables** ..... 183

**Appendix A. Subroutine DEXTEP** ..... 185

**Appendix B. Flotsam treatment** ..... 187

**Appendix C. Numerical solution of Maxwell-Stefan equation** ..... 189

**Appendix D. Numerical solution of non-equilibrium stage model (NESM)** ..... 191

**Appendix E. DETCHEM$^{\text{EVAPORATOR}}$** ..... 193

**Appendix F. Influence of numerical schemes for spatial derivatives** ..... 195

**Appendix G. Kinetic theory** ..... 199

**Appendix H. Reaction mechanism for hydrogenation of nitrobenzene** ..... 201

**Curriculum Vitae** ..... 203

# Chapter 1 Introduction

Within an emerging trend of process intensification, structured catalytic reactors are attractive for efficient and effective multiphase reaction engineering. Prolific chemical processes utilize such structured reactors to produce chemicals, fuels and drugs in many industrial areas relating petrochemicals, fine chemicals, pharmaceuticals and biochemicals. Among a number of structured reactors, the monolith reactor is considerably focused as a promising cutting-edge technology to circumvent the problems in conventional reactors, e.g. maldistribution of liquid and hotspot caused by partial wetting of catalyst. This type of reactor has been mainly used for converting harmful exhaust gases in the automotive industry. Nowadays the usage of this reactor grows not only for such gas phase reactions (reduction of pollution, catalytic combustion and selective oxidation) but also for multiphase reactors accompanying gas-liquid flow therein. When the superficial velocity of gas-liquid mixtures is sufficiently low, the flow in monolith channel develops a segmented two-phase slug flow with elongated gas bubbles, so-called Taylor flow [131]. Among the several possible flow patterns in monolith reactor, Taylor flow offers the best mass transfer properties [54] by means of a very thin liquid film between bubbles and catalytic wall, as well as large interfacial surface area [65]. Several studies have assessed hydrodynamics and transport phenomena of Taylor flow in such a capillary reactor [89]. Interfacial mass transfer within Taylor flow is governed by liquid phase diffusion coefficient [67], linear velocity [27] or gas superficial velocity [122].

Numerical approach facilitates having a keen insight into this beneficial flow type and enables analyzing the details of physico-chemical processes in monolith reactor. For this purpose, this doctoral study aims at the development of a computer code covering both gas-liquid hydrodynamics and heterogeneous chemical kinetics for catalytic reactions. Helmholtz Energy Alliance [51] organized a project “Energy-efficient Chemical Multiphase Processes”, and assigned the present study as a part of this project. The project emphasizes the needs of energy efficient industrial processes as one of the major future challenges to achieve international climate goals with sustaining industrial competitiveness. The targets are multiphase chemical reactions and associated industrial processes as are the major industrial energy consumers. Helmholtz-Zentrum Dresden-Rossendorf (HZDR) coordinates this project involving the scientific competence of two Helmholtz institutes (HZDR, KIT), four universities (TUD, RUB,

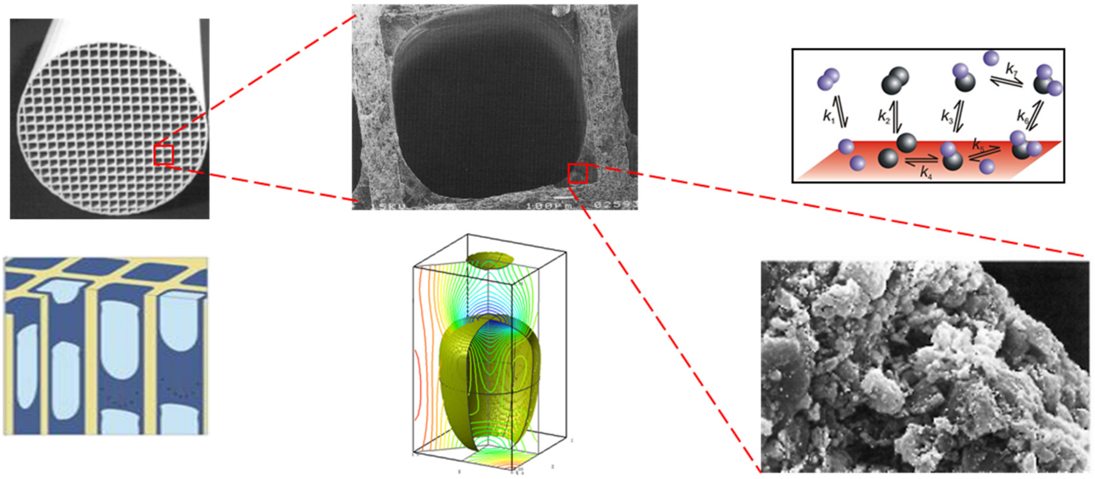

Reactor modeling

Bubble flow in single channel
(TURBIT-VOF)

Surface reaction in the pore
(DETCHEM$^{TM}$)

Fig. 1.1: The objective for the simulation of reactive gas-liquid flow in monolith reactor.

TUHH, TUD) and one Fraunhofer institute (IKTS). The research work of the alliance is divided into five Work Packages (WP). WP1 focuses on system analysis to determine the optimization potential on a system level. WP2 is regarding chemical reactions and device technologies for optimal reaction control in structured reactors. The interest of WP3 is multiphase flow and mass transfer on a device level. WP4 relates to the modeling and simulation (e.g. theoretical multiscale modeling) for optimization and design strategies. WP5 aims at the development of measuring techniques to acquire high-resolution data for reaction control and code validation. The present study is involved in WP4.

The purpose of this study is to develop a computer code that allows the numerical investigation of heterogeneously catalyzed reactive gas-liquid flows. Computation of reactive gas-liquid flow necessitates considering the interactions among different physical phenomena, which include two-phase flow hydrodynamics, heat and mass transfer (in a phase and across interfaces) as well as chemical kinetics. These phenomena span a wide range of length and time scale and covering the scales is essential for computation, therefore. Fig. 1.1 presents the modeling concept of gas-liquid Taylor flow in catalytic monolith reactor. Generally, the monolith reactor can be characterized by a single representative channel. Thus, a single channel of monolith reactor is chosen for the computational domain. In the single channel configuration, TURBIT-VOF [112] can solve the interface evolution of gas-liquid flow and associated mass transport in liquid phases. Meanwhile, DETCHEM$^{TM}$ [30] solves chemical reactions at the reactive wall. To achieve the goal of this project, these two well-validated in-house codes are coupled to deal with both gas-liquid hydrodynamics and mass transfer accompanying catalytic reactions. The hydrogenation of nitrobenzene to aniline is selected as a sample reaction, and considered as a heterogeneous reaction at the catalyzed monolith wall.

## 1.1 Numerical simulation of gas-liquid Taylor flow in catalytic monolith reactor

As mentioned earlier, the physico-chemical phenomena in chemical reactors underlie a wide range of the scales. The scale can be defined somewhat arbitrary in nature and depends on the extent of the reactor in usage. The smallest scale could be the molecular scale wherein there is an interaction between various molecules such as collision, absorption and reaction. In order to eliminate the consideration of this scale, the kinetic expression is commonly utilized. However, it is often necessary to use detail mechanisms because either the global kinetics lack accuracy or a more detailed description of the production procedure is required. The second smallest scale that may be considered is nano-scale, which is the scale of the pore in a porous medium such as washcoat. This scale can be modeled by a treatment of porous medium as a continuum material. Micro-scale or even millimeter scale can be used to take into account the washcoat itself. Moreover, the larger scale, the size of reactor, can be applied to analyze the whole reactor system, e.g. reactor network. It spans at least four orders of magnitude to cover the entire physical phenomena appearing in a micro reactor system. The phenomenological model for such chemical reactors thus describes a multi-scale problem.

Besides bridging various scales, choosing a scale of interest and suitable approximations for the other scales are crucial to determine the efficiency and accuracy of the modelling. For example, a representative channel is generally considered from the bundle of monolith channels to characterize the detail physical and transport phenomena inside the channel [28, 33, 56], while several channels are still considered to define the design and optimization parameters [59]. For simulation of gas-liquid flows with the single channel configuration, some studies assume the shape of bubbles, and focus more on the mass transport phenomena in liquid phase [31, 66], while the flow of both phases can be solved to examine the overall concentration behaviors [107, 110]. Most of the studies employ an artificial concentration to evaluate the qualitative trend of mass transfer around Taylor bubbles [95, 110, 120]. Consideration of real physical properties for mass transfer and reaction is still lacking.

For catalytic liquid phase hydrogenation, slurry or fluidized-bed reactors were mostly used in industrial [73] and academic area [34, 64, 136]. However, with a recent trend of process intensification and miniaturization, the micro reactor technique is attempting to change the classical concept of reactors. Coupling reaction in catalytic membrane reactor has been studied for minimization of heat losses and chemical processes [2]. Falling film reactor has been investigated to obtain a thin and stable film thickness to enhance the mass transfer [149]. Also, a study reports that the gas-liquid Taylor flow can activate reactions even under an ambient condition with nanoparticle catalyst coated at the reactor wall [76].

## 1.2 Hydrogenation of nitrobenzene to aniline

As a precursor of many chemical products from a sponge in the kitchen to insulation in the building, aniline is one of the most important chemical compounds, assisting human life in recent years. Aniline plays a decisive role for more than 300 different chemical products in the chemical industry. The largest application of aniline is producing 4,4-methylene-di-para-phenylene isocyanate (MDI) used for polyurethanes in constructions, furniture and automotive industry. It is also widely used for other applications, e.g. rubber processing, dyes and pigments, agricultural chemicals and pharmaceutical industries [73]. To produce aniline, nitrobenzene is an essential raw material that is chemically reduced during the catalytic hydrogenation process. Both gas and liquid phase hydrogenations are available, where there is no difference in yield and product quality, but liquid phase production is known to have some advantages for chemical processes [73].

## 1.3 Numerical methods

Theory and modeling methods can be conveniently classified into four groups, depending on the length and time scales to which they imply: electronic, atomistic, mesoscale and continuum scales [44]. For engineering fluid dynamic applications, only mesoscale and continuum scale methods can produce physically meaningful results with reasonable computational effort [147]. The Lattice-Boltzmann method is one of the representative methods in the mesoscale simulation, which solves the particle dynamics and provides the information to build the macroscopic behaviors. Continuum scales can be described by well-known macroscopic conservation laws assuming that the scale is large enough for the matter to behave continuously in the space it occupies. Thus, these two scales are usually of interest in computational fluid dynamic (CFD) simulations.

These numerical methods are further classified into several types according to the treatment of phase information. The macroscopic simulations usually do not resolve the phase interface. In two-phase flow, Euler-Euler approach employs a Eulerian point of view, focusing a fixed view window to monitor therein the movement of the matters in both bulk and dispersed phases. The results of Euler-Euler method do not contain the trace of dispersed phase but only consist of space- and time-averaged information in the monitoring area. The phase information is stored as a fraction of certain phase, and it is therefore solved by an interpenetrating field equation which is valid in the entire domain [69]. Another widely used approach for macroscopic simulations is Euler-Lagrange approach [19], which considers the trace of the dispersed phase with Eulerian approach for bulk phase. In Euler-Lagrange method, the equations of motion for dispersed phase are solved with surrounding velocity field. The solutions of dispersed phase affect the Eulerian equations as source terms. These two macroscopic approaches are often used to simulate the whole reactor tank that contains numerous bubbles or drops.

### *Hydrodynamics*

The interface-resolving method plays an important role in hydrodynamic simulations of microfluidic devices where the determining interface is decisive for an accurate solution. This numerical method is also called as direct numerical simulation. Within the category of interface-resolving method, several numerical techniques have been developed with different interface capturing processes such as volume-of-fluid method [62], level-set method [129], front-tracking method [138] and phase-field method [71]. Volume-of-fluid method and level-set method resolve sharp interface with zero interfacial thickness. These methods solve topological equations for modeling interface evolution. Volume-of-fluid method reconstructs the interface with volume fraction and normal vector of the interface plane in the cell, while level-set method extracts the interface by an interpolation of the zero level set of smooth scalar function. The volume-of-fluid method has advantageous volume (and mass) conservation properties but also has complexities in interface reconstruction step. In contrary, the advantage of level-set method is its ability to capture the changing complex interfacial shape, but the defective mass conservation is one of the known disadvantages. Front tracking method is a sort of immersed boundary method, in which the interface movements are continuously tracked by a set of Lagrangian marker points. Since the interface is represented by the boundary conditions located at the exactly same position of the interface, it is straightforward to handle the multiple interfaces at a single cell with this method. However, an additional model is required in case of merging interface.

Apart from the methods mentioned above, phase-field method is a diffuse interface method which postulates the finite width at the interfacial area [71]. Eliminating topological equations give a great advantage of modeling interface. No additional model is necessary for the merging and adhesion, e.g. wetting phenomena on the surface. Cai [13] shows that the phase-field method is promising tools to predict the rising and splitting phenomena. However, there is an issue of parameters for determining interfacial thicknesses. Besides, several methods (color-function volume-of-fluid, conservative level-set and moment-of-fluid) have been studied for direct numerical simulation of two-phase flow as well. All these methods allow having detail insight into the transport phenomena in multiphase flow and assist improving and optimizing industrial applications, e.g. in micro process engineering [45, 47, 150].

***Mass transfer across a phase interface***

In addition to the difficulties of interface evolution, numerical methods for interfacial mass transfer suffer from two further difficulties, namely (i) the concentration jump at the interface and (ii) thin boundary layers with large concentration gradients normal to the interface. To tackle these difficulties, two different approaches have been developed especially. Two-field (or two-scalar) approach solves separate concentration equations for each phase [7, 9, 10, 84], while single-field approach solves a single interpenetration equation of concentration in the entire domain. To fulfil thermodynamic equilibrium and component flux continuity at the interface, a special numerical treatment of diffusion term is essential for both in single-field and two-scalar approaches. Single-field method is further classified into two types of the approach according to the modeling concentration at the interface. In several studies [25, 53, 101], the discontinuity of concentrations across the phase interface is numerically preserved. Otherwise, the concentration field of certain phase is transformed, which allows solving continuous concentration at the interface [8, 55, 110, 113, 148]. Moreover, the (moving) interface computed by such an interface-capturing method is often not aligned with the mesh cell boundaries but divides the mesh cell volume into two subdomains, which may also cause the position dependency of numerical solutions. In TURBIT-VOF, Onea et al. [110] implemented a single-field volume-averaged species transport equation with additional term regarding the concentration jump as a form of volume-averaged diffusive fluxes of mixture concentration. The additional term is implicitly computed by diffusive mass fluxes at the interface, which is suggested by Davidson et al. [24].

## 1.4 Multicomponent diffusion

Convection and diffusion are representative mechanisms of mass transport in nature. For the multicomponent system, convective mass flux is naturally obtained with known velocity field, while diffusive mass flux is not straightforwardly defined due to the complex interactions between molecules. Therefore, modeling diffusion has played an important part for most of the engineering problems accompanying mass transfer. Basically, the diffusion is a natural phenomenon of molecular movement driven by the concentration gradient. In the classical Fick's law of diffusion, the diffusive flux of species is defined by a linear relation of the concentration gradient, which is similar to Newton's law of viscosity and Fourier's law of conduction [6]. This simple but general approach can initiate the studies on diffusive mass transfer in a mathematical way.

Fick's law is derived with an assumption of binary system where a species diffuses into the other species. It is also valid for the dilute condition in which the species are diluted by large excess of certain species components [132]. However, the practical engineering problems associated with chemical reactions mostly consist of multicomponent system where more than two species undergo mass transfer. The diffusion in multicomponent system, so-called multicomponent diffusion can be significantly different from the binary diffusion, obviously. In addition to the Fick's law, Maxwell-Stefan equation is proposed to describe the multicomponent system as well. This equation is based on the independent works of Maxwell [102] and Stefan [127], which are derived from collision dynamics of molecules [6, 23, 132]. Also, Furry [35] and Williams [143] re-derives the equation of multicomponent diffusion by macroscopic conservation equations of all species [92]. In Maxwell-Stefan equation, the concentration gradient is a linear function of the mass fluxes, while the mass flux is a linear combination of the concentration gradient in Fick's law. These two approaches (Fick's law and Maxwell-Stefan equation) are the major formulations of multicomponent diffusion. Plenty of studies regarding practical mass transfer can be classified into these two formulations.

Beyond the mathematical formulations, Chapman [15] and Enskog [32] model the transport properties for binary gas mixtures by detailed kinetic theory. Later, Curtiss and Hirschfelder [22] extend this Chapman-Enskog method to multicomponent gas mixtures. For general investigation of the driving forces of diffusion, these two formulations are associated with thermodynamically irreversible process [5, 21], which is originally developed by Onsager [111]. The use of generalized Fick's law and Maxwell-Stefan equations with computational fluid dynamics is examined by Gandhi [36], who notes that currently the diffusion model is essential in many computational problems relating to mass transport phenomena. The detailed history of multicomponent diffusion theory is well summarized in Bird et al. [5].

## 1.5 Objectives

With remarkable advantages of gas-liquid Taylor flow reactor as mentioned in this chapter, the subject of this study is the development of a computer code that allows the numerical investigation of reactive gas-liquid flows in a single channel of monolith reactor. For this purpose, two well-developed computer codes, TURBIT-VOF [112] and DETCHEM$^{TM}$ [30] have been coupled. Hence, the interface evolution of two-phase flow and the associated mass transport in both phases is described by TURBIT-VOF, while the detailed chemical reactions at the catalytic walls are modeled by DETCHEM$^{TM}$.

The simulations of flow and mass transport for large numbers of bubbles are out of reach with current computation power even for the two-dimensional problem. For efficient numerical investigations, this study adopts, therefore, the following strategies; (i) the Taylor flow is ideal (i.e. the bubbles and liquid slugs have identical shape and velocity), and (ii) there is no feedback of mass transport and reactions on hydrodynamics. With these assumptions, hydrodynamic simulations of a single Taylor flow have been performed in the unit cell with periodic boundary conditions until a quasi-steady bubble shape and velocity field are obtained. The velocity fields are transformed into the moving reference frame of the bubble. The flow fields in the moving frame are further utilized for solving unsteady species transport equations which account for the mass transfer from the gas into the liquid phase. Overall, our approach allows studying the time-dependent reactive mass transfer with “frozen” but realistic hydrodynamics and reasonable computational effort.

The novelty of this study emerges in the process of devising a numerical methodology for modeling reactive Taylor flow. Hydrogenation of nitrobenzene is the reaction of interest in this study. Taylor flow of a low viscous fluid has been numerically taken into account with real physical properties for the first time. Moreover, the multispecies two-phase mass transfer has been investigated by virtue of multi-component and interfacial diffusion models. The catalyzed reaction is modeled by both global one-step reaction mechanism (with four bulk species) and detailed kinetic mechanism that covers additional ten surface species. The developed computer code finally enables analyzing not only the bulk species distributions in the fluid phase but also the surface species behaviors at the catalyzed wall.

To sum up, the main goals of this study are:

1. Coupling TURBIT-VOF and DETCHEM$^{TM}$, which enables the calculation of gas-liquid flow and associated mass transfer with detailed catalytic reaction mechanism, simultaneously.
2. Extension of the mass transfer routine in TURBIT-VOF for the calculation of mass transfer involving multi-component diffusion.
3. Study on the reaction mechanisms for hydrogenation of nitrobenzene to aniline.
4. Investigation of gas-liquid mass transfer characteristics within a Taylor flow accompanying heterogeneous reaction.

# Chapter 2 Mathematical description

This chapter is devoted to mathematical formulations for calculating gas-liquid Taylor flow with catalytic surface reaction. Section 2.1 describes the equations of mass and momentum conservations for gas-liquid flow. Numerical method of interface evolution (volume-of-fluid method) is introduced in Section 2.2. Next, the species conservation equation is outlined in Section 2.3. Section 2.4 details the numerical approaches for reactive two-phase mass transfer. Finally, multispecies diffusion models are introduced in Section 2.5.

## 2.1 Equations for hydrodynamics

TURBIT-VOF is an in-house volume-of-fluid computer code with piecewise linear interface calculation (PLIC) method on a staggered Cartesian grid [112]. This code was developed for direct numerical simulation of two-phase hydrodynamics and validated with the solutions of Taylor bubbles in a square mini-channel [33]. The special numerical model for two-phase mass transfer has also been implemented for the case of transient interfacial mass transfer of single species [110]. The assumptions employed in TURBIT-VOF for hydrodynamic calculations are as follow:

- Constant temperature
- Constant fluid properties (e.g. density and viscosity)
- Constant volume of the bubble
- Gravity/buoyancy is neglected
- No phase change
- No feedback of mass transfer on hydrodynamics

The physical properties depend highly on temperature and pressure. In constant temperature and constant mean pressure, they are usually a function of mixture composition. Nonetheless, TURBIT-VOF focuses only on the case where the fluid properties are constant during the calculation. The reason is that in practical reactive two-phase mass transfer, the produced concentration in liquid phase is very small as compared to the concentration of liquid solvent. Therefore, it can be assumed that the liquid composition is constant during the calculation time that covers only a short moment, where the changing liquid composition is sufficiently small to be neglected. This is the main assumption corresponding to the first three assumptions of the solver mentioned above. Based on these assumptions, the present study mainly deals with the diluted condition where the concentrations of individual species are much smaller than that of diluent. In diluted condition, the heat of reaction can be negligible as well, which complies with the assumption of constant temperature. Since the volume of bubbles keeps constant during the calculation, the bubble shrinking phenomena induced by mass transfer cannot be considered as well as condensation and evaporation. Heterogeneous reactions are only taken into account in the present study.

With these assumptions, the solver computes the non-dimensional single-field Navier-Stokes equations, the liquid volume fraction equation and species transport equation, simultaneously. This section introduces the governing equations and those numerical implementations.

### *Non-dimensional continuity and momentum equations*

For two immiscible incompressible fluids with constant physical properties, Sabisch [123] derived the non-dimensional single-field conservation equations for mass and momentum. Based on the single-field formulation, two-phase mixture properties, $\mathbf{u}_{\mathrm{m}}^{*}$, $\rho_{\mathrm{m}}^{*}$ and $\mu_{\mathrm{m}}^{*}$, are defined by

$$\mathbf{u}_{\mathrm{m}}^{*} := \frac{1}{u_{\mathrm{ref}}} \frac{f \rho_{\mathrm{L}} \bar{\mathbf{u}}_{\mathrm{L}}^{\mathrm{V_L}} + (1-f)\rho_{\mathrm{G}} \bar{\mathbf{u}}_{\mathrm{G}}^{\mathrm{V_G}}}{f\rho_{\mathrm{L}} + (1-f)\rho_{\mathrm{G}}}, \tag{2.1}$$

$$\rho_{\mathrm{m}}^{*} := f + (1-f)\Gamma_{\rho}, \tag{2.2}$$

$$\mu_{\mathrm{m}}^{*} := f + (1-f)\Gamma_{\mu} \tag{2.3}$$

where $f$ denotes the volume fraction of liquid, and $\bar{\mathbf{u}}_{\mathrm{L}}^{\mathrm{V_L}}$, $\bar{\mathbf{u}}_{\mathrm{G}}^{\mathrm{V_G}}$ in Eq. (2.1) are the intrinsic mean velocities averaged over the volume of the respective phase within a mesh cell. With these two-phase mixture properties and the dimensionless values defined in Table 1, the non-dimensional mass-averaged continuity and momentum equations are given by

$$\nabla^{*} \cdot \mathbf{u}_{\mathrm{m}}^{*} = 0, \tag{2.4}$$

Table 1: Definitions of dimensionless parameters and numbers for non-dimensional governing equations.

| Dimensionless parameters | | Dimensionless numbers | |
|---|---|---|---|
| Length | $\mathbf{x}^* := \mathbf{x}/L_\text{ref}$ | Reynolds | $Re_\text{ref} := \dfrac{\rho_\text{ref} L_\text{ref} u_\text{ref}}{\mu_\text{ref}}$ |
| Time | $t^* := t/t_\text{ref} = t u_\text{ref}/L_\text{ref}$ | | |
| Pressure | $p^* := p/(\rho_\text{ref} u_\text{ref}^2)$ | Weber | $We_\text{ref} := \dfrac{\rho_\text{ref} L_\text{ref} u_\text{ref}^2}{\sigma}$ |
| Density ratio | $\Gamma_\rho := \rho_\text{G}/\rho_\text{ref}$ | | |
| Viscosity ratio | $\Gamma_\mu := \mu_\text{G}/\mu_\text{ref}$ | Eötvös | $E\ddot{o}_\text{ref} := \dfrac{(\rho_\text{ref} - \rho_\text{G}) g L_\text{ref}^2}{\sigma}$ |
| Interfacial area concentration | $a_\text{int}^* := a_\text{int} L_\text{ref}$ | | |
| Interface curvature | $\kappa^* := \kappa L_\text{ref}$ | Froude | $Fr_\text{ref} := \dfrac{g L_\text{ref}}{u_\text{ref}^2}$ |
| Spatial gradient | $\nabla^* := L_\text{ref} \nabla$ | | |
| Temporal gradient | $\partial/\partial t^* := (L_\text{ref}/u_\text{ref})\partial/\partial t$ | Euler | $Eu_\text{ref} := \dfrac{p_0 - p_{L_\text{axial}}}{\rho_\text{ref} u_\text{ref}^2}$ |
| Concentration | $c_i^* := c_i/c_\text{ref}$ | | |
| Diffusivity | $D^* := D/D_\text{ref}$ | Peclet | $Pe_\text{ref} := \dfrac{L_\text{ref} u_\text{ref}}{D_\text{ref}}$ |
| Diffusive flux | $\mathbf{j}_i^{\text{V}*} := \mathbf{j}_i^{\text{V}*} L_\text{ref}/(c_\text{ref} D_\text{ref})$ | | |

$$\begin{aligned} \frac{\partial\left(\rho_\text{m}^* \mathbf{u}_\text{m}^*\right)}{\partial t^*} + \nabla^* \cdot \rho_\text{m}^* \mathbf{u}_\text{m}^* \mathbf{u}_\text{m}^* &= -\nabla p^* + \frac{1}{Re_\text{ref}} \nabla^* \cdot \mu_\text{m}^* \left[\nabla \mathbf{u}_\text{m}^* + \left(\nabla \mathbf{u}_\text{m}^*\right)^\text{T}\right] + \frac{a_\text{int}^* \kappa^* \hat{\mathbf{n}}_\text{int}}{We_\text{ref}} \\ &\quad -(1-f)\frac{E\ddot{o}_\text{ref}}{We_\text{ref}} \hat{\mathbf{e}}_g + Fr_\text{ref} \hat{\mathbf{e}}_g + \frac{Eu_\text{ref}}{L_\text{axial}^*} \hat{\mathbf{e}}_\text{axial} \end{aligned} \tag{2.5}$$

Four additional source terms on the right hand side of Eq. (2.5) represent the surface tension, buoyancy, gravity and axial pressure difference, respectively. $\hat{\mathbf{n}}_i$ in the surface tension term means the unit normal vector of interface toward liquid phase. $\hat{\mathbf{e}}_g$ appearing in the buoyancy and gravity term denotes the unit vector in the direction of gravity. $\hat{\mathbf{e}}_\text{axial}$ in the axial pressure difference term represents the unit vector in axial direction. These equations are solved by finite volume method in the structured staggered grid. An explicit third-order Runge-Kutta method is employed for time integration, whereas central difference and upwind schemes are available for the approximation of spatial derivatives. In this study, upwind scheme is selected (see Appendix F).

### *Non-dimensional volume fraction equation*

According to the definition of $f$, for $f = 1$ the cells are filled with liquid, while for

$f = 0$ the cells are filled with gas. In the interfacial cells where both phases exist in the mesh cell instantaneously, $f$ takes any value between 0 and 1. The transport of the liquid volume fraction is defined by an advection equation as

$$\frac{\partial f}{\partial t^*} + \nabla^* \cdot f\mathbf{u}_{\mathrm{m}}^* = 0 \tag{2.6}$$

In the solution procedure, the liquid volume fraction is calculated simultaneously with Eq. (2.4) and (2.5). Due to the large gradient of $f$ at the interface, Eq. (2.6) is not solved by classical discretization schemes because this would give rise to a numerical smearing of the interface. Instead, the interface is resolved in geometrical way to avoid the artificial thickness of interface. Thus, volume-of-fluid method is classified as a sharp interface method. Wörner [147] summarized there are several zero interface thickness models: moving mesh, front-tracking, level-set, interface reconstruction volume-of-fluid method, and finite interface thickness models: color function volume-of-fluid, conservative level-set and phase-field method.

## 2.2 Numerical method for hydrodynamics

***Volume-of-Fluid (VOF) method***

Volume-of-fluid (VOF) method is developed by Hirt and Nichols [62] for numerical simulation of two-phase flow. The main idea of this method is to solve additional transport equation for volume fraction of phases. As shown in the name of the code, TURBIT-VOF employs VOF method for interface evolution. A major advantage of VOF method as compared to the level-set and front-tracking method is its excellent conservation of mass in both phases. To keep the interface numerically sharp, VOF solves Eq. (2.6) by transforming the advection term to surface integral by Gauß divergence theorem. This procedure requires the phase distribution at the cell face and this information can be obtained by interface reconstruction process.

Two types of reconstruction schemes are generally used in VOF method. Simple Line Interface Calculation (SLIC) method assumes that the interface is orientated in parallel to the cell face, while in Piecewise Linear Interface Calculation method (PLIC) the interface is illustrated by a plane whose orientation is defined by a unit normal vector. In cuboid type mesh cell, the interface defined by SLIC is always orientated either horizontally or vertically against the cell face. On the other hand, the interface orientation in PLIC method is computed by the volume fractions in neighboring mesh cells, which can resolve the actual shape of interface with sufficient number of mesh cells. A known disadvantage of PLIC method is that the interface in two neighboring mesh cells is not continuous at the cell face between both mesh cells.

***EPIRA***

TURBIT-VOF utilizes Exact Plane Interface Reconstruction Algorithm (EPIRA) which is a special numerical method developed by Sabisch [123]. This method yields a linearly-accurate interface reconstruction on a three-dimensional structured orthogonal non-equidistant grid. In case of having two neighboring cells that contain interface, the reconstruction method determines a unit normal vector of the interface and a position of the interface at the cell face. When the interface is placed between lower and upper faces of both mesh cells, the interface can be exactly defined in geometrical way. However, if the interface crosses the lower (or upper) faces of the cell, the additional information of adjacent cells that the interface passes through is required. For this case, EPIRA considers the extended cells that contain the original and additional cells in the lower and/or upper direction so that it enables the interface geometrically defined therein. Thus, the extension of cell is performed by considering adjacent cells when the basic pair of cells cannot determine the slope of the interface plane exactly. In some cases where the direction of extension is ambiguous, additional statements are required to define the direction of extension. The procedure to determine the direction of extension is detailed in Appendix A. With the slope obtained with or without extension, the position of interface is determined by iteratively shifting the plane until the correct liquid volume fraction is found. The interface reconstruction is completed by determining slope and the position of the interface at the cell face. Further numerical technique regarding the treatment of possible numerical errors is described in Appendix B.

## 2.3 Equations for mass transfer

Mass transfer takes place with concentration difference. This physical phenomenon can be mathematically expressed by several classical approaches as well as numerical models established with those mathematical relations. This section describes the definitions and mathematical relations for two-phase mass transfer. The constituent of mixture can be defined in various types with regard to the applications. For single-phase, mole fraction or mass fraction is widely used, while concentration is more convenient to measures for two-phase. The mathematical expressions are therefore reviewed by these three different types of the mixture definitions [132]. In TURBIT-VOF, concentration is chosen for the expression of species composition. However, other notations still appear in order to analyze and compare the results with the reference data presented in several validation cases in Chapter 3. All quantities are convertible.

### *Definitions and partial mass balances*

For the mixture comprised of $n$ chemical species, thermodynamic state is determined by $n$ partial mass densities $\rho_1,...,\rho_n$, by $n$ partial velocities $\mathbf{u}_1,...,\mathbf{u}_n$ of the constituents (with respect to a fixed frame of reference) and by the temperature $T$. With different interests of applications, the mixture composition is described by three types of species composition, mole fraction, mass fraction and volume fraction. According to the three types of composition, the velocity of the mixture and the flux relative to the chosen velocity are also defined separately as described in Table 2.

With these definitions, the diffusive flux for each type of composition is defined by relevant terms for the respective type of composition

$$\mathbf{J}_i := c_i(\mathbf{u}_i - \mathbf{U}) \text{ and } \sum_{i=1}^{n} \mathbf{J}_i = 0 \tag{2.7}$$

Table 2: Notation for parameters in mole, mass and volume reference frame.

| Type of composition | Mole | Mass | Volume |
|---|---|---|---|
| Amount of constituent | $X_i := c_i / c_\mathrm{t}$<br>Mole fraction | $y_i := \rho_i / \rho_\mathrm{t}$<br>Mass fraction | $\phi_i := x_i\bar{V}_i / \sum x_i\bar{V}_i = c_i\bar{V}_i$<br>Volume fraction |
| Total amount of mixture | $c_\mathrm{t} := \sum_{i=1}^{n} c_i$<br>Molar concentration | $\rho_\mathrm{t} := \sum_{i=1}^{n} \rho_i$<br>Mass density | $\bar{V}_\mathrm{t} := 1 / \sum_{i=1}^{n} c_i = 1 / c_\mathrm{t}$<br>Mixture molar volume |
| Velocity | $\mathbf{U} := \sum_{i=1}^{n} X_i\mathbf{u}_i$<br>Molar-average velocity | $\mathbf{u} := \sum_{i=1}^{n} y_i\mathbf{u}_i$<br>Mass-average velocity | $\mathbf{u}^\mathrm{V} := \sum_{i=1}^{n} \phi_i\mathbf{u}_i$<br>Volume-average velocity |
| Flux | $\mathbf{N}_i := c_i\mathbf{U}_i$,<br>$\mathbf{N}_\mathrm{t} = \sum_{i=1}^{n} \mathbf{N}_i = c_\mathrm{t}\mathbf{U}$<br>Molar flux | $\mathbf{n}_i := \rho_i\mathbf{u}_i$,<br>$\mathbf{n}_\mathrm{t} = \sum_{i=1}^{n} \mathbf{n}_i = \rho_\mathrm{t}\mathbf{u}$<br>Mass flux | $\mathbf{n}_i^\mathrm{V} := c_\mathrm{t}\phi_i\mathbf{u}_i$,<br>$\mathbf{n}_\mathrm{t}^\mathrm{V} = \sum_{i=1}^{n} \mathbf{n}_i^\mathrm{V} = c_\mathrm{t}\mathbf{u}^\mathrm{V}$<br>Molar flux by volume fraction |

$$\mathbf{j}_i := \rho_i(\mathbf{u}_i - \mathbf{u}) \text{ and } \sum_{i=1}^{n} \mathbf{j}_i = 0 \tag{2.8}$$

$$\mathbf{j}_i^{\mathrm{V}} := c_i(\mathbf{u}_i - \mathbf{u}^{\mathrm{V}}) \text{ and } \sum_{i=1}^{n} \bar{V}_i \mathbf{j}_i^{\mathrm{V}} = 0 \tag{2.9}$$

and fluxes of species $i$ are given by

$$\mathbf{N}_i = \mathbf{J}_i + c_i \mathbf{U} = \mathbf{J}_i + X_i \mathbf{N}_{\mathrm{t}} \tag{2.10}$$

$$\mathbf{n}_i = \mathbf{j}_i + \rho_i \mathbf{u} = \mathbf{j}_i + y_i \mathbf{n}_{\mathrm{t}} \tag{2.11}$$

$$\mathbf{n}_i^{\mathrm{V}} = c_{\mathrm{t}} \bar{V}_i \mathbf{j}_i^{\mathrm{V}} + c_{\mathrm{t}} \phi_i \mathbf{u}^{\mathrm{V}} = c_{\mathrm{t}} \bar{V}_i \mathbf{j}_i^{\mathrm{V}} + \phi_i \mathbf{n}_{\mathrm{t}}^{\mathrm{V}} \tag{2.12}$$

The partial mass balance equations corresponding to mole, mass and volume are accordingly

$$c_{\mathrm{t}}\left(\frac{\partial X_i}{\partial t} + \mathbf{U} \cdot \nabla X_i\right) + \nabla \cdot \mathbf{J}_i = R_i \tag{2.13}$$

$$\rho_{\mathrm{t}}\left(\frac{\partial y_i}{\partial t} + \mathbf{u} \cdot \nabla y_i\right) + \nabla \cdot \mathbf{j}_i = r_i \tag{2.14}$$

$$\frac{\partial c_i}{\partial t} + \nabla \cdot c_i \mathbf{u}^{\mathrm{V}} + \nabla \cdot \mathbf{j}_i^{\mathrm{V}} = r_i^{\mathrm{V}} \tag{2.15}$$

where $\mathbf{U}$, $\mathbf{u}$ or $\mathbf{u}^{\mathrm{V}}$ are the velocity field, $\mathbf{J}_i$, $\mathbf{j}_i$ or $\mathbf{j}_i^{\mathrm{V}}$ are the diffusive fluxes and $R_i$, $r_i$ or $r_i^{\mathrm{V}}$ are the source/sink term by chemical reactions. Without homogeneous reaction, the source term is set to zero. The equation (2.15) cannot take the same form as equation (2.13) and (2.14) because there is no conservation law of volume, in general [132].

***Non-dimensional species transport equation***

As mentioned in the beginning of this section, TURBIT-VOF employs concentration as a type of composition for calculation of mass transfer. Therefore, the concentration equation Eq. (2.15) is considered to account for the mass transfer in two-phase condition. The use of concentration is more effective for the composition of liquid mixture as it is common in literature concerning two-phase mass transfer. However, the computational fluid dynamics usually come up with the mass-average velocity from the mass conservation. Though all definitions of equations must be consistent in principle, the current version of TURBIT-VOF solves the volume-average concentration equation, mass-average continuity Eq. (2.4) and momentum equations Eq. (2.5), indeed. The difference among the use of different type of velocities is discussed in section 3.5.

The volume-average concentration equation can be derived from Eq. (2.15). With dimensionless parameters defined in Table 1, unsteady three-dimensional single-field concentration equation is given in non-dimensional form as

$$\frac{\partial c^*_{\mathrm{m},i}}{\partial t^*} + \nabla^* \cdot \left( c^*_{\mathrm{m},i} \mathbf{u}^*_{\mathrm{m}} \right) = -\frac{1}{Pe_{\mathrm{ref}}} \mathbf{j}^{\mathrm{V}*}_{\mathrm{m},i} \tag{2.16}$$

where $\mathbf{u}^*_{\mathrm{m}}$ is the mass-average velocity defined in Eq. (2.1) and $Pe_{\mathrm{ref}}$ is the reference Peclet number given in Table 1. Since homogeneous reaction is not considered in Eq. (2.16), the source term shown on the right hand side of Eq. (2.15) disappears. $c_{\mathrm{m},i}$ in Eq. (2.16) denotes the non-dimensional two-phase mixture concentrations for $i$'th species,

$$c^*_{\mathrm{m},i} = f c^*_{\mathrm{L},i} + (1-f) H_i \cdot c^*_{\mathrm{G},i} \tag{2.17}$$

where $f$ is the liquid volume fraction within a mesh cell. $c_{\mathrm{L},i}$ and $c_{\mathrm{G},i}$ are the concentration of $i$ 's species in liquid and gas phase, respectively. Normally, m indicates the mixture of composition in the single-phase multispecies diffusion, but in this section, it represents the mixture of gas and liquid phase. Furthermore, $H_i$ is the dimensionless Henry number as

$$H_i := \frac{c^*_{\mathrm{L},i}}{c^*_{\mathrm{G},i}} \tag{2.18}$$

It represents the ratio of concentration on both sides of interface according to the thermodynamic equilibrium. When $H_i \neq 1$, a concentration jump occurs at the interface. However, the definition of mean concentration, Eq. (2.17) makes the concentration profile continuous at the interface, which benefits from avoiding sharp concentration difference in numerical point of view. The non-dimensional diffusive flux on the right hand side of Eq. (2.16) is given by

$$\mathbf{j}^{\mathrm{V}*}_{\mathrm{m},i} = -\nabla^* \left( D^*_{\mathrm{m},i} \nabla^* c^*_{\mathrm{m},i} \right) \tag{2.19}$$

where $D^*_{\mathrm{m},i}$ is the dimensionless two-phase mixture diffusivity,

$$D^*_{\mathrm{m},i} = f D^*_{\mathrm{L},i} + (1-f) D^*_{\mathrm{G},i} \tag{2.20}$$

## 2.4 Numerical method for mass transfer

In the numerical procedure of transport equations, TURBIT-VOF utilizes 3rd order Runge-Kutta method and upwind scheme for time and spatial derivatives, respectively. These numerical schemes are identically used to solve the species transport equations for two-phase mass transfer. Numerical methods in the solution procedure are described in this section. The subsections are organized as follows. The discretized species transport equation is given in Section 2.4.1, and its boundary conditions are defined by discretized equations in Section 2.4.2. Section 0 introduces the continuous concentration diffusion model (CCDM) developed for considering mass transfer across the phase interface more accurately. Finally the concept of coupling TURBIT-VOF and DETCHEM$^{\text{TM}}$ is presented in Section 2.4.4.

### 2.4.1 Discretization

The convective and diffusive fluxes in Eq. (2.16) are discretized by upwind and 2nd order central difference scheme, respectively. As discussed by Ghidersa [39], the centered difference scheme is more suitable for the bulk region of each fluid, while the upwind scheme prevents the oscillations of the transported quantity, e.g. concentration at the interface between phases. In this study, upwind scheme is chosen for the species transport equations as well as the momentum equation (see Appendix F).

***Convective term***

$$
\begin{aligned}
&\nabla^* \cdot \left(c^*_{\mathrm{m},i}\mathbf{u}^*_{\mathrm{m}}\right)_{i,j,k} \\
&= \frac{1}{\Delta x^*}\Big\{u^*_{\mathrm{m},x;i+1/2,j,k}\Big[0.5\Big(1+\mathrm{sgn}\Big(u^*_{\mathrm{m},x;i+1/2,j,k}\Big)\Big)c^*_{\mathrm{m},i;i,j,k}+0.5\Big(1-\mathrm{sgn}\Big(u^*_{\mathrm{m},x;i+1/2,j,k}\Big)\Big)c^*_{\mathrm{m},i;i+1,j,k}\Big] \\
&\qquad -u^*_{\mathrm{m},x;i-1/2,j,k}\Big[0.5\Big(1+\mathrm{sgn}\Big(u^*_{\mathrm{m},x;i-1/2,j,k}\Big)\Big)c^*_{\mathrm{m},i;i-1,j,k}+0.5\Big(1-\mathrm{sgn}\Big(u^*_{\mathrm{m},x;i-1/2,j,k}\Big)\Big)c^*_{\mathrm{m},i;i,j,k}\Big]\Big\} \\
&+\frac{1}{\Delta y^*}\Big\{u^*_{\mathrm{m},y;i,j+1/2,k}\Big[0.5\Big(1+\mathrm{sgn}\Big(u^*_{\mathrm{m},y;i,j+1/2,k}\Big)\Big)c^*_{\mathrm{m},i;i,j,k}+0.5\Big(1-\mathrm{sgn}\Big(u^*_{\mathrm{m},y;i,j+1/2,k}\Big)\Big)c^*_{\mathrm{m},i;i,j+1,k}\Big] \\
&\qquad -u^*_{\mathrm{m},y;i,j-1/2,k}\Big[0.5\Big(1+\mathrm{sgn}\Big(u^*_{\mathrm{m},y;i,j-1/2,k}\Big)\Big)c^*_{\mathrm{m},i;i,j-1,k}+0.5\Big(1-\mathrm{sgn}\Big(u^*_{\mathrm{m},y;i,j-1/2,k}\Big)\Big)c^*_{\mathrm{m},i;i,j,k}\Big]\Big\} \\
&+\frac{1}{\Delta z^*_k}\Big\{u^*_{\mathrm{m},z;i,j,k+1/2}\Big[0.5\Big(1+\mathrm{sgn}\Big(u^*_{\mathrm{m},z;i,j,k+1/2}\Big)\Big)c^*_{\mathrm{m},i;i,j,k}+0.5\Big(1-\mathrm{sgn}\Big(u^*_{\mathrm{m},z;i,j,k+1/2}\Big)\Big)c^*_{\mathrm{m},i;i,j,k+1}\Big] \\
&\qquad -u^*_{\mathrm{m},z;i,j,k-1/2}\Big[0.5\Big(1+\mathrm{sgn}\Big(u^*_{\mathrm{m},z;i,j,k-1/2}\Big)\Big)c^*_{\mathrm{m},i;i,j,k-1}+0.5\Big(1-\mathrm{sgn}\Big(u^*_{\mathrm{m},z;i,j,k-1/2}\Big)\Big)c^*_{\mathrm{m},i;i,j,k}\Big]\Big\}
\end{aligned}
\tag{2.21}
$$

where

$$\operatorname{sgn}\left(x\right)=\begin{cases} 1, & \text{for } x>0 \\ 0, & \text{for } x=0 \\ -1, & \text{for } x<0 \end{cases} \tag{2.22}$$

***Diffusive term***

$$\begin{aligned}
&-\left(\frac{1}{Pe_{\text{ref}}}\mathbf{j}^{\text{V}*}_{\text{m},i}\right)_{i,j,k} \\
&=\frac{1}{Pe_{\text{ref}}}\left\{\frac{1}{\Delta x^{*2}}\left[D^{*}_{\text{m},i;i+1/2,j,k}\left(c^{*}_{\text{m},i;i+1,j,k}-c^{*}_{\text{m},i;i,j,k}\right)-D^{*}_{\text{m},i;i-1/2,j,k}\left(c^{*}_{\text{m},i;i,j,k}-c^{*}_{\text{m},i;i-1,j,k}\right)\right]\right. \\
&\quad+\frac{1}{\Delta y^{*2}}\left[D^{*}_{\text{m},i;i,j+1/2,k}\left(c^{*}_{\text{m},i;i,j+1,k}-c^{*}_{\text{m},i;i,j,k}\right)-D^{*}_{\text{m},i;i,j-1/2,k}\left(c^{*}_{\text{m},i;i,j,k}-c^{*}_{\text{m},i;i,j-1,k}\right)\right] \\
&\quad\left.+\frac{1}{z_{k+1/2}-z_{k-1/2}}\left[D^{*}_{\text{m},i;i,j,k+1/2}\left(\frac{c^{*}_{\text{m},i;i,j,k+1}-c^{*}_{\text{m},i;i,j,k}}{z_{k+1}-z_{k}}\right)-D^{*}_{\text{m},i;i,j,k-1/2}\left(\frac{c^{*}_{\text{m},i;i,j,k}-c^{*}_{\text{m},i;i,j,k-1}}{z_{k}-z_{k-1}}\right)\right]\right\}
\end{aligned} \tag{2.23}$$

## 2.4.2 Boundary conditions

In TURBIT-VOF, two types of computational domain are available with different set of boundary conditions. According to the type of problem, TURBIT-VOF solves either the rectangular channel flow or the flow between two parallel plates in Cartesian coordinate. The boundary condition of $y$-direction is always periodic condition, while the boundary condition of $z$-direction is always the wall. The boundary condition of $x$-direction is periodic or wall condition in accordance with the type of problem. Based on the discretized fluxes given in section 2.4.1, the boundary condition for each flux at the wall in $z$-direction is given by

***Convective flux***

$$\frac{\partial}{\partial z^{*}}\left(c^{*}_{\text{m},i}u^{*}_{\text{m}}\right)_{k=1}=\frac{1}{\Delta z^{*}_{k=1}}\left(u^{*}_{\text{m},z;k=1.5}\frac{c^{*}_{\text{m},i;k=1}\Delta z^{*}_{k=2}+c^{*}_{\text{m},i;k=2}\Delta z^{*}_{k=1}}{\Delta z^{*}_{k=1}+\Delta z^{*}_{k=2}}-u^{*}_{\text{m},z;k=\text{wall}}\frac{c^{*}_{\text{m},i;k=1}+c^{*}_{\text{m},i;k=-1}}{2}\right) \tag{2.24}$$

***Diffusive flux***

$$-\left(\frac{1}{Pe_{\text{ref}}}j^{\text{V}*}_{\text{mz},i}\right)_{i,j,k}=\frac{1}{Pe_{\text{ref}}}\left\{\frac{1}{z^{*}_{k=1.5}}\left[D^{*}_{\text{m},i;k=1.5}\left(\frac{c^{*}_{\text{m},i;k=2}-c^{*}_{\text{m},i;k=1}}{z^{*}_{k=2}-z^{*}_{k=1}}\right)-D^{*}_{\text{m},i;k=\text{wall}}\left(\frac{c^{*}_{\text{m},i;k=1}-c^{*}_{\text{m},i;k=\text{wall}}}{z^{*}_{k=1}}\right)\right]\right\} \tag{2.25}$$

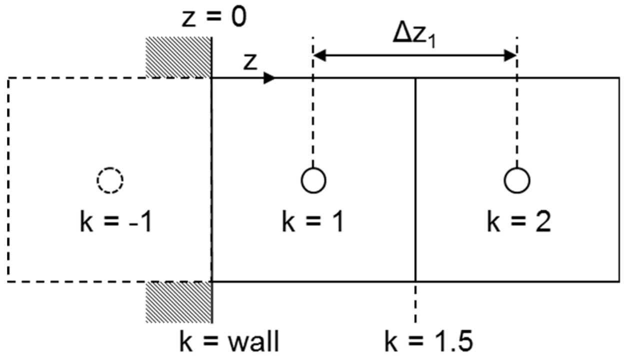

Fig. 2.1: Definition of the cells and those cell-centered indices near the boundary $(z=0)$.

According to the staggered grid, the concentration and the physical properties such as diffusivity are stored at the cell center, while the velocity is placed at the cell face. Fig. 2.1 shows the indices of the cells near the wall boundary. When there is no flux at the boundary, $u^*_{\mathrm{m}z;k=\mathrm{wall}}$ is equal to zero so that the right hand side of Eq. (2.24) is zero. If there is a convective flux at the boundary, $u^*_{\mathrm{m}z;k=\mathrm{wall}}$ and $c^*_{\mathrm{m},i;k=-1}$ are required. $c^*_{\mathrm{m},i;k=-1}$ is the concentration at the virtual mirrored cell of the first cell, and is approximated by a linear extrapolation. To define the diffusive flux at the boundary, the diffusivity at the boundary cell is additionally required. In this study, the diffusivity at the wall boundary is assumed the same as that of the first cell.

### 2.4.3 Continuous concentration diffusivity model (CCDM)

The definition of two-phase mixture concentration $c^*_{\mathrm{m}}$ enables treating the physical discontinuous concentration field as continuous concentration to ease the numerical procedure for mass transfer across the interface. In this continuous concentration formulation, the diffusivity at the interface cell is defined by Eq. (2.20). However, this two-phase mixture diffusivity $D^*_{\mathrm{m},i}$ is not sufficient to satisfy the mass conservation at the interface precisely. Therefore, special numerical treatments are required for the mesh cells containing both phases in order to ensure the continuity of physical mass flux across the interface. For this purpose, Onea et al. [110] adopted a numerical model into TURBIT-VOF, which revises the mixture diffusivities at the cells containing both phases. In the present study, this model is called as continuous concentration diffusivity model (CCDM). Let $k$ and $k+1$ denote the positions of two neighboring cell centers. Then, the revised two-phase mixture diffusivity at the position of the mesh cell face $k+1/2$ is computed as

$$D^*_{\mathrm{m},i;k+1/2} = \left( F_{i;k+1/2} \frac{{\lambda_{i;k+1/2}}^{-0.5}}{D^*_{\mathrm{m},i;k}} + G_{i;k+1/2} \frac{1.5 - \lambda_{i;k+1/2}}{D^*_{\mathrm{m},i;k+1}} \right)^{-1} \tag{2.26}$$

where

$$\lambda_{i;k+1/2} = \max\left[\min\left(f_{i;k} + f_{i;k+1}, 1.5\right), 0.5\right] \tag{2.27}$$

Here, it is $F_{i;k+1/2} = H_i$ for $f_k = 0$ and $0 < f_{k+1} \le 1$, and $F_{i;k+1/2} = 1$ otherwise. Similarly, it is $G_{i;k+1/2} = H_i$ for $f_{k+1} = 0$ and $0 < f_k \le 1$ and $G_{i;k+1/2} = 1$ otherwise. CCDM was validated with analytic/numerical solutions of one-dimensional transient diffusive mass transfer of a single species across a planar/cylindrical interface [110]. Although the author used mixture diffusivity for the name of this revised diffusivity, it is named two-phase mixture diffusivity in this study to avoid confusion between the mixture of species and the mixture of phases.

### 2.4.4 Data exchange between TURBIT-VOF and DETCHEM$^{\mathrm{TM}}$

In the coupled solver, TURBIT-VOF plays a role as a base code that interacts with embedded DETCHEM$^{\mathrm{TM}}$ subroutines. Fig. 2.2 introduces the calculation procedure of the coupled solver for a single time step. In the beginning, the data fields are initialized by initial conditions or restart conditions in TURBIT-VOF. Then, TURBIT-VOF starts solving volume of fluid, momentum and species transport equation. Meanwhile, DETCHEM$^{\mathrm{TM}}$ library provides the reaction rate, thermodynamic properties, transport properties of species mixture and other relevant properties for calculating reactions. Reaction mechanism and basic information for thermodynamic (e.g. polynomial coefficients) and transport properties (e.g. Lennard-Jones parameters) are prerequisite as they are given by additional input files for DETCHEM$^{\mathrm{TM}}$. To obtain the reaction rates, TURBIT-VOF firstly delivers the mole fraction, temperature and pressure at the previous time step (*n*-1), and then DETCHEM$^{\mathrm{TM}}$ calculates the reaction rates explicitly with the given data from TURBIT-VOF. After the reaction rates are obtained from DETCHEM$^{\mathrm{TM}}$, TURBIT-VOF updates the boundary conditions and finds the solution for the current time step (*n*). Coupled solver repeats this procedure in every time step to obtain the transient solution of reactive mass transfer.

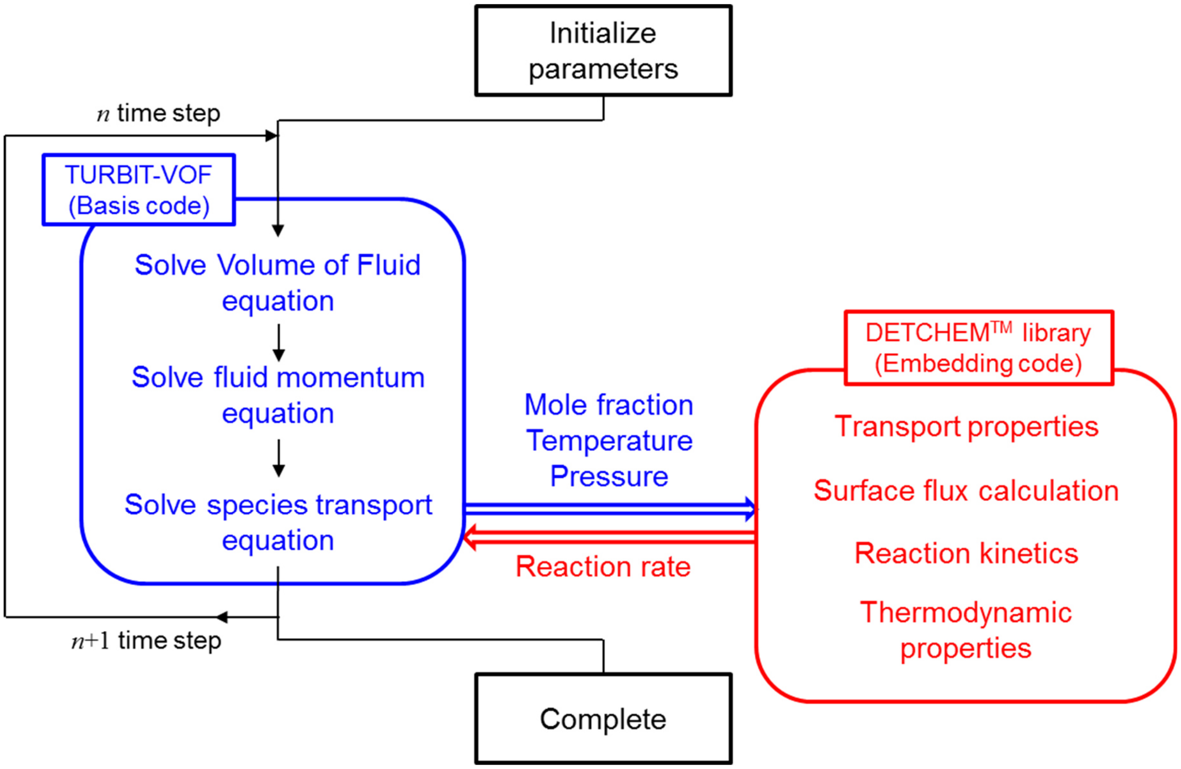
Initialize parameters
$n$ time step
TURBIT-VOF (Basis code)
Solve Volume of Fluid equation
Solve fluid momentum equation
Solve species transport equation
Mole fraction
Temperature
Pressure
Reaction rate
DETCHEM™ library (Embedding code)
Transport properties
Surface flux calculation
Reaction kinetics
Thermodynamic properties
$n$+1 time step
Complete

Fig. 2.2: Schematic diagram of coupling TURBIT-VOF and DETCHEM$^{\text{TM}}$.

For reactive mass transfer, TURBIT-VOF solves concentration equation while DETCHEM$^{\text{TM}}$ library calculates the reaction rates for boundary conditions. However, the equations of both solvers do not directly match because TURBIT-VOF consists of non-dimensional equations, whereas DETCHEM$^{\text{TM}}$ utilizes dimensional equations. Therefore, a transformation procedure between two solvers needs to convert the dimensional values into dimensionless values, or vice versa. Fig. 2.3 details the data exchanging procedure between TURBIT-VOF and DETCHEM$^{\text{TM}}$ library. Since heterogeneous reaction is only considered, this transformation appears only at the boundary condition of reactive wall. As a first step of data exchange, the concentration at the reactive wall can be estimated by a linear extrapolation and the non-dimensional concentration is transformed to the dimensional one for the input of DETCHEM$^{\text{TM}}$. After the transformation, the rate of surface reaction for $i$’th species can be obtained by

$$\dot{s}_i = \sum_k \nu_{ik} k_k \prod_i c_i \tag{2.28}$$

where $\nu_{ik}$ is the stoichiometric coefficient for $i$’th species in $k$'th reaction and $k_k$ is the rate

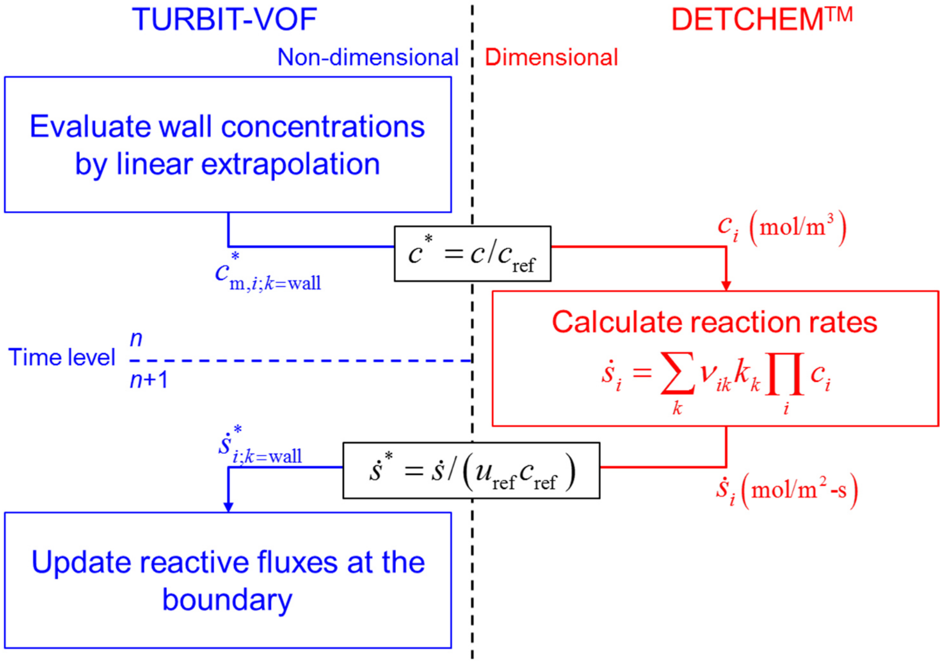
TURBIT-VOF
DETCHEM™
Non-dimensional
Dimensional
Evaluate wall concentrations by linear extrapolation
$c^* = c/c_{\mathrm{ref}}$
$c^*_{\mathrm{m},i;k=\mathrm{wall}}$
$c_i$ (mol/m³)
Calculate reaction rates
$\dot{s}_i = \sum_k \nu_{ik} k_k \prod_i c_i$
Time level
n
n+1
$\dot{s}^*_{i;k=\mathrm{wall}}$
$\dot{s}^* = \dot{s}/(u_{\mathrm{ref}} c_{\mathrm{ref}})$
$\dot{s}_i$ (mol/m²-s)
Update reactive fluxes at the boundary

Fig. 2.3: Data exchanging procedure between TURBIT-VOF and DETCHEM$^{\mathrm{TM}}$ at the reactive wall boundary.

constant of $k$ 'th reaction, which defined by Arrhenius type equation.

The concentration $c_i$ in Eq. (2.28) stands not only for the bulk species $c_{\mathrm{G},i}$ but also for the surface species $c_{\mathrm{S},i}$ adsorbed on the catalytic wall. The concentration of surface species is obtained by the surface coverage fraction $\theta_i$ with the relation $c_{\mathrm{S},i} = \Gamma_{\mathrm{S}}\theta_i/\psi_i$, where $\Gamma_{\mathrm{S}}$ is the surface site density and $\psi_i$ is the number of sites occupied by one particle of the species $i$ [30]. In present study, $\psi_i$ is assumed to be unity so that only one species particle occupies one site. Thus, the surface coverage is prerequisite to obtain the rate of surface reaction in Eq. (2.28). In general, the rates of changing surface coverage by absorption, surface reaction and desorption are much faster than the rate of changing bulk species by diffusion. Therefore, time-integrated surface coverages are used to estimate the surface reaction rate in DETCHEM$^{\mathrm{TM}}$ library. For this purpose, DETCHEM$^{\mathrm{TM}}$ employs inner iterations for the time integration of following equation:

$$\frac{dc_i}{dt} = \dot{s}_i \tag{2.29}$$

DETCHEM$^{\mathrm{TM}}$ integrates Eq. (2.29) to obtain surface species. In this integration, the gas concentration given by TURBIT-VOF is kept constant as it is assumed to be slower than the surface species movement, and the concentration of surface species (or coverages) only vary until the given time interval. To match the different time scales in two solvers, the time for integration is set to the same as the time step width used for solving species transport equation in TURBIT-VOF. The time step for the integration is 1/1000 of the time step for concentration equation so that 1000 inner iterations are used for this integration. At quasi-steady state, both terms in Eq. (2.29) become zero. When the solution reaches to the quasi-steady state during the integration process, the iteration is stopped, and DETCHEM$^{\mathrm{TM}}$ uses this quasi-steady surface coverage to calculate reactions. After the time integration, the reaction rates are calculated by Eq. (2.28) with the integrated surface coverage. The reaction rates are retransformed to non-dimensional forms by $\dot{s}_i^* = \dot{s}_i / u_{\mathrm{ref}} c_{\mathrm{ref}}$. Finally, the estimated non-dimensional reaction rate is applied to the reactive boundary flux in TURBIT-VOF:

$$\dot{s}_i^* = \frac{1}{Pe_{\mathrm{ref}}} j_{\mathrm{m},i}^{\mathrm{V}*} \tag{2.30}$$

where $j_{\mathrm{m},i}^{\mathrm{V}*}$ represents the constituent of dimensionless molar diffusive flux normal to the wall and $\dot{s}_i^*$ denotes the dimensionless reactive flux by surface reaction.

## 2.5 Modeling multicomponent diffusion

In the generalized Fick’s law of multicomponent system, the diffusion of a species is influenced not only by its own concentration gradient, but also by the concentration profile of the other species. Complex interactions between diffusing components (so-called cross-effects) may occur [6, 132] which cannot be described by the binary diffusion approximation. For multicomponent diffusion, the generalized Fick’s law requires the matrix of diffusivities for each species pair, which is not intuitively obtained by measurements since it contains also off-diagonal diffusivity. However, only binary diffusion coefficients are necessary for the Maxwell-Stefan equation. With the advantageous Maxwell-Stefan diffusivity and the similarity of the two formulations, the Fick’s diffusivity matrix can be obtained from the Maxwell-Stefan diffusivity by inversion of matrix [103, 132]. This so-called multicomponent model is widely used in analytical studies [86, 126] and in numerical applications [104, 137].

To avoid the costly matrix manipulations of the multicomponent diffusion model, Wilke [141] suggested an effective diffusivity model which assumes that a species diffuses into a mixture of the other species. It is also called dilute approximation model [6, 91] or mixture-averaged diffusion model [98]. This model can be used in diluted condition but has, in a strict point of view, limitations due to a violation of the overall mass conservation with omitting information of off-diagonal diffusivity as compared to the multicomponent model [6]. Nevertheless, the effective diffusivity model is also widely used in numerical simulations [29, 57, 74, 80, 139]. Studies have been conducted for the validity of effective diffusivity model in several application areas. They claim that the effective diffusivity model is sufficiently accurate in the area of modeling catalytic reactor [91, 124], while using effective diffusivity model causes significant errors in combustion simulations [26, 81].

In addition to the gaseous single-phase mass transfer introduced in previous paragraphs, the multicomponent diffusion is applied for the investigation of interfacial mass transfer as well. There have been many studies relating multicomponent separation process based on the film model which assumes that the mass transfer essentially occurs in the thin film region adjacent to the phase interface [132]. Krishnamurthy and Taylor [90] developed a non-equilibrium stage model (NESM) which divides the reactor into multi-stages wherein the mass and energy are balanced for each phase. The matrix of mass transfer coefficient for NESM can be estimated by Maxwell-Stefan equation [116]. This model was usually applied to the reactive separation process. Later, a mathematical model and its calculation method for heat and mass transfer with reaction in laminar falling liquid film were provided by Kenig et al. [85]. They extended their model for the heterogeneous reaction [82]. The developed models for both homogeneous and (quasi-) heterogeneous reactions are verified by numerical and linearized analytical approaches [83]. Finally, they provided a general analytical solution to the linearized diffusion-reaction problem for the multicomponent unsteady film model [86]. Also, the multicomponent system has been studied by computational fluid dynamic simulation coupled with the interface reconstruction methods. By level set method, hydrodynamic field is prescribed for adsorption of carbon dioxide in a falling film micro-contactor [16], and coupled mass and momentum transfer has been investigated within stagnant and rising droplet in toluene-water-acetone system [84]. Also, volume-of-fluid method is employed for the validation of interfacial mass transfer in multicomponent vapor-liquid flows [49]. However, most of these numerical studies use the binary diffusion coefficient, which cannot account for the multicomponent effect, or even directly assume the binary system for focusing more on the interfacial mass transfer. Only a few studies consider the multicomponent interfacial diffusion with the diffusivity matrix of which constant element diffusivity is independent on the composition [12, 20]. Both diffusion models have not been incorporated with the interfacial mass transfer on the moving interface so far.

This section is devoted to the mathematical modeling of diffusive fluxes in multicomponent systems. The classical theories of diffusion, Fick's law and Maxwell-Stefan equation, are firstly reviewed and the diffusion models, multicomponent model and effective diffusivity model are introduced. For derivation, only one-dimension is considered in this section. The diffusive flux vectors then simplify to $\mathbf{J}_i = (0,0,J_i)^{\mathrm{T}}$, $\mathbf{j}_i = (0,0,j_i)^{\mathrm{T}}$, and $\mathbf{j}_i^{\mathrm{V}} = (0,0,j_i^{\mathrm{V}})^{\mathrm{T}}$, where $J_i$, $j_i$, and $j_i^{\mathrm{V}}$ denote the diffusive fluxes of species $i$ in $z$-direction. One dimensional vectors with $n-1$ species are therefore defined as $\mathfrak{J} := \left(J_1, J_2, \ldots, J_{n-1}\right)^{\mathrm{T}}$, $\mathfrak{j} := \left(j_1, j_2, \ldots, j_{n-1}\right)^{\mathrm{T}}$, and $\mathfrak{j}^{\mathrm{V}} := \left(j_1^{\mathrm{V}}, j_2^{\mathrm{V}}, \ldots, j_{n-1}^{\mathrm{V}}\right)^{\mathrm{T}}$ for effective notation.

## 2.5.1 Generalized Fick's law

Fick's law represents the relation between the diffusive flux and the gradient of species by means of diffusion coefficient. For the mixture with $n$ species, $n-1$ species are independent by the definition of mixture composition. The fluxes of $n-1$ constituents and the gradients of the $n-1$ species are independent as well. Due to the linear relationship between the fluxes and the gradient, general Fick's law for $n$ species is written in a matrix form as

$$\mathfrak{J} = -c_{\mathrm{t}} \mathbb{D} \nabla \mathbf{X}, \tag{2.31}$$

where $\mathbf{X} = (X_1, X_2, ..., X_{n-1})^{\mathrm{T}}$ denotes the vector of $n-1$ mole fractions and $\mathbb{D}$ is a diffusivity matrix given by

$$\mathbb{D} = \begin{bmatrix} D_{1,1} & \cdots & D_{1,n-1} \\ \vdots & \ddots & \vdots \\ D_{n-1,1} & \cdots & D_{n-1,n-1} \end{bmatrix} \tag{2.32}$$

Accordingly, the generalized Fick's laws for the mass and volume reference frame are defined with related quantities as $\mathfrak{j} = -c_{\mathrm{t}} \mathbb{D}^{\circ} \nabla \mathbf{y}$ and $\mathfrak{j}^{\mathrm{V}} = -c_{\mathrm{t}} \mathbb{D}^{\mathrm{V}} \nabla \mathbf{c}$ with $\mathbb{D}^{\circ} \leftrightarrow D_{i,j}^{\circ}$ and $\mathbb{D}^{\mathrm{V}} \leftrightarrow D_{i,j}^{\mathrm{V}}$. The multicomponent Fick's diffusion coefficients can be transformed from one reference velocity frame to the other as well [132].

The diffusivity matrix $\mathbb{D}$, $\mathbb{D}^{\circ}$ or $\mathbb{D}^{\mathrm{V}}$ plays an important role to close the equations of general Fick's law. In binary systems ($n = 2$), the relation between the diffusive flux and the composition gradient of one species is simplified via a (scalar) binary diffusion coefficient $D_{i,j} = \text{Đ}_{i,j} > 0$ which can be obtained from experiments [132]. For $n > 3$ the Fick's diffusivities are not the same as the binary diffusion coefficients because the Fick's diffusivities implicitly depends on the $n$ 'th species. Thus, the elements of Fick's diffusivity matrix are not determined intuitively. In general, the non-diagonal elements are non-zero with a positive or negative sign and are a complicate function of composition [132].

## 2.5.2 Maxwell-Stefan equation

Maxwell-Stefan equation is also one of the widely used methods for the diffusion in multicomponent systems. Based on the kinetic theory, Maxwell-Stefan equation begins with the molecular collisions. For ideal fluids that assume only binary collisions exist between molecules, the gradient of species composition is defined by

$$\nabla X_i = -\sum_{j=1}^{n} \frac{\left(X_i n_j - X_j n_i\right)}{c_{\mathrm{t}} Đ_{i,j}} \tag{2.33}$$

It can be also written in $n-1$ dimensional matrix form [132]

$$\mathfrak{J} = -c_{\mathrm{t}} \mathbb{B}^{-1} \nabla \mathbf{X} \tag{2.34}$$

From the Eq. (2.33), the diagonal elements $B_{i,i}$ and the off-diagonal elements $B_{i,j}$ of the square matrix $\mathbb{B}$ are determined as

$$B_{i,i} = \frac{X_i}{Đ_{i,n}} + \sum_{\substack{k=1 \\ i \neq k}}^{n} \frac{X_k}{Đ_{i,k}}, \quad B_{i,j} = -X_i \left( \frac{1}{Đ_{i,j}} - \frac{1}{Đ_{i,n}} \right) \tag{2.35}$$

where $Đ_{i,j} > 0$ denotes the Maxwell-Stefan diffusivity. Since, the Maxwell-Stefan diffusivity ($Đ$) is only defined for the species pair whose constituents are not the same ($i \neq j$), it generally means the binary diffusion coefficient. For the binary mixture ($n = 2$), as mentioned in the previous section, the binary diffusion coefficient ($Đ$) is equal to the Fick's diffusivity ($D$). It is mathematically verified as well because the Eq. (2.31) and the Eq. (2.34) are identical when $n = 2$. Thus, the advantage of Maxwell-Stefan equation is that only binary diffusivities for each species pair are required even for the mixtures of more than three species. In general form including non-ideal fluids, the matrix of thermodynamic factors $\mathbb{G}$ appears

$$\mathfrak{J} = -c_{\mathrm{t}} \mathbb{B}^{-1} \mathbb{G} \nabla \mathbf{X} \tag{2.36}$$

which accounts for non-ideality effect.

### 2.5.3 Multicomponent model

As mentioned, the estimation of diffusivity matrix of Fick's law $\mathbb{D}$ is not straightforward, whereas the binary diffusion coefficient for Maxwell-Stefan equation $Đ$ can be obtained from experiments. A relation between those formulations is necessary to use Maxwell-Stefan diffusivity in the Fick's diffusivity matrix. By comparing Eq. (2.36) with Eq. (2.31) it is

$$\mathbb{D} = \mathbb{B}^{-1}\mathbb{G} \tag{2.37}$$

This relation represents the multicomponent model. For ideal fluids the thermodynamic factor is assumed to be unity so that $\mathbb{G} = \mathbb{I}$. Hence, the elements in the diffusivity matrix $\mathbb{D}$ of generalized Fick's law are determined by inverting the matrix $\mathbb{B}$ of Maxwell-Stefan equation. However, the matrix inversion requires computational effort depending on the number of species, which leads the multicomponent model to be computationally expensive. For ternary mixture, there is a direct transformation of Maxwell-Stefan diffusivities to Fick's diffusivities [132].

### 2.5.4 Effective diffusivity model

To avoid the costly matrix manipulation in multicomponent model, effective diffusivity model has been suggested as an alternative [141]. It assumes that one species diffuses though the mixture of the other species. By this assumption, the matrix inversion is eliminated and the effective diffusion coefficients $D_{i,\mathrm{eff}}$ for all species can be easily obtained as

$$D_{i,\mathrm{eff}} = \frac{1 - X_i}{\sum\limits_{\substack{j=1 \\ j \neq i}}^{n} \frac{X_j}{Đ_{i,j}}} \tag{2.38}$$

With the simplified scalar diffusivity, the diffusive flux of effective diffusivity model is given by

$$\mathfrak{J} = -c_\mathrm{t}\mathbf{D}_\mathrm{eff}\nabla\mathbf{X} \quad \text{where} \quad \mathbf{D}_\mathrm{eff} = (D_{1,\mathrm{eff}}, D_{2,\mathrm{eff}}, \ldots, D_{n,\mathrm{eff}})^\mathrm{T}. \tag{2.39}$$

Effective diffusivity model can save computational time not only by skipping the manipulation of diffusivity matrix but also with solving the individual partial mass balance equations because the influence of other species (off-diagonal elements) disappears. Thus, this model is widely used even if it contains immanent limitation by vanishing minor fluxes.

# Chapter 3 Validations

This chapter presents the validations of numerical models for computing hydrogenation of nitrobenzene within a Taylor flow. First, Section 3.1 describes the example cases of two-phase flow between two parallel plates. This validation aims at the verification of coupled solver for two-phase hydrodynamics. The solutions of two-dimensional velocity profiles with different viscosity ratio are compared with analytic solutions given in the literature.

The numerical solutions of partial mass balance equations are validated with several example cases of multispecies two-phase mass transfer. Multicomponent model (MCM) and effective diffusivity model (EDM) are considered to take into account the multicomponent diffusion phenomena, while continuous concentration diffusivity model (CCDM) is implemented to satisfy the mass conservation between two phases. Three subsections deal with the details of those models namely, (i) multispecies mass transfer within a single phase (Section 3.2), (ii) mass transfer across the interface between two phases (Section 3.3) and (iii) practical example for multispecies mass transfer across the interface (Section 3.4). Additionally, Section 3.5 introduces the influence of dilution on the multispecies diffusion models and investigates the usage of

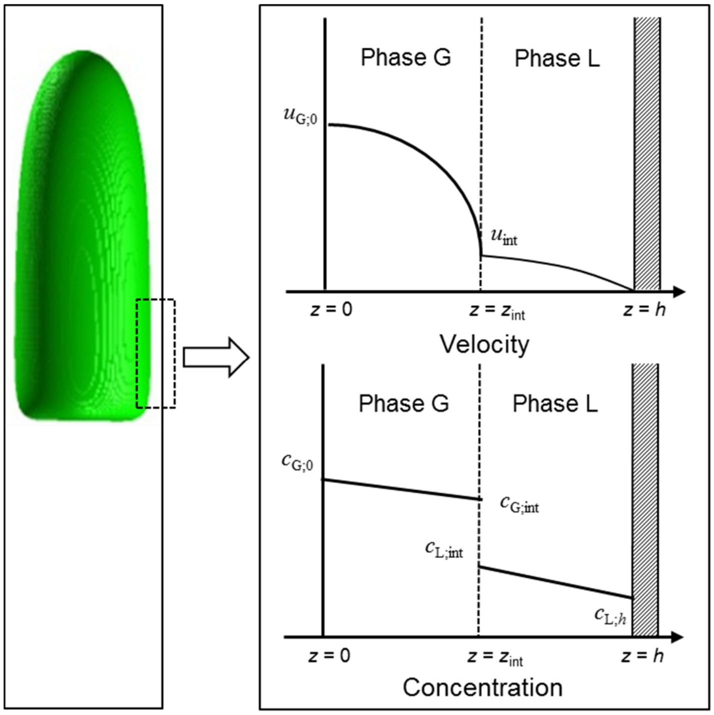

Fig. 3.1: Schematic diagram of the examples for two-phase flow and mass transfer across the interface.

different types of velocity according to the definition of composition. All cases regarding mass transfer utilize one-dimension domain along the $z$ -axis.

For simplicity, the validation cases in following subsections use the computational domain where the interface is located in the middle of domain as shown in Fig. 3.1. The liquid film region is one of the most important parts of the study on the mass transfer within gas-liquid flow, as the mass traveling to the reactive wall must pass through this region. Therefore, the validation cases focus on the flow and mass transfer near the liquid film with simplified one- or two-dimensional domain. This computational domain can be regarded as a part of liquid film region in a Taylor flow, in which the mass transfer occurs from gas bubble to liquid phase [66]. The results and figures presented in these sections have been referred to Woo et al. [145].

Finally, the reaction mechanisms for hydrogenation of nitrobenzene are validated in Section 3.6. Two test cases are chosen from literature and revisited by using DETCHEM$^{TM}$ solver as a numerical pre-study. Both example cases employ one-step global reaction model with different test conditions. As a solution of zero-dimensional reactor equation, the concentration profiles of reactant and product are obtained over the reaction time. DETCHEM$^{BATCH}$ solver is utilized for the calculation.

## 3.1 Hydrodynamics: Two-layer Poiseuille flow

Though TURBIT-VOF is already well verified by former researchers, a two-phase hydrodynamics of the coupled solver has been validated again in order to understand the solution procedure and to verify the solver capability before dealing with a Taylor flow. The test case for validation of two-phase flow is a Poiseuille flow between two parallel plates where the phase interface is placed at the middle of the flow region. The test case refers to the numerical investigation carried out by Leclaire et al. [94]. As a feasibility test of the solver, different viscosity ratios are applied to the test example. Thus, the velocity profiles with respect to the viscosity ratio are compared to those analytical solutions provided in the literature.

Fig. 3.2 shows the schematic diagram and boundary conditions of the test problem. Between the two infinite plates, the flow is initialized with the two fluids divided into upper and lower sides by phase interface at the middle of the domain ($z = 0$). The thickness of each fluid region is set to $h$ so that the total channel height ($L_{ref}$) is $2h$. The velocity is driven by pressure difference along the domain, which finally forms a developed shape as a function of viscosity

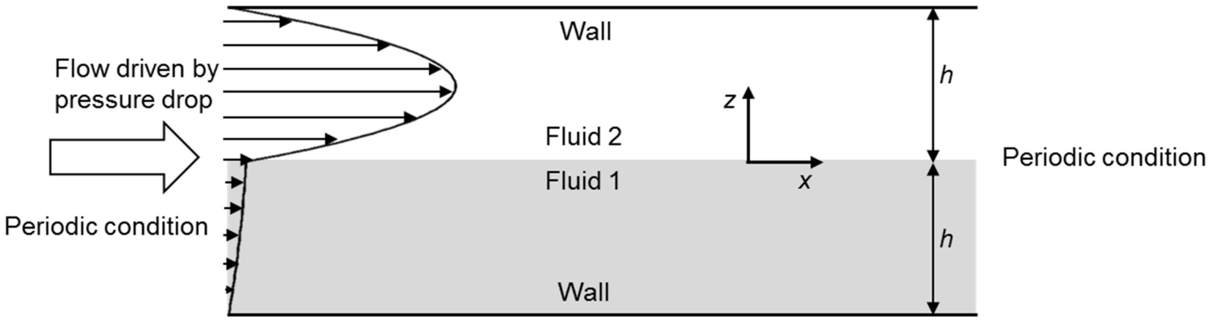

Fig. 3.2: Sketch of the test conditions for layered Poiseuille flow.

ratio at steady state. Periodic boundary conditions are applied to the left and right side of the domain. Upper and lower boundary conditions are a no-slip wall.

With this configuration, the analytical solution of one-dimensional velocity profile is [94]:

$$u=\begin{cases}\dfrac{Gh^2}{2\mu_1}\left[-\left(\dfrac{z}{h}\right)^2+\dfrac{z}{h}\left(\dfrac{\mu_1-\mu_2}{\mu_1+\mu_2}\right)+\dfrac{2\mu_1}{\mu_1+\mu_2}\right] & \text{for } -h\le z\le 0\\ \dfrac{Gh^2}{2\mu_2}\left[-\left(\dfrac{z}{h}\right)^2+\dfrac{z}{h}\left(\dfrac{\mu_1-\mu_2}{\mu_1+\mu_2}\right)+\dfrac{2\mu_2}{\mu_1+\mu_2}\right] & \text{for } 0\le z\le h\end{cases} \tag{3.1}$$

where $\mu_1$ and $\mu_2$ are the viscosity of fluid 1 and 2, respectively. The pressure difference driving the velocity profile is given by

$$G=\frac{u_{\text{int}}\left(\mu_1+\mu_2\right)}{h^2} \tag{3.2}$$

where $u_{\text{int}}$ denotes the velocity at the center of the domain ( $z=0$ ).

A two-dimensional computational domain is defined with a different number of mesh cells in wall-normal ( $z$ ) direction to analyze the grid dependency of numerical solutions. However, the cell number in axial ( $x$ ) direction is fixed to four cells where the periodic boundary is applied to both sides of this direction. The axial length of the domain is set to the same as the reference length of this test case $L_{\text{axial}}=L_{\text{ref}}=2h$. As described in Eq. (2.5), the non-dimensional form of the pressure drop is specified by dimensionless Euler number defined in Table 1. Substituting Eq. (3.2) with Euler number, the dimensionless pressure difference in axial length $L_{\text{axial}}$ is defined by

$$\nabla p^*_{\text{axial}}=\frac{Eu_{\text{ref}}}{L_{\text{axial}}}=\frac{2}{h}\left(\frac{u_{\text{int}}}{u_{\text{ref}}}\right)\frac{\left(1+\Gamma_\mu\right)}{Re_{\text{ref}}} \tag{3.3}$$

where $\Gamma_\mu$ represents the viscosity ratio defined in Table 1. In accordance with Leclaire et al. [94], the velocity at the center of the channel and the viscosity of fluid 1 are specified as $4.5\times10^{-5}$ m/s and $1/6\,\mathrm{Pa\cdot s}$, respectively. The viscosity of fluid 2 is, therefore, determined by the given viscosity of fluid 1 and viscosity ratio. The reference length of the computational domain $L_{\mathrm{ref}}$ is 1m for this case, and the reference Reynolds number $Re_{\mathrm{ref}}$ is 6 where $u_{\mathrm{ref}} = 1\,\mathrm{m/s}$ and $\rho_{\mathrm{ref}} = 1\,\mathrm{kg/m^3}$.

Fig. 3.3 presents the velocity profiles for the viscosity ratios of 0.01 and 0.001. It compares the numerical solutions to those analytic solutions with a different number of mesh cells in $z$ -direction. According to the viscosity ratio, the shape of the velocity profile differs, and the velocity difference between two fluids is increasing as viscosity ratio increases. In this case, the computational cells (20, 40, 60, 80 and 100 cells) are uniformly distributed in $z$ -direction. With three viscosity ratios (0.1, 0.01 and 0.001), the numerical solutions are overall in reasonable agreement with those analytical solutions. The deviations from analytic solutions, however, grow with decreasing number of cells. Table 3 describes the maximum values of velocities and the relative errors of maximum velocities between analytic and numerical solutions ($:= (u_{\mathrm{max,analytic}} - u_{\mathrm{max,numerical}})\,/u_{\mathrm{max,analytic}} \times 100$). The largest error occurs where the number of cells is smallest. With 20 cells the relative error for $\Gamma_\mu$=0.1 is smaller than 5%, while those for $\Gamma_\mu$=0.01 and 0.001 are larger than 5% and almost close to 10%. Also, for $\Gamma_\mu$=0.1 a hundred cells are sufficient to lower the error smaller than 1%, while the errors of other two cases are still

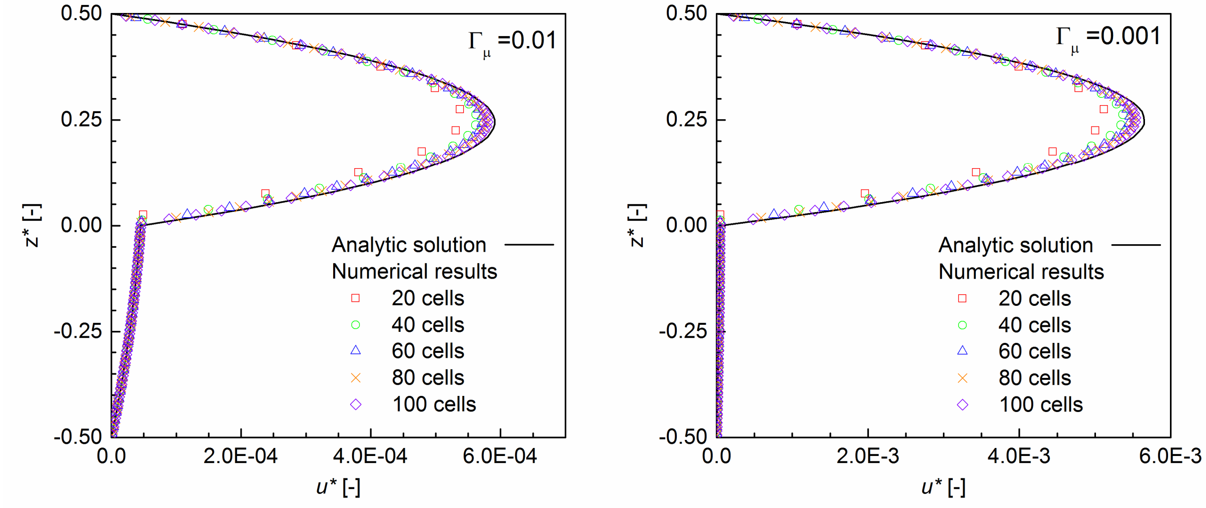

(a) (b)

Fig. 3.3: Velocity profiles for $\Gamma_\mu$=0.01 (a) and 0.001 (b). Comparison between analytic solutions and numerical results with a different number of cells in the z-direction.

Table 3: Maximum velocities and the relative errors of maximum velocities between analytic solutions and numerical results with a different number of mesh cells in the z-direction.

| Cells | Max. velocity, m/s | | | Relative error of max. velocity, % | | |
|---|---|---|---|---|---|---|
| | $\Gamma_\mu$=0.1 | $\Gamma_\mu$=0.01 | $\Gamma_\mu$=0.001 | $\Gamma_\mu$=0.1 | $\Gamma_\mu$=0.01 | $\Gamma_\mu$=0.001 |
| 20 | 8.28E-05 | 5.38E-04 | 5.12E-03 | 4.20 | 9.00 | 9.37 |
| 40 | 8.45E-05 | 5.62E-04 | 5.37E-03 | 2.16 | 4.89 | 4.93 |
| 60 | 8.51E-05 | 5.72E-04 | 5.46E-03 | 1.46 | 3.24 | 3.32 |
| 80 | 8.55E-05 | 5.77E-04 | 5.51E-03 | 1.10 | 2.35 | 2.46 |
| 100 | 8.56E-05 | 5.80E-04 | 5.53E-03 | 0.88 | 1.89 | 2.08 |

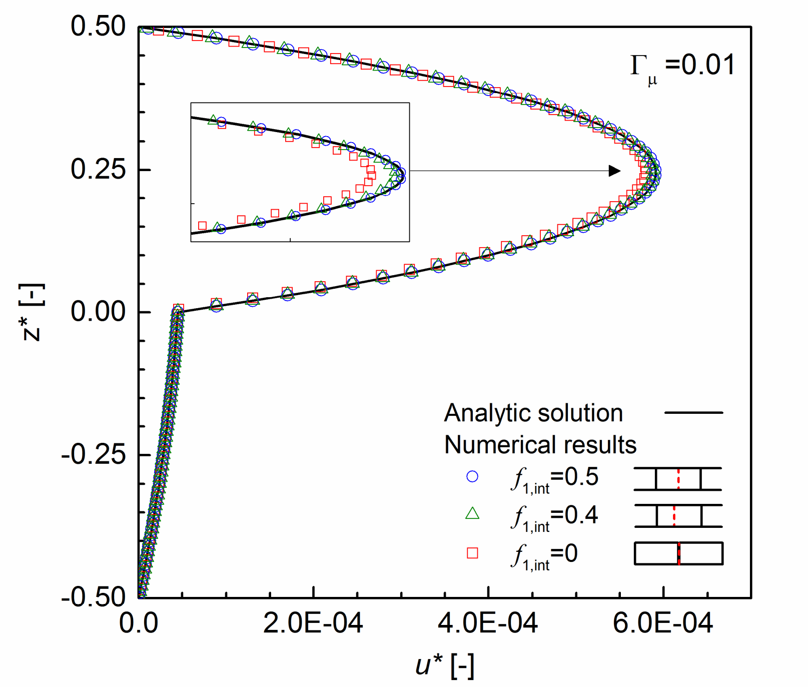

Fig. 3.4: Velocity profiles for different interface locations. Comparison of numerical solutions with analytic solution for $\Gamma_\mu$=0.01.

larger than 1% even with a hundred mesh cells.

Secondly, the influence of the interface position in a mesh cell is investigated with $\Gamma_\mu$=0.01. The results in Fig. 3.3 have an even number of mesh cell with uniform distance where the domain is exactly divided into two regions with half of cells. Thus, the interface is located at the center of the domain and is aligned with the cell face. In this comparison, the position of interface is varied with respect to the volume fraction of fluid 1, $f_{1,\text{int}}$. Fig. 3.4 shows the velocity profiles with three interface locations $f_{1,\text{int}}$=0 (interface aligned with face), 0.5 and 0.4 (interface in cell) and compares those results with analytical solutions for $\Gamma_\mu$=0.01. The velocity profiles where the interface is placed in the cell ( $f_{1,\mathrm{int}}$ =0.5, 0.4) are closer to the analytic velocity profiles than that of the other case where the interface position overlaps with the cell face ( $f_{1,\mathrm{int}}$ =0). It is also shown that the case for $f_{1,\mathrm{int}}$ =0.5 is more accurate than that for $f_{1,\mathrm{int}}$ =0.4 so that the numerical solution is most accurate when the interface is located at the middle of the interfacial cell. For this case, the maximum velocities and relative errors of the maximum velocities are also described in Table 4. The maximum velocity is almost linearly increased as $f_{1,\mathrm{int}}$ increases. Consequently, the position of interface affects the accuracy of the numerical solution, indeed.

In addition to the study on the interface position in mesh cell, a result with fully non-equidistance grid is also compared to the result with uniform mesh cell. The cell size distribution for non-equidistance grid is calculated by a hyperbolic tangent function:

$$z_k = \frac{1}{\sqrt{1-d_\mathrm{g}}} \tanh\left[\left(\frac{2k}{n_\mathrm{cells}} - 1\right) \tanh^{-1}\left(\sqrt{1-d_\mathrm{g}}\right)\right] \tag{3.4}$$

where $z_k$ denotes the position of $k$ 'th node and $n_\mathrm{cells}$ is the number of cells in $z$ -direction. $d_\mathrm{g}$ is the grid refinement parameter, and the value is specified to 0.1 in this case. The number of cells for each phase is $n_\mathrm{cells} = 20$ and the cells are distributed by the position $z_k$ in Eq. (3.4). One additional cell is added to the middle of the domain in order to place the interface at the cell center. Thus, the non-equidistance grid with 41 cells is generated as displayed in Fig. 3.5. Fig. 3.5 compares the velocity profiles of non-equidistance grid with 41 cells to the previous equidistance results with 101 cells and its analytical velocity profile. While the velocity profiles with less than 60 uniform cells show distinct differences from the analytic solution, the results with 41 non-equidistance cells comply very well. This indicates that the non-equidistance grid can dramatically reduce the number of cells required for the sufficiently accurate numerical solution. Though using non-equidistance grid causes another difficulty on the interface reconstruction process of volume-of-fluid method, it may be remarkable that the position of the

Table 4: Maximum velocities and the relative error of maximum velocities between the analytic and numerical solutions with different locations of interface.

| $f_{1,\mathrm{int}}$ | Max. velocity, m/s | Relative error of max. velocity, % |
|---|---|---|
| 0 | 5.80E-04 | 1.89% |
| 0.4 | 5.88E-04 | 0.48% |
| 0.5 | 5.90E-04 | 0.12% |

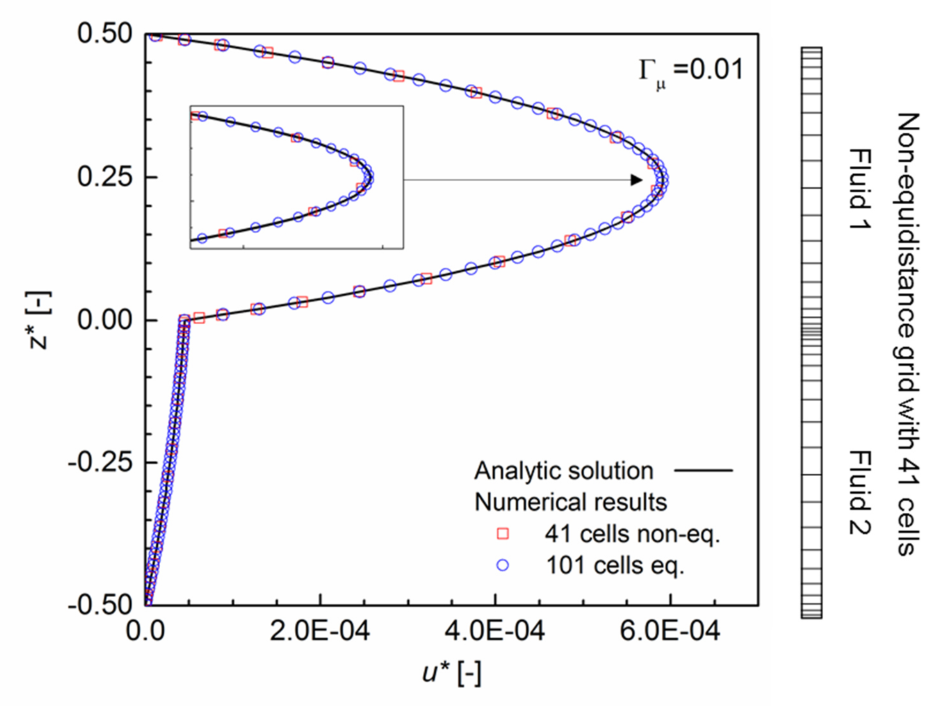

Fig. 3.5: Numerical results with 41 non-equidistance cells (shown in right side) and with 101 equidistance cells. Comparison of velocity profiles between numerical results and analytic solution.

mesh cells and the location of interface influence the efficiency and the accuracy of numerical solutions for interfacial mass transfer.

## 3.2 Multispecies mass transfer within a single phase

This section mainly deals with the validations of multispecies diffusion model within a single phase. In two example cases, the results from multicomponent model (MCM) and effective diffusivity model (EDM) are compared with experiments and/or solutions of Maxwell-Stefan (MS) equations. The first case is the Stefan diffusion problem of ternary mixture, and the second case considers the diffusion with surface reaction. Uniform flux is specified in the entire computational domain to consider the non-zero total molar flux. Species compositions are represented by mole fraction for mass transfer in a single phase. Therefore, the velocity mentioned in this section is the molar-average velocity, accordingly.

A ternary mixture ($n=3$) is chosen for multispecies test cases to avoid the extra computational effort for the matrix inversion of MCM. The species are indicated by subscripts 1, 2 and 3, and the corresponding MS diffusivities are $Đ_{1,2}$, $Đ_{1,3}$ and $Đ_{2,3}$. The elements of $2\times2$

diffusivity matrix of multicomponent model are described as $D_{1,1}$, $D_{1,2}$, $D_{2,1}$ and $D_{2,2}$, while $D_{1,\mathrm{eff}}$ and $D_{2,\mathrm{eff}}$ represent the effective diffusivity of species constituent by EDM. For $n=3$, the mole fraction of species 3 is not solved by Eq. (2.16), but determined from the relation $x_3 = 1 - x_1 - x_2$. The computational domain is $0 \le z \le h$ with $h$, the height of the domain. With the reference length defined as $L_\mathrm{ref} = h$ the dimensionless computational domain is then $0 \le z^* \le 1$. This domain is divided by 40 uniform mesh cells.

## 3.2.1 Stefan diffusion for a ternary mixture

This test case is based on the example case in Taylor & Krishna [132] (see example 2.1.1 in their book) and deals with the ternary diffusion in a Stefan tube according to the experiment by Carty and Schrodt [14]. A binary liquid mixture of acetone (1) and methanol (2) evaporates and diffuses into the ambient air (3) which is treated as a single component in the example. Fig. 3.6 shows a sketch of the computational domain for present example. Test conditions are summarized in Table 5.

At the liquid surface ($z=0$) the equilibrium compositions of the mixture are specified ($X_{1;0} = 0.319$ and $X_{2;0} = 0.528$), while at the end of tube the mole fractions of vapors are set to zero ($X_{1;h} = X_{2;h} = 1 - X_{3;h} = 0$). The total concentration is computed from the ideal gas law. As mentioned, uniform flux is specified in the domain, which corresponds to an evaporative flux of liquid mixture to the air. The molar-average velocity is determined by the total flux and total concentration as

$$U = N_\mathrm{t} / c_\mathrm{t} \tag{3.5}$$

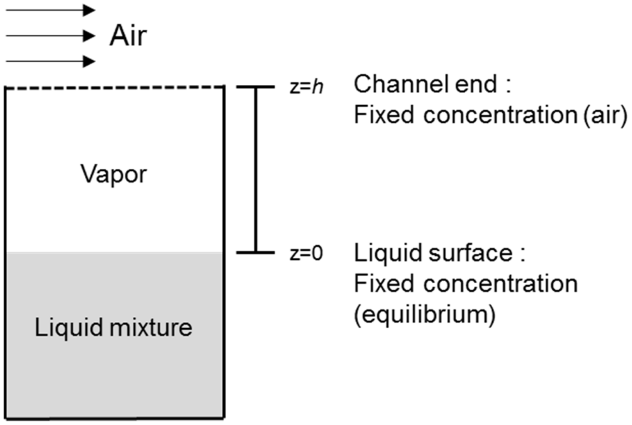

Fig. 3.6: Schematic diagram of the Stefan diffusion example.

Table 5: Summary of test conditions for the Stefan diffusion example.

| | |
|---|---|
| Temperature (K) | 328.5 |
| Pressure (kPa) | 99.4 |
| Total concentration ( $\mathrm{mol/m^3}$ ) | 36.4 |
| Tube length (m) | $h = L_{\mathrm{ref}} = 0.238$ |
| Diffusivity ( $\mathrm{m^2/s}$ ) | $Đ_{1,2} = 8.48\times10^{-6}$<br>$Đ_{1,3} = 13.72\times10^{-6}$<br>$Đ_{2,3} = 19.91\times10^{-6}$ |
| Total flux ( $\mathrm{mol/m^2s}$ ) | $4.91\times10^{-3}$ |
| Reference Peclet number | 0.238 |

so that $U = 1.35\times10^{-4}\mathrm{m/s}$ for this case. In Taylor & Krishna [132], the MS equations are solved by a fourth-order Runge-Kutta method and the computed total evaporative flux at the liquid-vapor interface is given in Table 5. More recently, Newman [108] solved MS equations numerically for the same system by the film, penetration and boundary layer models. Binary diffusion coefficients of three species pairs are provided by Taylor and Krishna [132].

Fig. 3.7 shows the mole fractions calculated by MCM and EDM, and compares them

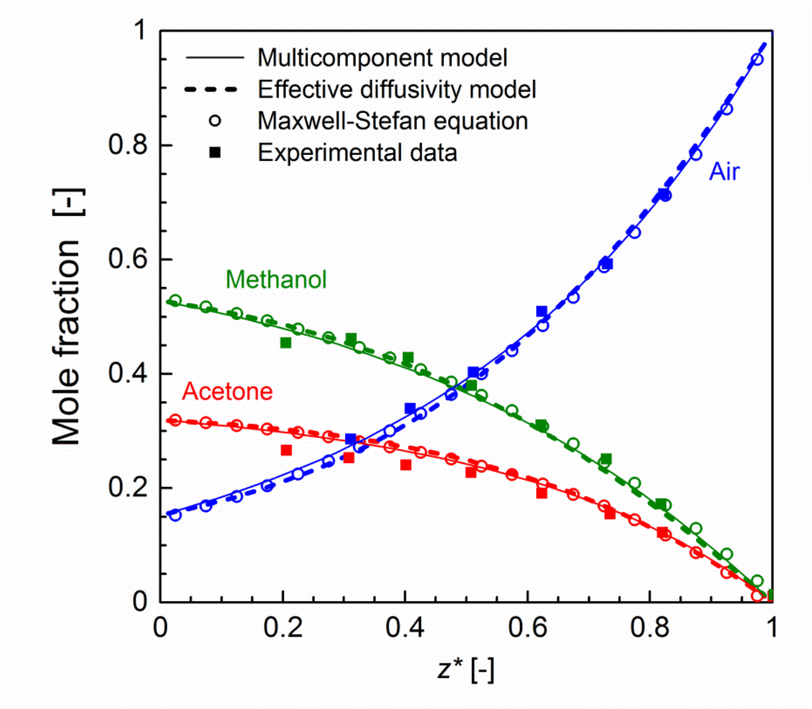

Fig. 3.7: Comparison of predicted mole fraction by the MCM and EDM with experimental data [14] and numerical solution of the MS equations.

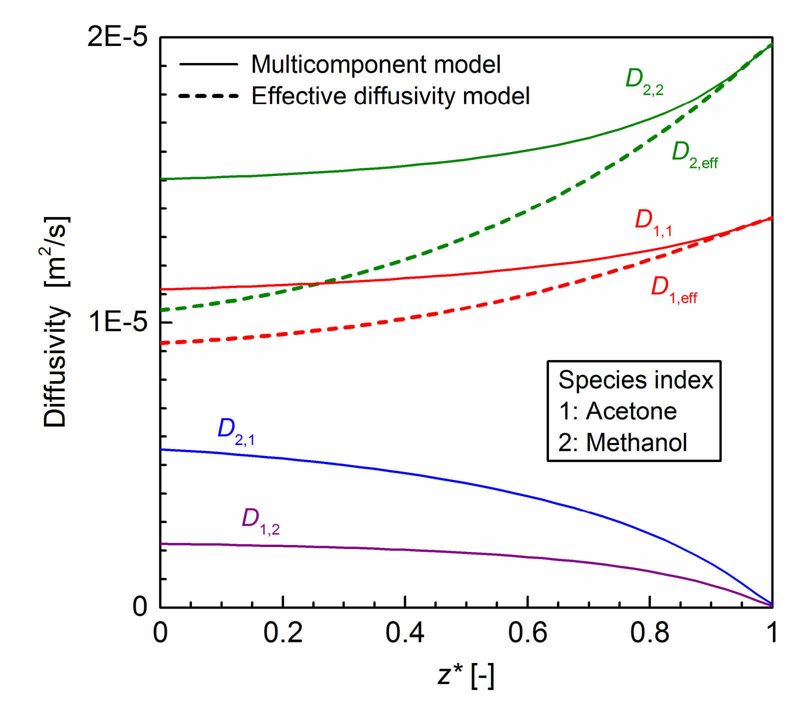

Fig. 3.8: Diffusivities of MCM and EDM for the Stefan diffusion example.

with the measured data of Carty and Schrodt [14] and numerical solutions of MS equation (see Appendix C). As expected from the boundary conditions, the mole fractions of acetone and methanol gradually decrease from the gas-liquid interface to the end of channel, while the mole fraction of air increases in the same direction. The results of MCM and EDM are in excellent agreement with the numerical solution of MS equation, and these numerical solutions are in reasonable compliance with the experimental data. The results of MCM are slightly closer to MS equation and experimental data but the overall differences between both diffusion models are very small. For the mole fraction of air, the largest differences occur in the range $0.1 < z^* < 0.5$ but are still below 2.3% for MCM and below 4.3% for EDM. Thus, the difference between both diffusion models is not significant, and consequently effective diffusivity model predicts sufficiently well with low computational cost.

For more detail comparison of both diffusion models, the elements of diffusivity matrix of both models are analyzed as shown in Fig. 3.8. The comparison of diffusivities from both models draws two remarkable points. First, the difference between two diffusion models depends on the species composition. The gap between diagonal diffusivities from both models is largest at the gas-liquid interface ($z^* = 0$) and gradually decreases along the $z^*$-axis. For $z^* > 0.95$, the two diagonal diffusivities from both models are visually not distinguished. Accordingly, the off-diagonal elements of MCM are largest at $z^* = 0$ and drop to zero along $z^*$-axis with decreasing compositions of acetone and methanol. To analyze this behavior, the diffusivity profiles in Fig. 3.8 are compared with the species profiles in Fig. 3.7. In the left part of the domain, the mole fractions of acetone and methanol are higher than the mole fraction of air, while in right part of the domain the mole fractions of the two species are much smaller than air. Likewise, the differences between diagonal elements of diffusivity from both models are large in the left part of the domain, where the mole fractions of acetone and methanol are higher than that of air. In this case, air plays a role as a carrier species. However, the differences are almost negligible in the region where the mole fractions of acetone and methanol are much lower than the carrier species so that the two species are diluted. This remarkable effect of dilution is further discussed in Section 3.5.

The second point is that the local mole fractions computed by two diffusion models are almost the same even where the difference of diagonal elements from two models is quite obvious. This behavior may be explained by combined convective and diffusive mass transport. The ratio of both contributions is characterized by the Peclet number. The (binary) Peclet number is defined as

$$Pe_{i,j} = \frac{L_{\text{ref}} U}{D_{i,j}} \tag{3.6}$$

The respective values for the three species pairs are $Pe_{1,2} = 3.79$, $Pe_{1,3} = 2.34$ and $Pe_{2,3} = 1.61$. All these values are bigger than unity, which indicates that the convective mass transport is stronger than the diffusive one for this case. Thus, it may imply that the diffusivity difference does not significantly influence the species profiles in diluted conditions where the diffusion is not predominant mechanism.

### 3.2.2 Ternary diffusion with heterogeneous reaction

The second test case is a reaction-diffusion problem for the mixture of three species, $CO_2$ (1), $O_2$ (2) and CO (3). This case is according to the example 19.4-3 in Bird et al. [6] which provides an analytic solution of MS equation. It describes the mass transfer to a catalytic solid surface where CO oxidation $2CO + O_2 \rightarrow 2CO_2$ occurs. For the sake of simplicity, one-step

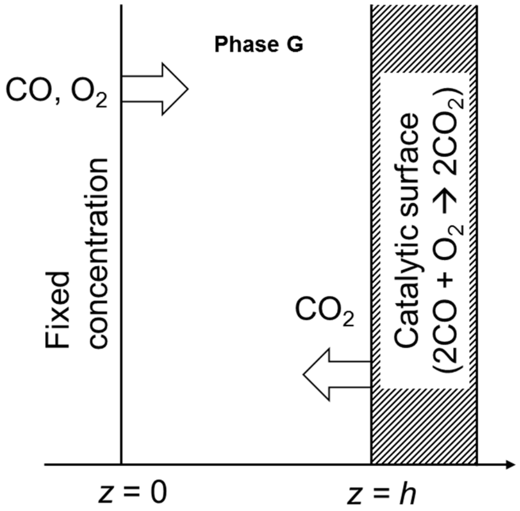

Fig. 3.9: Sketch for the ternary diffusion of $CO$ , $O_2$, and $CO_2$ with catalyzed heterogeneous reaction.

Table 6: Summary of test conditions for the ternary diffusion with heterogeneous reaction.

| | |
|---|---|
| Temperature (K) | 300 |
| Pressure (kPa) | 101.325 |
| Domain length (m) | $h = L_{ref} = 1$ |
| Diffusivity ( $m^2/s$ ) | $Đ_{1,2} = 1.526\times10^{-5}$<br>$Đ_{1,3} = 1.528\times10^{-5}$<br>$Đ_{2,3} = 2.064\times10^{-5}$ |
| Total flux ( $mol/m^2s$ ) | $5\times10^{-5}$ |
| Reference Peclet number | 1 |

global reaction is only considered with an arbitrary rate constant.

Fig. 3.9 shows the computational domain and boundary conditions. Constant mole fractions ( $X_{1;0} = 0.1$ and $X_{2;0} = 0.2$ ) are set to the left boundary ( $z^* = 0$), whereas the reactive flux is specified for the right wall ( $z = h = L_{ref}$ ). The molar flux of $CO_2$ production is arbitrary given as $N_1 = -10^{-4}\,mol/m^2s$, and the molar fluxes for consumption of other two species are obtained by stoichiometry

$$-\frac{1}{2}N_1 = N_2 = \frac{1}{2}N_3 \tag{3.7}$$

The total molar flux consumed at the catalytic wall is, therefore, estimated by the definition of total flux as

$$N_{\mathrm{t}} = N_1 + N_2 + N_3 = -\frac{1}{2} N_1 \tag{3.8}$$

The test conditions for this test case are summarized in Table 6. The binary diffusivities for three species pairs are computed from kinetic theory [6]. From the Lennard-Jones parameters of species, the collision integral for the diffusivity is estimated by the curve-fitted equation. Then the diffusivity of species pair can be obtained at a certain temperature and pressure. To obtain an analytic solution of MS equation, the diffusivity for CO and CO2 $Đ_{1,2}$ is assumed to be the same as the diffusivity for O2 and CO2 $Đ_{1,3}$ because those values shown in Table 6 are actually almost the same [6]:

$$Đ_{1,2} = Đ_{1,3} = 1.528\times10^{-5}\,\mathrm{m^2/s} \tag{3.9}$$

With this assumption, the analytic solution of MS equation for this test case is given by

$$X_1 = -2 + (X_{1;0} + 2)\exp\left(-\frac{N_1 z^*}{2c_{\mathrm{t}} Đ_{1,2}}\right) \tag{3.10}$$

$$X_2 = 1 - \frac{1}{3}(X_{1;0} + 2)\exp\left(-\frac{N_1 z^*}{2c_{\mathrm{t}} Đ_{1,2}}\right) - \left(\frac{1}{3} - X_{2;0} - \frac{1}{3}X_{1;0}\right)\exp\left[-\left(\frac{3}{2}\frac{Đ_{1,2}}{Đ_{2,3}} - 1\right)\frac{N_1 z^*}{c_{\mathrm{t}} Đ_{1,2}}\right] \tag{3.11}$$

The molar fluxes in Eq. (3.7) can be directly used for this analytic solution of MS equation. From the definition of molar flux Eq. (2.10), the boundary conditions at the right wall ($z^* = 1$) are given by

$$j_1 = n_1 - n_{\mathrm{t}} X_1 = n_1\left(1 + \frac{1}{2}X_1\right) \tag{3.12}$$

$$j_2 = n_2 - n_{\mathrm{t}} X_2 = \frac{1}{2} n_1 (X_2 - 1) \tag{3.13}$$

The governing equations of numerical simulation for this case are identically used as for the previous test case. Accordingly, the uniform convective flux is also applied for the non-zero total molar flux induced by the reaction. The constant (molar-average) velocity in the whole computational domain is estimated by Eq. (3.5) and it is $U = 1.23\times10^{-6}\,\mathrm{m/s}$.

Fig. 3.10 shows the mole fractions computed by MCM and EDM and compares them to the analytic solution of MS equations, Eq. (3.10) and Eq. (3.11). Additionally, it also shows the

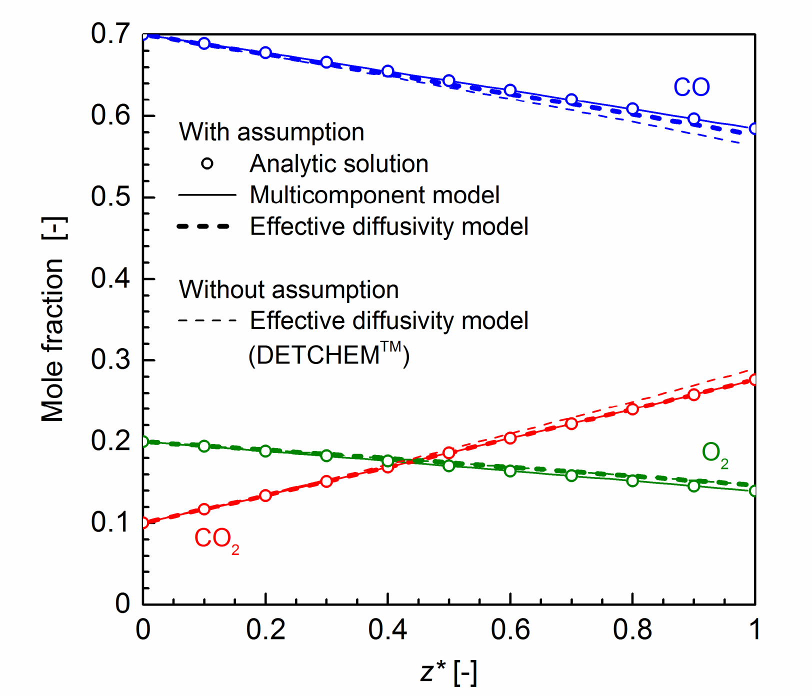

Fig. 3.10: Mole fraction profiles for the ternary diffusion with heterogeneous reaction. Comparison of MCM and EDM (with and without assumption $Đ_{1,2}$=$Đ_{1,3}$) with an analytical solution of the MS equation.

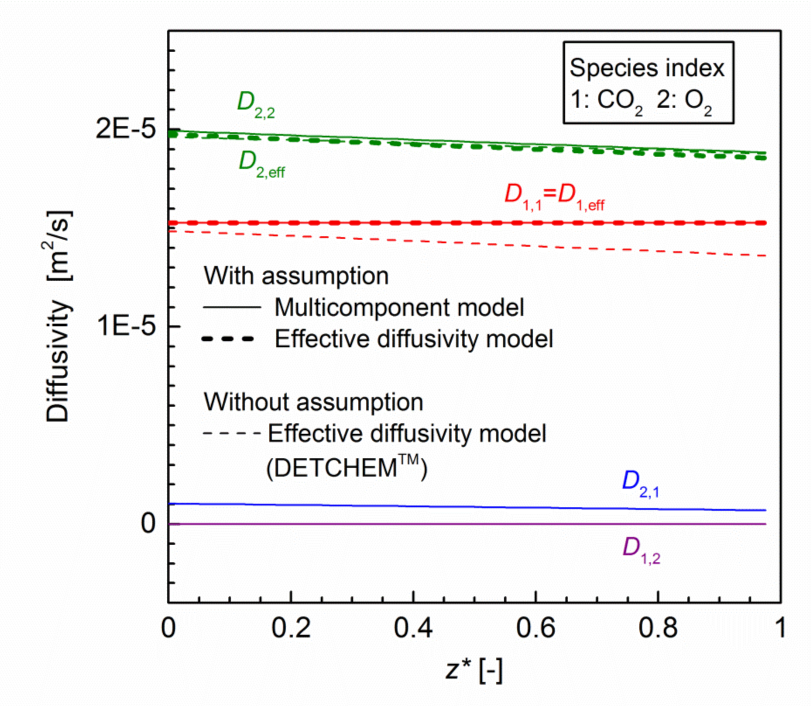

Fig. 3.11: Diffusivity profiles for the ternary diffusion with heterogeneous reaction. Comparison of MCM and EDM (with and without assumption $Đ_{1,2}$=$Đ_{1,3}$).

result of EDM without assumption where $Đ_{1,2}$ is not assumed to be the same as $Đ_{1,3}$ but is set as $1.526\times10^{-5}\,\mathrm{m}^2/\mathrm{s}$. The results without assumption are obtained by DETCHEM$^{TM}$ code. These results are used to crosscheck the implemented diffusion model and to analyze the effect of the assumption $Đ_{1,2}$=$Đ_{1,3}$. In Fig. 3.10, the mole fraction of $CO_2$ increases from left to right with producing $CO_2$ by catalytic reaction at the right wall ($z^*=1$). In contrary, it is plausible that the mole fraction of CO and $O_2$ decrease with increasing $z^*$. For all three species, the mole fraction profiles are almost linear against the distance $z^*$. The results of MCM are in excellent agreement with the analytic solution of MS equation. For EDM with the simplifying assumption $Đ_{1,2}$=$Đ_{1,3}$, the numerical results of $CO_2$ mole fraction is exactly the same as those of analytic solution and MCM because the diffusivity of $CO_2$ is always fixed by assumption. The mole fractions of $O_2$ and CO deviate slightly from the analytic solution. The deviation is growing as $z^*$ is increasing. The reason is the composition-dependent diffusivities from both models. For EDM without assumption, $CO_2$ mole fraction is overestimated as compared to the analytic solution, while the other numerical results are identical. This small deviation can represent the underestimation of diffusive flux by using the assumption. Nevertheless, the results of both EDMs are in reasonably good compliance with the analytic solution of MS equations. The mole fraction profiles for $O_2$ are almost identical for both models, while for $CO_2$ and CO the maximum differences are 4.9% and 2.3% at $z^*=1$, respectively.

Fig. 3.11 shows the comparison of the diffusivity profiles by MCM and two EDMs (with and without assumption). For $CO_2$ the diffusivities $D_{1,1}$ and $D_{1,\mathrm{eff}}$ with assumption are equal and, moreover, the off-diagonal diffusivity $D_{1,2}$ is zero. Thus, the diffusivity matrix of MCM and EDM with assumption is identical, which causes the identical mole fraction profile of $CO_2$. However, for EDM without assumption, the diffusivity of $CO_2$ differs from $D_{1,1}$ of MCM. The difference in diffusivity is the reason for the different mole fraction profile of $CO_2$ in Fig. 3.10. For $O_2$, $D_{2,\mathrm{eff}}$ profiles with and without assumption and $D_{2,2}$ profile are almost identical. The comparison of these diffusivity profiles shows the validity of the assumption. Due to the cross-coefficient diffusivity $D_{2,1}$, $O_2$ mole fraction profiles in Fig. 3.10 show slight differences between EDMs and MCM.

The binary Peclet numbers for this test case are $Pe_{1,2}=Pe_{1,3}=8.06\times10^{-2}$ and $Pe_{2,3}=5.96\times10^{-2}$. The values are much smaller than unity, which illustrates that the convective flux (reactive flux in this case) is much smaller than the diffusive flux. From this test case, one may also infer that EDM can replace MCM even where the diffusion is more important than the convection (or reaction). Of course, in a pure diffusion problem below the micro scale, the results of mole fraction may also highly depend on the diffusivity. Nevertheless, it is remarkable that the difference of diffusivity does not significantly affect the multispecies mass transfer on an engineering scale covered by Fick's law.

# 3.3 Mass transfer across the interface between two phases

This part is devoted to the verification of continuous concentration diffusion model (CCDM) implemented by Onea et al. [110], which is the model for mass transfer between two phases described in Section 0. In order to focus on the interfacial mass transport phenomena, the following two test cases are considered with a binary mixture, so that only one species is concerned with binary diffusivities for each phase. $c_i$ is, therefore, written as $c$ in the subsections. In the first test case, the influence of using CCDM is investigated with a transient interfacial mass transfer example, and the second case is a parametric study on the diffusivity ratios, Henry numbers and reaction rates. In these test cases, the phase interface is placed at the middle of domain as shown in Fig. 3.1, which can be considered as a part of liquid film region in Taylor flow where the mass transfer most actively occurs due to the thin thickness of the liquid film. The computational domain is one-dimension with 40 uniform mesh cells, which is identical to the previous section.

## 3.3.1 Validation of CCDM for transient two-phase mass transfer

The validation cases in this section concern the transient diffusive mass transfer across a phase interface in order to investigate the influence of CCDM. This test case refers to one of the examples of Onea et al. [110] where the time-dependent analytical solutions are available. For initial condition, the uniform concentration $c_{\mathrm{G}}^{0} = c_{\mathrm{ref}} = 1\,\mathrm{mol/m^3}$ is specified in gas phase ($0 < z < z_{\mathrm{int}}$) and zero concentration $c = c_{\mathrm{L}}^{0} = 0$ is used in liquid phase ($z_{\mathrm{int}} < z < h$). The dimensionless analytic solution for $c^* := c / c_{\mathrm{ref}}$ in an infinite one-dimensional domain reads [18]

$$c^* = \begin{cases} \dfrac{1+H\sqrt{D_{\mathrm{L}}/D_{\mathrm{G}}}\,\mathrm{erf}\left[(z^*_{\mathrm{int}}-z^*)/2\sqrt{D_{\mathrm{G}}t}\right]}{1+H\sqrt{D_{\mathrm{L}}/D_{\mathrm{G}}}} & \text{for} \quad z^* < z^*_{\mathrm{int}} \\ \dfrac{H\,\mathrm{erfc}\left[(z^*-z^*_{\mathrm{int}})/2\sqrt{D_{\mathrm{L}}t}\right]}{1+H\sqrt{D_{\mathrm{L}}/D_{\mathrm{G}}}} & \text{for} \quad z^* > z^*_{\mathrm{int}} \end{cases} \tag{3.14}$$

where $D_{\mathrm{G}}$ and $D_{\mathrm{L}}$ denote the diffusivity of species for gas and liquid phase, respectively. $H$ is the Henry number. When $H \neq 1$, the concentration profile is discontinuous at the interface $z = z_{\mathrm{int}}$.

As shown in Fig. 3.1 a computational domain is defined for numerical calculations within a finite domain length $h = L_{\mathrm{ref}} = 1\,\mathrm{m}$. The gradient free boundary condition is applied to both sides of the domain. The Eq. (2.16) is solved with the identical initial condition used for analytic solutions. For a meaningful comparison between numerical solutions in the finite domain and analytical solutions in the infinite domain, calculations are performed until the concentrations at $z^* = 0$ and $z^* = 1$ do not deviate from the respective initial values. In this example, the diffusivity of gas phase is fixed as $D_{\mathrm{G}} = 0.05\ \mathrm{m}^2/\mathrm{s}$, while the diffusivity in liquid phase $(D_{\mathrm{L}})$ is varied with respect to the diffusivity ratio $\Gamma_D := D_{\mathrm{G}}/D_{\mathrm{L}}$. Henry number $(H)$ is set to unity in

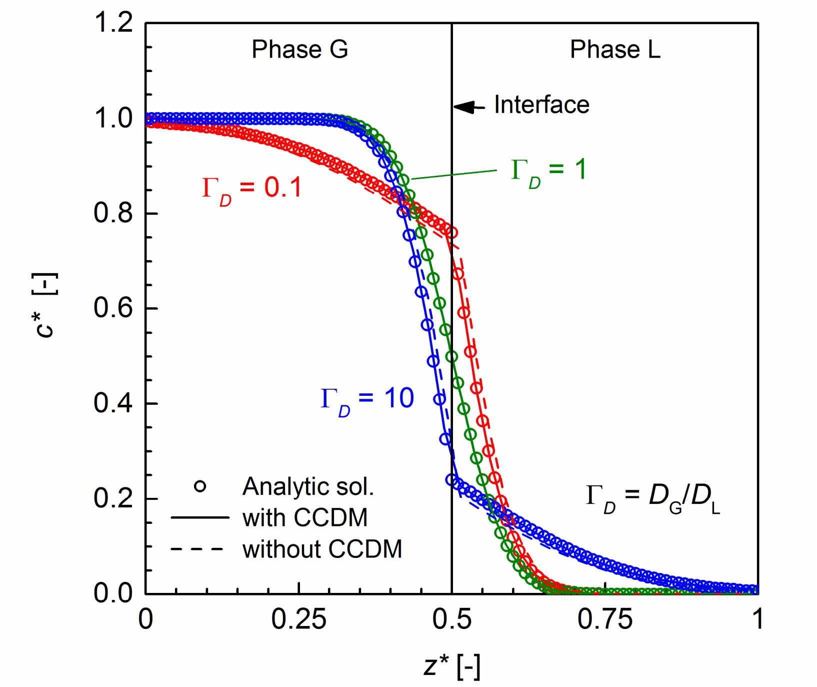

Fig. 3.12: Instantaneous concentration profiles for three different values of the diffusivity ratio ($H = 1$, $f_{\mathrm{int}} = 1$, $t = 0.05\,\mathrm{s}$). Comparison of analytical and numerical solution with and without CCDM.

order to keep continuous concentration at the interface and focus on the effect of CCDM. For this purpose, the same computations are performed for both with CCDM and without CCDM. Moreover, the position of interface in a mesh cell is also considered to check its influence on the solution. The relative position of the interface in a mesh cell is defined by liquid volume fraction in the cell ( $f_{\text{int}}$ ) as displayed in the inset of Fig. 3.13.

Fig. 3.12 shows the concentration profiles obtained from analytical solutions and numerical simulations for $f_{\text{int}}=1$ at $t=0.05\text{s}$. It compares both results with three different diffusivity ratios $(\Gamma_D)$. For unity diffusivity ratio $\Gamma_D=1$, there is no difference between the diffusivities in two phases as defined. Then the test case corresponds therefore to a single phase diffusion problem. Since the concentration profile is continuous at the interface and the CCDM plays no role for this condition, the results with and without CCDM are exactly identical. For diffusivity ratios 0.1 and 10, the diffusion rates in each phase are different, and the concentration gradient is then discontinuous at the interfaces. With CCDM, the numerical results are in good agreement with the analytical solution of Eq. (3.14), while the concentration profiles without CCDM slightly deviate where $\Gamma_D \neq 1$. This amount of deviation may be regarded as a loss of accuracy in the calculation without CCDM.

To analyze the effect of the interface position within a mesh cell, simulations with six different interface locations are performed for $\Gamma_D=0.1$ with and without CCDM. Fig. 3.13 (a) shows the analytical and numerical concentration profiles with and without CCDM for different

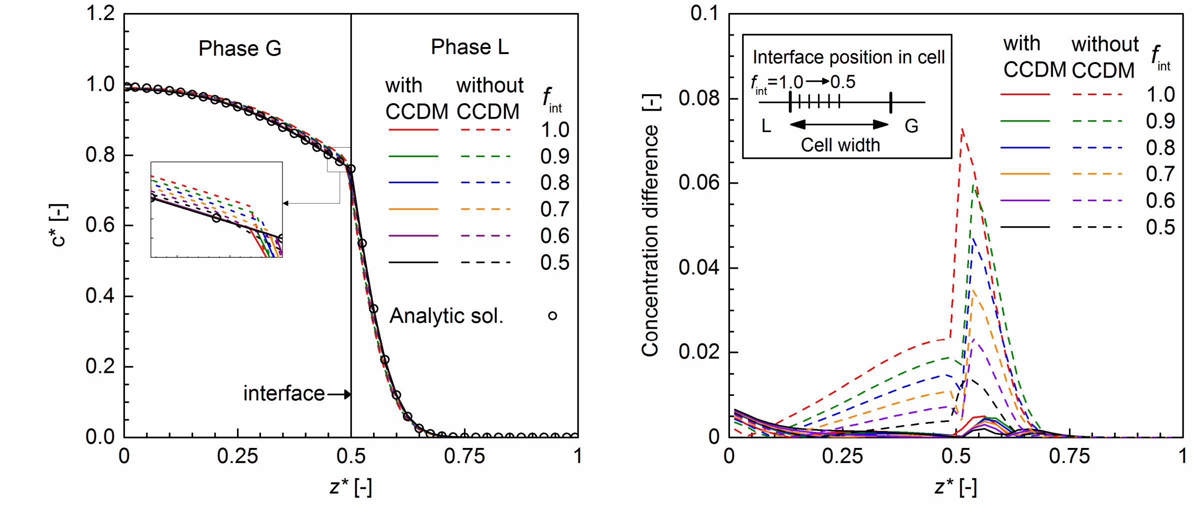

(a) (b)

Fig. 3.13: Concentration profiles of analytical and numerical solution with and without CCDM for different interface locations within a mesh cell (a), and differences between analytic and numerical solutions normalized by $c_{\text{ref}}$ (b).

interface locations. With CCDM, the concentration profiles do not visually deviate even in the zoom-in figure near the interface, while the profiles without CCDM clearly differ from the analytical solution in the zoom-in figure. It is more clearly shown in Fig. 3.13 (b) which displays the normalized difference between numerical and analytical concentration profiles. With CCDM, the differences from analytical solutions are approximately one order of magnitude smaller than those without CCDM. The largest error with CCDM (0.0047 for $f_{\text{int}} = 1$) is smaller than the smallest error without CCDM (0.0134 for $f_{\text{int}} = 0.5$). For $0 < f_{\text{int}} < 0.5$ which is not displayed, the errors are generally even smaller. The maximum error without CCDM records 0.0124 at $f_{\text{int}} = 0.1$, while the largest error with CCDM is only 0.0049 at $f_{\text{int}} = 0.4$. The series of results highlights the importance of CCDM even for $H = 1$. Note that the increase of deviation in the region $0 < z^* < 0.1$ originates from the zero gradient boundary condition at $z^* = 0$ and is thus without relevance here.

Both with and without CCDM, the differences are decreasing as $f_{\text{int}}$ decreases from 1 to 0.5. This represents that the deviation from the analytical solution is smallest when the interface is located at the middle of the mesh cell, while it is largest when the interface coincides with the mesh cell boundary. In the finite volume based code TURBIT-VOF, the diffusivity at the cell face is required to calculate the diffusive flux between two adjacent cells. If the interface is located at the middle of a mesh cell, which means each cell face belongs to each phase, the diffusivity at the cell face can be easily determined as the diffusivity of respective phase. If the interface is aligned with the cell face between two neighboring mesh cells, the diffusivity at this cell face is then ambiguous in the single-field formulation. In the practical three-dimensional simulation, the interface location is determined by a geometric interface reconstruction algorithm of VOF method. The interface orientation is hardly parallel to the cell face as what this one-dimensional example case shows. Consequently, it is clear that CCDM is an indispensable element of the present numerical method for an accurate numerical simulation of interfacial mass transfer.

### 3.3.2 Parametric study on the two-phase mass transfer

Next test case is the numerical parametric study on the reactive mass transfer across a planar interface in terms of diffusivity ratio, Henry number and reaction rate. For computation, one-dimensional computational domain is defined with the length $h = 1\text{m}$. At left wall $z = 0$ a

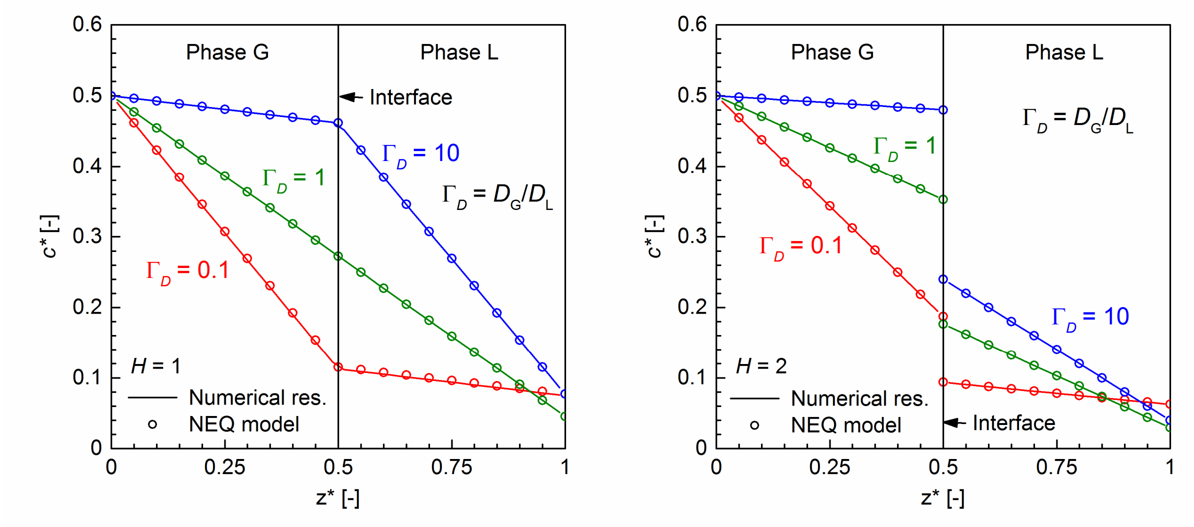

(a) (b)

Fig. 3.14: Concentration profiles for steady-state two-phase reactive mass transfer ( $k = 10\ \mathrm{m/s}$ ). Comparison between numerical and NESM solution for three different diffusivity ratios and two different Henry number. ( $H = 1$ (a) and $H = 2$ (b)).

fixed concentration ( $c_\mathrm{m} = 1$ ) is specified, while a reactive flux ( $j_\mathrm{m}^\mathrm{V} = \dot{s} = -kc_\mathrm{m}$ ) with an arbitrary rate constant $k$ is applied to the right wall ( $z = h$ ). With variable diffusivity ratio, the lower diffusivity of the two phases is always set to $1\,\mathrm{m}^2/\mathrm{s}$. The numerical solution is compared with the solution of the non-equilibrium stage model (NESM) provided by Kenig et al. [82], which is regarded as an analytical model for two-phase mass transfer with a heterogeneous reaction in this study (see appendix D).

Fig. 3.14 shows the concentration profiles for different diffusivity ratios (0.1, 1 and 10) and Henry numbers (1 and 0.5) with constant reaction rate, $k = 10\,\mathrm{m/s}$. The numerical results for all test conditions are in excellent agreement with those of NESM. They illustrates that a higher/lower diffusivity in a phase drives a lower/higher concentration gradient in respective phase. In the results with the diffusivity ratio $\Gamma_D = 10$ in Fig. 3.14 (a) where the diffusion in gas phase is ten times faster than that in liquid phase, the concentration gradient in gas phase is low due to the fast diffusion and the gradient in liquid phase shows the opposite behavior. In other words, the diffusivity ratio governs the concentration gradient for both phases in the mass transfer between two phases. Fig. 3.14 (b) shows the case with non-unity Henry number which results in the discontinuous concentration at the interface. The continuous concentration $c_\mathrm{m}$ is transformed back into the discontinuous physical concentration for the visualization. In Fig. 3.14 (b), the diffusivity in a phase affects the concentration gradient in respective phase as well.

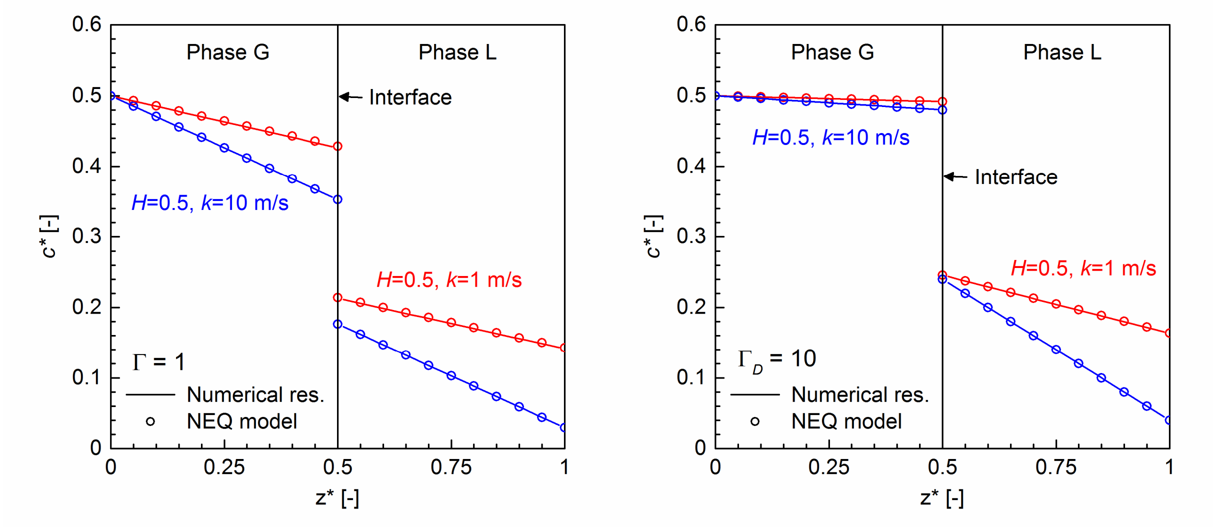

(a) (b)

Fig. 3.15: Concentration profiles for steady-state two-phase reactive mass transfer ($H = 0.5$, $\Gamma_D$=1 (a) and 10 (b)). Comparison between numerical and NESM solution for two different reaction rates.

The interesting point is that the concentrations at the right wall are not identical for three diffusivity ratios even though the reaction rate is the same for all cases. The wall concentration for $\Gamma_D$=1 is lower than the wall concentrations for $\Gamma_D = 0.1$ and $\Gamma_D = 10$ which are equal. The reason is the different diffusive flux. The diffusive fluxes for the case with $\Gamma_D$=0.1 and $\Gamma_D$=10 are larger than the case with $\Gamma_D$=1 because in the former two cases the diffusivity in a certain phase is ten times higher than that for the latter case.

Fig. 3.15 shows the numerical results with different reaction rate and different diffusivity ratios $\Gamma_D$=1 and $\Gamma_D$=10. The effect of the reaction rate is shown by comparing the results for $k = 1$ m/s and $k = 10$ m/s. The numerical solutions, in this case, are in very good agreement with those of NESM as well. In Fig. 3.15 (a), the concentration gradients in both phases are identical because $\Gamma_D = 1$. However, the concentration gradients for two reaction rates are different. Since the consumption of species at the reactive wall relies on the reaction rate, the mass flux is then higher for the case with $k = 10$ m/s than that for the case with $k = 1$ m/s. Fig. 3.15 (b) shows the cases with $\Gamma_D$=10. Although the concentration gradient is not identical due to the non-unity diffusivity ratio, this case also shows the same trend of concentration profiles against the reaction rate as shown in Fig. 3.15 (a). From these results, it is found out that the concentration gradients for both phases are governed by the reaction rate at the wall. In addition, CCDM is well validated by this parametric study for the interfacial mass transfer with both transient and steady-state conditions.

# 3.4 Multispecies mass transfer across the phase interface

As a combined validation case of multispecies and multi-phase mass transfer, this test case considers the practical $H_2$ - $O_2$ ternary diffusion across the phase interface with a heterogeneous chemical reaction. The three species involved are $H_2$ (1), $O_2$ (2) and $H_2O$ (3). As for the other cases in Section 3.3, the phase interface is shown in Fig. 3.1 and it is located in the middle of the one-dimensional computational domain. The left half of the domain is gaseous state so that $H_2O$ exists as water vapor, while the right half is water in liquid state. As described in the assumptions (Section 2.1), there is no phase change from gaseous to liquid $H_2O$ or vice versa. Additionally, only $H_2$ and $O_2$ are assumed to undergo mass transfer across the interface while $H_2O$ is an ambient species for both phases. The test conditions are summarized in Table 7. The diffusivities for gaseous phase are estimated from kinetic theory [6, 121], and the diffusivities in liquid phase and Henry numbers are taken from Cussler [23] and Sander [125], respectively. The diffusivities in both phases differ approximately in three orders of magnitude. A large concentration jump appears at the interface according to the high Henry number, which is typical for many practical multiphase applications.

The boundary conditions at $z^* = 0$ are fixed concentration ($c_1^* = 0.001$, $c_2^* = 0.001$ and $c_3^* = 0.998$). The reactive flux is specified at $z = h$ according to the rate equation as

$$\dot{s}_i^* = k\nu_i c_1^* c_2^* \tag{3.15}$$

where the stoichiometric relation of the reaction is $-\nu_1 = -2\nu_2 = \nu_3$ and the rate constant $k$

Table 7: Summary of test conditions for $H_2$-$O_2$ ternary reaction diffusion across the phase interface.

| | |
|---|---|
| Temperature (K) | 298 |
| Pressure (kPa) | 101.325 |
| Domain length (m) | $h = L_{\text{ref}} = 1$ |
| Diffusivity ( $m^2/s$ ) | $Đ_{1,2(G)} = Đ_{1,2(L)} = 7.992\times10^{-5}$<br>$Đ_{1,3(G)} = 8.068\times10^{-5}$<br>$Đ_{2,3(G)} = 2.099\times10^{-5}$<br>$Đ_{1,3(L)} = 4.50\times10^{-8}$<br>$Đ_{2,3(L)} = 2.10\times10^{-8}$ |
| Henry number (-) | $H_1 = 52.36$<br>$H_2 = 31.35$ |

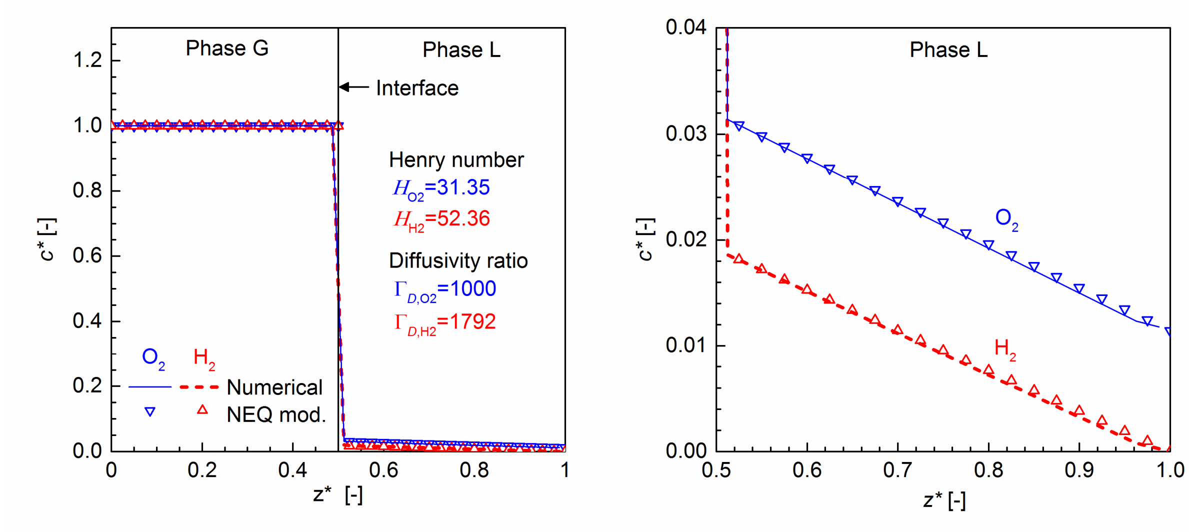

(a) (b)

Fig. 3.16: Concentration profiles for two-phase reactive mass transfer of $H_2$-$O_2$-$H_2O$ mixture. (a): entire domain, (b): zoom-in for liquid region.

is arbitrary specified as $k = 1$ m/s . As concluded in section 3.2, EDM is sufficiently accurate for the multispecies mass transfer. Therefore, only EDM is considered for the numerical calculation in this test case. The steady-state numerical results are compared with the results of NESM where the diffusivities are, however, calculated by MCM in combination with CCDM.

Fig. 3.16 shows the concentration profiles for $H_2$ and $O_2$. In Fig. 3.16 (a), the concentrations of both species in gaseous phase are seen as almost uniform. The previous case shows that the gradient of a certain phase depends on the diffusivity ratio. Thus, almost flat concentration profiles in this figure are caused by the high diffusivity ratio (high diffusivities in gas phase). At the interface, the concentrations drop dramatically according to the high Henry number so that the concentrations in liquid phase are very small. Since the concentration profiles in liquid phase are not clearly shown due to the large concentration difference between two phases, Fig. 3.16 (b) zooms in the liquid region. In liquid phase, the concentrations of both species decrease toward the right wall where the surface reaction takes place. Generally, the computed results agree very well with the results of NESM again. Fig. 3.17 compares the elements of diffusivity matrix in EDM and MCM (from NESM) for gas and liquid phase. This can also be regarded as a comparison of the two diffusion models in a practical application. In gas phase, the estimated diffusivity elements are uniform due to the uniform concentration profiles shown in Fig. 3.16. The diffusivity elements in liquid phase are also almost uniformly distributed.

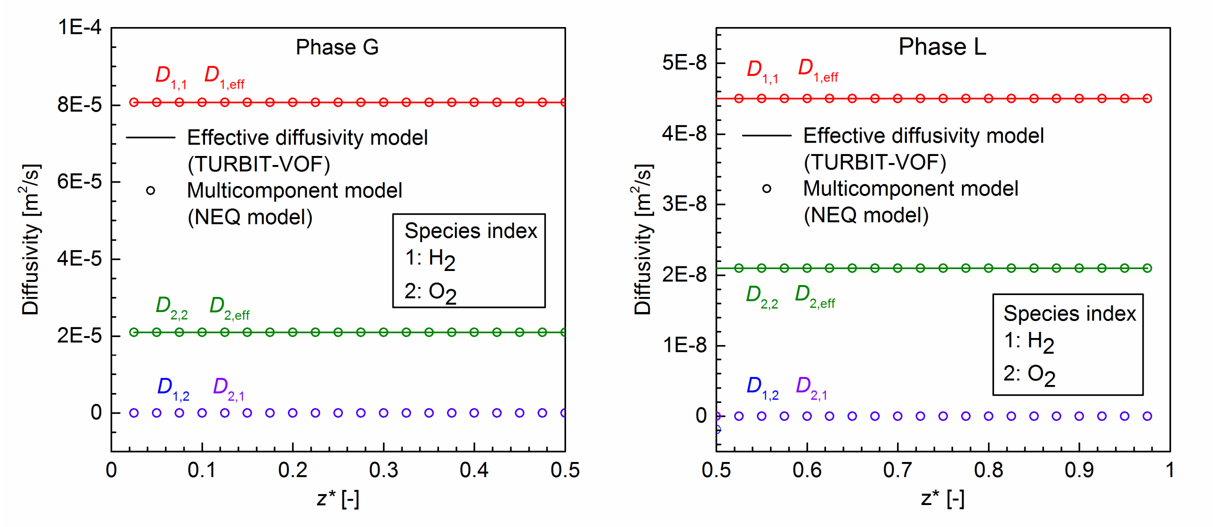

(a) (b)

Fig. 3.17: The elements of the diffusivity matrix in (a) gas phase and (b) liquid phase for $H_2$-$O_2$-$H_2O$ mixture. Comparison of EDM (numerical solution) and MCM (by NESM).

In addition, the change in the species composition is relatively small because $H_2$ and $O_2$ are diluted by $H_2O$ in this condition, which lowers the composition-dependency of the diffusivities. In liquid phase, the concentrations of dissolved species are extremely small as compared to the $H_2O$ concentration. In such a highly diluted condition, the diffusivity in liquid phase becomes almost uniform as well. The remarkable point is that the computed uniform diffusivities in each phase are almost identical to its binary diffusion coefficients in respective phases. A number of studies [8, 16, 99, 121] agree with this finding that the binary diffusion coefficient can be directly used for estimating diffusive mass transfer in liquid phase. Nevertheless, in case the liquid composition changes by liquid phase reactions, the multispecies diffusion model is still essential to determine the composition-dependent diffusivities correctly.

## 3.5 Influence of dilution

A couple of results in previous sections illustrate that there is only negligible difference between the diffusivities of MCM and EDM. Accordingly, the computed mole fraction (or concentration) profiles from two diffusion models are very similar. The results of Stefan tube example and $H_2$-$O_2$ ternary diffusion problem reveal that the differences in diffusivities of both diffusion models are very small especially when the mole fractions of respective species are relatively small, but increase with increasing its fraction. In this section, the difference between both diffusion models is investigated to analyze the influence of dilution with respect to the mixture composition.

For this purpose, a ternary system involving 2-propanol (1), water vapor (2) and nitrogen (3) is chosen with prescribed species composition displayed in Fig. 3.18. Here, nitrogen is regarded as a diluent and its mole fraction is increasing as $z^*$ approaches to unity, where 2-propanol and water vapor are diluted with increasing $z^*$. The binary diffusion coefficients for the three species pairs are taken from literature [132]; the corresponding values are $Đ_{1,2} = 15.99\times10^{-6}\ \mathrm{m^2/s}$, $Đ_{1,3} = 14.43\times10^{-6}\ \mathrm{m^2/s}$ and $Đ_{2,3} = 38.73\times10^{-6}\ \mathrm{m^2/s}$, respectively. To analyze the diffusion models in terms of dilution, a degree of dilution $\delta$ is defined as

$$\delta = \frac{\sum_{i=1}^{n-1} x_i}{x_n} = \frac{x_1 + x_2}{x_3} \tag{3.16}$$

where $x_n$ represents the mole fraction of carrier species in the mixture. For $\delta < 1$ the mole fraction of $n$'th species is larger than the sum of mole fractions of all other species. When $\delta$ is much smaller than unity, $n-1$ species can be treated as diluted by $n$'th species, which is considered as a diluted condition. The profile of $\delta$ for the given species composition is shown in

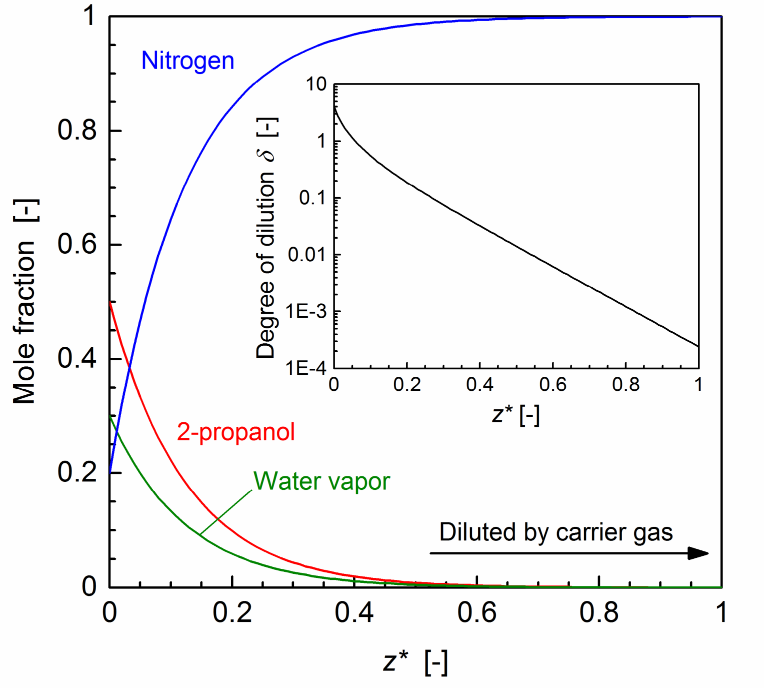

Fig. 3.18: Prescribed mole fraction profiles for studying the dilution effect. The inset shows the profile of the respective degree of dilution as defined by Eq. (3.16).

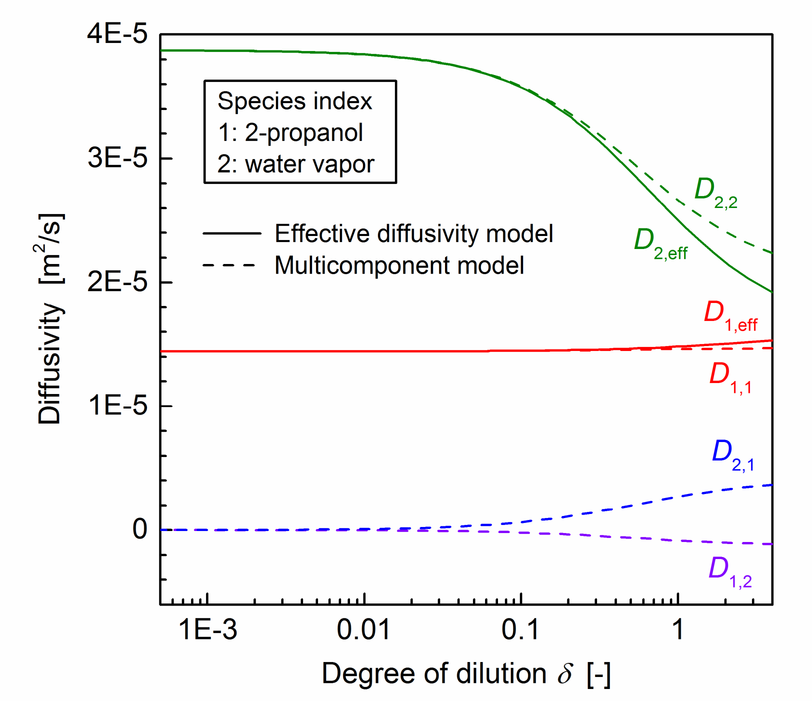

Fig. 3.19: Diffusivities of MCM and EDM with respect to the degree of dilution.

the inset of Fig. 3.18.

Fig. 3.19 shows the diffusivities estimated by MCM and EDM with the prescribed mole fraction profiles. It is figured out that the diagonal diffusivities of MCM ( $D_{1,1}$ and $D_{2,2}$ ) and EDM ( $D_{1,\mathrm{eff}}$ and $D_{2,\mathrm{eff}}$ ) are almost identical in a wide range of $\delta$ parameter. For $\delta < 0.1$, the difference between MCM and EDM is invisibly small, and the corresponding diffusivities of both models are almost overlapped. Accordingly, the cross-coefficient diffusivities ( $D_{1,2}$ and $D_{2,1}$ ) of MCM are almost close to zero in this region. As a result, both diffusion models predict almost the same mole fraction in diluted condition. Even though the Stefan tube (Section 3.2.1) and the ternary reaction-diffusion examples (Section 3.2.2) are not in the diluted condition (where the difference of diffusivity is obvious), EDM predicts plausible results as compared to those of MCM as well. In conclusion, the results of the series of validation cases provide good evidence that EDM is applicable for the practical multispecies diffusion problems.

As described in Section 2.3, diffusive flux is defined with respect to the different velocities according to the definition of composition. TURBIT-VOF solves the mass-average velocity based on the concept of mass conservation. However, it employs concentration as a composition of species since concentration is more useful for the gas-liquid mixture. For single species, all velocities with various definition described in Table 2 are the same, while theses values may differ for mixture. In this section, the dependency of the three velocity definitions on the composition is investigated with the same prescribed mole fraction profiles shown in Fig. 3.18. To this end, only z-direction velocity ($U_z$) is considered, and the total flux in this direction is assumed to be zero ($N_t = 0$) for the whole computational domain. With this assumption and the definition of molar flux in Table 2, the velocity of individual component $U_i$ is defined by Eq. (2.10) as

$$U_i = J_i / c_\mathrm{t} X_i \tag{3.17}$$

The diffusive fluxes $J_i$ are computed by MCM with the elements of diffusivity matrix displayed in Fig. 3.19. The total concentration is $c_\mathrm{t} = 40.2\,\mathrm{mol/m^3}$ where the temperature is 30 °C and the pressure is $1\times10^5$ Pa. The mole fraction can be converted to the mass fraction with molecular species weights $m_1 = 60.1\,\mathrm{g/mol}$, $m_2 = 18.01\,\mathrm{g/mol}$ and $m_3 = 14.0\,\mathrm{g/mol}$, while it is converted to the volume fraction with molar species volumes $\overline{V}_1 = 0.022\,\mathrm{m^3/mol}$, $\overline{V}_2 = 0.014\,\mathrm{m^3/mol}$ and $\overline{V}_3 = 0.011\,\mathrm{m^3/mol}$. From these data, the molar-average velocity, the volume-average velocity, and the mass-average velocity can be evaluated by the definitions of each velocity described in Table 2.

Fig. 3.20 compares the three different velocities with respect to the degree of dilution.

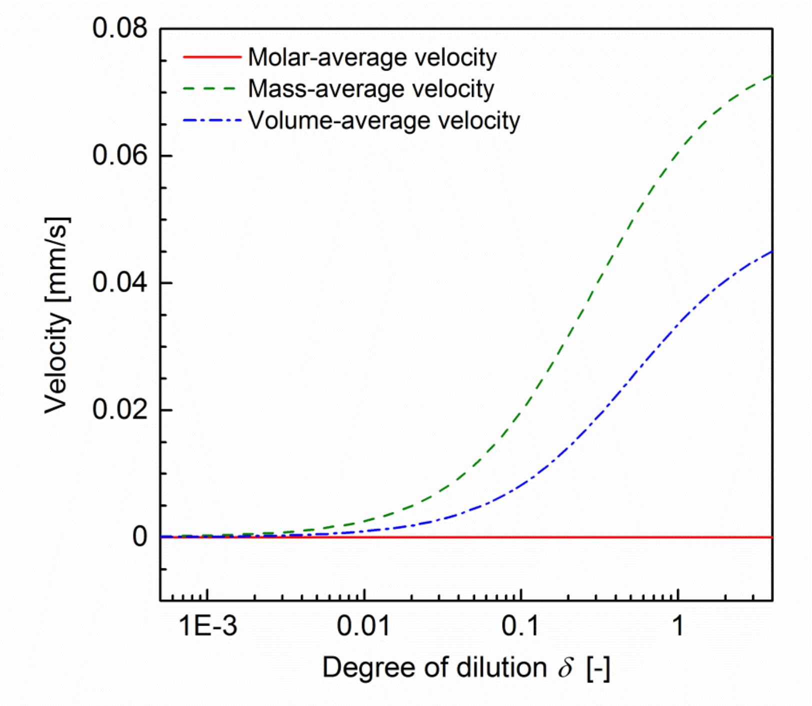

Fig. 3.20: Dependence of differently averaged velocities on the degree of dilution.

According to the assumption ($N_t = 0$), the molar-average velocity ($N_t = c_t U$) becomes zero. The mass-average velocity and volume-average velocity gradually deviate from the molar-average velocity and those differences from molar-average velocity lower as $\delta$ decreases. However, even for $\delta = 0.01$ where the species are diluted, the differences are still noticeable. This result implies that the values of three velocities are not sufficiently close each other even in the diluted condition. The difference may be negligible in highly diluted condition where $\delta < 0.001$, e.g. mass transfer in liquid phase as the present study focuses. Nevertheless, choosing the right velocity definition comes up with the right estimation of the diffusive flux.

## 3.6 Validation of reaction kinetics for hydrogenation of nitrobenzene

This section is devoted to the validation cases that focus on the use of reaction mechanisms for hydrogenation of nitrobenzene producing aniline. The catalyzed reduction mechanism consists of several intermediate reaction steps which highly depend on the catalyst utilized in the process. This reaction has been investigated since the 19th century. The Haber mechanism is a classic and well-known mechanism which proposes a three-step process accompanying nitrosobenzene and phenylhydroxylamine intermediates. Based on this mechanism, many experimental and analytical studies of the reaction were performed in a wide range of conditions with respect to the phase, solvent and catalyst. Despite a large excess of references regarding this reaction, only a few studies have handled the mechanistic details.

The proposed mechanisms until the 1980s were mostly based on the empirical correlation which is a simple function of the fractional order of reactants [134]. Wisniak and Klein [144] investigated the mechanisms and those rate constants by means of numerical optimization procedure even though their conclusion was no plausible mechanism was found. Later, Petrov et al. [114] developed kinetic models over the copper catalyst with a set of rate constants. They also validated their models by experimentation. Instead of Haber mechanism, Gelder et al. [37] suggested a new mechanism from the detailed analysis of surface reaction mechanisms for nitrobenzene and nitrosobenzene, but they did not provide the reaction rates which are required for the computation. Despite such studies, the mechanism is not fully elucidated for most of the catalyst within various conditions. Instead, the reaction process technique regarding liquid-gas or liquid-solid mass transfer, solubility, operating pressure and stirring speed has been more interested to analyze the conversion efficiency with simplified global reaction mechanism, e.g. Langmuir-Hinshelwood type mechanism [34, 64, 87, 135]. Recently, density functional theory analyzes the detail reaction paths and activation energies of each reaction step [100, 151].

The molecular formula for the global reaction of hydrogenation of nitrobenzene is

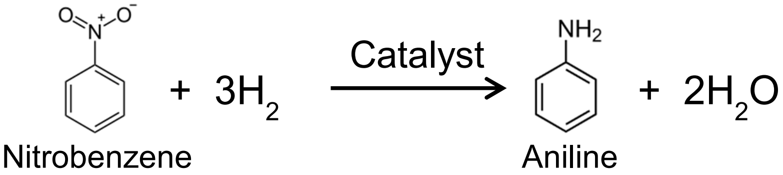

(3.18)

where one nitrobenzene molecule reacts with three hydrogen molecules and then it produces one aniline and two $H_2O$ molecules. Although hydrogenation of nitrobenzene is widely used and very well-known reaction process, the detail reaction mechanism for this reaction has been very seldom investigated. In this study, two reaction mechanisms are chosen. The first one is simplified one-step kinetic model suggested by Höller et al. [64]. The second mechanism is based on Frikha et al. [34] which considers the diffusion limit arising from the interfacial mass transfer. Both studies are conducted in a batch reactor. For the validations of the reaction kinetics, several relevant results on those references are revisited by DETCHEM$^{\mathrm{EVAPORATOR}}$ with user-defined subroutine [30].

### 3.6.1 Simplified one-step kinetic model

Based on the chemical equation of hydrogenation of nitrobenzene Eq. (3.18), Höller et al. [64] provided an Eley-Rideal type one-step reaction mechanism. According to the Eley-Rideal model, catalytic reactions are assumed to be the rate-determining steps of overall reaction rate. The adsorption of nitrobenzene to the catalyst and reaction with non-adsorbed hydrogen in liquid phase are neglected for simplicity. Thus, the rate equation is

$$\dot{r} = k' m_{\mathrm{cat}} \frac{K_{\mathrm{NB}} c_{\mathrm{NB}}}{1 + K_{\mathrm{NB}} c_{\mathrm{NB}}} \tag{3.19}$$

where $K_{\mathrm{NB}}$ denotes the equilibrium constant corresponding to the assumed nitrobenzene adsorption. $k'$ is the modified rate constant defined by $k' = k c_{\mathrm{H2}}$. With the modified rate constant, the concentration of nitrobenzene can only be considered in the rate equation. This simplified

Table 8: Summary of test conditions for the validation case of simplified one-step kinetic model.

| | |
|---|---|
| Temperature (K) | 323 |
| $H_2$ partial pressure (bar) | 4, 7, 10, 12.5 |
| Reactor volume (l) | 0.5 |
| Molecular weight (g/mol) | $m_{NB}=123.06,\ m_{AN}=93.13$<br>$m_{H2}=2.01,\ m_{H2O}=18.02$ |
| Catalyst | Pd/EGF β-HCOONa ( $m_{cat}=0.24\mathrm{g}$ )<br>Pt/EGF β-$H_2$ ( $m_{cat}=0.4\mathrm{g}$ ) |
| Stirring speed (rpm) | 1300 |

one-step reaction mechanism does not take into account any mass transfer limitations.

The test conditions are described in Table 8. In this case, two catalysts are employed with different hydrogen partial pressure. The corresponding rate constants $k'$ are estimated for each test condition. Since the temperature of batch reactor is uniformly controlled in the experiment, a constant temperature is specified for the numerical calculation. The first case utilizes an alumoborosilicate glass fibers (GF) type β catalyst with pretreatment of HCOONa (Pd/EGF β-HCOONa [64]) in 7 bar of hydrogen partial pressure. The initial concentration of nitrobenzene $c_{NB,0}$ is set to 0.14 mol/l, while the concentration of aniline is initially zero. The rate constant $k'$ and equilibrium constant for nitrobenzene $K_{NB}$ are given as $0.74\ \mathrm{mol}\left(\mathrm{l}\cdot\mathrm{s}\cdot\mathrm{g}_{\mathrm{cat}}\right)^{-1}$ and 7.2 $\left(\mathrm{mol/l}\right)^{-1}$, respectively.

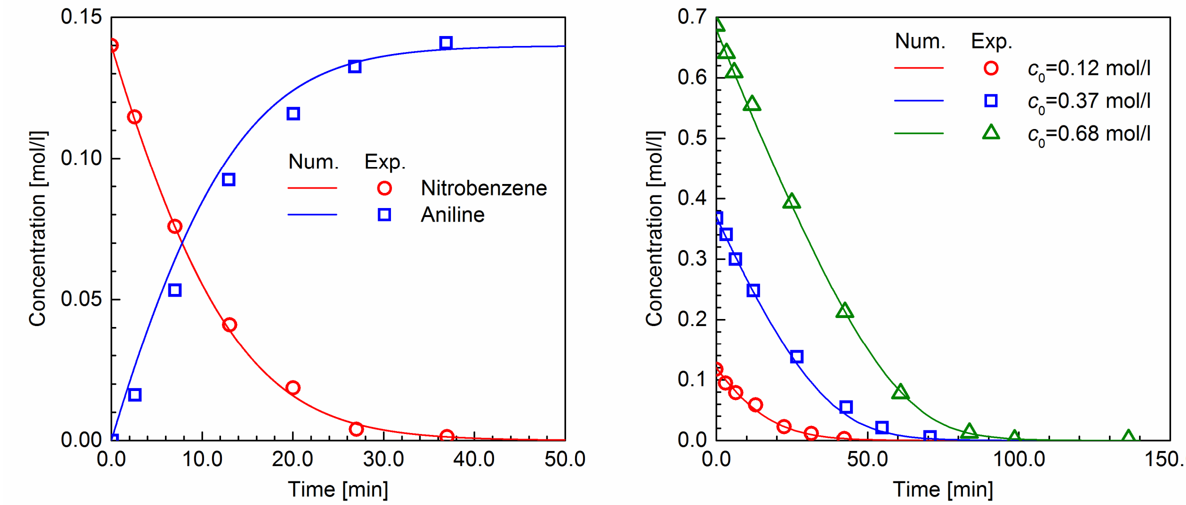

Fig. 3.21 Comparison between numerical solutions and experimental results [64]. (a) Concentration profiles of nitrobenzene (reactant) and aniline (product) over time. (b) Concentrations of nitrobenzene according to the different initial concentration

The numerical results are generally in very good agreement with the experimental data provided in Höller et al. [64]. Fig. 3.21 (a) presents the predicted and measured concentration profiles for the first case as a function of time. During the reaction process, nitrobenzene is consumed whereas aniline is produced, simultaneously. In numerical results, the consumption rate of nitrobenzene is exactly the same as the production rate of aniline since the same reaction rate in Eq. (3.19) is applied to both consumption and production. In experimental data, however, the gradients of consumption and production differ. It may be caused by the existence of by-products of the reaction, which cannot be considered in the one-step global kinetic model in this study.

Secondly, the same type catalyst with pretreatment of H2 (Pt/EGF β-$H_2$) is employed with various initial concentration of nitrobenzene $c_{\mathrm{NB},0} = 0.12$, $0.37$ and $0.68\ \mathrm{mol/l}$. For this case, the hydrogen partial pressure is also kept to 7 bar, and the reaction parameters are $k' = 0.31$ mol $\left(\mathrm{l}\cdot\mathrm{s}\cdot\mathrm{g}_{\mathrm{cat}}\right)^{-1}$ and $K_{\mathrm{NB}} = 7.0\ \left(\mathrm{mol/l}\right)^{-1}$. The weight of catalyst is $m_{\mathrm{cat}} = 0.4\,\mathrm{g}$. Fig. 3.21 (b) illustrates the comparison of concentration profiles between numerical results and experimental data. This figure compares the decrease of nitrobenzene concentrations due to the reaction. It turns out that the kinetic model with given reaction parameters can capture the trend of measured

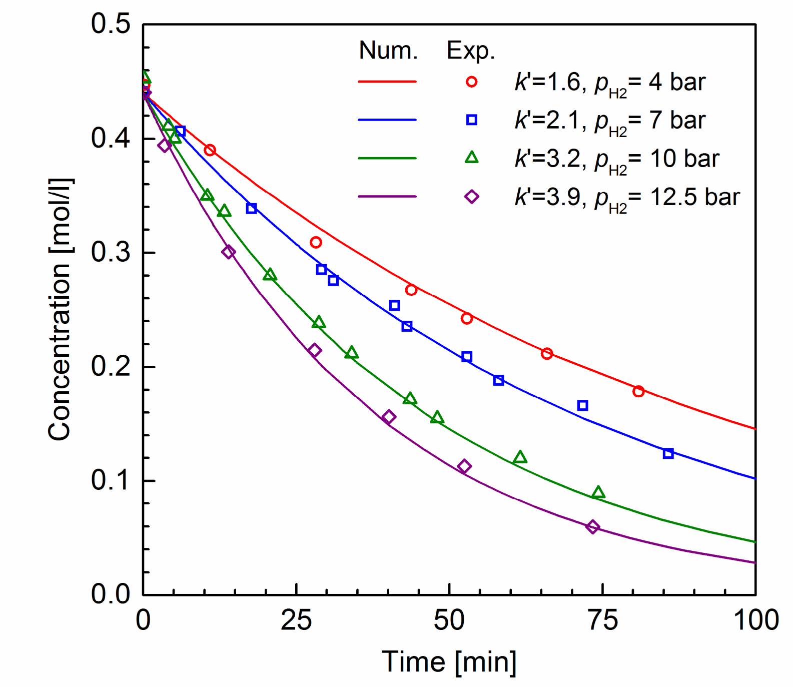

Fig. 3.22: Comparison of concentration profiles according to the different rate constant $k'$ corresponding to the hydrogen partial pressure.

data with different initial concentrations. This figures out that the simplified model with two reaction parameters is suitable for a wide range of nitrobenzene concentration at a certain temperature and pressure.

Finally, the effect of hydrogen partial pressure is considered with four different values of partial pressure. The same catalyst is used as for the previous case (Pt/EGF β-H2, $m_{\mathrm{cat}} = 0.4\mathrm{g}$). Different rate constants are required for each hydrogen partial pressure, and the respective values are $k'$ =1.6, 2.1, 3.2 and 3.9 $\mathrm{mol}\left(\mathrm{lsg}_{\mathrm{cat}}\right)^{-1}$ for $p_{\mathrm{H}_2}$ =4, 7, 10 and 12.5 bar. The initial concentration is $c_{\mathrm{NB},0} = 0.44$ mol/l and the equilibrium constant is $K_{\mathrm{NB}} = 0.15\ \left(\mathrm{mol/l}\right)^{-1}$.

Fig. 3.22 shows the concentration profiles with different partial pressure and compares the predicted and measured data. Again, the numerical results are in very good agreement with the experimental data. Thus, all of the results in Höller et al. [64] are perfectly recomputed by DETCHEM$^{\mathrm{TM}}$ solver. In the sequel, the reaction kinetic model validated with DETCHEM$^{\mathrm{TM}}$ is directly applicable to the coupled solver by using the same DETCHEM$^{\mathrm{TM}}$ interface.

## 3.6.2 Reaction kinetics with gas-liquid mass transfer limitation

Next case is the validation of another one-step reaction kinetics proposed by Frikha et al. [34]. A distinct point of this mechanism is the consideration of mass transfer limitation in the mass transfer between gas and liquid phases. The experimentation of Frikha et al. [34] was performed in the semi-batch reactor shown in Fig. 3.23. In this reactor, hydrogen is added to the reactor with keeping its partial pressure constant. Therefore, the added amount of hydrogen is

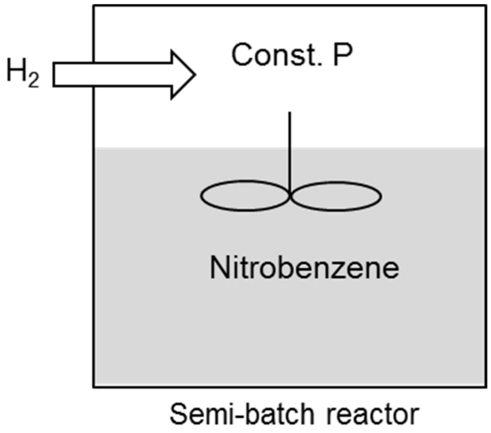

Fig. 3.23: Conceptual sketch for the semi-batch reactor in Frikha et al. [34].

exactly the same as the consumed amount of hydrogen by the reaction. With this concept, the global reaction mechanism is developed by Frikha et al. [34]. The consumption rate of hydrogen in the semi-batch reaction is given by

$$\dot{r}_{\mathrm{H}_2} = \frac{p_{\mathrm{H}_2} / H_{\mathrm{H}_2}}{1/[k\exp\left(-E/RT\right)\rho_{\mathrm{cat}} c_{\mathrm{NB}}^{1/3}] + 1/[k_{\mathrm{L}} a]} \tag{3.20}$$

where $p_{\mathrm{H}_2}$ is the hydrogen partial pressure and $\rho_{\mathrm{cat}}$ is the density of catalyst. The Eq. (3.20) consists of three terms, one numerator and two denominators. The numerator of the equation represents the hydrogen concentration transferred into liquid phase. $H_{\mathrm{H2}}$ is the Henry coefficient of hydrogen into liquid nitrobenzene as

$$H_{\mathrm{H2}} = 1\times 10^{4} \exp\left(\frac{551}{T}\right). \tag{3.21}$$

The first term of the denominator in Eq. (3.20) represents the inverse of reaction rate at the catalytic surface. $k$ and $E$ denote the rate constant and the activation energy of the reaction, respectively. Finally, the second term of denominator indicates the inverse of mass transfer coefficient of hydrogen between gas and liquid phase (nitrobenzene) written as

$$k_{\mathrm{L}} a = 4.17\times 10^{-12} T^{2.52} \omega^{3.1} \tag{3.22}$$

where $\omega$ is the stirring speed of the semi-batch reactor. The denominator in Eq. (3.20), the inversed values, stands for the harmonic mean of the reaction rate and the mass transfer coefficient so that the actual apparent reaction rate is dominated by the combination of these two parameters.

Table 9: Summary of test conditions for the validation case of reaction kinetics with gas-liquid mass transfer limitation.

| | |
|---|---|
| Pressure (kPa) | $p$ =300 |
| Volume of nitrobenzene (l) | 0.75 |
| Stirring speed (rpm) | $\omega$ =2000 |
| Catalyst | Pellet type with 5% palladium |
| Density of catalyst (kg/m$^3$) | $\rho_{\mathrm{cat}}$ =1.5 |
| Pellet size (μm) | < 20 |
| Specific surface area (m$^2$/g) | 1000 |

One relevant test case is chosen from Frikha et al. [34] for the validation of their reaction kinetics. The test conditions of the selected case are summarized in Table 9. Hydrogen partial pressure in gaseous phase is defined by $p_{H2} = X_{H2}p$. In the simulation, it is assumed that only hydrogen exists in gas phase ($X_{H2} = 1$) and no evaporation occurs from liquid phase. Therefore, the hydrogen partial pressure $p_{H2}$ is equal to the total pressure $p$ with this assumption. Molecular weights of species are given in Table 8 in section 3.6.1. The rate constant $k$ and activation temperature $E/R$ are $1023\,\mathrm{m^3/kg \cdot s}$ and $2422\,\mathrm{K}$, respectively. In contrast with the previous example in Section 3.6.1, the temperature, in this case, is not controlled to be constant during the reaction. Fig. 3.24 (a) plots the temperature profile obtained from the experiment. Temperature increases slightly in the beginning, decreases almost linearly during the most of the reaction time and finally drops sharply. To take into account this temperature variation to the numerical simulation, the temperature profile is linearly estimated from the experimental data and given as an input for the solver.

Fig. 3.24 (b) displays the nitrobenzene conversion profile evaluated from the results and compares it to the experimental data [34]. According to the reaction progress, the conversion of nitrobenzene is increasing and finally approaching unity. In this case, the numerical result is in reasonable agreement with the measured values from the literature. There are several possible reasons of the remaining deviation. The first one may be the estimation of the temperature as illustrated in Fig. 3.24 (a). In addition, the assumption of gaseous mole fraction for this

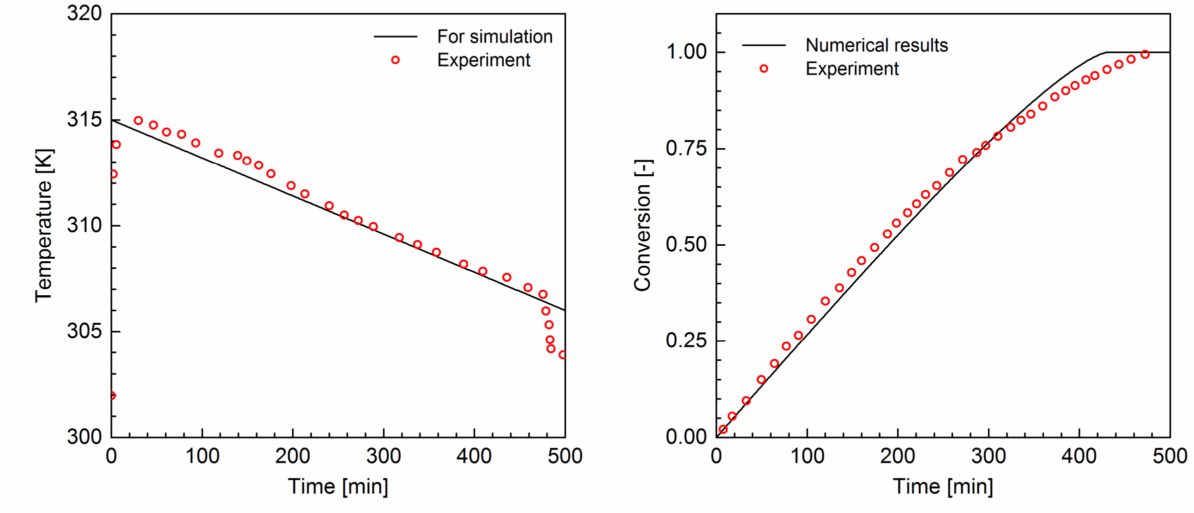

(a) (b)

Fig. 3.24: (a) Temperature profile from the experiment [34] and estimated temperature profile for the computation by curve-fitting from the experimental data. (b) Comparison of predicted and measured values for conversion of nitrobenzene.

calculation ( $X_{\mathrm{H2}} = 1$ ) can influence the deviation. The Henry coefficient and mass transfer coefficient utilized may also cause the error because the values in this calculation are only for the pure nitrobenzene, while the real values would be a function of liquid composition. Despite small deviation being observed, this reaction mechanism including mass transfer limitation is successfully validated by DETCHEM$^{\mathrm{TM}}$ solver as well. The reaction rate at the catalytic surface may be more accurately estimated with consideration of mass transfer limitation. The only apparent reaction rate can be obtained, otherwise.

# Chapter 4

# Parametric studies on Taylor flow for artificial fluid systems

This chapter concerns the numerical pre-studies of flow and mass transfer within a Taylor flow. An artificial fluid system is selected before dealing with the real fluid system whose physical properties are harsh for numerical simulation. Section 4.1 presents a numerical parametric study of Taylor flows with different combinations of governing parameters. This parametric study focuses mainly on the influences of Reynolds and capillary numbers which are the major governing parameters for the shapes of the Taylor bubble. In the sequel, the effect of density and viscosity ratios are investigated in following Section 4.2. Section 4.3 describes a grid dependency test to figure out the reasonable size and number of mesh cells for both hydrodynamic and mass transfer calculations. Finally, a numerical technique, moving reference frame is introduced in Section 4.4. The computational domains for all test cases in this chapter are two-dimensional symmetric condition against the centerline of the bubble.

## 4.1 Characteristics of gas-liquid Taylor flow

Since the selected reaction of the present study is hydrogenation of nitrobenzene where gas hydrogen is transferred into liquid nitrobenzene, the physical properties of those species are necessary for the calculation. The gas-to-liquid density and viscosity ratio of this set of fluids are $6.515\times10^{-4}$ and $5.495\times10^{-3}$, respectively. These values are relatively low as compared to those for the other Taylor flows which are successfully computed by TURBIT-VOF. To classify the Taylor flows, two additional dimensionless numbers are introduced as

$$Ca := \frac{\mu u_{\mathrm{B}}}{\sigma}, \quad Mo := \frac{g\mu_{\mathrm{L}}^{4}\left(1-\Gamma_{\rho}\right)}{\rho_{\mathrm{L}}\sigma^{3}} \tag{4.1}$$

Capillary number ($Ca$) represents the ratio of viscous force and surface tension. Morton number ($Mo$) characterizes the fluid system and is also used to estimate the numerical instability for the hydrodynamic solutions of Taylor flows. In general, the lower Morton number the fluid system has, the less numerically stable its solution becomes. The value of $\log_{10} Mo$ for nitrobenzene and hydrogen mixture is -9.23. This low Morton number may cause the numerical solution to be unstable. Therefore, an artificial fluid system is chosen as a pretest before dealing with the real fluid system comprised of nitrobenzene and hydrogen. The physical properties of the chosen artificial fluid system are given in Table 10. The Morton number of this fluid system is -2.36, which is higher than that of the real fluid system and known to be more stable. Thus, the numerical parametric study of 2D Taylor flow is conducted in various conditions with the artificial fluid system to understand those influences on numerical solutions and to determine the suitable range of the test condition for the real fluid system.

Table 11 shows the six test conditions selected with different (quasi-steady) bubble velocities and channel heights $h$. Axial pressure difference along the unit cell $\Delta p_{\mathrm{UC}}$ is used as a variable to control the steady bubble velocity. Unit cell length $L_{\mathrm{UC}}$ is specified as three times of $h$ of each case. The initial size of the bubble is determined in accordance with $h$. The bubble thickness for case A1, A3, A6, where the expected film thickness is relatively thick due to the high bubble velocity, is set to $0.6h$, while the bubble thickness for the other cases is set to $0.9h$ to consider the thin initial film thickness. The initial length of the bubble is sum of the channel height and bubble thickness (e.g. $L_{\mathrm{B}} = 1.6h$ for the case A1). The gas volume fraction of case A1, A3, A6 is 0.29, and for other cases it is 0.51. Density and viscosity ratios are 0.1 and 0.001, respectively. $u_{\mathrm{ref}}$ is set to unity for all cases.

Table 10: Physical properties of an artificial fluid system.

| Properties | Liquid | Gas | G/L Ratio |
|---|---|---|---|
| Density, $\mathrm{kg/m^3}$ | 100 | 10 | 0.1 |
| Viscosity, $\mathrm{Pa \cdot s}$ | 0.05 | $5\times10^{-5}$ | 0.001 |
| Surface tension, $\mathrm{N/m}$ | 0.05 | - | - |

Table 11: Test conditions of the parametric study for variable bubble velocity and channel height.

| Case | $h$, m | $L_{\mathrm{UC}}$, m | $t_{\mathrm{ref}}$, s | $\Delta p_{\mathrm{UC}}$, $\mathrm{N/m^3}$ | $Re$ | $Ca$ |
|---|---|---|---|---|---|---|
| A1 | 0.001 | 0.003 | 0.0005 | 83333 | 3.73 | 1.87 |
| A2 | 0.01 | 0.03 | 0.005 | 83.3 | 3.58 | 0.18 |
| A3 | 0.01 | 0.03 | 0.005 | 833 | 33.04 | 1.65 |
| A4 | 0.1 | 0.3 | 1 | 0.167 | 3.93 | 0.020 |
| A5 | 0.1 | 0.3 | 1 | 1 | 31.12 | 0.16 |
| A6 | 0.1 | 0.3 | 1 | 8.33 | 288.6 | 1.44 |

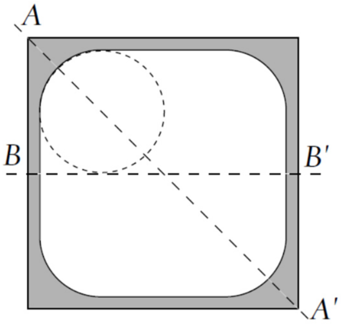

Fig. 4.1: The shape of a bubble and surrounding liquid film for Ca < 0.04 at the cross-section of a square channel (adapted from Kreutzer [88]).

In technical applications, Taylor bubbles in a square channel have different shapes according to the bubble size and channel aspect ratio. Several studies [88, 150] reported that for $Ca < 0.04$ bubble shapes are non-axisymmetric and its cross section is rounded rectangular. The thickness of the flattened liquid film is almost constant as shown in Fig. 4.1. Due to the rounded rectangular cross-sectional area, a Taylor bubble in such channels can be represented by a two-dimensional symmetric bubble (as cross section BB') with assuming that the effect of corners is neglected. Therefore, the computational domain can be set to two-dimension in this study. The domain and boundary conditions for the 2D simulation are depicted in Fig. 4.2. The boundary condition of upper side is a no-slip wall. Later in the simulation of mass transfer, the catalyzed surface reaction takes place at this upper wall so that the reactive fluxes normal to the wall are applied to this boundary. The boundary condition of lower side is symmetry. The reference length is accordingly a half of channel height ($L_{\text{ref}} = 0.5h$). With the symmetric condition calculation time is saved, and numerical errors causing non-symmetrical effect are inherently

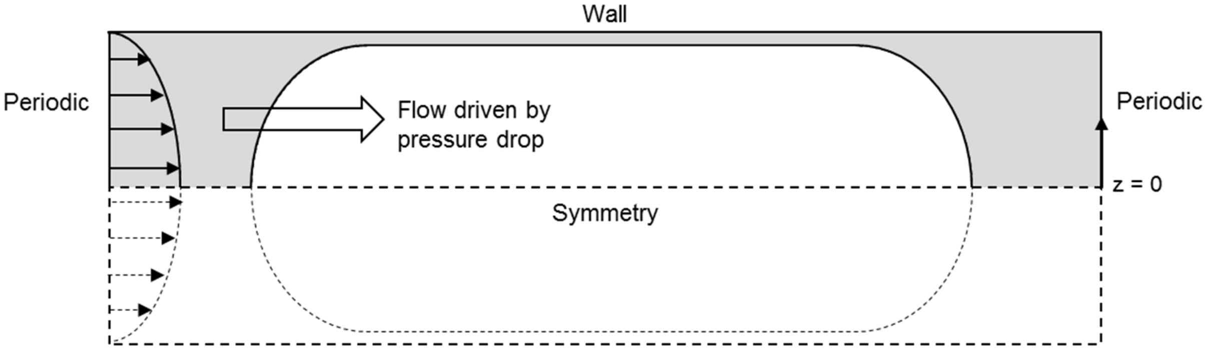

Fig. 4.2: The symmetrical computational domain and its boundary condition for 2D Taylor flow.

eliminated. Left and right sides are specified as a pair of periodic boundary condition. A parabolic velocity profile is initially given for the whole computational domain. This calculation employs a uniform grid, but the number of cells is chosen with the expected film thickness for each case; 240×2×40 cells are used for case A4 where the bubble velocities are relatively small, while 150×2×25 cells are used for the other cases. After starting the simulation, the initial shape of the bubble is developing, and finally, it reaches to the quasi-steady state where the bubble is just moving through the flow without changing its shape. The calculation is conducted with monitoring the time evolution of the bubble velocity until the bubble velocity becomes constant at the quasi-steady state.

Fig. 4.3 displays terminal bubble shapes and velocity profiles evaluated by both moving reference frame (MRF) and fixed reference frame (FRF) for the six test cases. The velocity in MRF is shown in the lower half part of each figure. This velocity is evaluated by subtraction of mean bubble velocity from the velocity in FRF. Therefore, the velocity near the wall is almost zero in FRF, while in MRF it is represented as a bypass velocity against the flow direction. In Fig. 4.3, the results show various bubble shapes depending on the different bubble velocities. According to the bubble velocity, the test cases are divided into three types, case A1, A3, A6, case A2, A5 and case A4. The case A1 and A3 whose bubble velocities are relatively high show thick liquid film and concave shape at the rear part of the bubble. In these cases, the MRF velocity shows that a circulating flow field only appears inside the bubble. However, in the other cases, the recirculation zone is additionally observed between the bubbles. In case A6, the flow cannot even form a regular shape of Taylor bubble. The film thicknesses of case A2 and A5 are thinner than those of case A1 and A3. For case A4 where the bubble velocity is relatively small, the film thickness is very thin as expected. The axial velocity distributions for case A1 to A5 are stable, while that of case A6 shows complicated behavior inside the bubble. Relatively high Reynolds number may cause the complex and irregular velocity field shown in case A6. To validate the hydrodynamic solutions, the results are assessed with a flow regime map for two-phase flow. Fig. 4.4 shows the pictorial diagram of Haase et al. [48] which presents the five different flow regimes in the circular mini-channel of $1\text{mm}$ diameter. According to the velocities of gas and liquid, two-phase flow presents five different types; bubbly flow, slug flow, slug annular flow, annular flow and churn flow. For the Taylor flow concerned in the present study, slug flow is the desirable type of the flow. Fig. 4.5 compares numerical results to the flow regime map provided by Akbar et al. [3], which is derived for two-phase flow in the same circular

(a) Case A1

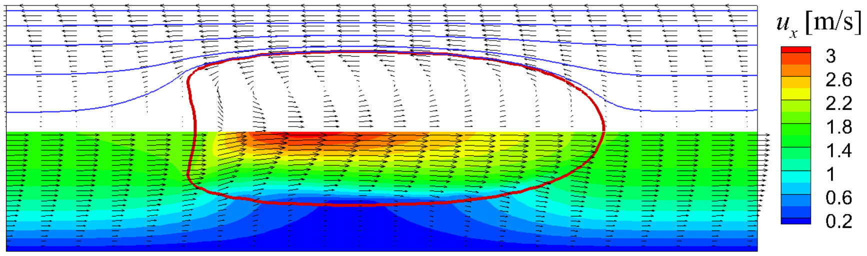

(b) Case A2

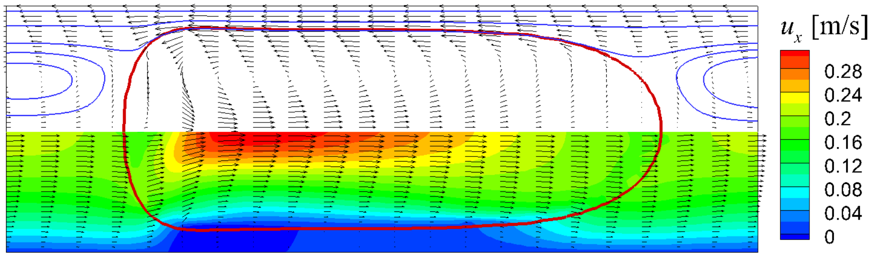

(c) Case A3

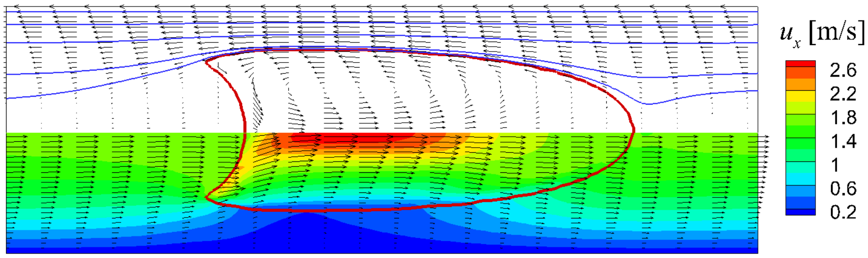

(d) Case A4

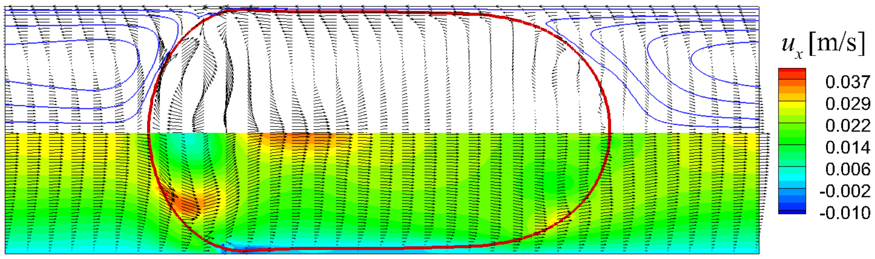

(e) Case A5

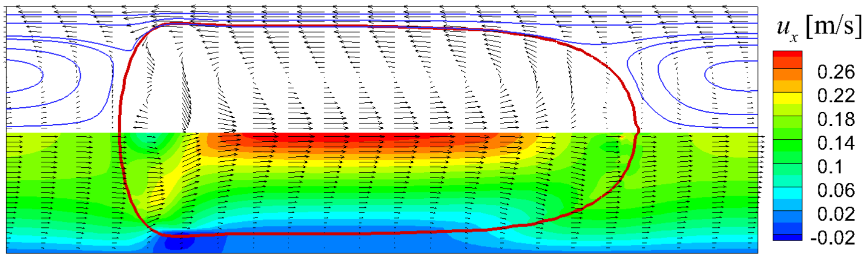

(f) Case A6

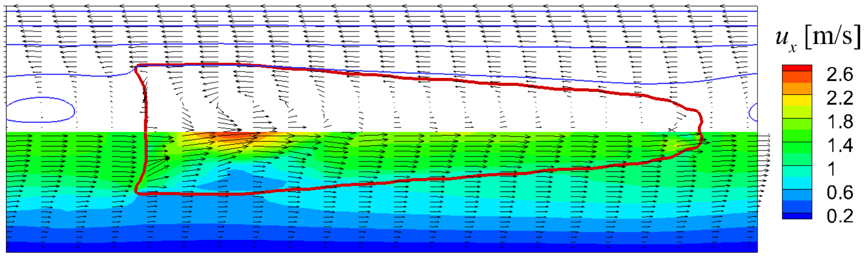

Fig. 4.3: Results of hydrodynamic test cases (upper half: streamlines and velocity in moving frame of the bubble, lower half: axial velocity ($u_x$) distributions and velocity vectors in fixed frame).

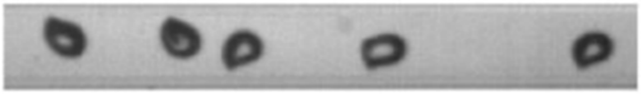

(a) Bubbly flow

(b) Slug flow

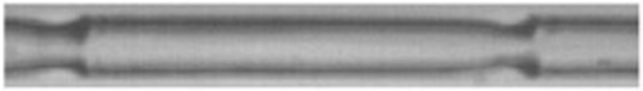

(c) Slug annular flow

(d) Annular flow

(e) Churn flow

Fig. 4.4: Five flow types of two-phase flow in a circular mini-channel (adapted from Haase et al. [48]).

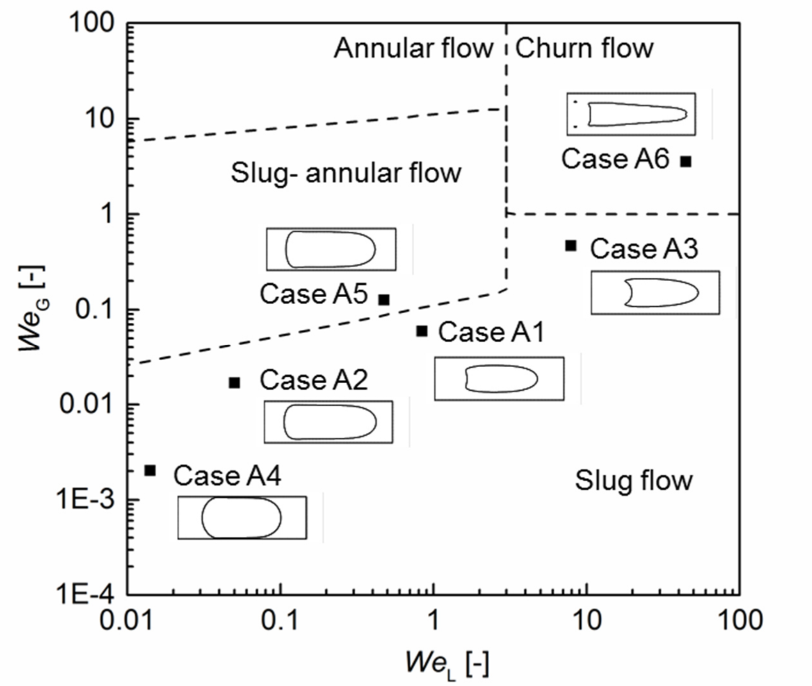

Fig. 4.5: Results of the artificial fluid system on flow regime map [3] with respect to Weber numbers of gas and liquid phases.

microchannel used for Fig. 4.4. This flow regime map consists of Weber numbers for gas and liquid phases, which are estimated by mean superficial velocities of each phase. Note that, the geometry for the numerical solutions is a rectangular channel (or a planar channel), while the flow regime map is evaluated with the circular channel. Even though the test conditions for flow regime map and numerical solutions are not exactly identical, this comparison provides an idea of checking whether the numerical solutions are in physically reasonable range.

In Fig. 4.5, most of the cases are located in the slug flow region. Case A2 and A4 which show a typical shape of a Taylor flow are in the slug flow regime. In case A1 and A3 whose bubble velocities are relative high, the bubble forms a bullet shape with thick liquid film, and concave shape appears at the rear part of the bubble. This kind of shapes is caused by the relatively high velocity against the channel diameter, which leads to a high capillary number. Nevertheless, these cases are in the slug flow regime as well. Case A5 is located slightly away from the slug flow regime and placed in the slug-annular flow regime. However, the bubble still forms a type of Taylor flow. Therefore, this small deviation in the flow regime map may be caused by the geometrical difference and be acceptable for further calculations. Case A6 whose bubble velocity and Reynolds number are high shows the highly distorted shape from a typical Taylor bubble. It turns out that this case is located in the churn flow regime. Thus, the test

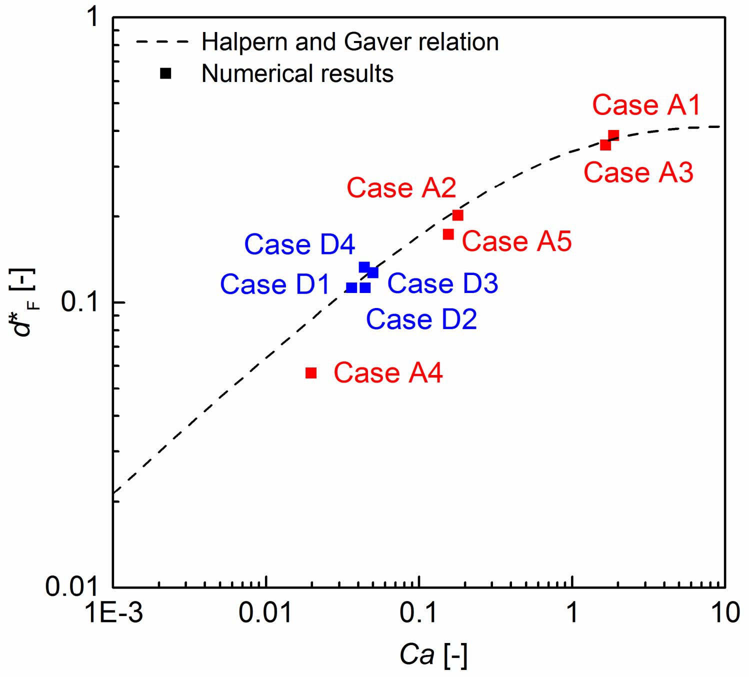

Fig. 4.6: Comparison of film thicknesses of test cases with Halpern and Gaver correlation [50].

conditions which result in either a churn flow as case A6 or concave shape at the rear bubble as case A1 and A3 should be avoided in the test conditions for the real fluid system. Though the flow criteria from Akbar et al. [3] correspond to the flow in a circular microchannel, they are also useful to qualitatively analyze the flow regimes of numerical results of 2D Taylor flows in this study.

In addition to the flow regime, the film thickness of the solution is validated with the literature data. The film thickness $d_{\mathrm{F}}$ is the distance between the bubble and the wall, and it is one of the most important parameters for mass transfer within a Taylor flow. For validation, the dimensionless thickness $d_{\mathrm{F}}^{*}$ of numerical solutions is estimated and compared to the study of Halpern and Gaver [50] which provides a correlation of film thickness for Bretherton problem in terms of capillary number:

$$d_{\mathrm{F}}^{*} = \frac{2d_{\mathrm{F}}}{L_{\mathrm{ref}}} = 0.417\left(1-\exp\left(-1.69Ca^{0.5025}\right)\right) \tag{4.2}$$

The capillary numbers for Eq. (4.2) are estimated by the bubble velocity.

Fig. 4.6 displays the film thickness of numerical solutions and the correlation from Eq. (4.2). The cases starting with D will be introduced later in Chapter 5. The thickness of liquid film shown in Fig. 4.3 is not uniform in such a short bubble. To estimate the film thickness of numerical solutions, an interpolated line for $f = 0.5$ is chosen as a corresponding line for the bubble shape. The distance between the wall and this line is measured at the first point where the gradient of this line becomes zero from the front of the bubble. Except for the case A6 which is in the churn flow regime, the predicted film thicknesses are generally in good agreement with the correlation. The film thickness of case A4 whose liquid film is relatively thin are slightly underestimated from the correlation. The reason may be that the grid (40 cells in wall-normal direction) is not sufficiently fine to resolve the flow in such a very thin film region. Nevertheless, for most of the conditions the solver can successfully compute the 2D Taylor flows with reasonably accurate film thickness.

To determine the test condition for real fluid system, the results of the artificial fluid system are redrawn on the diagram of dimensionless numbers. Thus, Fig. 4.7 shows the Reynolds-capillary diagram for the test conditions of the artificial fluid system. In this diagram, test conditions are clearly distinguished to the sub-regions. If the capillary number is small as case A4, the results show very thin film thickness. This complies with the former studies for

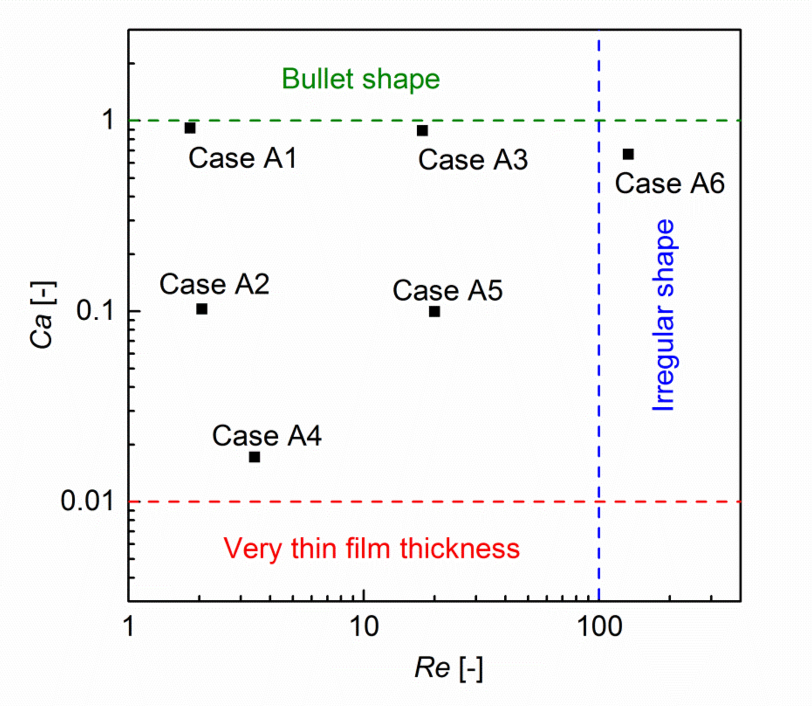

Fig. 4.7: Reynolds-capillary diagram for artificial fluid system.

Bretherton problems. This condition is, however, unfavorable for further computations because a very fine grid is then required to resolve such a very thin film flow. Also, case A6 which has both high Reynolds and capillary numbers should be avoided because the solution does not form a Taylor bubble anymore. Finally, the region where the capillary number is high as case A1 and A3 forms a bullet-shaped bubble. This condition is also not preferred for further investigations.

As a result of the study on the artificial fluid system, the range of test conditions for real fluid system can be more concretely defined. In addition to the test conditions of case A1, A3, A6 which are excluded from the flow regime, the condition of case A4 is also not considered to avoid a very fine grid. From *Re*-*Ca* diagram, the range of Reynolds and capillary numbers for desirable Taylor flow are approximately determined as $0.01<Ca<1.0$ and $Re<100$. Finally, it is found out that the test condition of case A2 is most suitable since the flow is in a slug flow regime and the film thickness agrees well with the correlation of Halpern and Gaver [50]. The guideline obtained by the series of results with the artificial fluid system provides a basic idea to determine the appropriate test conditions for the real fluid system which consists of nitrobenzene and hydrogen.

## 4.2 Influence of the gas density and gas viscosity

In addition to the effect of velocity and channel height relating to Reynolds and capillary numbers, this section takes into account another numerical parametric study concerning the density and viscosity ratio of gas and liquid composing a Taylor flow. For this purpose, gas density $\rho_{\mathrm{G}}$ and gas viscosity $\mu_{\mathrm{G}}$ are chosen for the variables in this section. The test case for this section is based on case A2 which shows most desirable and stable results in the previous section. Therefore, the channel height and velocity are identically set as $h = 0.01\,\mathrm{m}$ and $u_{\mathrm{ref}} = 1\,\mathrm{m/s}$ as well as the axial pressure difference, $\Delta p_{\mathrm{UC}} = 83.3\,\mathrm{N/m^3}$. Table 12 shows the test conditions of parametric study with regard to the ratio of dynamic viscosity $\Gamma_\mu$ and density $\Gamma_\rho$.

Table 12: Test conditions for numerical parametric study of the gas density and gas viscosity.

| Case | $\rho_{\mathrm{G}}$, $\mathrm{kg/m^3}$ | $\mu_{\mathrm{G}}$, $\mathrm{Pa \cdot s}$ | $\nu_{\mathrm{G}}$, $\mathrm{m^2/s}$ | $\Gamma_\rho$ | $\Gamma_\mu$ |
|---|---|---|---|---|---|
| B1 | 100 | $5\times10^{-3}$ | $5\times10^{-5}$ | 1 | 0.1 |
| B2 | 10 | $5\times10^{-4}$ | $5\times10^{-5}$ | 0.1 | 0.01 |
| B3 | 1 | $5\times10^{-5}$ | $5\times10^{-5}$ | 0.01 | 0.001 |
| B4 | 10 | $5\times10^{-5}$ | $5\times10^{-6}$ | 0.1 | 0.001 |
| B5 | 100 | $5\times10^{-5}$ | $5\times10^{-7}$ | 1 | 0.001 |

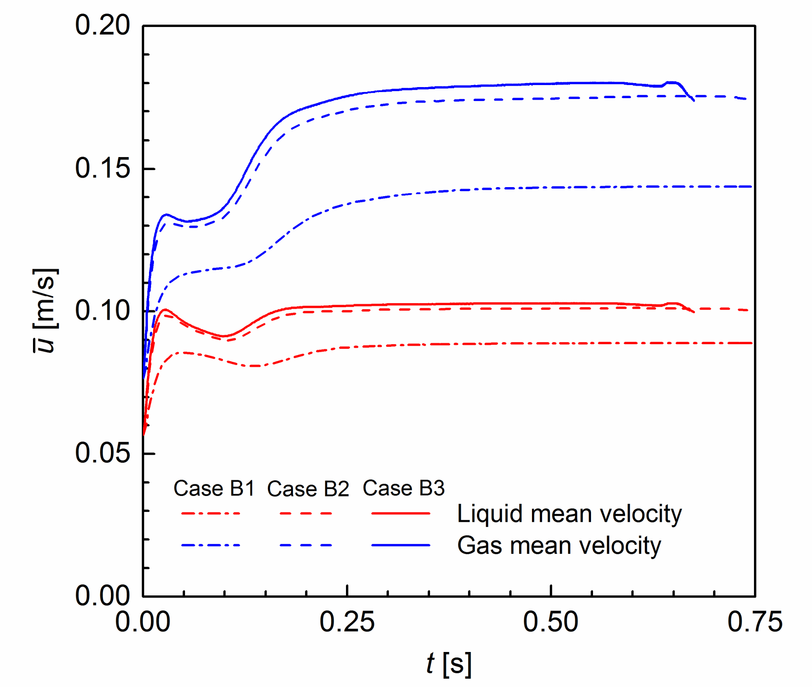

Fig. 4.8: Time evolution of mean velocities of Taylor flows for case B1~B3 (identical gas kinematic viscosity).

The liquid properties are the equally employed as Section 4.1 and given in Table 10. In case B1, B2 and B3, the different densities and viscosities of gaseous phase are utilized with an identical gas kinematic viscosity, $\nu_{\mathrm{G}}$ .

Fig. 4.8 displays the time evolution of mean velocities for gas and liquid phase during the calculation. This figure clearly shows there are differences among the cases. The solutions reach to the quasi-steady state after $t > 0.5\,\mathrm{s}$ . The mean terminal velocities of three cases differ despite

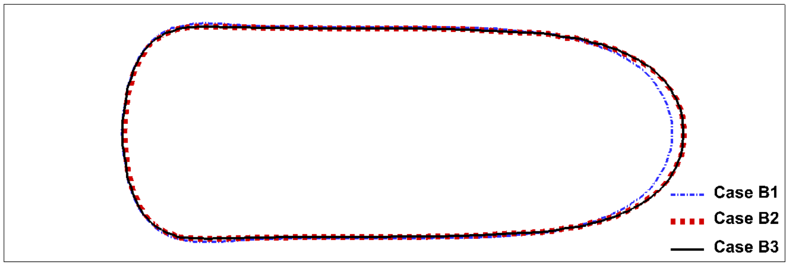

Fig. 4.9: Comparison of terminal bubble shapes for case B1~B3 with identical gas kinematic viscosity. $t$ =0.75s for case B1 and B2 and at $t$ =0.675s for case B3.

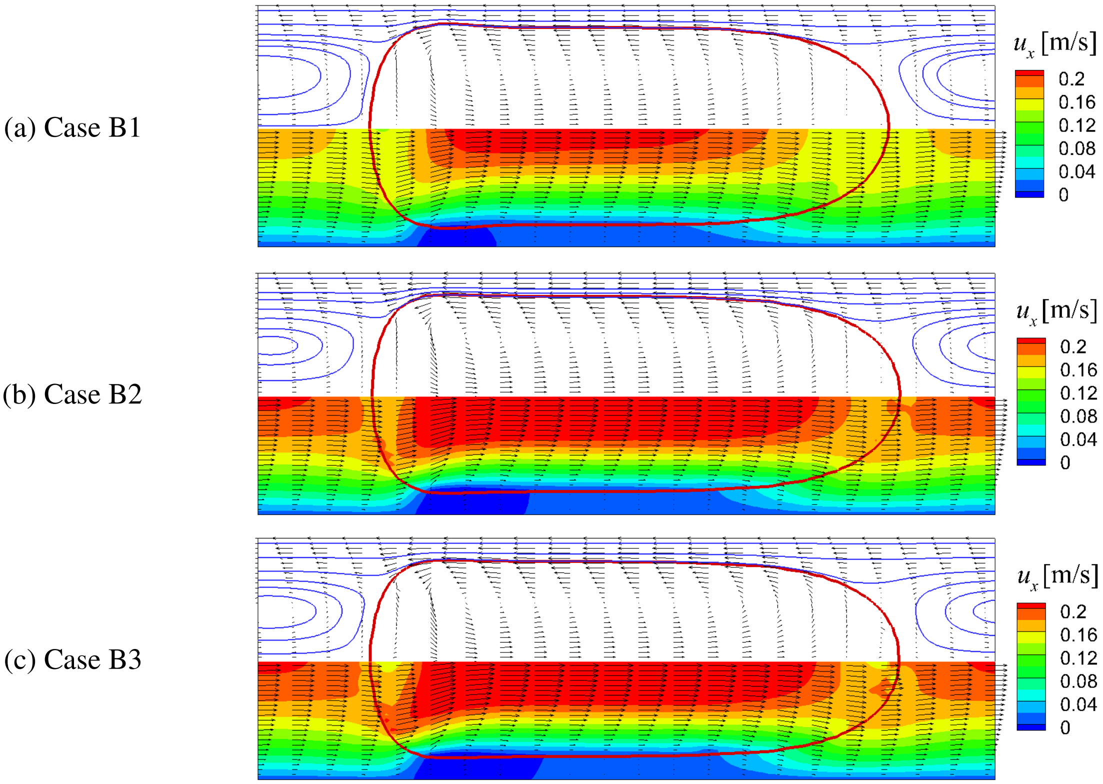

Fig. 4.10: Shape of the bubble and axial velocity field for case B1~B3 (upper half: streamlines and velocity in moving frame of the bubble, lower half: axial velocity ( $u_x$ ) distributions and velocity vectors in fixed frame). $t$ =0.75s for case B1 and B2 and at $t$ =0.675s for case B3.

having an identical gas kinematic viscosity. Case B3 whose $\Gamma_\rho$ is lowest even shows oscillating mean velocities near $t = 0.65\,\mathrm{s}$, which finally crashes the calculation due to the numerical instability.

Fig. 4.9 compares the steady bubble shapes of case B1~B3. Due to the different mean velocities, bubble shapes of three cases are not identical as well. Case B2 and B3 show similar bubble shapes because the differences of mean velocities between those cases are relatively small. These bubble shapes deviate from the shape of case B1 whose mean velocity is clearly different from case B2 and B3. Fig. 4.10 shows the axial velocity distributions of case B1~B3. Similarly, the velocity field of case B1 is obviously different from those of case B2 and B3, while the results of case B2 and B3 are similar. Velocity perturbation even occurs near the front and rear interface and it appears more frequently when $\Gamma_\mu$ is lower. Numerical instabilities in interface reconstruction algorithm may cause these unstable velocity behaviors. Thus, this parametric study concludes that numerical solutions can vary even with the identical gas kinematic viscosity due to the different combinations of density and viscosity for a certain phase.

In case B4 and B5, the gas densities are different from case B3, whereas the gas viscosities are kept identical. Therefore, $\Gamma_\mu$ of case B3, B4 and B5 are identical with different $\Gamma_\rho$. The gas kinematic viscosities for those cases differ, accordingly. The time evolutions of

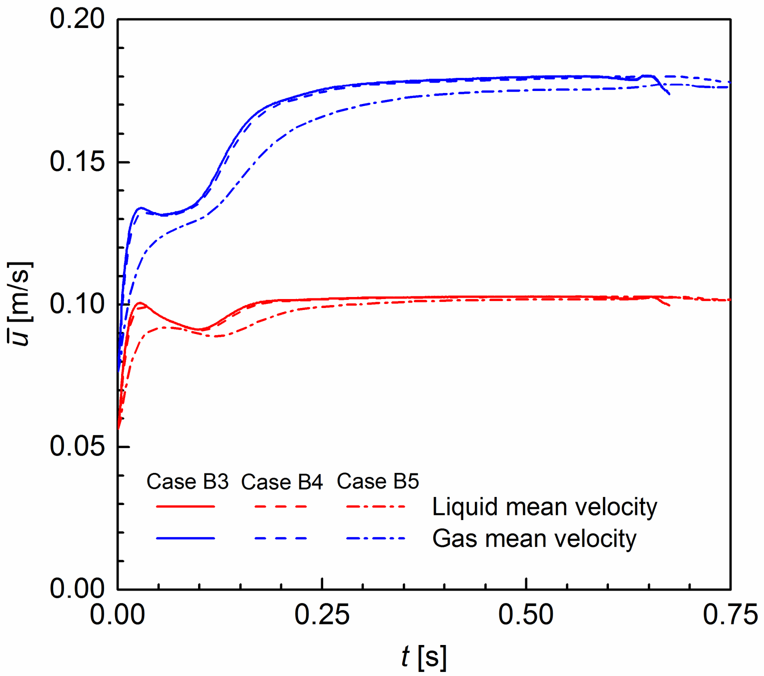

Fig. 4.11: Time evolution of mean velocities of Taylor flows with different density ratios (case B3~B5).

mean velocities for case B3, B4 and B5 are shown in Fig. 4.11. The liquid mean velocities of three cases are approaching almost a constant value after $t > 0.5\,\mathrm{s}$. The deviation of gas mean velocities is even very small at the end of the calculation. No critical numerical errors occur on case B4 and B5 which employ relatively high $\Gamma_\rho$. These two cases are numerically more stable than case B3, obviously. Fig. 4.12 compares the bubble shapes of case B3~B5, and they are visually almost identical. Also, Fig. 4.13 shows the axial velocity fields for case B4 and B5. The magnitudes and distributions of velocities for these two cases are very similar to those of case B3. The only difference of the velocity field appears at the front and rear part of the bubble where the numerical errors may occur. The problematic velocity perturbation decreases by growing $\Gamma_\rho$. Therefore, the case B5 shows the most stable velocity field in the cases with an identical $\Gamma_\mu$.

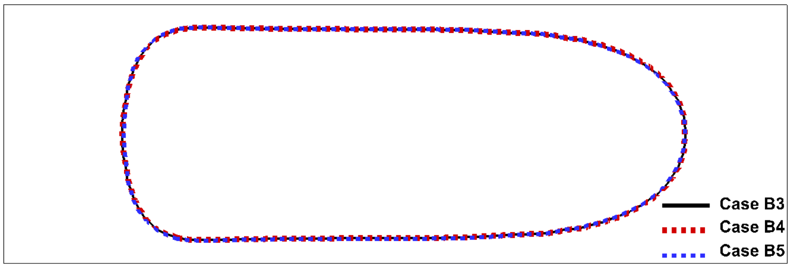

Fig. 4.12: Comparison of the terminal bubble shapes with different density ratio (case B3~B5). $t$=0.675s for case B3 and at $t$=0.75s for case B4 and B5.

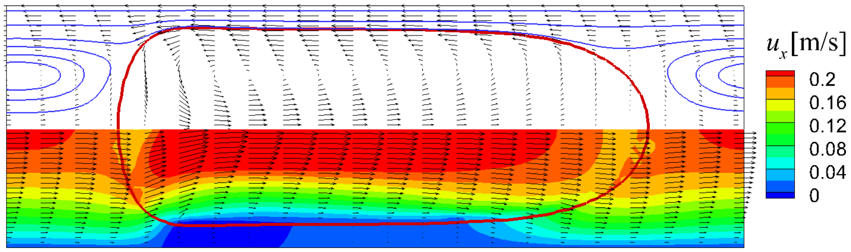
(a) Case B4

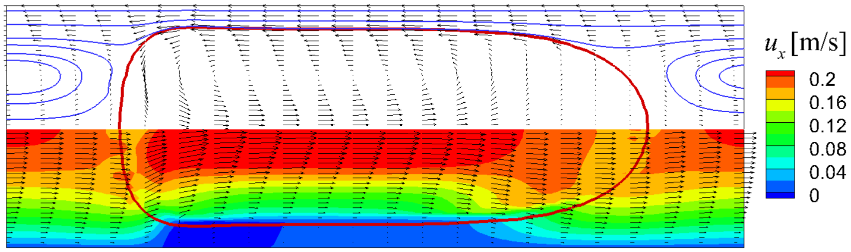
(b) Case B5

Fig. 4.13: The bubble shapes and velocity fields with different density ratio (case B4 and B5). $t$=0.675s for case B3 and at $t$=0.75s for case B4 and B5.

This parametric study figures out that the dynamic viscosity ratio plays an important role to determine the bubble shape and velocity field at quasi-steady state. Even with an identical gas kinematic viscosity, the numerical solutions can vary according to the dynamic viscosity ratio. However, the influence of density ratio on the steady solution is almost negligible. Moreover, it turns out that the solution with a relatively high gas to liquid density ratio is numerically more stable. Therefore, higher density ratio is better to keep the solution numerically stable and better to capture the physical behaviors without disturbance from numerical artifacts. Assuming density ratio of unity gives rise to a plausible numerical solution as with original density ratio. Therefore, the density ratios in further calculations are unity.

## 4.3 Grid dependency test

Numerical solutions in the discretized computational domain depend on the quality of discretization technique evidently. In the present study that utilizes a finite volume method, the size of cells directly affects the resolution of numerical solutions, and the number of cells affects the computational cost. Using a large size of mesh cells may cause inaccurate numerical solutions due to the insufficient cells for resolving the gradients of matters correctly, while using a small size of cells results in a large number of cells to be computed. To compromise the number of cells between resolution and calculation time, the least number of cells whose solution is reasonably accurate may be appropriate.

This is the general purpose of grid dependency test. The grid dependency test in this section aims to determine the proper number of mesh cells for both hydrodynamic and mass transfer calculations. Table 13 describes the details of mesh configurations used in the grid dependency test. The test condition of case A2 in Section 4.1 is considered again with a different number of mesh cells (case C1 is identical to case A2).

Table 13: The number of cells and cell sizes of meshes for the grid independency test.

| Case | $N_x$ | $N_z$ | $\Delta x / h$ | $\Delta z / h$ |
|---|---|---|---|---|
| C1 | 150 | 25 | 0.02 | 0.02 (uniform) |
| C2 | 240 | 40 | 0.0125 | 0.0125 (uniform) |
| C3 | 300 | 50 | 0.01 | 0.01 (uniform) |
| C4 | 200 | 37 | 0.015 | 0.015 (bulk region) and 0.003 (near wall) |

***Hydrodynamic calculation***

Fig. 4.14 plots the temporal evolution of mean velocities during the calculation. The difference among the mean velocities from different meshes is very small. The liquid mean velocity of case C1 whose number of cells is smallest deviates less than 1% from the other two velocities. This small deviation of mean velocity does not significantly affect the overall velocity field indeed. Fig. 4.15 compares the bubble shape from different meshes at $t = 0.5\text{s}$. It shows that the bubble shapes from three meshes are almost identical. The velocity fields of mesh C2 and C3, which are not shown here, are also very similar to the velocity profile of mesh C1 which is already shown in Fig. 4.3 as case A2. To analyze the velocity fields in detail, Fig. 4.16 compares

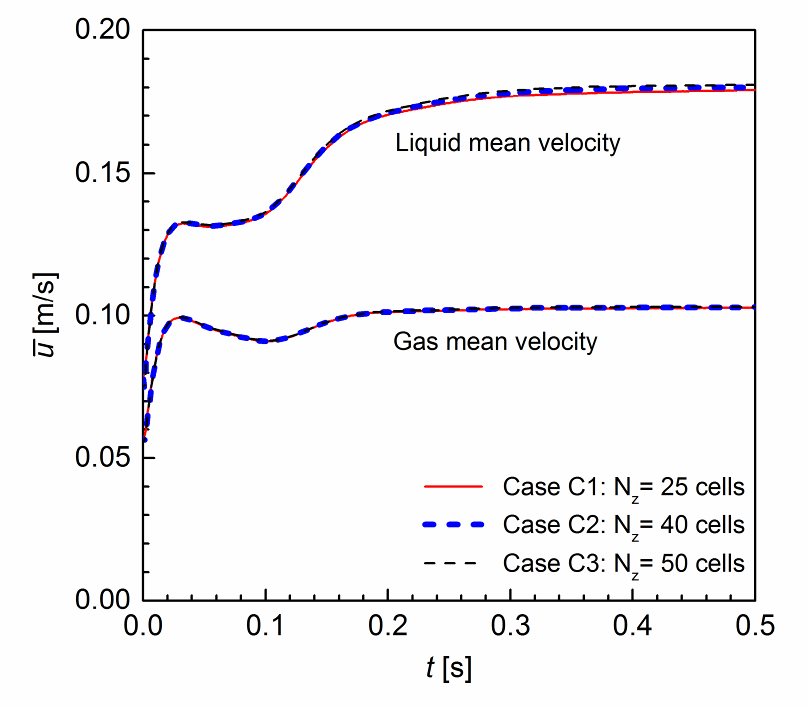

Fig. 4.14: Time evolution of mean velocities of Taylor flows with different number of mesh cells.

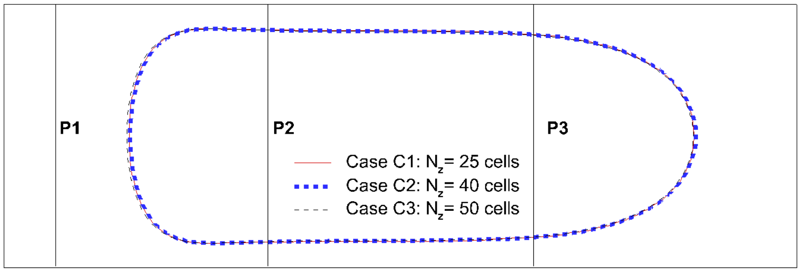

Fig. 4.15: Comparison of terminal bubble shapes computed with different number of mesh cells.

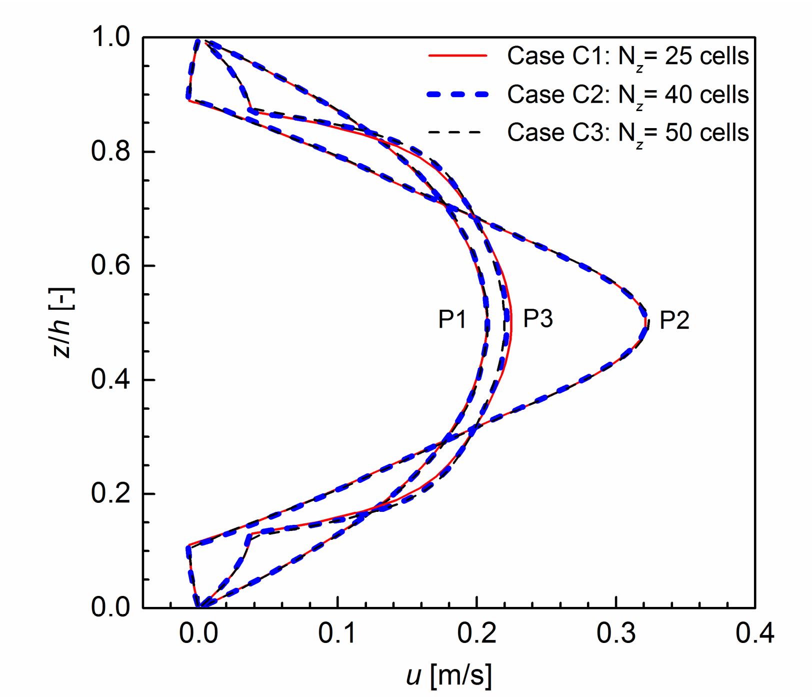

Fig. 4.16: Wall-normal profiles of axial velocity at the position of P1, P2 and P3 with different mesh cells ($t = 0.5\text{s}$).

the wall-normal profiles of axial velocity at the position P1, P2 and P3 displayed in Fig. 4.15. The axial velocities from three meshes are also almost identical for both inside and outside of the bubble at those points. In these comparisons, the solution of mesh C1 has almost no difference from that of the finer meshes so that the mesh C1 is already sufficient to avoid the dependency on the number of mesh cells. The cell size ($\Delta x / h$ or $\Delta z / h$) used in mesh C1 is 0.02, and this value is, therefore, sufficiently small for the grid-independent numerical solutions for Taylor flow considered in the present study.

### *Mass transfer calculation*

In the sequel, the grid-dependency test for mass transfer calculation is performed in the same meshes utilized for hydrodynamic cases. Based on the hydrodynamic solution at $t = 0.5\text{s}$ where it reaches to the quasi-steady state, an arbitrary concentration (1 mol/m$^3$) is specified in gaseous phase and starts transferring to liquid phase. The diffusivities of species in gas and liquid phases are also arbitrary specified as $D_{\text{G}} = 1\times10^{-4}\,\text{m}^2/\text{s}$ and $D_{\text{L}} = 1\times10^{-9}\,\text{m}^2/\text{s}$, respectively. The values are, however, in the same order of magnitude for the diffusivity of hydrogen in gas and liquid phases. Schmidt number ($Sc := \mu_{\text{L}} / (\rho_{\text{L}} D_{\text{L}})$) is usually assessed for evaluation of mass transfer. In this case, *Sc* is $5\times10^5$, which is extremely high with the artificial density and viscosity set to the case A2. Higher Schmidt number requires more cells to resolve the thinner concentration boundary layer. The Schmidt number of hydrogen in nitrobenzene is 279 at 0.7 MPa and 516 at 0.1 MPa. Therefore, the grid which is suitable for such a high Schmidt number can be straightforwardly acceptable for the nitrobenzene-hydrogen real fluid system. The dimensionless Henry number for this case is set to 0.1.

Fig. 4.17 shows the concentration field of coarsest mesh (case C1) and finest mesh (case C3) at two time instants ($t = 0.625\text{s}$ and $0.75\text{s}$). During the calculation, the species is propagating from the bubble into liquid phase. Due to the velocity field and the bubble movement, most of the mass transferred into liquid is observed at the rear part and the front-

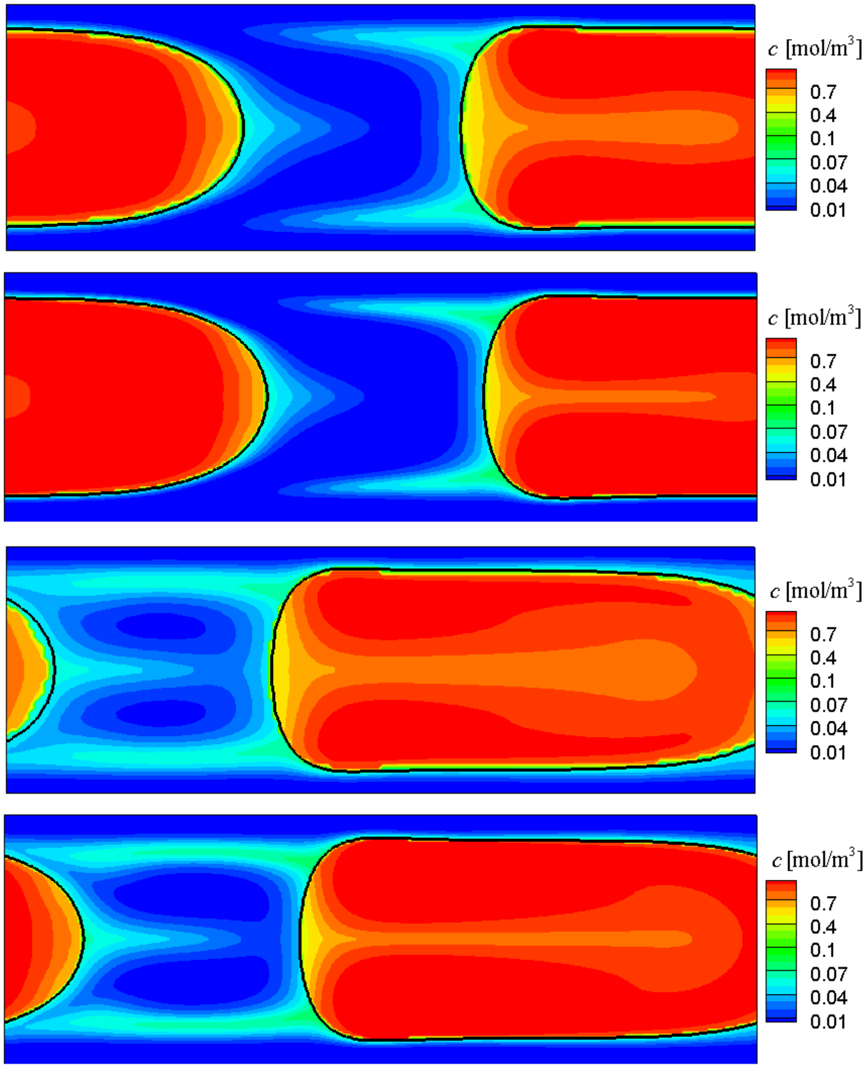

(a) Case C1 ($\mathrm{N}_z = 25$) at $t = 0.625\text{s}$

(b) Case C3 ($\mathrm{N}_z = 50$) At $t = 0.625\text{s}$

(c) Case C1 ($\mathrm{N}_z = 25$) at $t = 0.75\text{s}$

(d) Case C3 ($\mathrm{N}_z = 50$) at $t = 0.75\text{s}$

Fig. 4.17: Concentration distributions computed with difference mesh cells at $t = 0.625\text{s}$ and $0.75\text{s}$.

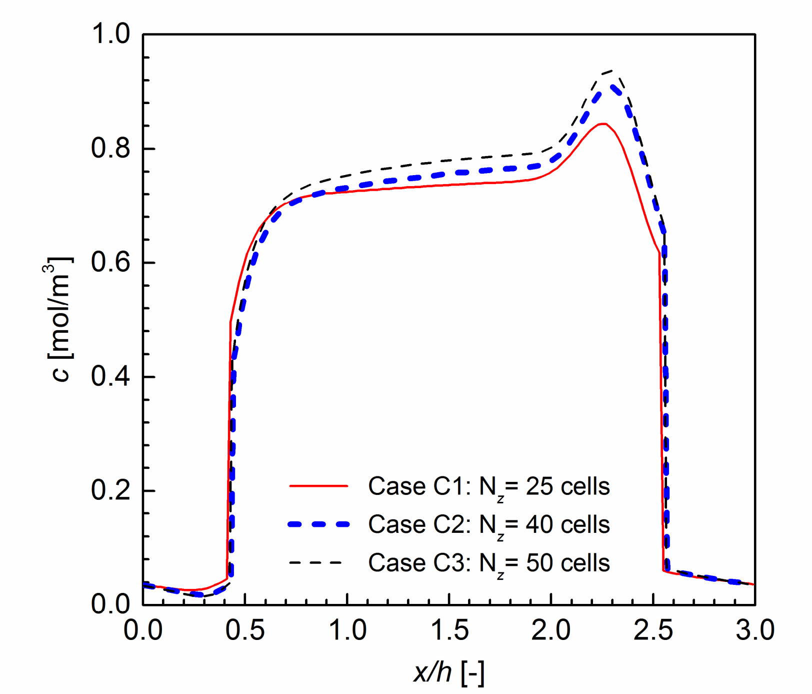

Fig. 4.18: Axial concentration profiles computed with difference mesh cells at the centerline ( $z = 0$ ) for $t = 0.75\,\mathrm{s}$ .

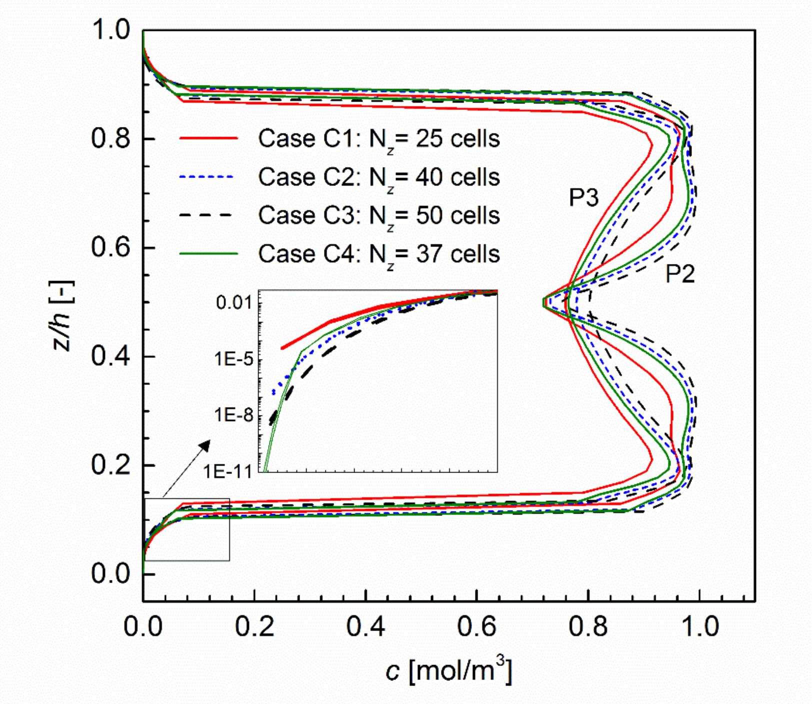

Fig. 4.19: Wall-normal concentration profiles computed with different number of mesh cells at the position of P2 and P3 ( $t = 0.75\,\mathrm{s}$ ).

center part of the bubble. Finally, the transferred mass circulates between the bubbles. The species circulation appears inside the bubble as well. In contrary of the hydrodynamic solutions, the mass transfer results in Fig. 4.17 present the mesh dependency. More numerical diffusion takes place in the coarse mesh as shown in the center of the bubble. It represents that the concentration gradient is smeared by lack of the number of mesh cells.

To examine the difference of concentration field by different meshes, Fig. 4.18 compares the concentration profiles of case C1, C2 and C3 at the centerline ($z = 0$) of the Taylor flow. The concentration profiles inside the bubble are different according to the mesh resolution. Though the difference of concentrations in gaseous phase is not significantly large and decreasing as the number of cell increases, the numerical solutions in gaseous phase still depend on the mesh quality. However, the difference of concentrations in liquid phase is reasonably small, and the results of mesh C2 and C3 are almost identical in liquid region. Fig. 4.19 displays the concentration profiles in wall-normal direction with different meshes. As shown in the centerline profiles, the difference inside the bubble is notable, while there is almost no visible difference in liquid phase. Since case C4 utilizes five finer cells ($\Delta z / h$ =0.003) near the wall, its result is only shown in the comparison of wall-normal concentration profiles. The size of mesh cells in case C4 (for cells in bulk region) is 0.015 where the value is a bit larger than that of case C2 (0.0125). Therefore, the result of case C4 is presumably close to the result of case C2. The inset of Fig. 4.19 shows the zoom-in near the wall in log scale. The deviation of solutions is growing in the direction to the wall. For uniform grid (case C1, C2 and C3), finer mesh can capture higher gradients and smaller values near the wall. In case C4, sharper gradient can be resolved by utilizing more cells near the wall where the higher gradient of concentration appears. From the results of different meshes, it is figured out that the cell size of 0.015 employed in case C4 is acceptable for the solution with reasonable resolution and computational time. Also, the fine mesh cells inside the liquid film are essential for resolving the concentration boundary layer forming in the thin liquid film of Taylor flow. Thus, the mesh of case C4 is chosen for both hydrodynamic and mass transfer simulations for the real fluid system.

## 4.4 Moving reference frame approach for mass transfer

Numerical simulations of mass transfer within a gas-liquid Taylor flow requires high computational cost even for the artificial fluid system that assumes higher density and viscosity

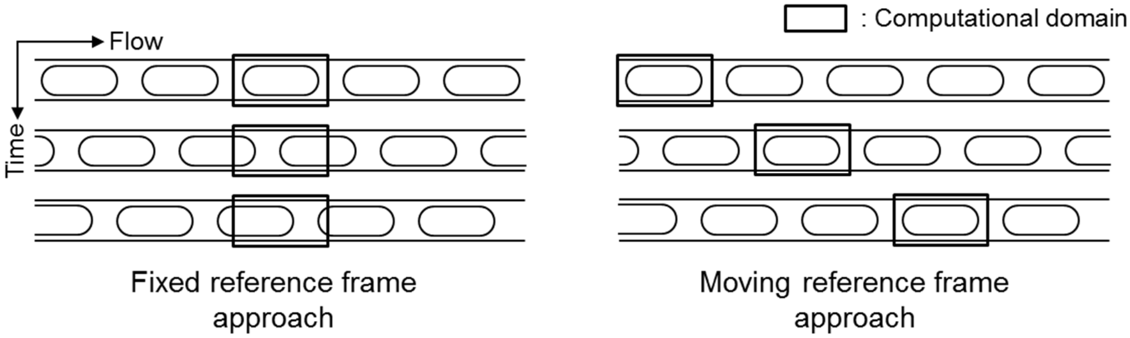
: Computational domain
Flow
Time
Fixed reference frame approach
Moving reference frame approach

Fig. 4.20: Conceptual diagram of fixed reference frame and moving reference frame approaches.

ratio to avoid any potential numerical instabilities. The real fluid system that requires higher time and space resolutions may necessitate much longer computation time. Several numerical studies focusing on the mass (or heat) transfer in slug flow utilizes, therefore, the concept of moving reference frame in order to accelerate their computation [31, 106, 130].

Fig. 4.20 introduces the concept of fixed reference frame (FRF) and moving reference frame (MRF) approaches. Computation domain with the unit cell configuration displayed in Fig. 4.2 is a typical domain of FRF with periodic boundary condition. After the solution reaches to the quasi-steady state, the solution is just moving by the flow with the steady flow pattern around the bubble. If the computational domain is moving with the exactly same velocity of the bubble, the relative velocity inside the domain is always kept the same. This is the basic idea of MRF approaches. In MRF, the computational domain holds the bubble in the frame whose velocity is identical to the bubble velocity. Then, the calculation of velocity field is not necessary at the quasi-steady state because the velocity field does not change anymore. Within so-called frozen velocity field, the mass (or heat) transfer can be computed without solving momentum equations, which mostly consumes the computational time. To obtain the MRF velocity field, the flow is calculated in FRF until the quasi-steady state. Once the flow reaches to the quasi-steady state, the bubble velocity is subtracted from the FRF velocity field, and the relative velocity field is frozen in MRF. The velocity fields of both approaches are already shown in Fig. 4.3, Fig. 4.10 and Fig. 4.13.

### *Mass transfer on moving reference frame*

Since the velocity and volume fraction is not assumed by such empirical correlations but obtained directly from the solution of VOF simulation, the bubble shape and the flow field inside

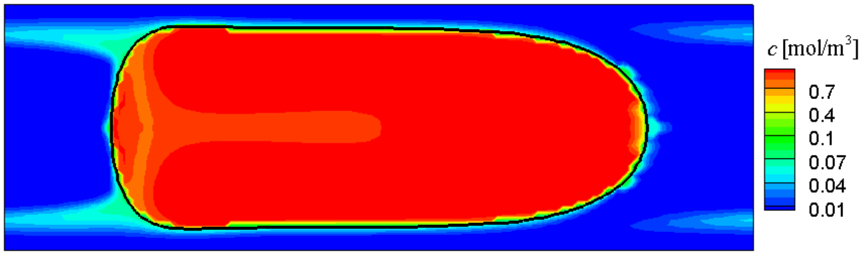

(a) $t = 0.625\,\text{s}$

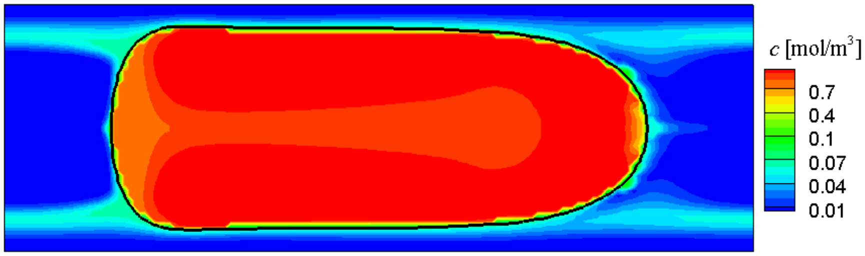

(b) $t = 0.75\,\text{s}$

Fig. 4.21: The concentration distributions computed in the frame of moving bubble at $t = 0.625\,\text{s}$ and $0.75\,\text{s}$ ($N_z = 25$).

the bubble are not omitted in this study despite using MRF for mass transfer calculations. Fig. 4.21 shows the results of mass transfer at $t = 0.625\,\text{s}$ and $0.75\,\text{s}$ in MRF. The calculation of mass transfer is started at $t = 0.5\,\text{s}$ as for the previous section. The concentration profiles in Fig. 4.17 (a) and (c) can be regarded as the results in FRF because the test conditions of those cases are identical to the cases of Fig. 4.21 (a) and (b). From the comparison of the results in FRF and MRF, it is found out that mass transfer in MRF is smaller than those observed in FRF. At the front-center of the bubble, the species moves forward due to the high axial velocity. In this region, much larger amount of species is transferred to liquid phase in FRF. At the rear part of the bubble, much larger propagation of concentration also appears in the results of FRF. In Fig. 4.17 (c), the concentration field in liquid phase already forms a circular shape, while in MRF shown in Fig. 4.21 (b) the concentration from rear bubble is just reaching to the front part of the next bubble.

### *Moving vs fixed reference frame*

To explore these differences, the concentration and velocity at the centerline ($z = 0$) is compared in different time instants. Fig. 4.22 compares the concentration fields in FRF (25 and 50 cells) and MRF (25 cells) at the centerline after 1000 time steps from the beginning of the mass transfer calculation. This comparison clearly explains why the concentration fields from

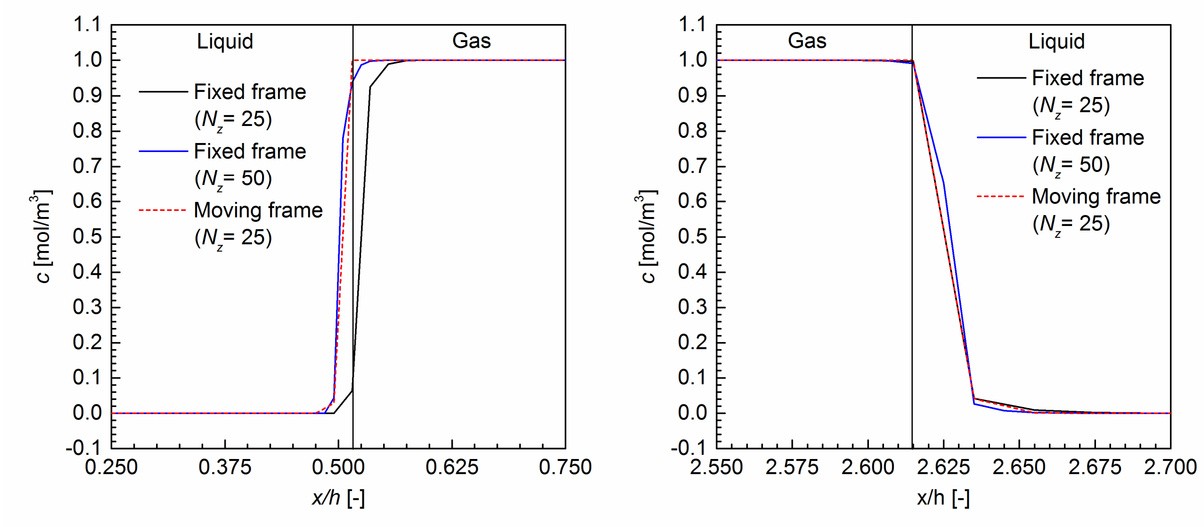

(a) (b)

Fig. 4.22: Concentration profiles at the centerline ($z=0$) near the gas-liquid interface (rear interface (a) and front interface (b)) after 1000 time steps. Comparison of the results between fixed frame approach (with 25 and 50 cells) and moving frame approach (with 25 cells).

both approaches are different, and why the result of FRF are over-predicted. In Fig. 4.22 (a), the result of coarse grid (25 cells) in FRF deviates from the other two concentration profiles: fine grid (50 cells) in FRF and the result of MRF (25 cells). The solutions of mass transfer in FRF still depend on the mesh quality. However, the result in the fine grid of FRF is close to that of MRF even if the grid for MRF is coarser. Since the calculation time for these plots is very short from the start of mass transfer, the concentration in a certain phase should be close to zero (for liquid phase) or unity (for gas phase). The values between zero and one should only appear in the cell containing interface. As shown in Fig. 4.22 (a), the result of MRF has only one point which may be the concentration at the interfacial cell, while the results of both 25 and 50 cells in FRF show two points where the concentration is between zero and one. This means that the interface is already moving toward the right direction in both FRF cases. Due to the movement of interface in FRF, the results of coarse grid cannot keep the sharp interfacial gradient because the thick interface of coarse grid smears the concentration gradient. Fig. 4.22 (b) shows the results of front part of the bubble. In this region, only the fine grid of fixed frame shows the movement of interface to one cell in the right direction. Therefore, the coarse cases ($N_z=25$) in both FRF and MRF show almost identical solutions, while the solution of fine grid in FRF deviates a bit from the other results.

With results obtained in previous sections, this comparison turns out two remarkable points of using different frames of reference. The first point is that the calculation in FRF with

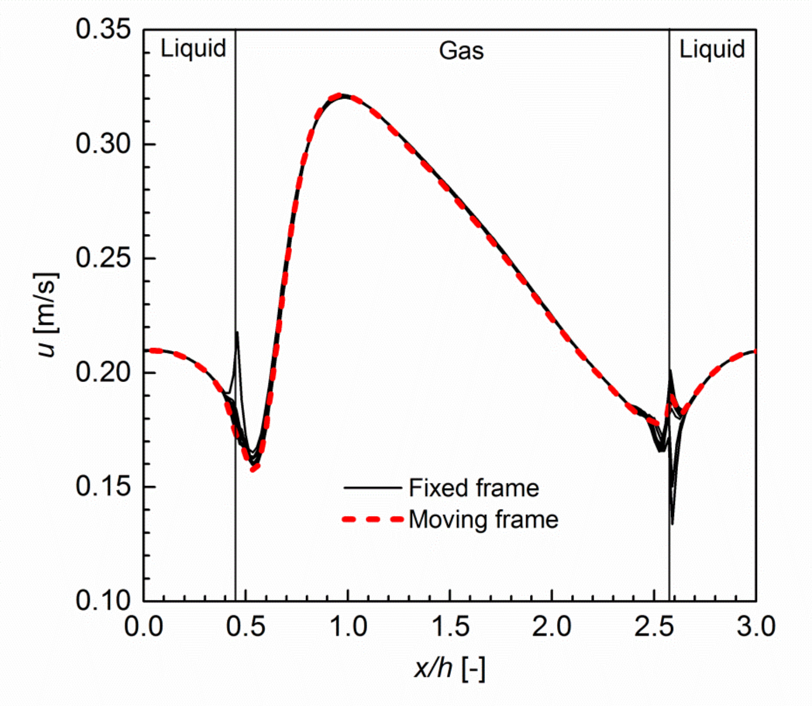

Fig. 4.23: Comparison of the centerline ( $z = 0$ ) velocity profiles of fixed frame approach and moving frame approach at ten different instants of the time.

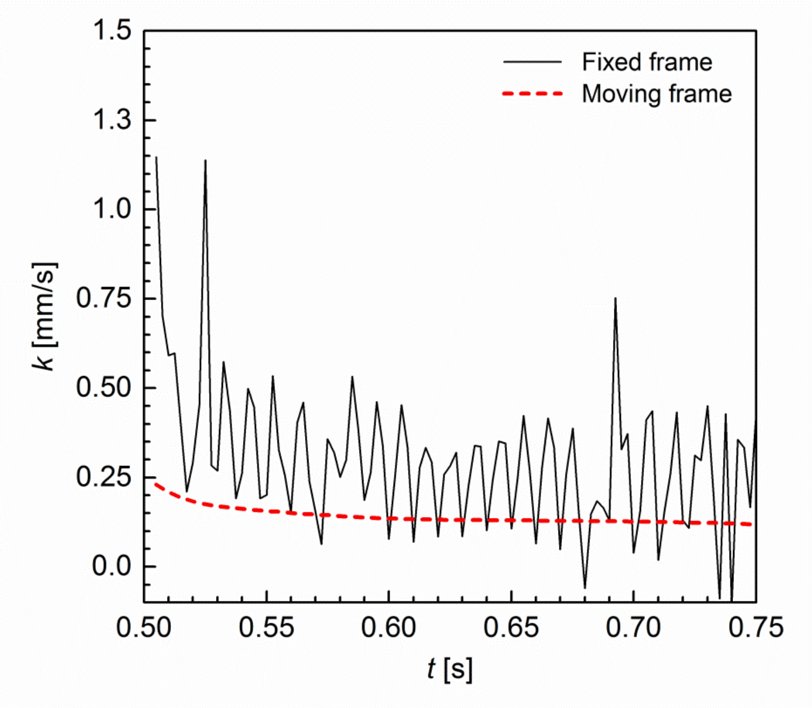

Fig. 4.24: Mass transfer coefficient obtained from both fixed and moving frame approaches.

high Schmidt number requires much finer grid to resolve the interfacial mass transfer where the position of interface moves perpendicular to the flow direction. In Fig. 4.22, the finer the grid is, the better the results become in FRF. However, it is still doubtful how many cells are required for the simulation because the results of 50 cells in Fig. 4.17 still differ from the results of MRF in Fig. 4.21. Thus, the grid in case with 50 cells ($\Delta x/h$=0.01) seems not enough to resolve the concentration gradients of this test case. This leads the outcome of the grid dependency test for mass transfer, the 37 cells are reasonably sufficient, to be wrong. The three cases considered in the grid dependency study, which show almost the same distributions of concentration in liquid phase, may only be valid near wall region. The results may still have the lack of the grid cells near the front and rear interfaces of the bubble with FRF.

The second point is that MRF does not require such a fine mesh since the interface is not moving during the calculation of mass transfer. It means that the grid dependency study is still valid excluding the movement of interface, and then 37 cells are reasonable for MRF. Furthermore, there is another reason why the FRF over-predicts the concentration fields. Fig. 4.23 shows the comparison of velocity profiles of FRF and MRF at the centerline ($z=0$). In FRF, the velocities at ten instants of time are selected and displayed by parallel translation. There are oscillations of velocity profiles in FRF at the front and rear meniscus, while the MRF velocity is constant because it is frozen by its definition. This oscillation may cause the over- or under-prediction of convective mass transfer near the interfacial region, obviously.

Finally, the mass transfer coefficients from both approaches are compared in Fig. 4.24. The overall mass transfer coefficient is given by [110]

$$k(t)=\frac{-\dfrac{1}{a_{\mathrm{int}}}\dfrac{\mathrm{d}}{\mathrm{d}t}\dfrac{\langle c_G(t)\rangle}{c_G^0}}{\dfrac{\langle c_G(t)\rangle}{c_G^0}-\dfrac{1}{(1-\varepsilon)}} \tag{4.3}$$

The mass transfer coefficient of FRF shown in Fig. 4.24 is highly oscillating, while there is only monotonic decreasing in the result of MRF. This erroneous behavior of mass transfer coefficient in FRF can also be caused by the reasons discussed in the last two figures regarding concentration and velocity profiles at the centerline. In this study with extremely high Schmidt number ($Sc=5\times10^5$), the FRF tends to give rise to an unphysical behavior of interfacial mass transfer as well as mass transfer coefficient. The series of comparison shown in this section concludes that MRF is more stable and appropriate with the relatively large size of mesh cells because the interface is fixed in a certain position of mesh cells and not moving during the calculation of mass transfer. Therefore, MRF is only considered in further simulations of the real fluid system with 37 cells (in $z$ -direction) as determined from the grid dependency test.

# Chapter 5

# Catalyzed hydrogenation of nitrobenzene within a Taylor flow

This chapter details the simulation procedure for hydrogenation of nitrobenzene within a Taylor flow. Section 5.1 introduces the physical properties required for setting simulation parameters. Test conditions for the real fluid system composed of nitrobenzene and hydrogen can be determined with these properties and the criteria based on the artificial fluid system in Chapter 4. To obtain a quasi-steady velocity field, the gas-liquid Taylor flows are computed firstly without mass transfer until the bubble shape, and the velocity fields are fully developed. Section 0 presents the test conditions and results of hydrodynamic simulations. In the sequel, the mass transfer is considered in the moving reference frame. The details on the test conditions and results of reactive mass transfer are described in Section 5.3. The reaction rates with different orders of magnitude are also considered to analyze its influence on the mass transfer efficiency. Section 5.4 presents a fundamental study accounting for a generated detailed kinetic mechanism based on the study of density functional theory. The detailed kinetic study can finally come up with a qualitative analysis of both bulk and surface species distributions within a Taylor flow accompanying surface reactions.

The assumptions for hydrodynamic simulations are described at the beginning of Chapter 2. Here, additional assumptions and configurations applied to the mass transfer calculations in this chapter are summarized as follows

- Mass transfer is computed with frozen velocity field by moving reference frame
- Bubble consists of pure hydrogen
- No evaporation of liquid species
- No homogeneous reaction
- Constant physical properties during calculation

# 5.1 Physical properties

The physical properties of chemical species in gas and liquid phases are a prerequisite for setting up the simulations of gas-liquid mass transfer. The non-dimensional single-field momentum equation Eq. (2.5) requires dimensionless numbers relating to density and viscosity in both phases as well as the surface tension of liquid. The relationships of dimensionless numbers are given in Table 1. For two-phase mass transfer, the solver further requires Peclet number and Henry number, which represent the diffusivity and solubility, respectively. Either theoretical models or empirical relationships can obtain these physical properties. In general, the gas-phase properties (e.g. density, viscosity) are easily estimated by well-known theories (e.g. ideal gas law, kinetic theory), while the liquid-phase properties still rely highly on experimental data. Thus, this section mainly introduces the required physical properties in liquid phase by means of empirical correlations and measured data. The gas phase properties that are still unknown (e.g. properties at high pressure) are investigated as well.

For hydrogenation of nitrobenzene, the gas phase species is hydrogen, and the liquid phase is a mixture of nitrobenzene, aniline and water which are reactants and products of the reaction of interest. During the reaction process, liquid nitrobenzene is gradually conversing to aniline, and the physical properties can be affected by the corresponding liquid composition as well. According to the aforementioned assumptions for the solver, the properties are, however, not changeable during the calculation. Therefore, in the present study, only a fixed composition of liquid and gas can be considered for with corresponding physical properties. Before calculation, the properties of potential solvents of this reaction, nitrobenzene, aniline and ethanol (only for solubility) are therefore investigated from literature. Properties measured at different temperatures come up with a correlation as a function of temperature. This correlation can cover the various range of temperature given in references and estimate the properties at a certain temperature required for the simulations. The operating conditions of catalytic liquid-phase hydrogenation in industrial slurry or fluidized-bed reactor are $363 \sim 573\,\mathrm{K}$ and $0.1 \sim 0.6\,\mathrm{MPa}$ [73]. Depending on the availability of physical properties and reaction kinetics in the literature, the temperature and the pressure in this study are, however, chosen as $323\,\mathrm{K}$ and $0.7\,\mathrm{MPa}$, respectively. Moreover, liquids are assumed as incompressible fluids so that the liquid properties are assumed to be independent of pressure. With this assumption, the liquid properties at

$0.1\,\mathrm{MPa}$ are utilized in calculations. However, the pressure dependency is considered for the properties of gas phase species.

### 5.1.1 Density and viscosity

In most studies [42, 105, 109], the fluid properties of nitrobenzene and aniline are only given at ±10 degrees of room temperature ($298\,\mathrm{K}$). Only a few studies [78, 93] provide the density and viscosity of nitrobenzene and aniline in a wide temperature range. Based mainly on the latter two references, the density and viscosity are approximated by two different fitting methods. Fig. 5.1 displays the density of nitrobenzene and aniline with respect to the temperature. These density profiles for both liquids descend linearly as temperature rises. Therefore, the least square estimation approximates plausible density profiles as compared to the measured data. Fig. 5.2 plots the viscosity of two liquids which shows a non-linear decrease against temperature. Therefore, the power law is chosen for the viscosity fitting to minimize the deviation from all experimental data. As intended, the power law correlation agrees well with measured data in a wide range of temperature. The largest difference appears at the lowest temperature ($288\,\mathrm{K}$) for

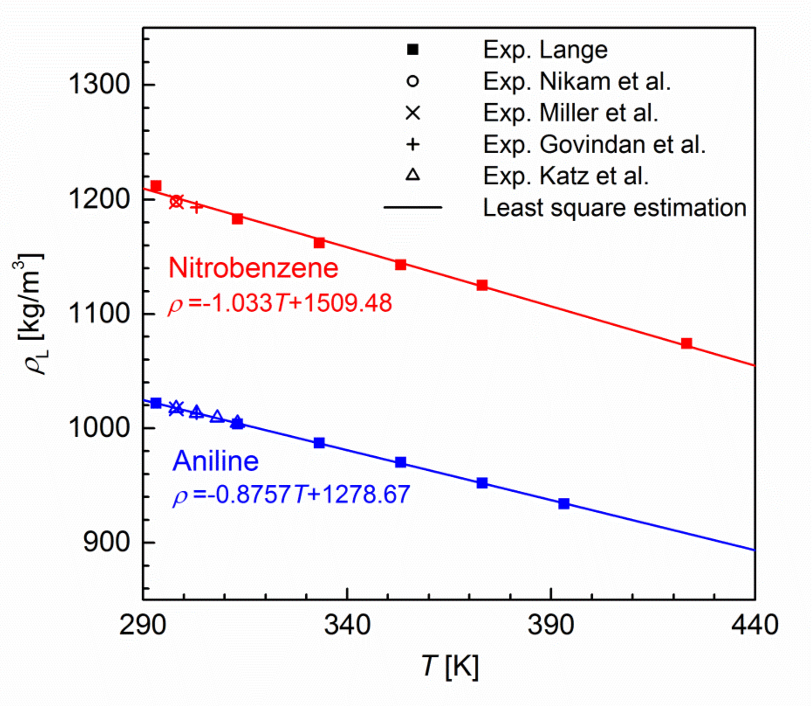

Fig. 5.1: Densities of nitrobenzene and aniline as a function of temperature. Estimation by least square method from the experimental data [42, 78, 93, 105, 109].

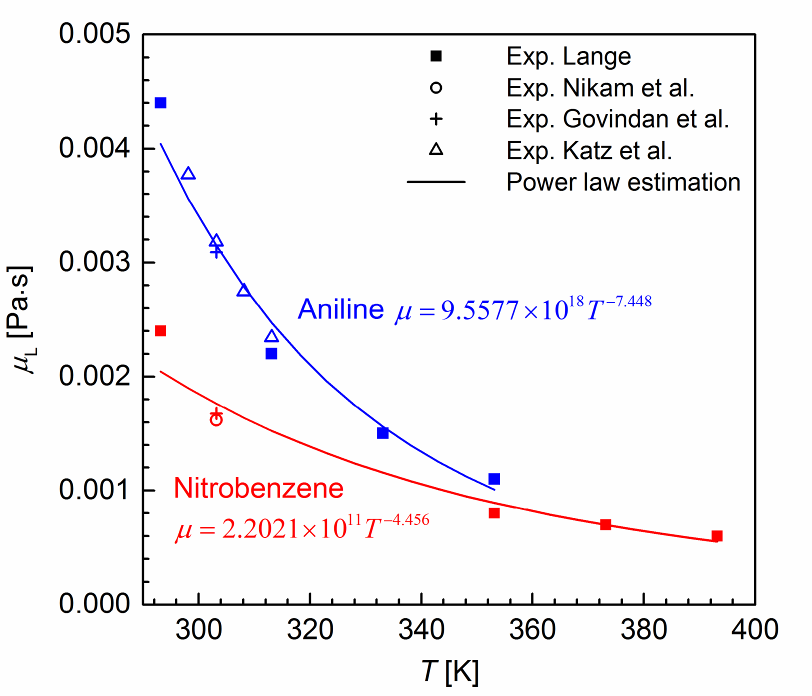

Fig. 5.2: Viscosities of nitrobenzene and aniline as a function of temperature. Estimation by power law from the experimental data [4, 42, 78, 93].

both liquids. In addition, Table 14 describes the density and viscosity of hydrogen in high pressure given by Gracki et al. [43]. With these data, the pressure-dependent physical properties of hydrogen are estimated by a least square method.

Table 14: Density and viscosity of hydrogen in high pressure [43].

| Pressure, MPa | density, $kg/m^3$ | Viscosity, $Pa \cdot s$ |
|---|---|---|
| 0.462 | 0.5 | 7.29E-06 |
| 0.926 | 1 | 7.30E-06 |
| 1.864 | 2 | 7.31E-06 |

## 5.1.2 Diffusivity

In hydrogenation of nitrobenzene, the species undergoing mass transfer pass not only through gaseous phase (hydrogen and/or nitrogen) but also through liquid phase (nitrobenzene, aniline and water). Therefore, two types of diffusivity are required; the diffusivity of gaseous species diffusing into liquid species and the diffusivity of gaseous species pair. For gas phase diffusion, hydrogen is only considered in the present study so that no multispecies (mutual) diffusion occurs inside the bubble. The self-diffusivity of hydrogen is obtained by kinetic theory

($D_{\mathrm{H2,H2}} = 1.66\times10^{-4}\,\mathrm{m^2/s}$), which accounts for the diffusion of hydrogen-hydrogen species pair. However, no concentration gradient exists in the Taylor bubble containing only a single hydrogen species, indeed. Therefore, the diffusion in gaseous phase is not taken into account in current test cases. However, in liquid phase, the multispecies diffusion takes place between gaseous and liquid species. Since liquid phase is mostly filled with nitrobenzene, the diffusivity of nitrobenzene is assumed to be very small so that the diffusion of nitrobenzene into the other species is neglected. Also, the diffusivity of liquid species diffusing to the gas phase, e.g. evaporation, is not considered according to the assumption of no phase change. Hence, the diffusivities of hydrogen (diffusing into nitrobenzene and aniline) and aniline (diffusing into nitrobenzene) are only taken into account in this calculation. However, no measured diffusivity data are available for those species pairs appearing in the hydrogenation process.

While the kinetic theory is suitable to predict transport properties of a gaseous mixture, there is no univocal theory for modeling diffusion coefficient in liquid phase. Since molecules in liquid phase are densely packed and strongly influenced by force fields of neighboring molecules, the diffusion coefficient in liquid phase is normally much smaller than that in gaseous phase [121]. For infinite dilute solution of A in B, where the concentration of A is relatively very small as compared to the concentration of B, the binary diffusion coefficient $D_{\mathrm{A,B}}$ can be assumed as a representative diffusion coefficient as concluded in Section 3.5. Thus, the binary diffusion coefficient of infinite dilute liquid solution is employed for the diffusivity of mass transfer calculations, and it is estimated by Wilke-Chang method [142] which is an older but still widely used correlation based on the empirical modification of Stokes-Einstein relation. The diffusivity of solute A into the solvent B in cm/s unit is given by

$$D_{\mathrm{A,B}} = \frac{7.4\times10^{-8}\left(\alpha m_{\mathrm{B}}\right)^{0.5} T}{\mu_{\mathrm{B}} V_{\mathrm{A}}^{0.6}} \tag{5.1}$$

where $m_{\mathrm{B}}$ and $\mu_{\mathrm{B}}$ are the molecular weight and the viscosity of solvent B, which are given in Table 8 and Fig. 5.2, respectively. $\alpha$ is an association factor which represents the average number of monomeric molecules clustered together in liquid phase [70]. Since nitrobenzene and aniline are non-associated and highly polar liquids [52], the association factors $\alpha$ in the present study are assumed to be unity as for the non-associated solvents in Wilke-Chang method. $V_{\mathrm{A}}$ is the molar volume of solute A at its normal boiling temperature, and the value for hydrogen and

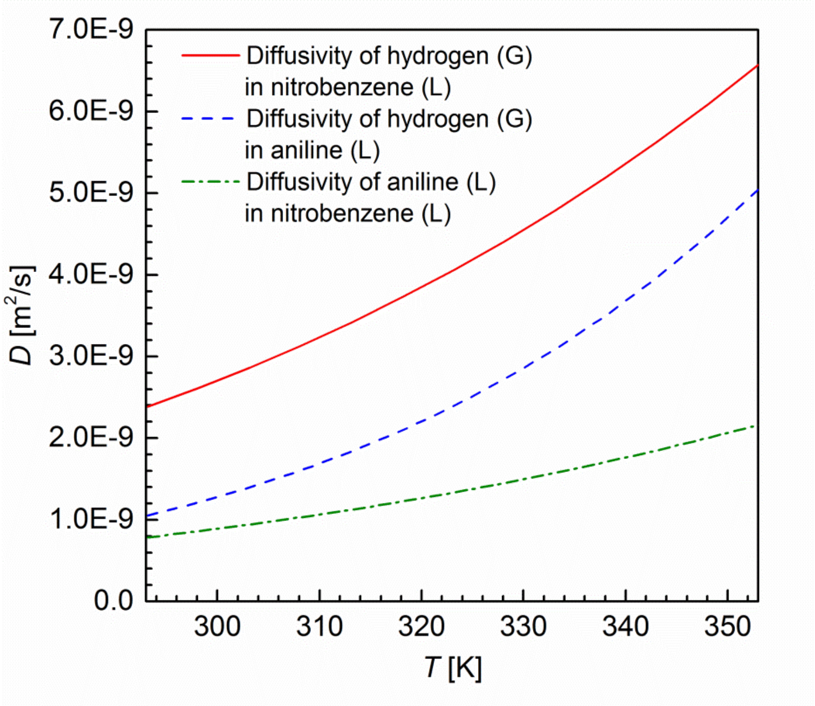

Fig. 5.3: Diffusivity of hydrogen in nitrobenzene and aniline, and diffusivity of aniline in nitrobenzene as a function of temperature.

aniline are 14.3 cm$^3$/mol [142] and 91.3 cm$^3$/mol [38], respectively. Based on these parameters, the diffusivities can be estimated by Wilke-Chang method as a function of temperature.

Fig. 5.3 plots the diffusivity of hydrogen in nitrobenzene and aniline, and the diffusivity of aniline in nitrobenzene with respect to the temperature. The three diffusivities estimated by Wilke-Chang method are in the same order of magnitude even if the solutes are in different phases (hydrogen is gas and aniline is liquid). All the values are increasing as temperature rises. This correlation provides a value of diffusivity at the temperature of interest for the further simulations.

### 5.1.3 Solubility

Solubility plays a crucial role in the interfacial mass transfer. The solubility of a gaseous species in a solvent accounts for the discontinuous concentration phenomenon across the interface where the gaseous species undergoes mass transfer into the liquid solvent. Radhakrishnan et al. [119] provided a correlation of hydrogen solubility for nitrobenzene and compared their results with experimental work by Gjaldbaek et al. [41] to crosscheck its validity. Also, Purwanto et al. [118] investigated the solubility of hydrogen in various liquids with their own correlation. Purwanto et al. [118] considered neither nitrobenzene nor aniline but presented the hydrogen solubility for ethanol that is normally used as an additional solvent to dilute nitrobenzene [135]. To verify empirical correlations, the studies from Radhakrishnan et al. [119] and Purwanto et al. [118] are revisited in this section, which comes up with the solubility of hydrogen in nitrobenzene and ethanol with respect to the temperature.

Based on the regular solution theory [61], Prausnitz and Shair [117] proposed a correlation of solubility for gaseous species in pure liquid as

$$-\ln x_{\mathrm{G}} = \ln\left(\frac{f_{\mathrm{G}}^{\mathrm{L}}}{f_{\mathrm{G}}}\right) + \frac{\phi_{\mathrm{L}}^{2} V_{\mathrm{G}} \left(\delta_{\mathrm{L}} - \delta_{\mathrm{G}}\right)^{2}}{RT} \tag{5.2}$$

where $V_{\mathrm{G}}$ is the molar volume of the hypothetical liquid hydrogen. $f_{\mathrm{G}}^{\mathrm{L}}$ and $f_{\mathrm{G}}$ represent the values of fugacity of the hypothetical liquid hydrogen and hydrogen at 101 kPa, respectively. $\phi_{\mathrm{L}}$ is the volume fraction of liquid species which can be assumed as unity in both references [118, 119]. $\delta_{\mathrm{L}}$ and $\delta_{\mathrm{G}}$ denote the solubility parameters of liquid and gas species (hydrogen), respectively. Based on the experimental data in Lemcoff [96], Radhakrishnan et al. [119] provided correlations of $f_{\mathrm{G}}^{\mathrm{L}}/f_{\mathrm{G}}$ and $V_{\mathrm{G}}$ ($\mathrm{m}^3/\mathrm{mol}$) for hydrogen as a function of temperature (K)

$$\ln\left(f_{\mathrm{G}}^{\mathrm{L}}/f_{\mathrm{G}}\right) = 3.111756 + 856.9404/T \tag{5.3}$$

$$\ln\left(V_{\mathrm{G}}\right) = -16.1347 + 3.0927\left(T/33 - 1\right)^{2/7} \tag{5.4}$$

and the solubility parameter of liquid $\delta_{\mathrm{L}}$ is given by

$$\delta_{\mathrm{L}} = \sqrt{\frac{\left(\Delta H_{\mathrm{L,vap}} - RT\right)}{V_{\mathrm{L}}}} \tag{5.5}$$

where $\Delta H_{\mathrm{vap}}$ is the heat of vaporization. Since the regular solution theory is only valid for the non-polar system, Lemcoff [96] introduced a corrected solubility parameter $\delta_{\mathrm{L,cor}}$ for the polar solvent ($\delta_{\mathrm{L}} > 18410\ \mathrm{J}^{1/2}\mathrm{m}^{-3/2}$) as

$$\delta_{\mathrm{L,cor}} = \frac{\delta_{\mathrm{L}}}{1.772\log\left(\delta_{\mathrm{L}} - \delta_{\mathrm{G}}\right) - 6.3757} \tag{5.6}$$

This corrected parameter is applied to the Radhakrishnan correlation as well. For the solubility parameter of gas species $\delta_{\mathrm{G}}$, Radhakrishnan et al. [119] assumed that $\delta_{\mathrm{G}}$ relates to temperature and the solubility parameter at 298 K as

$$\delta_{\mathrm{G}} = \sqrt{\frac{\Delta H_{\mathrm{G,vap}} - RT}{\Delta H_{\mathrm{G,vap}} - 298R}}\delta_{\mathrm{G,298}} \tag{5.7}$$

In Purwanto correlation, $f_{\mathrm{G}}^{\mathrm{L}}/f_{\mathrm{G}}$ and $\delta_{\mathrm{L,cor}}$ are calculated by correlations as [118]

$$\ln\left(f_{\mathrm{G}}^{\mathrm{L}}/f_{\mathrm{G}}\right) = -1.50 + 5.90\times10^{-3}T^{-1} - 1.47\times10^{-6}T^{-2} + 1.25\times10^{8}T^{-3} \tag{5.8}$$

$$\begin{aligned}\delta_{\mathrm{L,cor}} = \delta_{\mathrm{L}} / \{&4.493\times10^{-1} + 1.150\times10^{-1}\left(\delta_{\mathrm{L}} - \delta_{\mathrm{G}}\right) \\ &- 2.187\times10^{-3}\left(\delta_{\mathrm{L}} - \delta_{\mathrm{G}}\right)^{2}\}\end{aligned} \tag{5.9}$$

in a unit of $\mathrm{cal}^{0.5}\mathrm{cm}^{-1.5}$. The constant $V_{\mathrm{G}}$ and $\delta_{\mathrm{G}}$ are given by Katayama et al. [77] as $3.73\times10^{-5}\,\mathrm{m}^{3}/\mathrm{mol}$ and $7.835\times10^{3}\,\mathrm{J}^{0.5}\mathrm{m}^{-1.5}$, respectively. The parameters required for these correlations are described in Table 15. There is no satisfactory theory for predicting liquid-state parameters of a gas species, $\delta_{\mathrm{G}}$ at a temperature far greater than its critical temperature [119]. Therefore, the parameters summarized in Table 15 are not clearly defined by either theory or by experiments, but those are regarded as a part of the model in this study. Moreover, some properties (e.g. heat of vaporization $\Delta H_{v}$) are obviously different from reference to reference. Therefore, the known parameters from measured data are directly used or adapted to estimate the unknown parameters for other liquids which do not appear in the literature.

Fig. 5.4 (a) shows the Henry coefficient of hydrogen for nitrobenzene, aniline and ethanol as a function of temperature. In this temperature range, the measured solubility for the three solvents generally increases with rising temperature. The correlated values are also increasing by

Table 15: Summary of the estimation parameters of Radhakrishnan correlation for hydrogen solubility in pure liquids.

| Parameter | Nitrobenzene | Aniline | Ethanol |
|---|---|---|---|
| $\Delta H_{\mathrm{L,vap}}$ (J/mol) | 45500 | 52200 | 34500 |
| $\Delta H_{\mathrm{G,vap}}$ (J/mol) | 905 | | |
| $V_{\mathrm{L}}$ ($\mathrm{cm}^{3}/\mathrm{mol}$) | 102.6 | 91.3 | 58.4 |
| $\delta_{\mathrm{G,298}}$ ($\mathrm{J}^{0.5}\mathrm{m}^{-1.5}$) | 4435*1 | 6200*2 | 4435*1 |

*1: from Radhakrishnan et al. [119]
*2: Modified parameter for the Radhakrishnan correlation

temperature, and the slope of Purwanto correlation is steeper than that of Radhakrishnan. For nitrobenzene, Radhakrishnan correlation agrees better with their experimental data, while the result by Purwanto correlation deviates from the experimental data due to its high slope. However, the Purwanto correlation predicts better results for ethanol than the Radhakrishnan correlation. Though the deviation of Purwanto correlation from measured data is smaller, the result of Radhakrishnan model is also in reasonable agreement, and even better at 323 K. Therefore, the solubility of hydrogen in aniline is estimated by Radhakrishnan correlation with a modified solubility parameter of gas $\delta_{G,298}$ (see Table 15) in order to fit the experimental data.

For hydrogenation of nitrobenzene, the operation pressure is usually higher than the standard pressure to enhance the mass transfer of hydrogen into liquid solvent. In former validation cases, the reaction parameters are also estimated at 0.7 MPa (section 3.6.1) and 0.3 MPa (section 0). However, the study of solubility at high pressure is very seldom. To the author’s knowledge, only Radhakrishnan et al. [119] provided the solubility of hydrogen in nitrobenzene and methanol as a function of pressure. The data shows that the solubility is almost linear against the pressure without intercept in y-axis (solubility). Therefore, the solubility at high pressure is roughly calculated by a linear relation $y \approx ax$ whose gradient $a$ is obtained from the origin of the graph to the solubility value at 101 kPa. The solubility profiles by linear extrapolation are shown in Fig. 5.4 (b). The estimated data of nitrobenzene is also plausible as

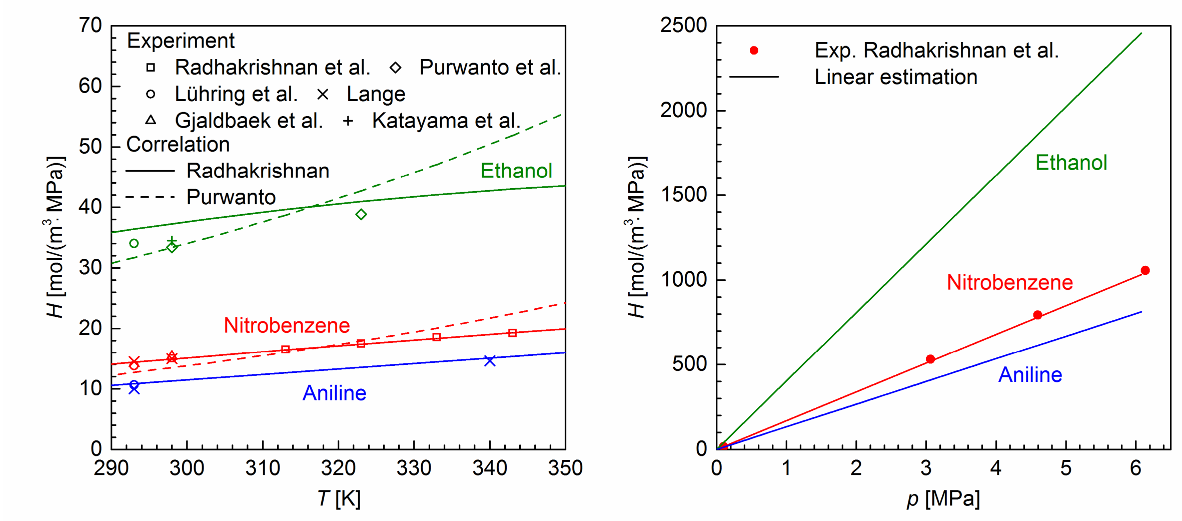

(a) (b)

Fig. 5.4: Henry coefficients of hydrogen in nitrobenzene, ethanol and aniline. (a) Comparison between correlated and measured values at 101 kPa as a function of temperature [40, 77, 93, 97, 118, 119]. (b) Estimation of Henry coefficient at high pressure (323K).

compared to the experimental data given by [119].

For non-dimensional computation, the dimensionless Henry number needs to be converted from the mole fraction of hydrogen in the solvent $X_{\mathrm{H2}}$ as

$$X_{\mathrm{H}_2} = pHV_{\mathrm{L}} \tag{5.10}$$

$$H^* \equiv \frac{c_{\mathrm{H}_2,\mathrm{L}}}{c_{\mathrm{H}_2,\mathrm{G}}} = \frac{X_{\mathrm{H}_2} / V_{\mathrm{L}}}{\rho_{\mathrm{H}_2} / m_{\mathrm{H}_2}} = \frac{pH}{\rho_{\mathrm{H}_2} / m_{\mathrm{H}_2}} \tag{5.11}$$

## 5.1.4 Surface tension

As aforementioned liquid properties, prediction of surface tension also depends on the experimental data given in the literature. Jasper [72] summarized the surface tensions of pure liquids which include nitrobenzene and aniline. This reference suggested the least square estimations for fitting their measured data in terms of temperature. Fig. 5.5 shows the estimated surface tensions by given correlations and compares them with other references. In Fig. 5.5, Jasper correlation [72] estimates decreasing surface tension as temperature rises. However, Lange [93] reported that the surface tensions of both nitrobenzene and aniline are constant from 20 ℃ to 100 ℃, which is in contrast to Jasper’s data. CRC Handbook [140] provides surface

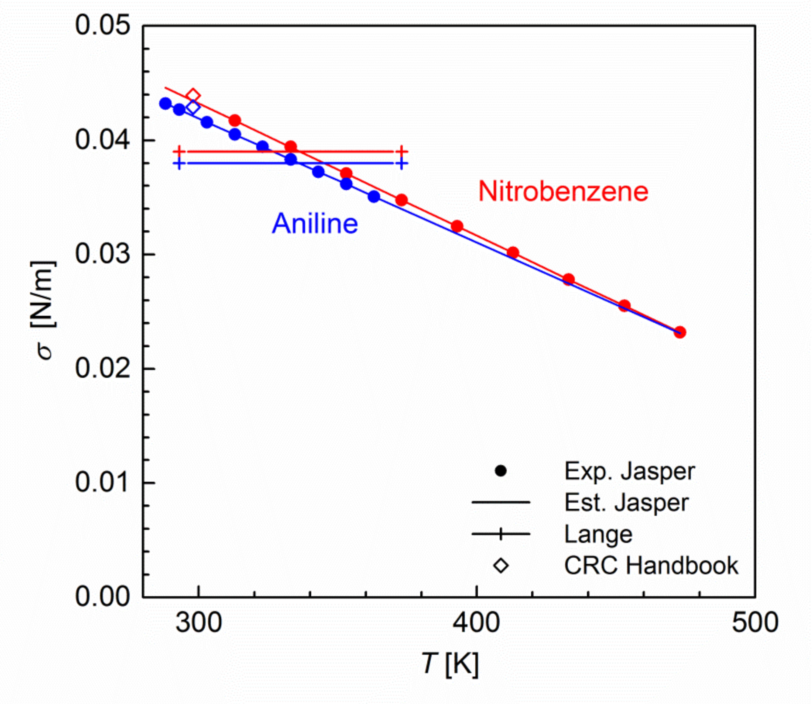

Fig. 5.5: Surface tension of nitrobenzene and aniline with respect to the temperature.

tensions for both liquids of interest at room temperature ($25\,^{o}\mathrm{C}$). Those values are close to the Jasper's estimation, while they are clearly different from Lange's report. Thus, the surface tension of nitrobenzene and aniline is, therefore, computed by Jasper's estimation.

## 5.2 Hydrodynamics for Taylor flow of hydrogen in nitrobenzene

After investigations of physical properties required for simulations, hydrodynamic simulations of Taylor flow are firstly conducted without considering mass transfer. Table 16 describes fluid properties of the real fluid system composed of hydrogen and nitrobenzene. Gas density is assumed the same as liquid density based on the findings in Section 4.2. The computational domain is two-dimension with symmetric boundary condition as shown in Fig. 4.2. The problem configuration and solution procedure are identical to the artificial fluid system shown in Chapter 4. The computational domain represents a unit cell wherein a Taylor bubble is moving periodically. As described in the assumptions of the solver, physical properties are constant during the simulation. In addition, the volume of the bubble is constant so that the expansion or shrink of the bubble cannot be considered in this calculation. Initially, a shape of the bubble is specified, and the shape is developing during the calculation. This development from the initial bubble shape is only a part of numerical solution procedure since the initially given bubble shape (as a capsule) does not exist in the real operation of reactors. This is the reason why the mass transfer is only considered after the bubble forms a terminal developed shape in quasi-steady state condition. Based on the study of the artificial fluid system, the upwind scheme is utilized, density ratio is set to unity, and 37 cells (case C4 in section 4.3) are used in the wall-normal direction.

Table 16: The physical properties of nitrobenzene and hydrogen at 298K and 0.7MPa.

| Properties | Nitrobenzene | Hydrogen | Ratio |
|---|---|---|---|
| Density, $\mathrm{kg/m^3}$ | 1175.8 | 0.766 | $6.51\times10^{-4}$ * |
| Viscosity, $\mathrm{Pa\cdot s}$ | $1.327\times10^{-3}$ | $7.293\times10^{-6}$ | $5.49\times10^{-3}$ |
| Surface tension, $\mathrm{N/m}$ | $4.05\times10^{-2}$ | - | - |

* Density ratio is assumed to be unity in numerical simulation

## 5.2.1 Determination of simulation parameters

Parametric study of the artificial fluid system in section 4.1 comes up with a range of test conditions which are favorable for numerical solutions of quasi-steady Taylor flow. Based on these findings, Reynolds number should be less than 100 to avoid numerical instabilities due to the high and complex velocity field. The reasonable capillary number is bigger than 0.01 to prevent using very fine mesh for resolving very thin liquid film region and is also less than 1.0 to avoid forming a concave shape at the rear bubble. From these criteria, the simulation parameters for the real fluid system of nitrobenzene and hydrogen can be determined by using dimensionless numbers.

Table 17 shows the dimensionless numbers for nitrobenzene with different bubble velocity and channel height. The shaded region corresponds to the criteria $Re < 100$ and $0.01 < Ca < 1$ for stable numerical solutions of quasi-steady Taylor flow. As shown in the table, the available channel heights are very small to keep Reynolds number less than 100. The smaller the channel height is, the harder it is manufactured, obviously. Therefore, the largest channel height ($h = L_{\text{ref}} = 100\,\mu\text{m}$) is chosen for simulations of the real fluid system. The chosen height is very small as compared to the normal size of monolith reactor whose cell density is 400 cpsi (corresponding to 1.27 mm of diameter for square channel). Nevertheless, an experimental study by Kataoka et al. [75] showed a possibility of using such a small channel ($h = 200\,\mu\text{m}$) which is in the same order of magnitude as the current study. It implies that the chosen channel is still in a possible range of manufacture. With the channel height, the range of bubble velocity is then $0.5 < u_{\text{B}} < 1.2\,\text{m/s}$ which results in capillary number bigger than 0.01 and Reynolds number not much higher than 100.

Table 17: Reynolds and capillary numbers for nitrobenzene with respect to the various bubble velocities and channel heights.

| bubble velocity (m/s) | 0.01 | 0.05 | 0.1 | 0.5 | 1 | 5 | 10 |
|---|---|---|---|---|---|---|---|
| capillary number | 0.000327 | 0.00164 | 0.00327 | 0.0164 | 0.0327 | 0.164 | 0.327 |
| channel height | | | | Reynolds number | | | |
| 10 μm | 0.089 | 0.44 | 0.89 | 4.4 | 8.9 | 44 | 89 |
| 50 μm | 0.44 | 2.2 | 4.4 | 22 | 44 | 221 | 443 |
| 100 μm | 0.89 | 4.4 | 8.9 | 44 | 89 | 443 | 886 |
| 500 μm | 4.4 | 22 | 44 | 221 | 443 | 2214 | 4429 |
| 1 mm | 8.9 | 44 | 89 | 443 | 886 | 4429 | 8858 |
| 5 mm | 44 | 221 | 443 | 2214 | 4429 | 22145 | 44290 |

### 5.2.2 Velocity field and bubble shape at quasi-steady state

Initial bubble shape is artificially specified as a half capsule in the symmetrical computational domain as shown in Fig. 4.2. From this initial condition, velocity and volume fraction fields are developing by time marching step until the quasi-steady state where the velocity field around the bubble is not changing but only moving with constant bubble velocity. The computed quasi-steady hydrodynamic solutions are prerequisites for further mass transfer simulation. Test cases are based on different combinations of velocity and channel heights in order to investigate the effect of those parameters on the solution of flow as well as mass transfer. All cases are computed from the same initial bubble shape with bubble thickness of $0.8L_{\mathrm{ref}}$, so that volume of the bubble is identical for all cases. $U_{\mathrm{ref}}$ is 1 m/s for all test conditions.

Based on the solutions of quasi-steady Taylor flow, Table 18 describes bubble velocities, channel heights, and corresponding Reynolds and capillary numbers. As shown in the table, reference lengths of case D1, D2 and D3 are identical, so that channel sizes of those cases are the same, while case D4 has the double reference length as compared to the other cases. From case D1 to D3, Reynolds and capillary number increase with increasing bubble velocity. Except for case D1, Reynolds numbers are bigger than 100, which is already higher than the criterion

Table 18: Test conditions of Taylor flow for hydrodynamic simulations of hydrogenation of nitrobenzene.

| Case | $h(\mu\mathrm{m})$ | $\bar{u}_{\mathrm{B}}$ (m/s) | $Re$ | $Ca$ | $\Delta p_{\mathrm{UC}}$ (N/m$^3$) | $a^*_{\mathrm{int}}$ |
|---|---|---|---|---|---|---|
| D1 | 100 | 1.109 | 98.2 | 0.036 | 167 | 0.272 |
| D2 | 100 | 1.358 | 120.3 | 0.044 | 250 | 0.269 |
| D3 | 100 | 1.523 | 134.9 | 0.050 | 333 | 0.273 |
| D4 | 200 | 1.336 | 236.7 | 0.044 | 67 | 0.279 |

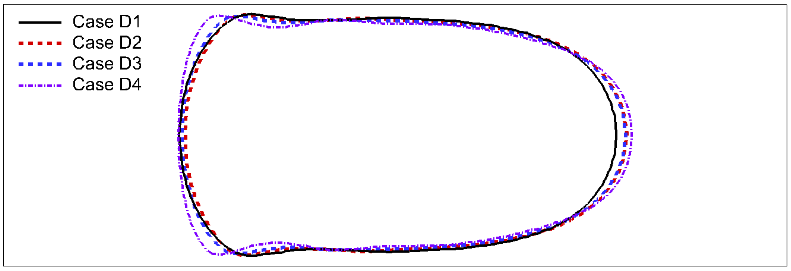

Fig. 5.6: Comparison of steady bubble shape for different cases given in Table 18.

determined from the artificial fluid system. In spite of high Reynolds numbers, stable velocity fields are obtained for case D1~D4 with low capillary numbers (*Ca*<0.05), which is not considered by the artificial fluid system as shown in the Reynolds-capillary diagram in Fig. 4.7.

Fig. 5.6 compares the terminal bubble shapes for different test conditions. Since capillary numbers of the test cases are not much different, overall shapes of the bubble for these three cases are quite similar, while the bubble shape for case D4 differs from the others. Film thicknesses of case D1, D2 and D3 are slightly widened due to the increase in capillary number.

(a) Case D1

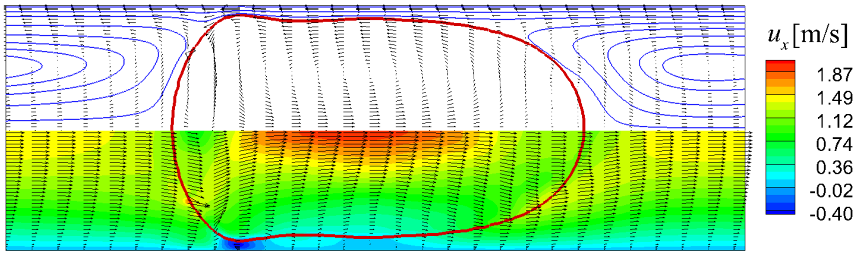

(b) Case D2

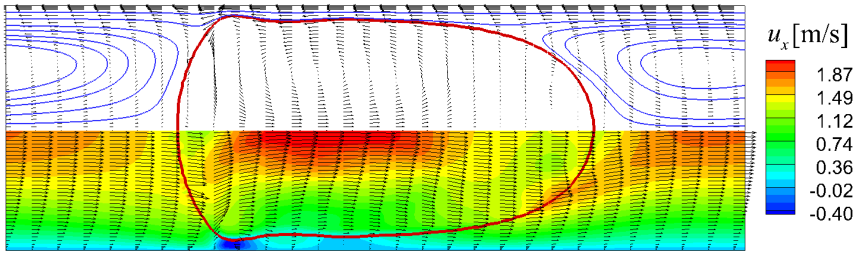

(c) Case D3

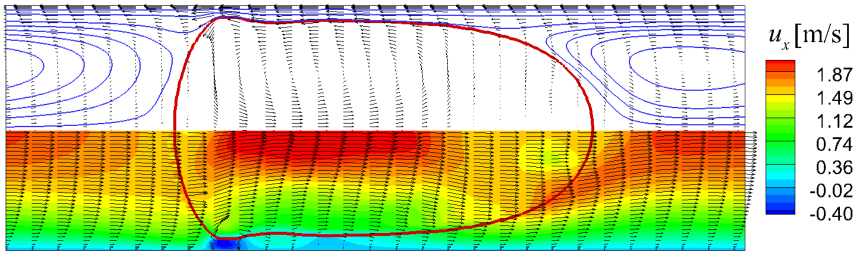

(d) Case D4

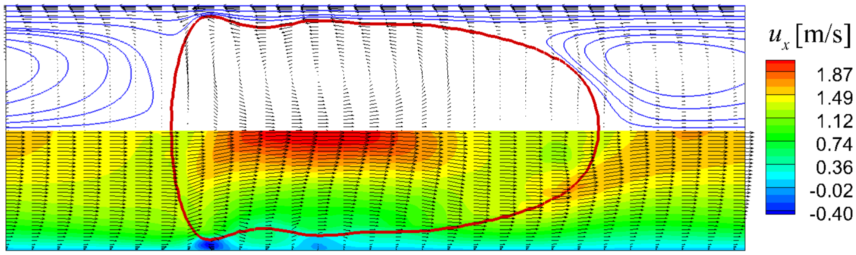

Fig. 5.7: The axial velocity distributions of hydrodynamics for the nitrobenzene/hydrogen Taylor flow (Upper half: streamlines and velocity of moving frame of the bubble, lower half: axial velocity ($u_x$) distributions and velocity vectors of fixed frame).

Capillary number of case D4 is close to that of case D2 so that the film thicknesses for those cases are almost the same. However, Reynolds number of case D4 is higher than the doubled Reynolds number of case D2. Therefore, the bubble shape of case D4, which shows more wavy liquid film and narrower cap of the rear bubble, is different from the other cases.

Fig. 5.7 displays the axial velocity fields of test cases in both fixed and moving reference frame. The MRF velocity is a relative velocity around the bubble within MRF. Therefore, the vectors of FRF velocity is directing to the flow direction, while the MRF velocity shows inner and outer recirculating flow patterns because it excludes the bubble velocity. Since MRF velocity shows flow behavior more clearly, it is widely used for analyzing flow field even for the results computed from FRF. In FRF velocity shown in Fig. 5.7, the highest point of velocity appears in the middle and is biased a bit rear side of the bubble. Backward flow appears near the rear cap of the bubble where the film region is thinnest. All test cases similarly show such velocity behaviors with different velocity magnitude. As mentioned in section 4.4, the erroneous velocity appears near the interface of the rear side of the bubble as well. This unphysical behavior might be caused by either the numerical instability of interface reconstruction method or modeling surface tensions [46] for such 2D test problems. The film thickness of test cases (case D1~D4) are compared with a correlation of Halpern and Gaver [50] as shown in Fig. 4.6. The film thickness thickens from case D1 to case D3 as expected from their capillary numbers. The estimated film thicknesses of three test cases are in very good agreement with the correlation, while case D4 deviates a bit from the correlation curve. Based on these flow fields composed of a different magnitude of velocity and reference length, following sections show the studies of reactive mass transfer within a gas-liquid Taylor flow.

## 5.3 Simulation of catalyzed hydrogenation of nitrobenzene within a Taylor flow

This section details the mass transfer of hydrogen into nitrobenzene and its reaction producing aniline based on the hydrodynamic fields in MRF obtained in section 0. The hydrogen concentration ( $380\,\mathrm{mol/m^3}$ at $323\,\mathrm{K}$ and $0.7\,\mathrm{MPa}$ ) is specified inside the bubble at the beginning of mass transfer calculation, while the concentration outside the bubble is either pure nitrobenzene (for section 5.3.1) or nitrobenzene saturated by hydrogen (for section 0). The concentration of nitrobenzene is $9554\,\mathrm{mol/m^3}$ at $323\,\mathrm{K}$. The extent of hydrogen concentration is relatively small as compared to nitrobenzene concentration. In addition, the liquid composition is not significantly affected by the small extent of produced aniline in the period considered in simulations as well. Therefore, fluid properties are assumed to be independent of the changing liquid composition in this calculation which complies with the assumption of the solver. The transport property such as diffusivity can also be assumed as a constant value during the simulation. The diffusivity values for pure nitrobenzene and pure hydrogen are $4.05\times10^{-9}\,\mathrm{m^2/s}$ and $1.58\times10^{-9}\,\mathrm{m^2/s}$, respectively. The corresponding Schmidt number in liquid phase is 279, and Henry number of hydrogen is set to 0.0335. Since this study focuses only on the pure hydrogen as gaseous species, the concentration of hydrogen is initially specified inside the bubble, and updated at every beginning of time step to avoid numerical artifacts causing fictitious concentration gradient in the gas bubble. Thus, the constant hydrogen concentration in bubble is $380\,\mathrm{mol/m^3}$ , and it is defined as a reference concentration. Therefore, the dimensionless concentration inside the bubble is always unity.

To consider the catalytic hydrogenation of nitrobenzene, the surface reaction rate is also essential for boundary condition at the reactive wall. Reaction kinetics are already investigated and validated in section 3.6. However, the reaction rates from the literature are volumetric reaction rate ( $\mathrm{mol/(m^3s)}$ ) estimated for pellet catalyst in the batch reactor. No study has provided the surface reaction rate ( $\mathrm{mol/(m^2s)}$ ) that is required for the present calculations. For boundary condition of catalytic hydrogenation process in this study, the surface reaction rate is assumed by a geometric conversion of the volumetric reaction rate. From reaction rates of Höller et al. [64], the rate of hydrogenation of nitrobenzene is given by

$$\dot{s} = k\frac{K_{\mathrm{NB}}c_{\mathrm{NB}}}{1+K_{\mathrm{NB}}c_{\mathrm{NB}}} \tag{5.12}$$

where $k$ is the rate constant for a volumetric reaction in a unit of $\mathrm{mol/(gsl)}$. For numerical simulation, $k$ should be converted to $\tilde{k}$ , the rate constant for surface reaction in unit of $\mathrm{mol/(m^2s)}$ with relation of

$$\tilde{k} = km_{\mathrm{cat}}/\tilde{a}_{\mathrm{cat}} \tag{5.13}$$

where $m_{\mathrm{cat}} = 0.24\,g$ is the mass of catalyst given by Höller et al. [64]. The unit of $\tilde{a}_{\mathrm{cat}}$ in Eq. (5.13) is $\mathrm{m^{-1}}$. This reference also provides the value of $a_{\mathrm{cat}}$ ($15\,\mathrm{m^2/g}$ ), however, in a different unit, so that $a_{\mathrm{cat}}$ needs to be converted to $\tilde{a}_{\mathrm{cat}}$ as well. The specific surface area for this case is defined by dividing the total catalytic surface area by bulk volume of the catalytic pellet. These two parameters are required for the estimation of $\tilde{a}_{\mathrm{cat}}$. The total catalytic surface area can be obtained as $m_{\mathrm{cat}}a_{\mathrm{cat}}$. However, the volume of pellet itself cannot be estimated, since the porosity of batch reactor is not given. Therefore, the reactor volume (1 liter for this case) is assumed the same as the bulk volume of the pellet. The assumed volume contains then not only the volume of pellet but also the volume of vacancy filled by liquid or gas. This assumption may cause the over- or under-prediction of species conversions in numerical solutions. With this assumption, the specific surface area is determined then as $\tilde{a}_{\mathrm{cat}} = 3600\,\mathrm{m}^{-1}$. Finally, the converted rate constant $\tilde{k}$ is $0.0987\,\mathrm{mol/(m^2s)}$.

## 5.3.1 Pure nitrobenzene

This section describes the mass transfer simulation of hydrogen transferred into pure nitrobenzene. The dimensional time step ($\Delta t^* \cdot t_{\mathrm{ref}}$) for mass transfer calculations is $5\times10^{-9}\,\mathrm{s}$. Fig. 5.8, Fig. 5.9 and Fig. 5.10 present the concentration fields of hydrogen and aniline at $t = 0.25$, 1.25 and $5\,\mathrm{ms}$, respectively. The result of water was not displayed because the production rate of water is exactly double of the aniline production rate according to the stoichiometry of one-step reaction mechanism. The obtained water concentration is exactly double of aniline concentration. In the figures, most of hydrogen is transferred from the rear part of the bubble and moves into the recirculation zone shown between the bubbles. The concentration fields in this recirculation zone show a symmetrical behavior so that two recirculating patterns appear at upper and lower regions, indeed. Due to the recirculating flow, the species at the front cap of bubble penetrates into the recirculation zone as well. In the meantime, aniline is mostly produced at the rear part of the bubble where the hydrogen concentration is highest at the wall. Produced aniline in the liquid film region moves backward by bypass velocity in the film region as for hydrogen.

As displayed in Fig. 5.8, the hydrogen concentration fields after $0.25\,\mathrm{ms}$ show different behaviors from case D1 to D4. The only difference among the case D1~D3 is the bubble velocity. Due to the increasing bubble velocity, more hydrogen is transferring from the front cap to the recirculation zone, which results in an increase of penetration length from case D1 to D3. Increasing bubble velocity also affects the penetration length of the species transferred from the rear bubble. Since channel height of case D4 is double as compared to the other cases, its

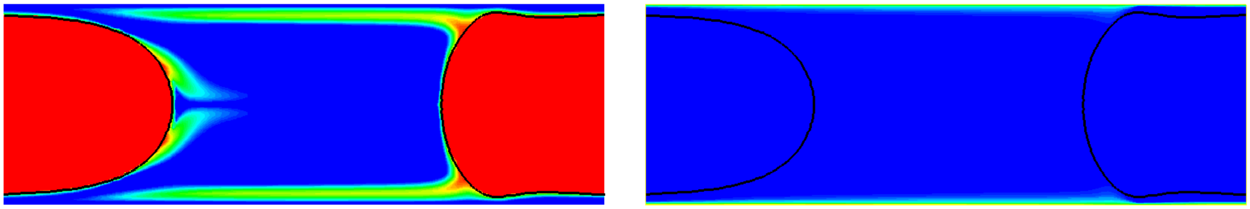

(a) case D1: hydrogen

(b) case D1: aniline

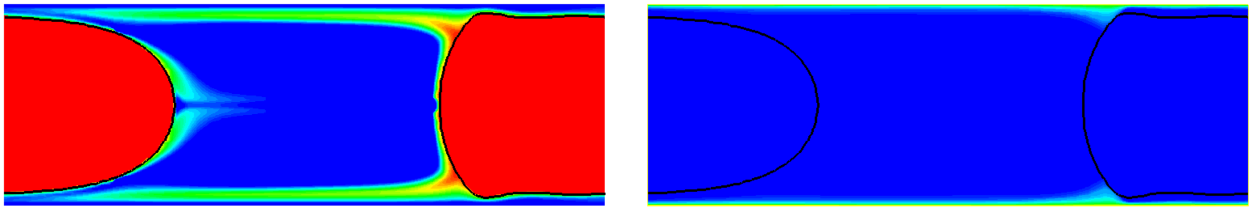

(c) case D2: hydrogen

(d) case D2: aniline

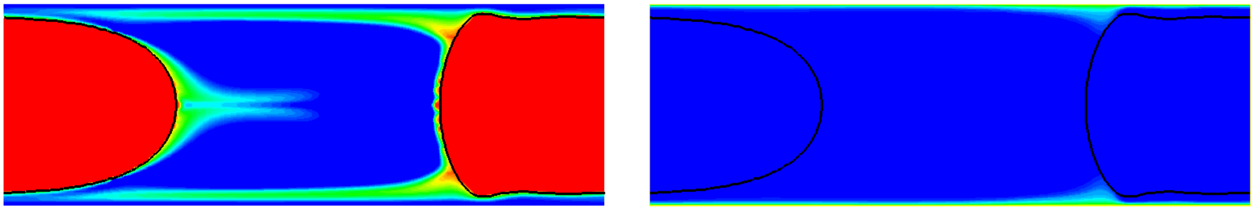

(e) case D3: hydrogen

(f) case D3: aniline

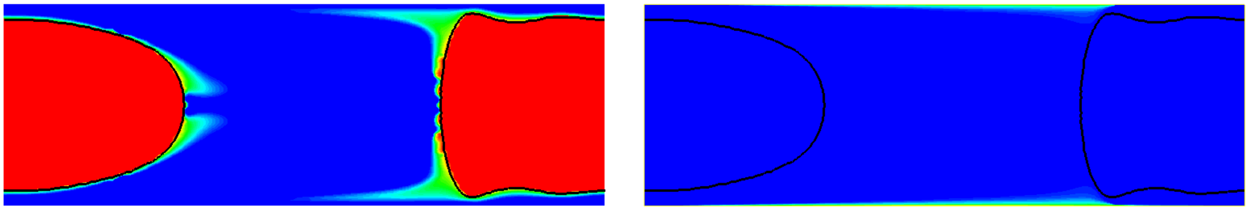

(g) case D4: hydrogen

(h) case D4: aniline

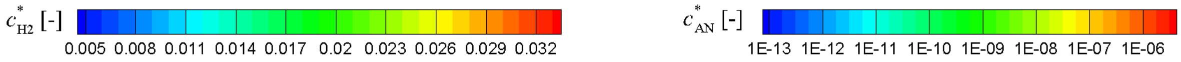

Fig. 5.8: Distributions of the hydrogen transferring into pure nitrobenzene and the produced aniline at $t = 0.25\,\mathrm{ms}$ ($c_{\mathrm{ref}} = 380\,\mathrm{mol/m^3}$).

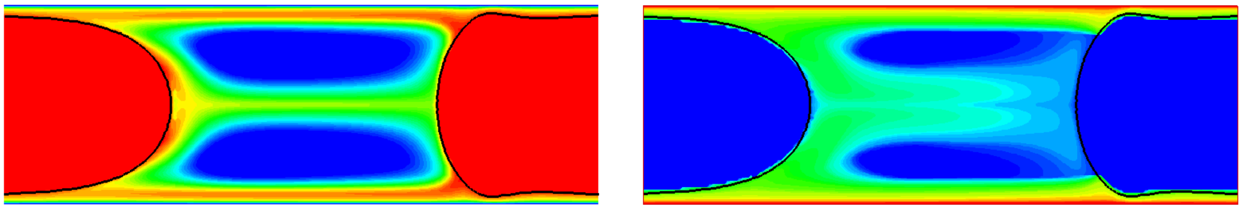

(a) case D1: hydrogen (b) case D1: aniline

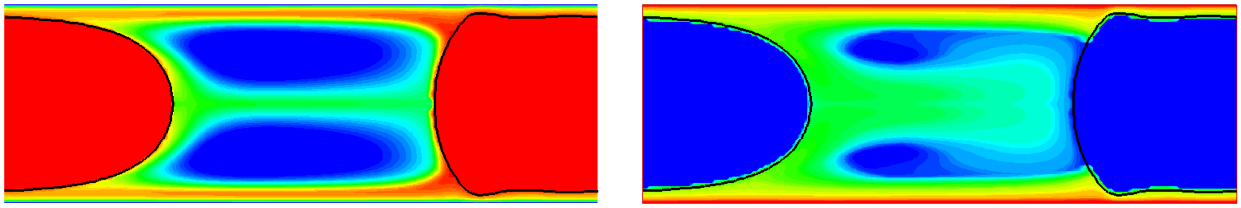

(c) case D2: hydrogen (d) case D2: aniline

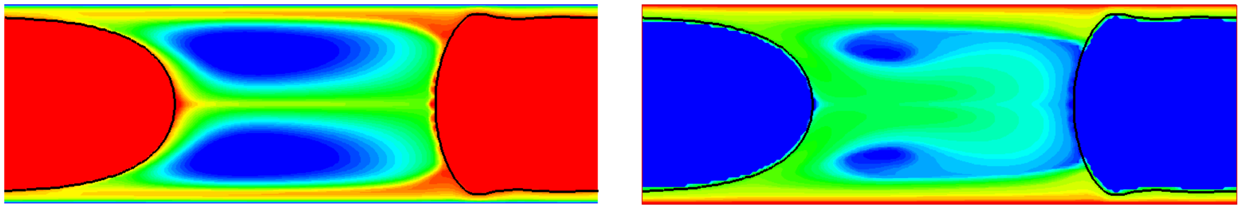

(e) case D3: hydrogen (f) case D3: aniline

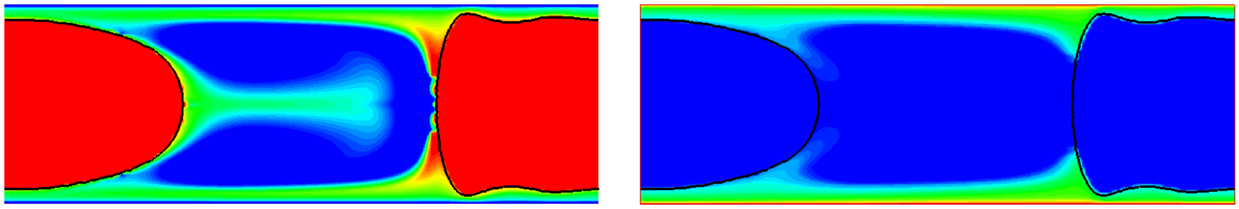

(g) case D4: hydrogen (h) case D4: aniline

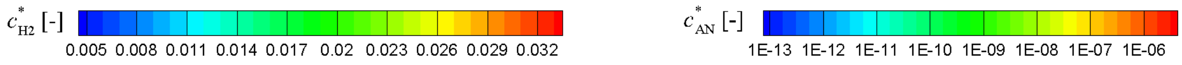

Fig. 5.9: Distributions of the hydrogen transferring into pure nitrobenzene and the produced aniline at $t = 1.25\,\text{ms}$ ($c_{\text{ref}} = 380\,\text{mol/m}^3$).

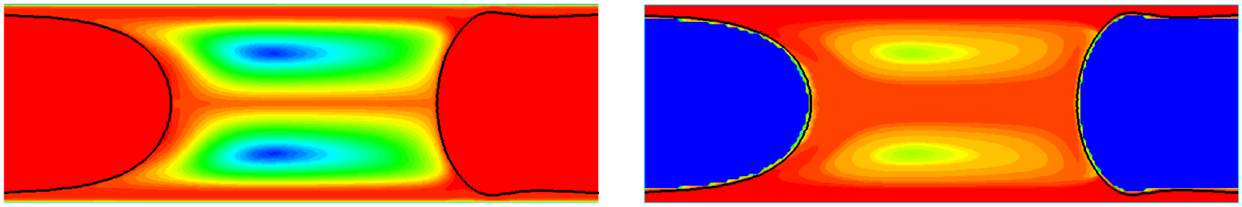

(a) case D1: hydrogen

(b) case D1: aniline

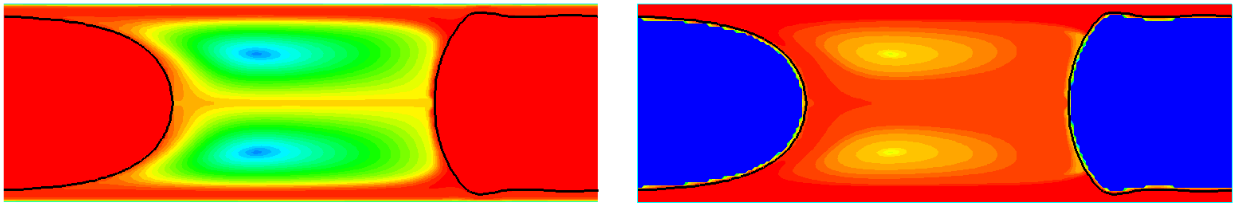

(c) case D2: hydrogen

(d) case D2: aniline

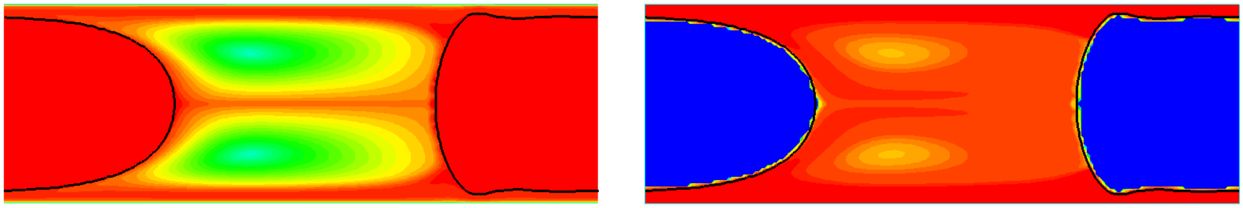

(e) case D3: hydrogen

(f) case D3: aniline

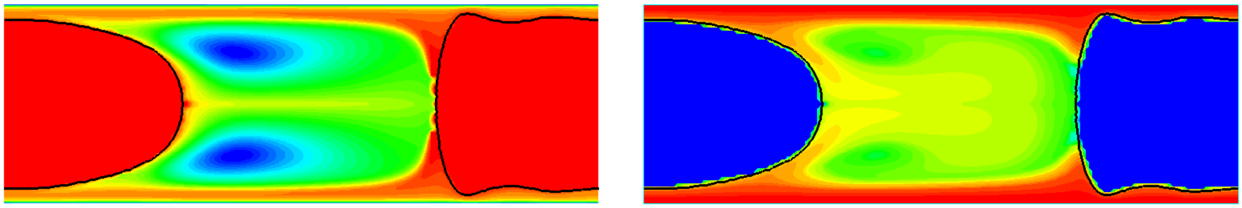

(g) case D4: hydrogen

(h) case D4: aniline

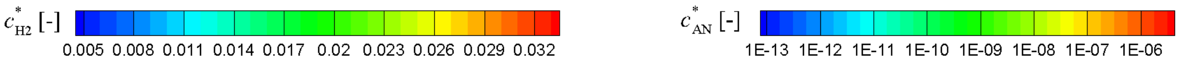

Fig. 5.10: Distributions of the hydrogen transferring into pure nitrobenzene and the produced aniline at $t = 5\,\text{ms}$ ($c_{\text{ref}} = 380\,\text{mol/m}^3$).

concentration field behaves quite different even if the bubble velocity is similar to that of case D2. With increasing length scale, case D4 shows shorter penetration of hydrogen species into the recirculation zone. Case D3 where the bubble velocity is highest among the test cases presents the highest production of aniline since high bubble velocity gives rise to high recirculation flow between the bubbles. Higher intensity of the recirculating flow may enhance the hydrogen mass transfer to the surface by stronger convective mass transfer. The influence of recirculation intensity is further discussed in Section 5.3.3.

Fig. 5.9 shows the results at $1.25\,\mathrm{ms}$. Hydrogen species starts circulating between the bubbles due to the recirculation flow. The concentration at the rear part of bubble is still highest , and concentration profiles in the recirculation zone differ according to the velocity field of each test case. Aniline is propagated from the liquid film to the recirculation zone and mixed by convective mass transfer. However, it is found out that most of aniline still remains near the wall. In the liquid film, diffusion is the dominant mechanism for mass transfer in wall-normal direction because almost no wall-normal flow exists. Fig. 5.10 shows the results at the later time instant, $t = 5\,\mathrm{ms}$. Both hydrogen and aniline species are well mixed between the bubbles. The concentration of hydrogen adjacent to the bubble almost reaches to the equilibrium concentration. The hydrogen concentration at the center of the recirculation zone is relatively low because of the vortex-mixing pattern. Low concentration of hydrogen also appears near the wall due to the consumption of reactions. For aniline, the concentration difference between the film region and the recirculation zone is gradually decreasing as reaction takes place. With the figures at three different time instants, it turns out that the time evolution of concentration fields and those mixing patterns depend on the different velocity and channel height, but the overall tendency of mass transfer is similar for all cases.

To analyze the difference among the results of test cases, Fig. 5.11 plots the wall-normal concentration profiles of hydrogen and aniline at three different positions. The concentration profiles are captured at $t = 15\,\mathrm{ms}$ when the mean concentration of hydrogen in liquid phase almost reaches to the equilibrium concentration. Fig. 5.11 (a) and (b) show the profiles of hydrogen and aniline at a certain position ($x^* = 1$) near the front cap of the bubble. No visible concentration difference appears among the test cases even in the zoom-in of liquid region where a large gradient of concentration may occur. The axial position of Fig. 5.11 (c) and (d) are the middle of recirculation zone ($x^* = 3$). The concentration profiles of test cases deviate at this

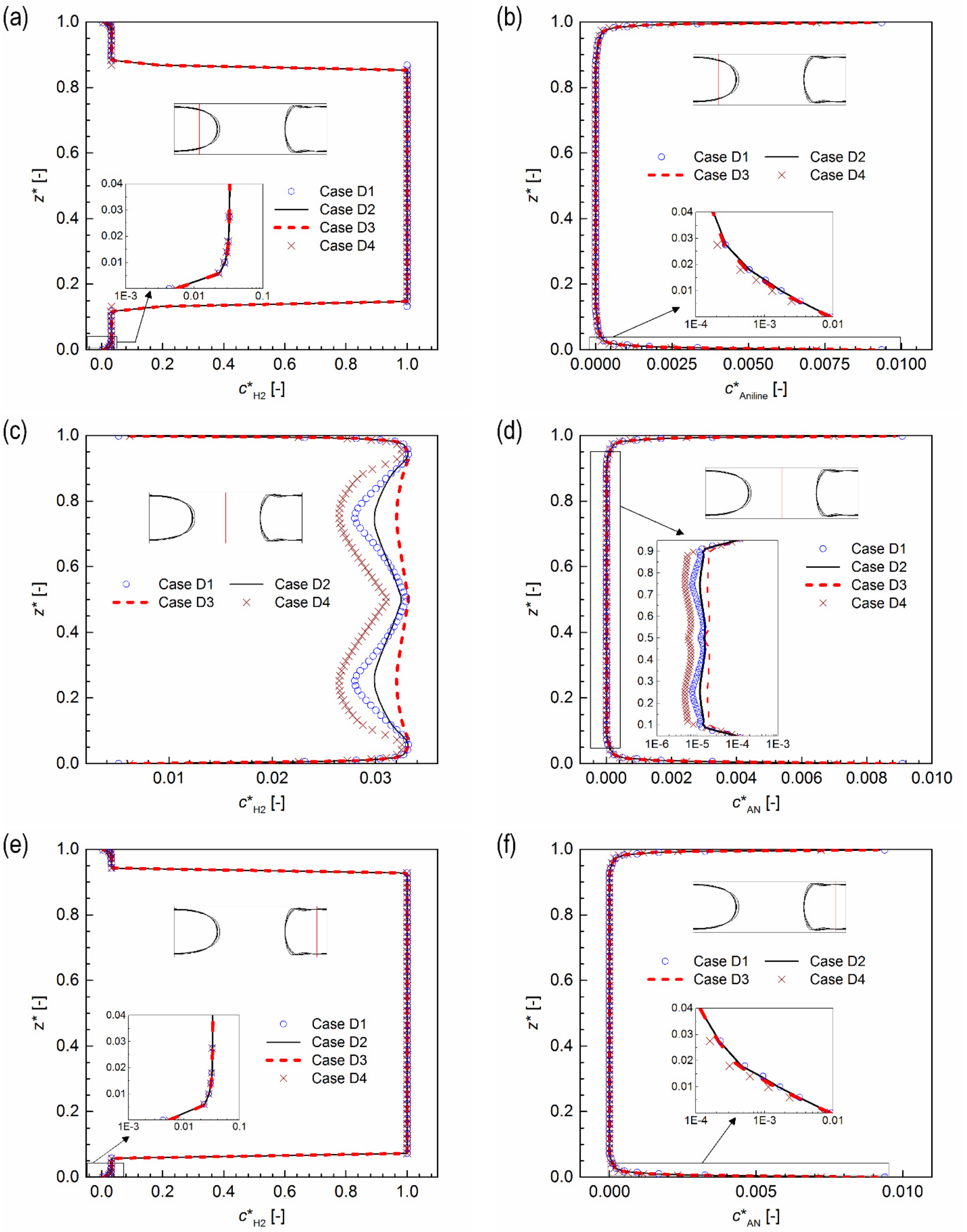

Fig. 5.11: Comparison of wall-normal concentration profile of hydrogen and aniline at three axial positions (front cap, recirculation zone and liquid film, $x^* = 1,\ 3,\ 5.6$) at $t = 15\,\text{ms}$.

point. This represents that higher mean velocity results in better mixing of species at the recirculation zone. In Fig. 5.11 (e) and (f) whose axial position crosses through the constant liquid film region ($x^* = 5.6$), the concentration distributions are almost identical among the test cases as for the results at the front bubble cap shown in Fig. 5.11 (a) and (b). The series of wall-normal distributions also conclude that the diffusive mass transfer predominates over convective mass transfer in liquid film region. Regardless of different bubble velocity, the wall-normal concentrations of aniline are almost the same for all cases because most of the produced aniline is transferred by diffusive mass transfer through the liquid film. Therefore, the film thickness plays a crucial role in mass transfer within a Taylor flow as the film thickness is the only parameter to make different concentration profiles shown in Fig. 5.11 (a) and (e).

Fig. 5.12 (a) compares the mean concentrations of hydrogen and aniline in liquid phase during calculations. Initially, the mean concentrations of hydrogen are rapidly increasing, and the gradients of the curve are gradually decreasing over time. The hydrogen concentrations will finally converge to the equilibrium concentration. On the other hand, almost no aniline exists at the beginning, and the amount of aniline increases gradually with growing its production rate. The absence of reactant (hydrogen) at the reactive wall causes the delay of production at the beginning of calculation. The aniline production rate decreases and converges at the end of calculation as well. These results confirm once again that the mixing in recirculation zone affects the overall amount of mass transfer as discussed earlier. Case D3 whose mean velocity is highest shows the highest mean hydrogen concentration in liquid phase as expected. However, the mean hydrogen concentration for case D1 and D2 are almost similar despite their different bubble velocities. This illustrates that the recirculation intensity is not only the factor affecting the mass transfer efficiency.

Moreover, the highest production of aniline appears in case D2 whose bubble velocity is in between those of case D1 and D3. Another possible factor is the variable diffusion length corresponding to film thickness which is a function of bubble velocity in this study. According to the capillary number, film thickness thickens when the bubble velocity increases. Consequently, an increase of bubble velocity improves the convective mass transfer in the recirculation zone, but it also causes a longer distance for diffusive mass transfer in the liquid film, simultaneously. Hence, case D2 shows the highest production of aniline by the tradeoff relation between the film thickness and the recirculation intensity. Results of case D4 deviate from the other results

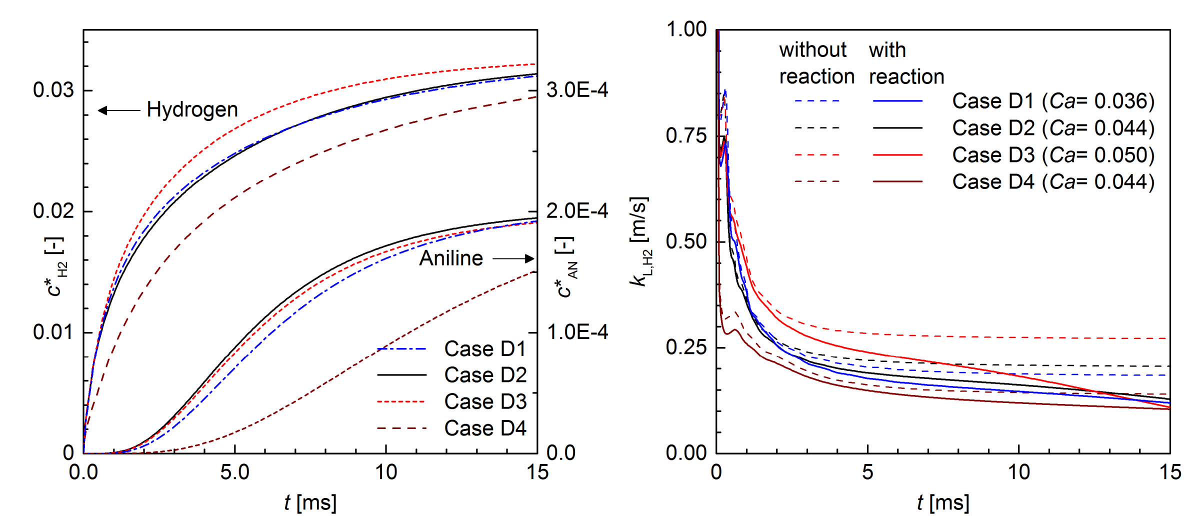

(a) (b)

Fig. 5.12: (a) Time evolution of mean concentrations of hydrogen and aniline within the pure nitrobenzene. (b) mass transfer coefficients of hydrogen into the pure nitrobenzene with and without reaction.

because the reference length of case D4 is twice of those for other cases. Therefore, case D4 requires almost double time to reach the same level of liquid mean concentrations of other cases. This implicates that the transferred amount of species into liquid phase may be linearly related to the length scale of problems. By analogy, $15\,\mathrm{ms}$ for this test condition whose channel height is $100\,\mu\mathrm{m}$ corresponds to $1.5\,\mathrm{s}$ for the channel of $1\,\mathrm{mm}$ height.

Mass transfer coefficients of hydrogen into pure nitrobenzene are estimated from the mean concentration of hydrogen in liquid phase. Since the concentration in gaseous bubble isfixed during the calculation, the Eq.(4.3) cannot be used in this problem as it yields the mass transfer coefficient by the temporal difference of gas mean concentration. Therefore, another form of the mass transfer coefficient is derived with liquid mean concentration and its changing rate as

$$k_{\mathrm{L,H_2}}(t) := \frac{\dfrac{\mathrm{d}\left\langle c^*_{\mathrm{H_2}}(t)\right\rangle}{\mathrm{d}t}}{c^*_{\mathrm{H_2(L),eq}} - \left\langle c^*_{\mathrm{H_2}}(t)\right\rangle} \frac{1}{a_{\mathrm{int}}} \tag{5.14}$$

where $a_{\mathrm{int}}$ represents the specific surface area of the interface.

Fig. 5.12 (b) plots the mass transfer coefficient computed by Eq. (5.14) for the cases with and without reaction. With reaction, case D3 whose bubble velocity is highest shows the highest mass transfer coefficient as well in a wide range of time. This represents that high bubble velocity gives rise to the high intensity of convective mass transfer in recirculation zone, and is beneficial for the mass transfer even if it thickens the liquid film. However, this curve rapidly drops after $10\,\mathrm{ms}$. In contrary, the concentration profiles of case D1 and D2 are almost linearly decreasing after $2.5\,\mathrm{ms}$. Finally, case D2 records the highest aniline concentration as shown in the figure. The mass transfer coefficient of case D4 is lowest according to its larger length scale. In addition, the mass transfer coefficients without reaction are compared to check the influence of the presence of reaction. In the beginning of mass transfer ($t < 2.5\,\mathrm{ms}$), the mass transfer coefficients with and without reaction are almost similar. After $t < 2.5\,\mathrm{ms}$, however, the mass transfer coefficient without reaction approaches to a certain value, while the mass transfer coefficient with reaction decreases continuously. This represents that surface reaction enhances the mass transfer in the gas-liquid system by a consumptive flux at the reactive wall. With reaction, the mean hydrogen concentration in liquid phase is lower than the concentration without reaction. The mass transfer enhancement in this study is observed as a reduction of mass transfer coefficient since the mass transfer coefficients are estimated by changing liquid mean concentration instead of the gas mean concentration. This comparison clearly shows the general trend of reactive gas-liquid mass transfer, so-called mass transfer enhancement effect, when surface reaction takes place.

### 5.3.2 Nitrobenzene pre-saturated with hydrogen

As discussed in the previous section, hydrogen undergoes mass transfer from the bubble to the reactive wall and is driven by the combination of diffusive, convective and reactive fluxes. In pure nitrobenzene, the computational domain is filled with the transferred hydrogen within 1s as shown in Fig. 5.12 (a). After a certain time, this hydrogenation process can be regarded as a reaction of nitrobenzene with saturated hydrogen in liquid phase of Taylor flow. Thus, understanding the reactive mass transfer after saturation of hydrogen in liquid phase is as important as the study on the initial gas-liquid mass transfer. This section focuses, therefore, on the reactive mass transfer with an assumption that the dissolved hydrogen is initially well mixed and it achieves an equilibrium state. For this purpose, the equilibrium concentration of hydrogen is initialized in the entire computational domain so that the hydrogen is saturated in liquid nitrobenzene before starting mass transfer computation.

Fig. 5.13 shows the results of hydrogen and aniline from the pre-saturated calculation. As

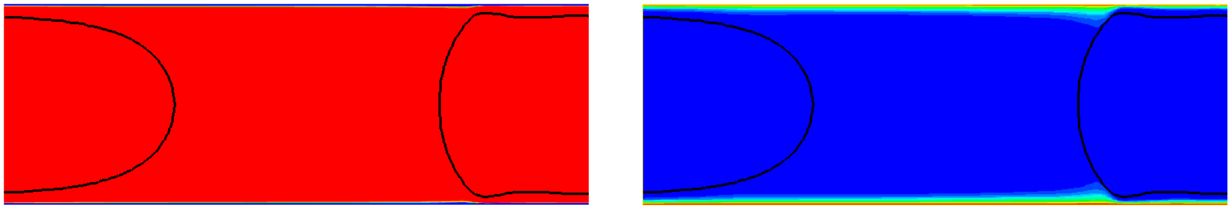

(a) hydrogen at $0.25\,\mathrm{ms}$ (b) aniline at $0.25\,\mathrm{ms}$

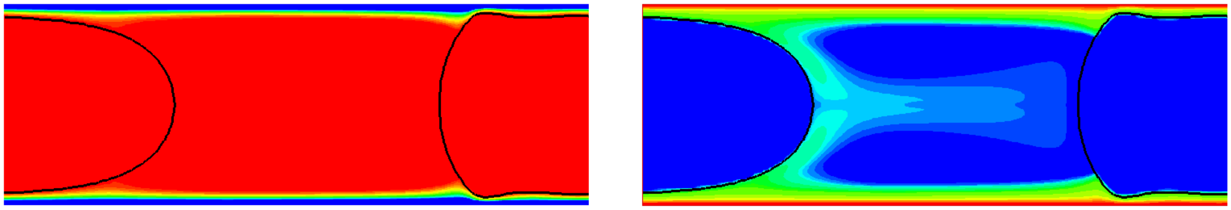

(c) hydrogen at $1.25\,\mathrm{ms}$ (d) aniline at $1.25\,\mathrm{ms}$

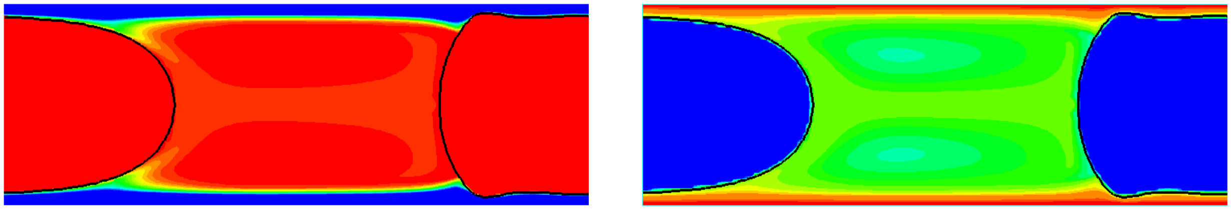

(e) hydrogen at $5\,\mathrm{ms}$ (f) aniline at $5\,\mathrm{ms}$

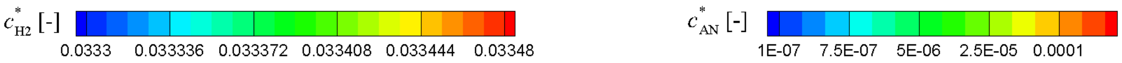

Fig. 5.13: Distributions of the hydrogen transferring into nitrobenzene pre-saturated by hydrogen, and the produced aniline for case D2 at different instants of the time $(t = 0.25,\ 1.25 \text{ and } 5\,\mathrm{ms})$.

described in Section 5.3.1, the species distributions among the test cases are very similar at a certain time instant. Therefore, only the results of case D2 are displayed in this section. Most of hydrogen is consumed near the reactive wall by surface reaction. Hydrogen between the bubbles circulates by convective mass transfer. Since the reactive flux is normal to the wall, the gradient of hydrogen concentration is mostly formed in the wall-normal direction. As reaction takes place, the hydrogen concentration in liquid film lowers due to the consumption, while the hydrogen concentration in the recirculation zone remains still high. The concentration of aniline shows almost inversed tendency against the hydrogen concentration. Thus, it also emphasizes that the concentration in liquid film plays a crucial role for surface reaction in gas-liquid Taylor flow. Since diffusion is also a dominant mechanism between the liquid film and the recirculation zone between bubbles, there is almost no visible interaction between the central part of recirculation

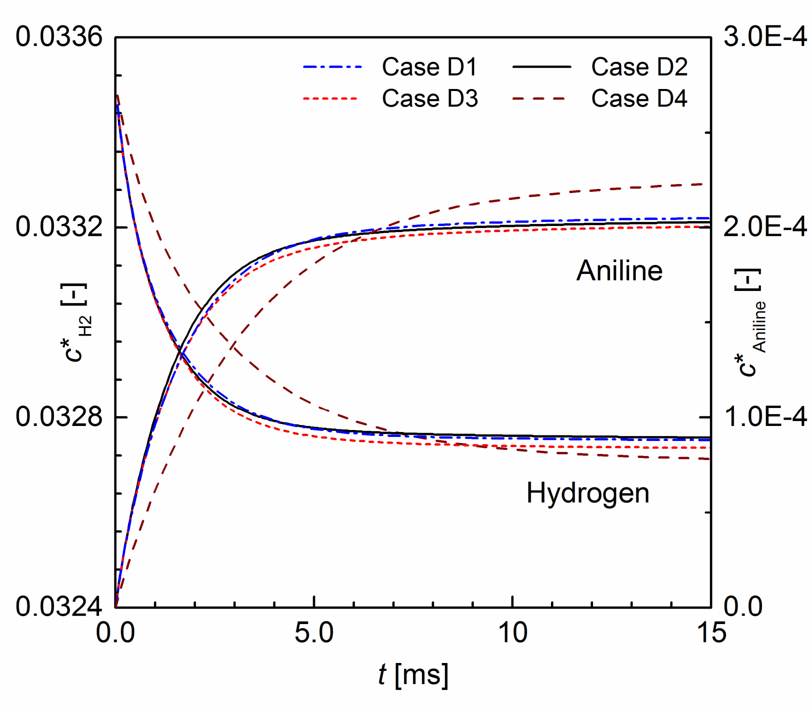

Fig. 5.14: Time evolution of mean concentrations of pre-saturated hydrogen and aniline in liquid phase.

zone and liquid film between the bubbles. Aniline is mostly distributed in liquid film region as well. Relatively small amount of aniline diffuses into the recirculation zone and circulates by convective mass transfer as for hydrogen.

Fig. 5.14 compares the mean concentration of hydrogen and aniline for case D1~D4. These results show that the mean concentrations of case D1, D2 and D3 are very similar in contrast with the pure nitrobenzene case in Fig. 5.12 which shows that the mean concentrations deviate with different bubble velocities. In such a pre-saturated condition, consumption of hydrogen (or production of aniline) is not significantly affected by the intensity of convective mass transfer in recirculation zone. Case D4 only shows the different hydrogen concentration caused by doubled channel height. Size of the channel is only the factor that influences the production of aniline as well. The increased distance between the bubble and the wall in case D4 may not cause the decrease of mass transfer significantly as hydrogen is initially saturated in the entire domain. The reason of difference may be the larger length scale which directly relates to the reference time ( $t_{\mathrm{ref}} = L_{\mathrm{ref}} / u_{\mathrm{ref}}$ ). In addition, the production rate (or consumption rate) is finally converging to a certain terminal values where the mass transfer rate and reaction rate are balanced.

### 5.3.3 Influence of recirculation and diffusion

The test cases with pure nitrobenzene figure out that the convective mass transfer caused by recirculating flow and diffusive mass transfer in liquid film may have a tradeoff relationship to the yield of aniline. To quantify these transport mechanisms, several characteristic times regarding recirculation intensity and diffusion are evaluated and analyzed in this section. Kececi et al. [79] investigated the recirculation time in the liquid slug of Taylor flow theoretically and numerically. The intensity of recirculation can be quantified by two characteristic times; the time for liquid to move from one end of the slug to the other end, $\tau_L$, and the time for liquid slug to travel a distance of its own length, $\tau_S$ [133]. Fig. 5.15 illustrates the concept of velocities and length scales required for those two characteristic times. The definition of characteristic times are

Table 19: Estimated characteristic velocities and lengths for case D1, D2 and D3.

| Case | $d_F$ (μm) | $u_B$ (m/s) | $u_S$ (m/s) | $L_B$ (μm) | $L_S$ (μm) |
|---|---|---|---|---|---|
| D1 | 11.0 | 1.109 | 0.247 | 166.3 | 133.672 |
| D2 | 11.3 | 1.358 | 0.274 | 167.9 | 132.088 |
| D3 | 12.7 | 1.523 | 0.264 | 169.0 | 131.011 |

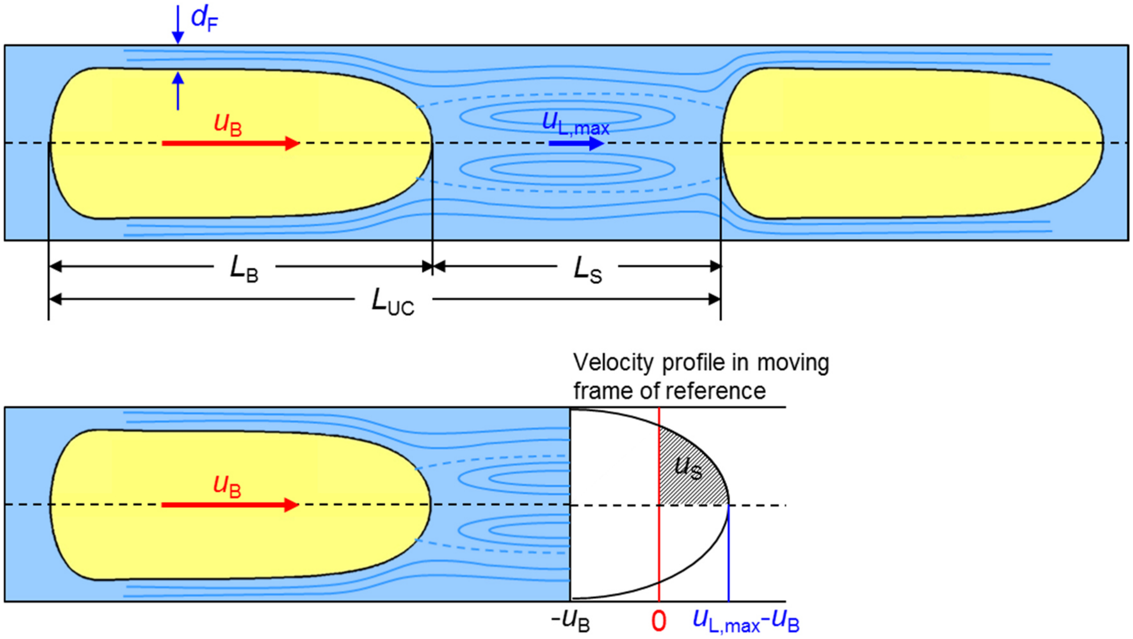

Fig. 5.15: Sketch of lateral view for Taylor flow. Definition of characteristic velocities and lengths. Fig. adapted from Wörner [146].

$$\tau_{\mathrm{L}} := \frac{L_{\mathrm{S}}}{u_{\mathrm{S}}}, \quad \tau_{\mathrm{S}} := \frac{L_{\mathrm{S}}}{u_{\mathrm{B}}} \tag{5.15}$$

To analyze the convective and diffusive mass transfer in liquid film, two characteristic times are additionally introduced. The first one is the film exposure time, $\tau_{\mathrm{F}}$ which represents the time for liquid film to be exposed during the passage of a bubble. $\tau_{\mathrm{F}}$ is estimated by bubble length, $L_{\mathrm{B}}$ and bubble velocity, $u_{\mathrm{B}}$, which is similar to the bubble exposure time used by Taylor and Krishna [132]. The other one is the characteristic diffusion time, $\tau_{\mathrm{D}}$ for the time of diffusive mass transfer within the distance of film thickness. The definitions of $\tau_{\mathrm{F}}$ and $\tau_{\mathrm{D}}$ are given by

$$\tau_{\mathrm{F}} := \frac{L_{\mathrm{B}}}{u_{\mathrm{B}}}, \quad \tau_{\mathrm{D}} := \frac{d_{\mathrm{F}}^2}{D_{\mathrm{H}_2}} \tag{5.16}$$

With characteristic velocities and lengths given in Table 19, Fig. 5.16 (a) compares four characteristic times evaluated by Eq. (5.15) and (5.16). As capillary number increases, $\tau_{\mathrm{S}}$ and $\tau_{\mathrm{F}}$ decrease because of the increasing bubble velocity. Although the slug lengths, $L_{\mathrm{S}}$ from case D1~D3 are slightly decreasing and those bubble lengths, $L_{\mathrm{B}}$ are increasing accordingly, the characteristic times are mainly governed by increasing $u_{\mathrm{B}}$. Meanwhile, $\tau_{\mathrm{L}}$ that relates to $u_{\mathrm{S}}$ behaves non-monotonically against capillary number. Since $u_{\mathrm{S}}$ of case D2 is highest among the cases, the characteristic time $\tau_{\mathrm{L}}$ for case D2 is shortest. The highest slug velocity of case D2 may cause the highest convective mass transfer in liquid slug region, which may also lead to the

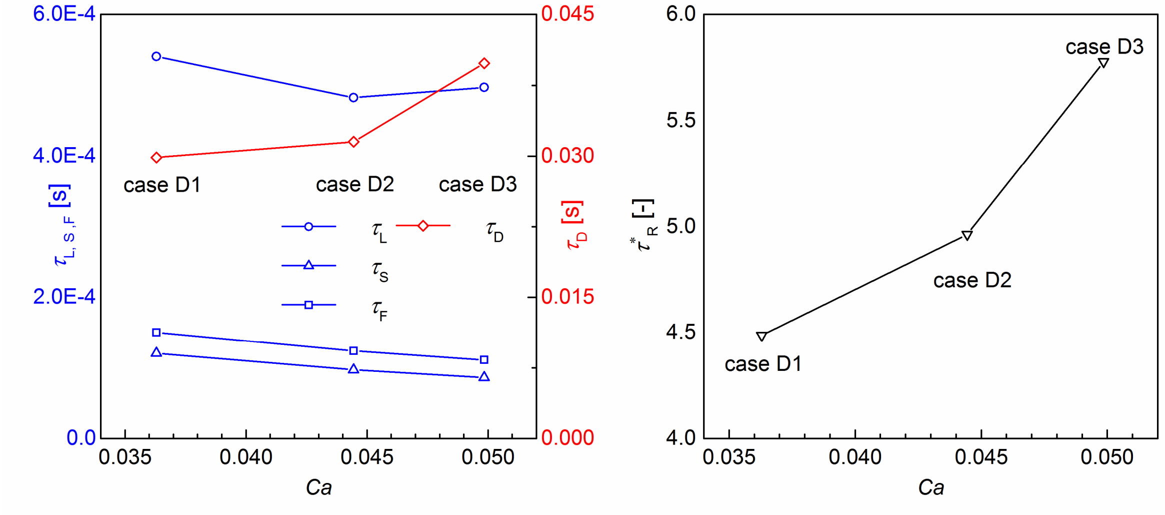

(a) (b)

Fig. 5.16: Comparison of four different characteristic times (a) and non-dimensional recirculation time (b) for test case D1, D2 and D3.

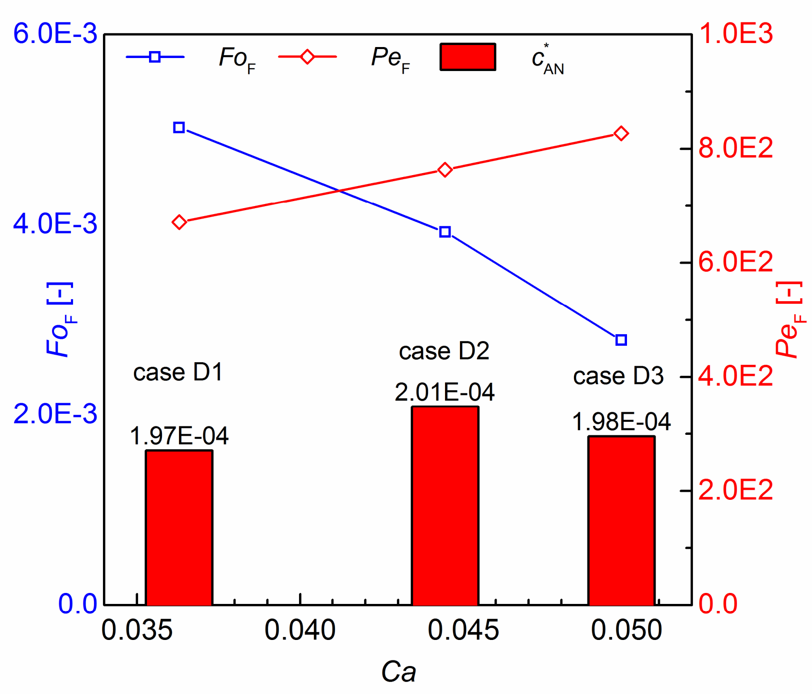

Fig. 5.17: Comparison of film Fourier number $Fo_F$ and film Peclet number $Pe_F$ with aniline conversions for test case D1, D2 and D3.

highest aniline yields among the test cases. Based on Eq. (5.16), the characteristic diffusion time, $\tau_D$ becomes longer with growing capillary number, which thickens the film thickness. Fig. 5.16 (b) shows the non-dimensional recirculation time defined by $\tau_R^* := \tau_L / \tau_S$ [133]. In spite of the non-monotonic change of $\tau_L$, the value of $\tau_R^*$ is monotonically increasing as capillary number increases from case D1 to D3. From these behaviors of characteristic times, it is figured out that the intensity of convective mass transfer becomes stronger with higher capillary number, while the diffusive mass transfer requires longer time as the distance of diffusion path increases. It also corresponds to the tendency shown in the time evolution of concentration fields in Fig. 5.10.

To quantify the influence of convective and diffusive mass transfer in Taylor flow, the Fourier and Peclet numbers for mass transfer are further analyzed. The definitions of two dimensionless numbers are

$$Fo_F := \frac{D_{H_2}\tau_F}{d_F^2} = \frac{\tau_F}{\tau_D}, \quad Pe_F := \frac{d_f u_S}{D_{H_2}} = \frac{\tau_D}{\tau_L}\frac{L_S}{d_F} \tag{5.17}$$

$Fo_F$ is the film Fourier number which represents the ratio between diffusive mass transfer rate and the square of diffusion path in liquid film region. $Pe_F$ is the film Peclet number which denotes the ratio between convective mass transfer due to the slug velocity and diffusive mass transfer within the liquid film. Thus, this $Pe_\mathrm{F}$ represents the ratio of two mass transfer mechanisms in liquid slug region within the distance of film thickness. Fig. 5.17 compares the two dimensionless numbers. As capillary increases $Fo_\mathrm{F}$ is decreasing, while $Pe_\mathrm{F}$ is increasing due to the increase of film thickness. The influence of $u_\mathrm{S}$ is turned out to be much smaller than that of $d_\mathrm{F}$ so that both numbers behave monotonically against capillary number. $Pe_\mathrm{F}$ and $Fo_\mathrm{F}$ behave in accordance with convective and diffusive mass transfer, respectively. Increasing $Ca$ leads convective mass transfer to be stronger, but also worsens diffusive mass transfer, concurrently. This complies with the previous speculation with the 2D concentration fields in Fig. 5.8, Fig. 5.9 and Fig. 5.10. However, these two numbers still cannot directly quantify the non-monotonic behaviors of aniline conversion with increasing capillary number. The only possible reason for the non-monotonic aniline yields is the non-monotonic behavior of slug velocity. With the tradeoff relationship between convective and diffusive mass transfer, it may implicate that convective mass transfer in liquid film plays a special role to govern the production efficiency of gas-liquid mass transfer within a Taylor flow.

This analysis finds out that there is a relation between convective mass transfer by recirculation and diffusive mass transfer in liquid film region. These two are the key mass transfer mechanisms interacting within a Taylor flow and influence apparent surface reaction rate as well. In non-reactive mass transfer shown in Fig. 5.12 (b), the mass transfer coefficients without reaction becomes higher as bubble velocity increases from case D1 to D3. This represents that the intensity of recirculation is the only factor to govern the mass transfer efficiency in the absence of reactive flux. However, if there is concentration flux at the wall, both convective and diffusive mass transfers play decisive roles for mass transfer efficiency in Taylor flow.

## 5.3.4 Influence of reaction rate on mass transfer

Mass transfer enhancement effect is observed in the results of pure nitrobenzene cases shown in Fig. 5.12 (b) in section 5.3.1. To explore the relation between the reaction rate and the mass transfer coefficient, mass transfer simulations are performed again with different orders of the reaction rate. Case D2 in section 5.3.1 is chosen for this section. To control the order of the reaction rate, a scaling factor $f_\mathrm{s}$ which is multiplied to the reaction rate defined in Eq. (5.12), is

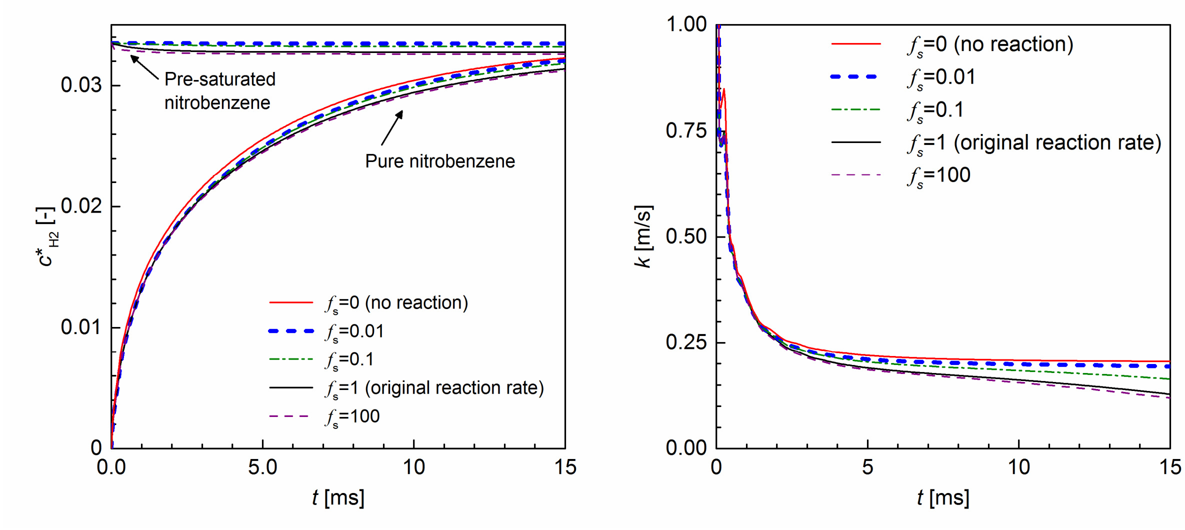

(a) (b)

Fig. 5.18: (a) Temporal evolution of mean concentration of hydrogen in liquid phase with various scaling factors of reaction rate ($f_s$). Comparison between the mass transfer of hydrogen into pure and pre-saturated nitrobenzene. (side by side), (b) mass transfer coefficient of hydrogen into the pure nitrobenzene with various scaling factors of reaction rate ($f_s$).

introduced.

Fig. 5.18 (a) displays mean concentrations of hydrogen transferred into both pure and pre-saturated nitrobenzene with different $f_s$. In pure nitrobenzene, the curves for $f_s = 0$ (only mass transfer without reaction) and $f_s = 1$ (with the same reaction rate of case D2 shown in section 5.3.1) deviate, and results of the other scaling factors are distributed near these two curves. The mean concentration of $f_s = 0.01$ is close to the result without reaction, $f_s = 0$. Although the results for $f_s = 0.01$ is already distinguished from the result for $f_s = 0$, this order of reaction rate is still too small as compared to the mass transfer rate for this case. The result for $f_s = 0.1$ is placed a little more apart from the mean concentration without reaction and closer toward the results with original reaction rate $f_s = 1$. Even with the high value of $f_s$ ($f_s = 100$), the result still remains near the result for $f_s = 1$. The series of results indicates that the reaction employed in this study is faster than the mass transfer rate because the overall mean concentration is not much increasing with higher scaling factor. The value of the reaction rate with $f_s = 0.1$ may be in the same order of magnitude of mass transfer rate as the results with scaling factor between $f_s = 0.1$ and 1 show distinct variation. Similar trends of mean concentration are observed in the pre-saturated condition; the results with $f_s \leq 0.1$ are in the vicinity of the equilibrium concentration, while the result for $f_s = 100$ is close to the result for $f_s = 1$.

The difference among the results with different $f_s$ is more clearly shown in the comparison of mass transfer coefficient. Fig. 5.18 (b) compares the mass transfer coefficients of liquid mean concentration with different values of $f_s$. As shown in the mean concentration behaviors in Fig. 5.18 (a), the mass transfer coefficient of $f_s = 0.01$ is placed near the case without reaction $(f_s = 0)$. The result for $f_s = 0.1$ is, however, more clearly distinguished from the results for $f_s = 0$ and 1 as compared to Fig. 5.18 (a). The result for $f_s = 100$ deviates slightly from the curve for $f_s = 1$. From the comparison of both mean concentration and mass transfer coefficient profiles, it is concluded that there is a mass transfer limit where the mass transfer coefficient is not further decreasing even with very high reaction rate. In other words, with mass transfer limit the mass transfer is not significantly enhanced even if the reaction rate is much higher than the mass transfer rate.

## 5.4 Detailed reaction mechanism

Though the coupled solver aims at simulating a two-phase flow with detailed kinetic mechanism, the subroutines embedded from DETCHEM$^{TM}$ are actually not utilized in the previous examples due to the absence of detailed reaction mechanism for hydrogenation of nitrobenzene (NB) to aniline (AN). Demonstration of successful coupling requires a proper example that covers both mass transfer within two-phase flow and reaction with detailed reaction mechanism. For this purpose, the hydrogenation of NB is modeled by a detailed reaction mechanism based on the study of density functional theory [151] (See Appendix H). With the own adapted reaction mechanism, this section introduces a qualitative analysis of reactive mass

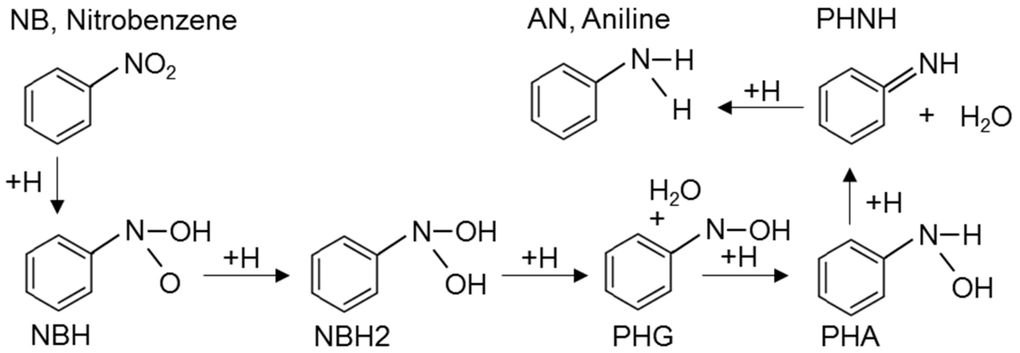

Fig. 5.19: Reaction path from NB to AN on the bimetallic catalyst of platinum and palladium (mechanism B of Zhang et al. [151]).

transfer within a Taylor flow.

The elementary reaction steps of hydrogenation of NB are shown in Fig. 5.19. Density functional theory comes up with activation energies of each reaction step. The pre-exponential factor $A$ is obtained with an assumption of transition state theory. Since the reaction mechanism was developed for the bimetallic catalyst of platinum and palladium [151], the results obtained with this mechanism cannot be directly compared with other results computed with global reaction mechanisms in section 3.6. This is the reason why this detailed reaction mechanism is only employed for qualitative analysis. In this section, the qualitative behaviors of bulk and surface species are mainly focused within a Taylor flow. As a preliminary study, the generated reaction mechanism is tested with an example of continuously stirred tank reactor (CSTR). In the sequel, two types of mass transfer calculation (with pure NB and initially saturated NB) are performed again as for the previous test cases.

## 5.4.1 Reaction in zero-dimensional problem (CSTR)

Before using the generated reaction mechanism for Taylor flow, it is firstly tested in a continuously stirred-tank reactor (CSTR) which is one of the example reactors in DETCHEM$^{\text{TM}}$. The pressure for this calculation is $0.4\,\text{MPa}$, and the reactor volume and catalytic surface area are set to 1 $\text{m}^3$ and 1 $\text{m}^2$, respectively. The temperature is initially given as $400\,\text{K}$, since the

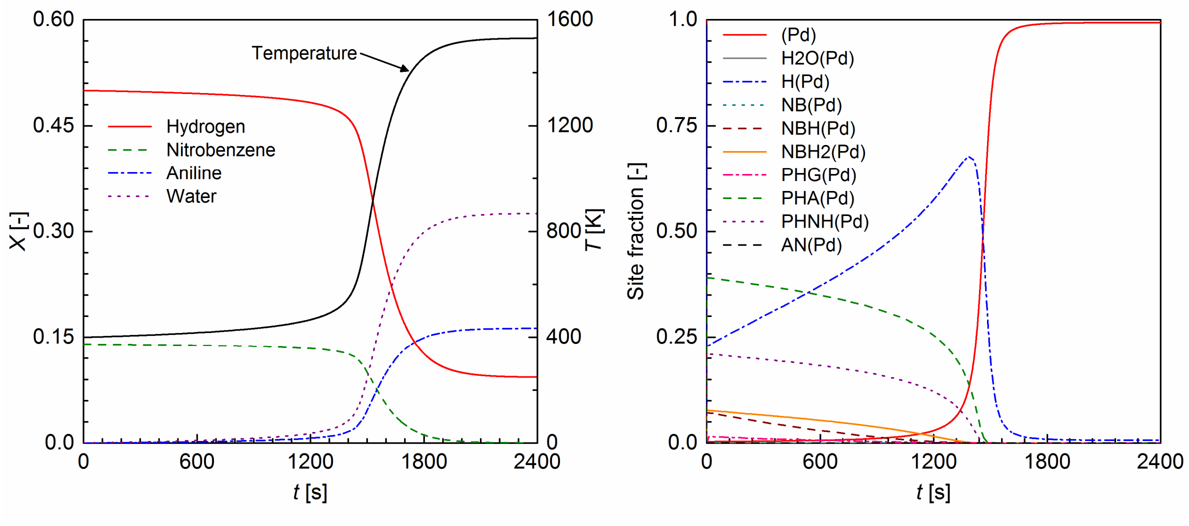

(a) (b)

Fig. 5.20: The result of CSTR calculation with detailed reaction mechanism. Temperature and mole fractions of bulk species (a) and site fractions of surface species (b).

minimum valid temperature for the mechanism is $400\,\mathrm{K}$. Initial mole fractions of nitrobenzene and hydrogen are 0.14 and 0.5, respectively. Nitrogen is used as an inert species. Surface sites are initially not occupied by any surface species so that the site fraction of palladium (Pd)=1. With these conditions, CSTR solver computes the zero-dimensional mass and energy balances in order to obtain the time evolution of species and temperature during the reaction process [30]. Thermodynamic properties for the species utilized in this reaction mechanism are estimated by the set of polynomial coefficients from Burcat and Ruscic [11].

The results of this preliminary example are given in Fig. 5.20. In the beginning of reaction, temperature and species change very slowly until $1400\,\mathrm{s}$ due to the low reaction rate in the low temperature region. At $1400\,\mathrm{s}$, temperature increases drastically and the consumption and production are accelerated, accordingly. After exhaustion of nitrobenzene reaction near $1900\,\mathrm{s}$, temperature and mole fraction of species are not changing anymore due to the absence of reactants. At the solid surface, hydrogen and intermediate species such as PHA(Pd), PHNH(Pd), NBH2(Pd), NBH(Pd) appear before $1400\,\mathrm{s}$ when reactions actively occur. After $1400\,\mathrm{s}$, almost all surface sites are returned to (Pd) again.

## 5.4.2 Detailed mechanism with pure nitrobenzene

After the test of reaction mechanism in CSTR, it is applied to one of the test cases with Taylor flow in order to analyze qualitative behaviors of bulk and surface species. As described in the previous section, the reaction mechanism is only valid for $T \geq 400\,\mathrm{K}$. However, most of the required physical properties are unknown for $400\,\mathrm{K}$. If the properties are known at $400\,\mathrm{K}$, this temperature is too low to activate the reaction as shown in Fig. 5.20. Therefore, in the present study focusing on the qualitative analysis, physical properties are estimated at $323\,\mathrm{K}$ as written in section 5.1, while the reaction temperature is separately set to $1500\,\mathrm{K}$ which is close to the light-off condition in Fig. 5.20. Since this reaction mechanism is not validated, applying $1500\,\mathrm{K}$ for reaction temperature is similar to the use of a fitting parameter $f_s$ in section 0 to scale the reaction rate. With this assumption, the flow field for this calculation can be chosen by one of the hydrodynamic results obtained with the physical properties at $323\,\mathrm{K}$ (shown in section 0). Hence, case D2 in section 5.3.1 is used as a basic flow field for this section as usual for the other sections. $F_{\mathrm{cat/geo}}$ which represents the specific surface area is set to unity. To analyze the local behavior of site fractions around a Taylor bubble, surface site density is specified as

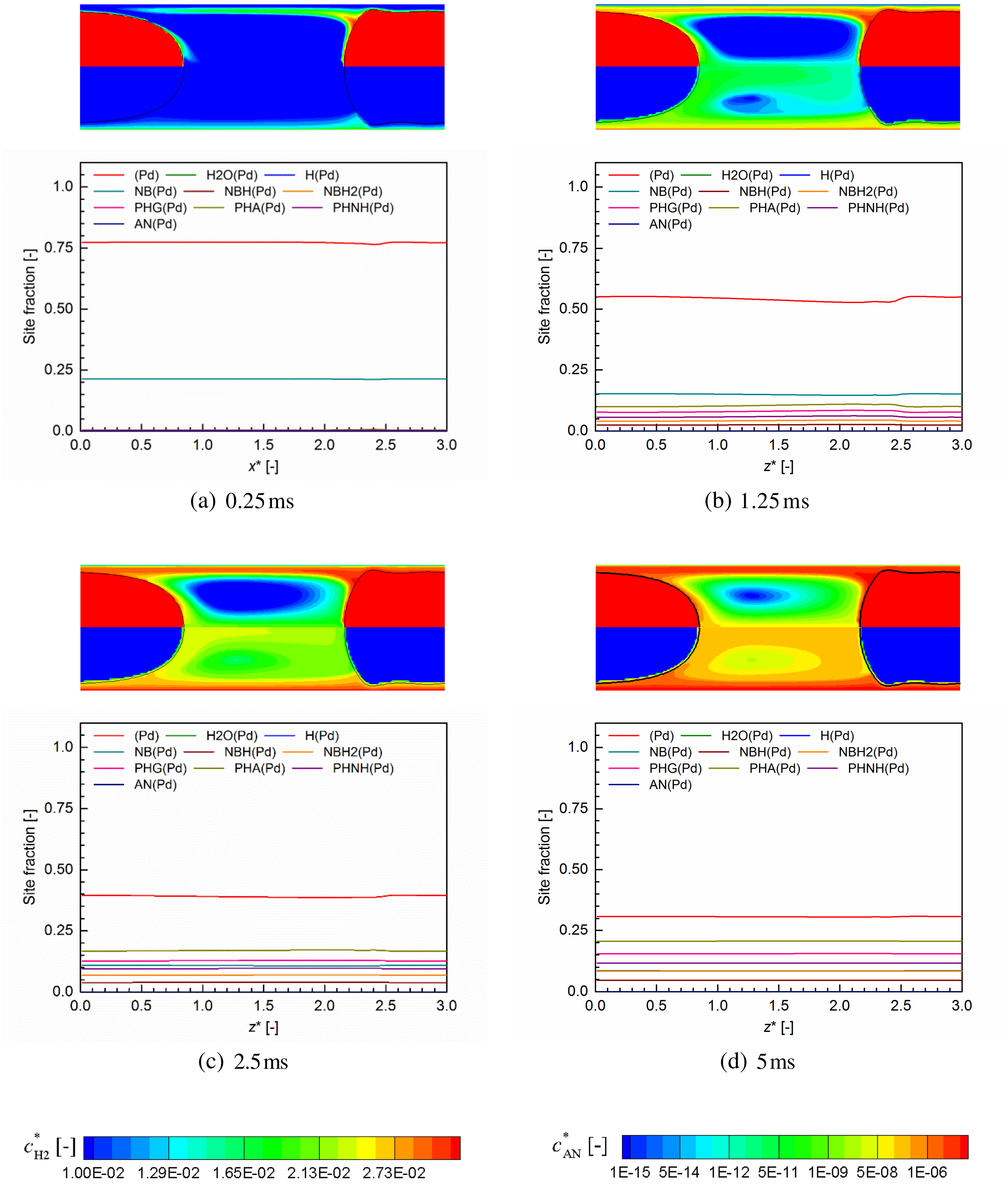

(a) 0.25 ms

(b) 1.25 ms

(c) 2.5 ms

(d) 5 ms

Upper half of channel

Lower half of channel

Fig. 5.21: Distributions of bulk species and site fractions of surface species at four different time instants (0.25, 1.25, 2.5, 5 ms). Results of mass transfer of hydrogen into pure nitrobenzene by detailed kinetic mechanism.

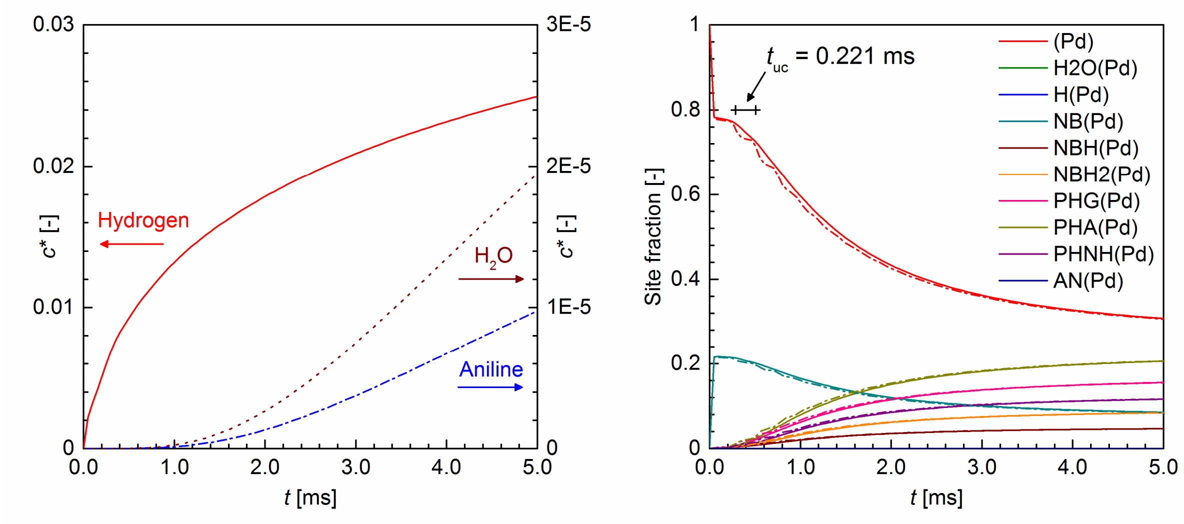

(a) (b)

Fig. 5.22: Time evolutions of bulk species (a) and coverage fraction of surface species (b) for the case starting with pure NB. (Solid line: average site fraction, dashed line: local site fraction at $x^* = 1.74$).

$1.55\times10^{-9}$ mol/m$^2$, which is four orders of magnitude smaller than the real value of the catalytic substrate.

Fig. 5.21 shows the results of reactive mass transfer in pure nitrobenzene. The results contain not only the distributions of bulk species but also the surface species profiles at the catalyzed wall, which is one of the advantages of using detailed reaction mechanism. The identical behaviors of bulk species are observed as for the case with global kinetic mechanism shown in section 5.3. High concentration gradient occurs in liquid film region due to the consumption and production of the species, while the species between bubbles circulates by convective mass transfer. Although $H_2O$ concentration is not given, it shows very similar behavior to the aniline concentration shown in Fig. 5.21. Meanwhile, surface species behave in accordance with the bulk species distributions. In the beginning of calculation, surface site is free of species as given by the initial condition. The site is, however, immediately occupied by approximately 20% of NB(Pd) as a result of inner iterations in DETCHEM$^{TM}$ library. As reaction takes place, surface species are gradually filled in surface sites. In the results at $0.25\,\text{ms}$, only (Pd) and NB(Pd) are observed, and the site fractions of the other intermediate species are almost zero. At $1.25\,\text{ms}$, intermediate species appear and those sitefractions are in the same order of NB(Pd) site fraction. The results show that there are axial variations of surface species profiles along $x$ axis. The magnitude of these variations is gradually decreasing over time. At the end of this calculation ($5\,\text{ms}$), site fractions of surface species are almost approaching to certain uniform values in the entire surface sites. During the computation, site fraction of Pd and NB are decreasing by time, while site fractions of AN and other intermediate species are increasing.

Fig. 5.22 displays temporal evolutions of bulk species in liquid phase and site fractions of surface species at the reactive wall. Similar to the concentration profile obtained with global reaction mechanism shown in Fig. 5.12, the concentration of hydrogen is increasing by mass transfer from gas bubble into liquid phase, and the concentration of AN and water species increase as products of the reaction. In this case, mean concentration of $H_2O$ is also displayed because the $H_2O$ production rate is determined by a couple of reaction steps, while it is exactly double of AN production rate in global kinetic mechanism. Fig. 5.22 (a) shows that the amount of produced water is almost double of AN, which complies with the stoichiometry of reaction. Fig. 5.22 (b) shows the time evolution of mean site fractions of surface species. As for the local distributions shown in Fig. 5.21, (Pd) and NB(Pd) mainly appear at the beginning of reaction, and the site fractions of those species decrease by reaction. However, the other species including intermediate species increase. In addition to the mean site fraction, the local site fractions are also displayed in Fig. 5.22. The time evolution of site fractions are measured at $x^* = 1.74$, an axial position near the rear part of bubble where the reaction is most active. The axial variation at the beginning of calculation causes a deviation between local and mean site fractions. Nevertheless, those curves are quite similar.

An interesting point is that there are oscillating patterns of local surface species at the beginning of computation. This is caused by the use of periodic boundary condition. With periodic condition, one assumes that identical bubbles are periodically placed at the front and back of the computational domain despite only one bubble being of interest for the calculation. When hydrogen is transferred from this bubble to liquid phase, it remains in the liquid film region and meets the next following bubble. In moving reference frame, it looks like the transferred species moves backward direction. This occurs identically at the front bubble. When the hydrogen transferred from the front bubble meets the bubble of interest, the concentration at the liquid film jumps with the amount of transferred species from the front bubble. This multi-bubble effect causes the oscillation of the local surface species in Fig. 5.22 (b). It turns out that the oscillating period is almost identical to the bubble breakthrough time in the unit cell, $t_{\mathrm{uc}} = u_{\mathrm{B}} / L_{\mathrm{axial}}$ which represents the required time for the bubble to travel the axial length of domain. The value of $t_{\mathrm{uc}}$ for this case is $0.221\,\mathrm{ms}$. With this breakthrough time, the bubble passes 22.6 times of the length of unit cell during this computation. Finally, the oscillation smears by time, since hydrogen is saturated in the liquid film region.

### 5.4.3 Detailed mechanism with pre-saturated nitrobenzene

Next, the mass transfer calculation with pre-saturated NB is performed with detailed reaction mechanism as well. $F_{\mathrm{cat/geo}}$ and surface site density are identically set as the pure NB case in section 0. In the results with pure NB shown in Fig. 5.21, the axial differences of surface species are decreasing, and finally, site fractions become almost uniform by the saturation of hydrogen in liquid phase. Since this is the case with pre-saturated NB where hydrogen is initially saturated, almost no axial differences of species concentration are observed. Only the overall amounts of surface species are changing as reaction takes place. Thus, local distributions of surface species are not given in this case, but only temporal evolution of bulk and surface species are shown in Fig. 5.23 (a). The time evolution of mean concentration is similar to the results with global mechanism shown in Fig. 5.14. The mean concentration of hydrogen in liquid phase decreases because the initially distributed hydrogen is consumed by the reaction. The concentration of aniline and water increases as products of the reaction. The mean hydrogen concentration declines very slowly. The slope of its curve which represents the consumption rate of hydrogen by reaction seems to be almost constant. Pre-saturation of hydrogen leads to more

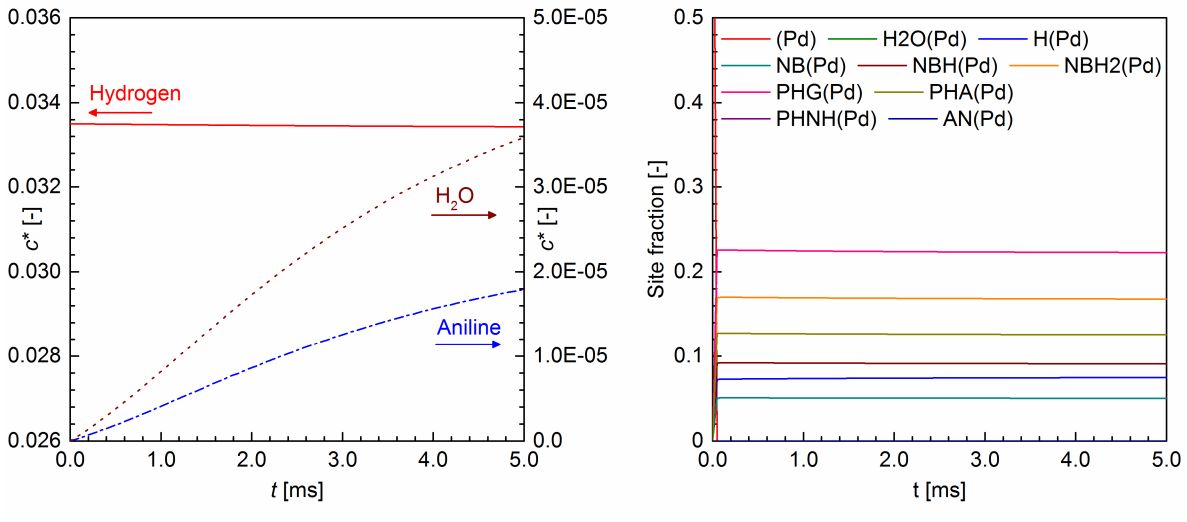

(a) (b)

Fig. 5.23: Time evolutions of bulk species (a) and site fractions of surface species (b) for the case with pre-saturated NB.

production of AN and $H_2O$ as compared to the case without pre-saturation in the previous section.

The time evolutions of mean surface species are also shown in Fig. 5.23 (b). The site fractions are almost not changed by time. The site fraction of (Pd) and NB(Pd) is almost zero and only intermediate species present at the surface during this calculation. In CSTR result shown in Fig. 5.20 (b), the intermediate species H(Pd) is highest when the reaction is most active. Due to the initially given hydrogen, the reaction actively takes place in this case, which may result in the presence and slight increase of H(Pd). It is also found out that surface sites are almost in equilibrium when the bulk species are in an equilibrium condition.

From the series of results computed with the detailed kinetic mechanism, it turns out that the detailed reaction mechanism is able to predict the qualitative aspects of consumption and production of the bulk and surface species. These results also allow investigation of intermediate surface species behaviors during the reaction. Although the reaction mechanism is not validated and the test conditions are not physically consistent due to the lack of the information of physical properties, this qualitative study explores the distributions of bulk and surface species for the catalytic hydrogenation of NB within a Taylor flow by means of the detailed reaction mechanism.

# Chapter 6

# Influence of liquid composition on mass transfer in liquid film

Despite moving reference frame reducing computational time, numerical simulations shown in previous chapters still cannot cover the whole hydrogenation process of nitrobenzene due to the large time scale according to the very long residence time. Also, nitrobenzene is transformed to aniline and water during the reaction process. Therefore, corresponding liquid properties depending on the liquid composition are affected by the reaction as well. However, the variable liquid property cannot be considered in the current coupled solver which assumes constant properties during the calculation. To take into account the influence of different liquid properties on mass transfer, a simplified numerical approach is, thus, chosen in this section.

Fig. 6.1 explains the one-dimensional model for mass transfer within the liquid film of a Taylor flow. Since the wall-normal velocity is almost zero in the liquid film, diffusive mass transfer predominates as presented in the previous section. The one-dimensional diffusion model is, therefore, proper to simplify the mass transport phenomena therein. The simplified model then assumes that the species from the gas bubble is transferred to the wall through the liquid film by diffusive mass transfer. The species distributions may relate to the position, time and the

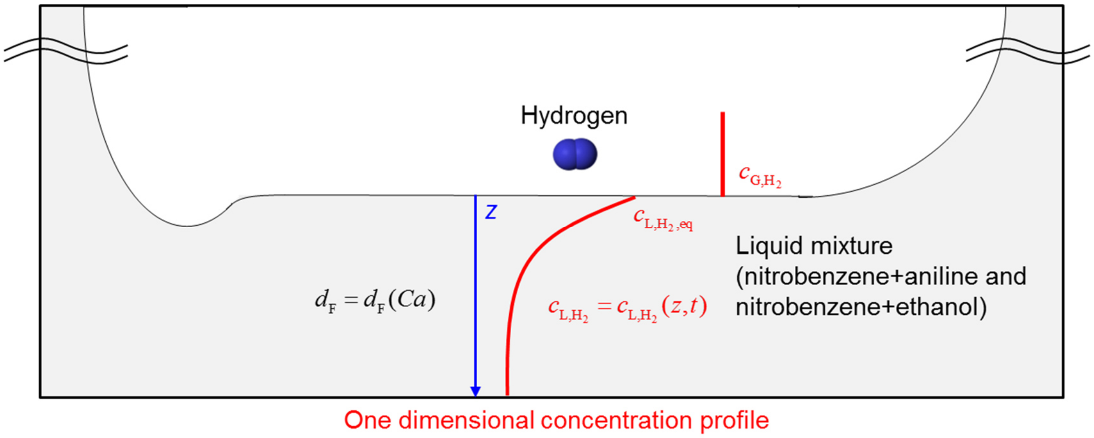
Hydrogen
$c_{G,H_2}$
$z$
$c_{L,H_2,eq}$
Liquid mixture (nitrobenzene+aniline and nitrobenzene+ethanol)
$d_F = d_F(Ca)$
$c_{L,H_2} = c_{L,H_2}(z,t)$
One dimensional concentration profile

Fig. 6.1: Conceptual diagram for simplified one-dimensional model for analyzing diffusive mass transfer in the liquid film with respect to the liquid composition.

diffusion length which corresponds to the film thickness as a function of capillary number in the present study.

With nitrobenzene, two potential constituents of liquid mixture in the hydrogenation of nitrobenzene are chosen; the first one is aniline as a product of the reaction, and the second one is ethanol as a usual solvent for the hydrogenation process [135]. Water is not considered in this study in order to avoid considering ternary mixture whose liquid properties are hard to estimate. Thus, nitrobenzene + aniline and nitrobenzene + ethanol mixtures are chosen for the example of mass transfer with changing liquid properties. Physical properties of those liquid mixtures are investigated in Section 6.1. Despite the normal operating temperature being 90~200°C [73], the temperature considered in this study is 303.13K because of the lack of physical properties in high temperature. With these properties, one-dimensional model estimates the diffusion in the liquid film concerning the liquid composition. Section 0 analyzes the results of diffusive mass transfer for the cases with fixed and variable capillary number. Finally, the findings come up with a relation between bubble length and saturation of liquid film, which can advise choosing the appropriate bubble length for mass transfer around a Taylor bubble.

## 6.1 Physical properties in binary liquid mixture

As described in Section 5.1, there are many well-known theories (i.e., ideal gas law, kinetic theory) for estimation of gas-phase physical properties, while the liquid-phase properties cannot be intuitively estimated. This applies to the estimation of liquid mixture as well, so that measured data or empirical correlations are also necessary to estimate the liquid mixture properties. Based on the pure liquid properties found in Section 5.1, the properties (density, viscosity, diffusivity, solubility and surface tension) of nitrobenzene + aniline and nitrobenzene + ethanol mixtures are investigated in the following subsections.

### 6.1.1 Density and viscosity of liquid mixture

The equation of state is not only essential for the properties of pure component but also for the mixture properties because they depend not only on the temperature, volume and pressure but also on the mixture composition. Ideal gas law is applicable to estimate the density of the gas mixture, but additional equation of state requires even for pure liquid. In ideal gas assumption, the total volume of gas phase mixture is always assumed to be constant during the mixing process, whereas there is no correlation of total volume of liquid mixture which is a variable according to the liquid composition. Poling et al. [115] summarized a number of studies about the estimations of mixture densities, but the author mentioned that there is no rigorous method to describe the interaction of different mixture components. Therefore, the estimation of the density of liquid mixtures still relies highly on empirical correlations.

Similarly, the viscosity of the gas mixture can be described straightforwardly by a linear function of gas composition, while the estimation of the liquid mixture viscosity requires a complex relationship especially for the liquids containing alcohol or water. Moreover, the liquid viscosity is sensitive to the molecular structures. Small association of molecules can significantly change the liquid viscosity [115]. In Irving [68], a lot of classical methods for the viscosity of liquid mixture are reported with various empirical parameters. Recently, UNIFAC-VISCO is known as a predictive and widely used method for many binary liquid mixtures and even for certain ternary and quaternary systems [17]. Despite UNIFAC VISCO being known as a powerful method, it is only recommendable in the absence of measured data [115]. In the present study, the density and viscosity of liquid mixture are therefore investigated with experimental data given from the literature.

Govindan et al. [42] conducted an experimental study for the binary mixture of nitrobenzene and certain aromatic bases, and provided polynomial coefficients for estimation of mixture density and viscosity. They measured the excess molar volume (for density) and excess viscosity which are defined as

$$V^{\mathrm{E}} = V_{\mathrm{m,\,real}} - V_{\mathrm{m,\,ideal}} \tag{6.1}$$

$$\mu^{\mathrm{E}} = \mu_{\mathrm{m,\,real}} - \mu_{\mathrm{m,\,ideal}} \tag{6.2}$$

where the excess value means the difference between measured (real) and molar averaged (ideal)

Table 20: Polynomial parameters to estimate the excess molar volume and excess viscosity of nitrobenzene + aniline and nitrobenzene + ethanol mixtures at 303.15K.

| Mixture | $\phi$ | $a_0$ | $a_1$ | $a_2$ | $a_3$ | $a_4$ |
|---|---|---|---|---|---|---|
| Nitrobenzene + aniline [42] | $V$ | 0.821 | -0.874 | 1.89 | 2.621 | -1.998 |
| | $\mu$ | -1.863 | 0.538 | -0.214 | 1.465 | -0.112 |
| Nitrobenzene + ethanol [109] | $V$ | -2.594 | 3.966 | 2.718 | -2.728 | |
| | $\mu$ | -0.687 | -0.19 | -0.511 | 0.284 | |

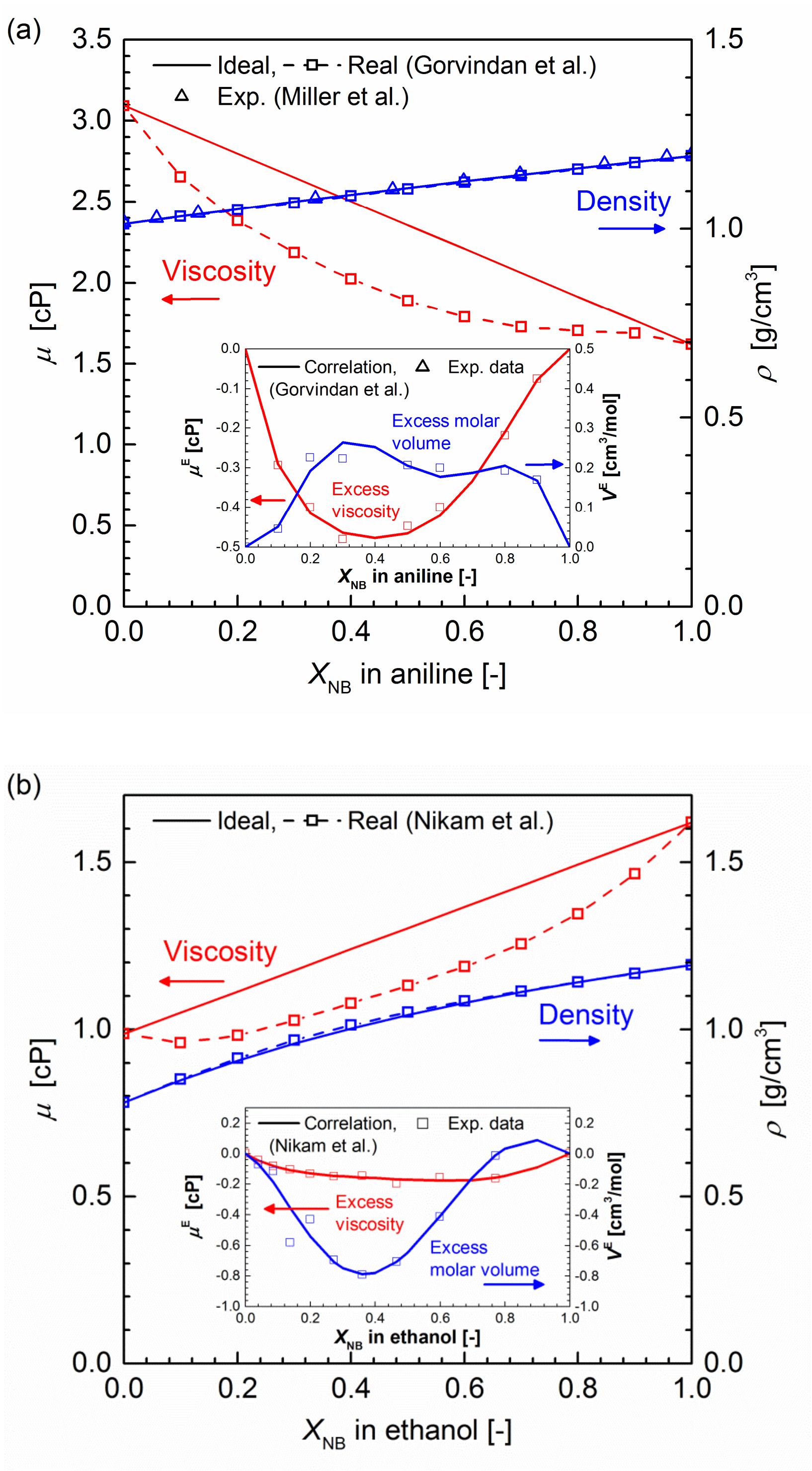

Fig. 6.2: Density and viscosity of nitrobenzene + aniline mixture (a) and nitrobenzene + ethanol mixture (b) by correlation and experimental data at 303.15K ([42, 105] for nitrobenzene + aniline and [109] for nitrobenzene + ethanol). Inset: Excess viscosity and molar volume.

values. The molar averaged quantity $\phi_{\mathrm{m,\ ideal}}$ ($\phi = V, \mu, \cdots$) is defined by

$$\phi_{\mathrm{m,\ ideal}} = \sum_i x_i \phi_i \tag{6.3}$$

For binary mixture of constituent 1 and 2, the excess parameters are given by the Redlich-Kister polynomial equation as

$$\phi^{\mathrm{E}} = X_1 X_2 \sum_{i=0}^{n} a_i \left( X_1 - X_2 \right)^i \tag{6.4}$$

where $a_i$ is a parameter for the polynomial which are given in Table 20 for nitrobenzene + aniline [42] (with $n = 4$) and nitrobenzene + ethanol [109] (with $n = 3$) mixtures. With the excess values in Eq. (6.4), the real values of density and viscosity can be obtained by Eq. (6.1) and (6.2).

Fig. 6.2 shows the density and viscosity of nitrobenzene + aniline and nitrobenzene + ethanol mixtures as a function of nitrobenzene mole fraction. Also, the excess viscosity and excess molar volume estimated by a correlation in Eq. (6.4) are compared with given experimental values ([42] for nitrobenzene + aniline and [109] for nitrobenzene + ethanol). For nitrobenzene + aniline mixture, the experimental data given by [105] are in good agreement with the estimated density. In Fig. 6.2 (a), the molar averaged properties (ideal) show almost linear relationship between the values of pure liquids (at $X_{\mathrm{NB}}$=0 and 1). Values of the excess molar volume are in order of 0.1 cm$^3$/mol where the molar volumes of pure liquid shown in Table 15 are three orders of magnitude higher. Due to the relatively small excess molar volume, the real density is almost the same as the molar averaged density and there is almost no influence of excess molar volume to the mixture density. However, the real viscosity obviously differs from the ideal viscosity for both mixtures. The excess viscosity is one order of magnitude smaller than the viscosity of pure components, which causes the large deviation between real viscosity and molar averaged (ideal) viscosity. Due to this excess viscosity effect, the viscosities of two liquid mixture show non-linear behavior against the liquid composition.

## 6.1.2 Diffusivity of hydrogen in liquid mixture

In the present section, multicomponent model and effective diffusivity model are revisited for estimating the diffusivity of hydrogen in liquid mixture. In Section 3.2, these two

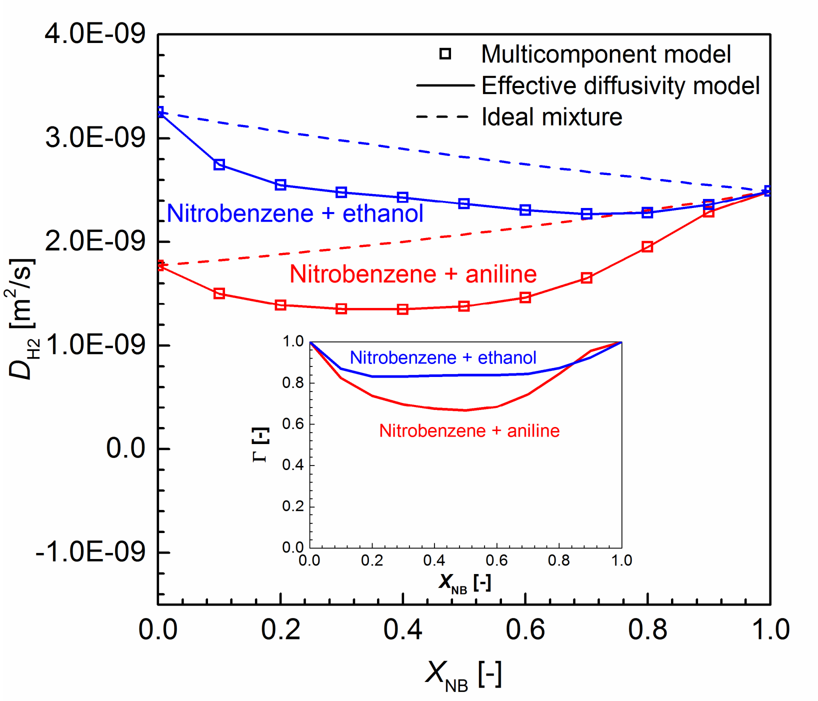

Fig. 6.3: Diffusivity of hydrogen in nitrobenzene + aniline and nitrobenzene + ethanol mixtures estimated by multicomponent model and effective diffusivity model for ideal and non-ideal fluid at 303.15K (inset: distribution of thermodynamic factor for those solutions with respect to composition).

diffusion models are studied only for the ideal fluid wherein only binary collisions take place. For ideal fluid, species profiles obtained by both models are almost the same, since the diffusivities in those models are virtually identical. However, ideal fluid assumption is not valid for the liquid where three (or more) molecule collisions occur sufficiently frequently in liquids and dense gases and contribute to the momentum transfer process. [132]. Therefore, both diffusion models consider the effect of non-ideal effect for the liquid mixture diffusivities in this section. In Eq. (2.37), $\mathbb{G}$ represents the thermodynamic factor which accounts for the non-ideal behavior. The hydrogen concentration in liquid phase is very small as compared to the other liquid species, and its influence on diffusion models is turned out to be negligible. Therefore, the hydrogen concentration in liquid phase is not considered for the estimation of thermodynamic factor for liquid mixtures. Without hydrogen, the ternary mixture in liquid phase can be regarded as a binary mixture, and then the matrix of thermodynamic factor $\mathbb{G}$ is simplified to a scalar $\Gamma$, which can be obtained by regular solution theory [132] as

$$\Gamma = 1 - 2\frac{\Delta G^{\mathrm{E}}}{RT} \tag{6.5}$$

where Gibb's excess energy for flow $\Delta G^{\mathrm{E}}$ is defined in [42] as

$$\Delta G^{\mathrm{E}} = \Delta G_{\mathrm{m}} - \left( X_1 \Delta G_1 + X_2 \Delta G_2 \right) \tag{6.6}$$

In Govindan et al. [42], the experimental values of $\Delta G^{\mathrm{E}}$ and those polynomial correlations are provided in terms of temperature so that $\Delta G^{\mathrm{E}}$ in this study is directly obtained from their correlations. For estimation of liquid mixture diffusivity, multicomponent model utilizes then the diffusivity defined in Eq. (2.37) with thermodynamic factor in Eq. (6.5). Also, effective diffusivity model for non-ideal fluid, Eq. (2.38), is rewritten with thermodynamic factor as

$$D_{i,\mathrm{eff}} = \Gamma \frac{1 - X_i}{\sum\limits_{\substack{j=1 \\ j \neq i}}^{n} \frac{X_j}{Đ_{ij}}} \tag{6.7}$$

Fig. 6.3 compares the diffusivities of hydrogen in nitrobenzene + aniline and nitrobenzene + ethanol mixtures estimated by two diffusion models. Also, the scalar thermodynamic factors Γ for those mixtures are given in the inset of the figure. The Γ curves show concave shapes due to the existence of Gibb's excess energy regarding the non-ideal effect, while Γ for ideal fluid is unity. With this thermodynamic factor, the diffusivities are also distributed concavely with respect to the mixture composition, while the mixture diffusivity of ideal mixture is linearly distributed between the two diffusivities of pure components. In addition, both diffusion models predict almost the identical diffusivities of hydrogen in the two liquid mixtures as for the ideal fluid in Section 5.1.2, since the scalar thermodynamic factor is just multiplied to the composition-dependent diffusivities for both models shown in Section 5.1.2.

## 6.1.3 Solubility of hydrogen in liquid mixture

The solubility of hydrogen in liquid mixtures (nitrobenzene + aniline and nitrobenzene + ethanol) can be obtained by two correlations provided by Prausnitz et al. [117] and Hildebrand et al. [60]. Prausnitz et al. [117] suggested a correlation of solubility for liquid mixture based on regular solution theory as

$$-\ln x_{\mathrm{G,m}} = \ln \left( \frac{f_{\mathrm{G}}^{\mathrm{L}}}{f_{\mathrm{G}}} \right) + V_{\mathrm{G}} \frac{\left( \bar{\delta}_{\mathrm{L}} - \bar{\delta}_{\mathrm{G}} \right)^2}{RT} \tag{6.8}$$

where the parameters are identically used as for the pure liquids described in Section 5.1.3. Additionally, the mean solubility parameters for gas and liquid, $\bar{\delta}_{\mathrm{L}}$ and $\bar{\delta}_{\mathrm{G}}$ are defined by

$$\bar{\delta}_l = \sum_{i=1}^{n} \phi_i \delta_{l,i}\,, \quad \bar{\delta}_g = \sum_{i=1}^{n} \phi_i \delta_{g,i} \tag{6.9}$$

and the volume fraction of liquid is

$$\phi_i = \frac{X_{\mathrm{L},i} V_{\mathrm{L},i}}{\sum_{j=1}^{n} X_{\mathrm{L},j} V_{\mathrm{L},j}} \tag{6.10}$$

Another correlation of solubility for liquid mixture proposed by Hildebrand et al. [60] has the form:

$$\ln X_{\mathrm{G,m}} = \phi_1 \ln X_{\mathrm{G},1} + \phi_2 \ln X_{\mathrm{G},2} - V_{\mathrm{G}} \beta_{12} \phi_1 \phi_2 \tag{6.11}$$

where

$$\beta_{12} = \frac{\left(\delta_{\mathrm{L},1} - \delta_{\mathrm{L},2}\right)^2}{RT} \tag{6.12}$$

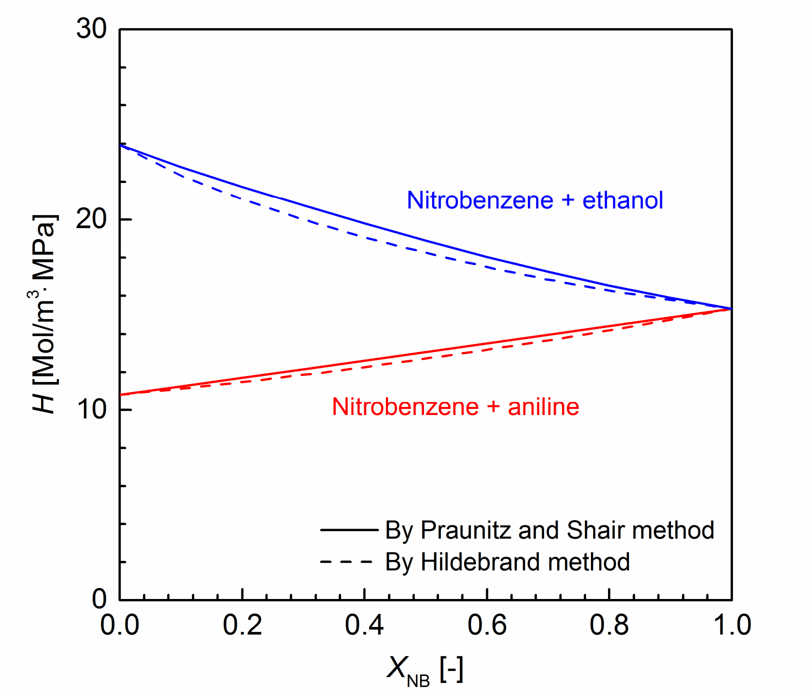

Fig. 6.4: Henry coefficient of hydrogen in the mixture of nitrobenzene + aniline and nitrobenzene + ethanol at 303.15K and 0.7 MPa by two correlations ([117] and [60]).

With the solubility and the required parameters for the pure liquids, the solubility of hydrogen for liquid mixtures is estimated by both Eq. (6.8) and Eq. (6.11). Fig. 6.4 shows the estimated solubility of hydrogen in the mixture of nitrobenzene + aniline and nitrobenzene + ethanol. Since the experimental data of the solubility of hydrogen in those liquid mixtures are not available, the estimated solubility values cannot be validated with measured data. Thus, Fig. 6.4 only compares the solubility values from two correlations. It is shown that the results of both correlations show almost the same behaviors against the changing liquid composition. Solubility changes almost linearly between the solubility values for two pure liquids (at $X_{\mathrm{NB}} = 0$ and $X_{\mathrm{NB}} = 1$). Although the difference between Henry coefficients from two correlation is very small, Hildebrand model tends to predict better results for the mixture consisting of nitrobenzene and methanol, where the percent error of Hildebrand method against the experimental data is slightly lower than that of Prausnitz method [119]. Therefore, the Hildebrand correlation is chosen for estimating solubility in liquid mixtures in this chapter.

### 6.1.4 Surface tension of liquid mixture

Surface tension plays a crucial role to determine the shape of the bubble in the gas-liquid two-phase flow. Estimating surface tension of liquid mixture is also complex as for the other liquid mixture properties introduced in former sections. Several theoretical approaches have been provided in the literature, but there has been no rigorous model for the surface tension of liquid mixture as well. Even if a model exists, it is still unclear to define the model parameters such as activity coefficient [128]. For the mixture of nitrobenzene and aniline, surface tensions of both constituents are, fortunately, almost identical as shown in Fig. 5.5. Then, the surface tension of those mixtures can be easily assumed identical and independent on the liquid composition. However, the surface tension of nitrobenzene at room temperature and pressure ($0.043\,\mathrm{N/m}$ [140]) is evidently different from that of ethanol ($0.022\,\mathrm{N/m}$ [1]) Therefore, a model is required to estimate the surface tension of nitrobenzene + ethanol mixture.

Two well-known models suggested by Hildebrand et al. [61] and Hoar et al. [63] are employed for estimation of mixture surface tensions in this section. Based on the assumption that both liquid and surface layer form ideal solution, the correlation by Hildebrand [61] is

$$\sigma = X_1\sigma_1 + X_2\sigma_2 - \left(\frac{A}{2RT}\right)(\sigma_1 - \sigma_2)^2 X_1 X_2 \tag{6.13}$$

where $A$ is the surface occupancy of molecules, which can be approximated by $A_1 \cong A_2 \cong (A_1 + A_2)/2 = A$. The surface occupancy of specie $i$, $A_i$ used in Eq. (6.13) is given by Hoar ad Melford [63] as

$$A_i = V_i^{2/3} N^{1/3} \tag{6.14}$$

where $N$ denotes Avogadro number.

Another approach provided by Hoar and Melford [63] is based on the regular solution:

$$\begin{aligned} \sigma &= \sigma_1 + \frac{RT}{A_1} \ln \frac{X_1'}{X_1} + \frac{W}{A_1}\left(l' X_2'^2 - X_2^2\right) \\ &= \sigma_2 + \frac{RT}{A_2} \ln \frac{X_2'}{X_2} + \frac{W}{A_2}\left(l' X_1'^2 - X_1^2\right) \end{aligned} \tag{6.15}$$

where $X_1'$ and $X_2'$ are mole fractions in the surface monolayer. Since this method deals with the binary mixture, $X_2$ is determined by 1-$X_1$ ($X_2' = 1 - X_1'$ as well). $l'$ is the model parameter in the range between 0.5 and 0.75, and $W = \Delta H_\mathrm{m} / (X_1 X_2)$. In order to obtain the value of $W$, the enthalpy of mixing $\Delta H_\mathrm{m}$, which represents the increase of enthalpy by addition of $X_1$ moles of liquid 1 to $X_2$ moles of liquid 2, is still required. The value of $\Delta H_\mathrm{m}$ can be estimated by Suri

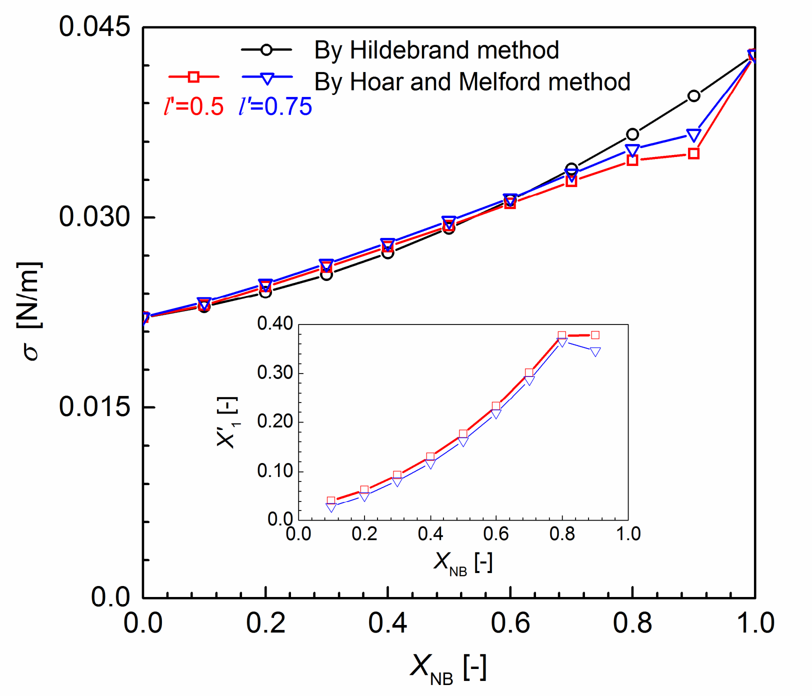

Fig. 6.5: Surface tension of nitrobenzene + ethanol mixture at 303.15K. Comparison of Hildebrand method [61] and Hoar and Melford method [63]. Inset: $X_1'$ for Hoar and Melfort method.

and Ramakrishna [128] from solubility parameter as

$$\Delta H_{\mathrm{m}} \cong \left(\delta_{\mathrm{L},1} - \delta_{\mathrm{L},2}\right)^2 V_{\mathrm{G}} \tag{6.16}$$

With these parameters, the surface tension of liquid mixture is iteratively computed by the estimation of $X_1'$ and $X_2'$. In each liquid composition $X_1$ and $X_2$, the upper and lower parts of the Eq. (6.15) are obtained with given $X_1'$ and $X_2'$. These $X_1'$ and $X_2'$ are iteratively approximated until the two parts of Eq. (6.15) match within 0.01% relative error.

As for the diffusivity estimation process in the previous section, experimental data of surface tensions for these mixtures are not available. Therefore, only the estimated values from two models are compared in Fig. 6.5. Fig. 6.5 shows that surface tension of nitrobenzene + ethanol mixture is monotonically increasing from surface tension of pure ethanol. Here, two different values of $l'$, 0.5 and 0.75, are considered for the Hoar and Melford equation. The estimated surface tension with two parameters are almost identical, and the results with $l'$=0.75 are slightly higher than those with $l'$=0.5. Surface tensions obtained by Hoar and Melford method are also close to the estimated surface tension by Hildebrand method in a wide range of composition. However, the values from two methods deviate where $X_{\mathrm{NB}}$ is higher than 0.8. Suri and Ramakrishna [128] reported that for most mixtures containing nitrobenzene Hoar and Melford model is recommendable with $l'$=0.5 and $W$ estimated by solubility parameter. However, the estimated surface tension by Hoar and Melford model does not show continuous behavior against liquid composition where $X_{\mathrm{NB}}$ is higher than 0.8 in Fig. 6.5, which does not look physically reasonable. These appear in both estimations with $l'$=0.5 and 0.75. As shown in the inset of Fig. 6.5, this strange behaviors are also observed in $X_1'$ which is the approximated parameter to estimate the surface tension in Hoar and Melford model. These erroneous results are probably caused by the misuse of model parameters for this mixture due to the lack of the information in the literature. Thus, Hildebrand method is employed for the further investigations.

## 6.2 Mass transfer rate of hydrogen in liquid film

As discussed in Section 5.3, for mass transfer within a Taylor flow the diffusive mass transfer in the liquid film plays an important role to control the overall reaction characteristics. Since flow direction in liquid film is mostly perpendicular to the wall-normal direction, the convective mass transfer in wall-normal direction is almost negligible in the liquid film region. Mass transfer in liquid film is, therefore, represented as a diffusive mass transfer where diffusivity and length of diffusion path are the key parameters to govern the mass transfer phenomena therein. According to the composition-dependent solubility in the liquid mixture, equilibrium concentrations change with respect to the liquid composition as well. Therefore, the diffusivity, film thickness and solubility, which depend on the liquid composition due to the reaction progress, are chosen as model parameters for the simplified one-dimensional model described in Fig. 6.1. With mixture properties obtained in Section 6.1, the mass transfer of hydrogen in nitrobenzene + aniline and nitrobenzene + ethanol Taylor flows can be investigated by the simplified model. By reducing dimensions of Eq. (2.15), the one-dimensional diffusion equation forms:

$$\frac{\partial c}{\partial t} = -\frac{\partial}{\partial z} J^V \tag{6.17}$$

In order to investigate the realistic diffusion time, the dimensional form of the equation is employed with real physical properties obtained in the previous section, while detailed numerical solutions in previous the chapters use non-dimensional configuration. The length of

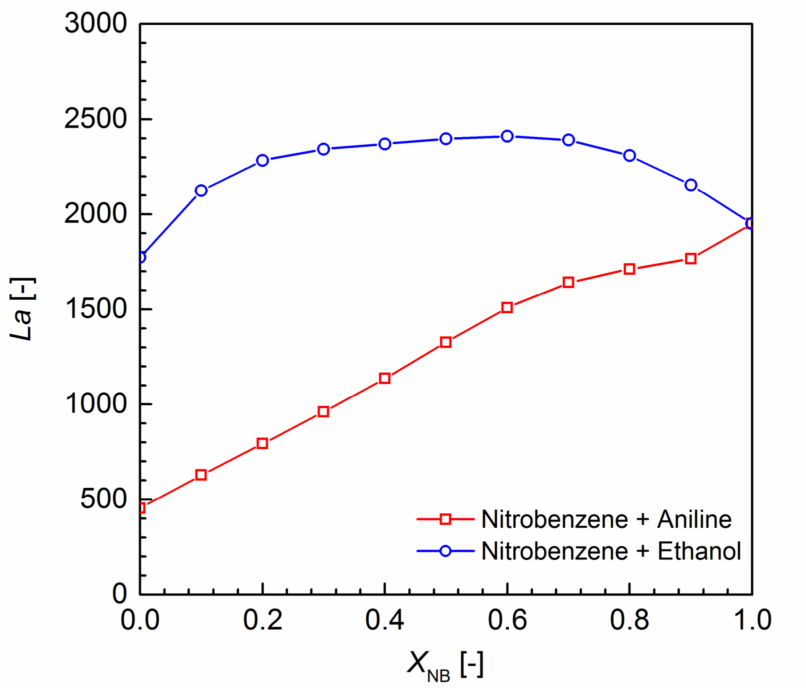

Fig. 6.6: Laplace number of nitrobenzene + aniline and nitrobenzene + ethanol mixtures with respect to changing liquid composition ( $L_{ref} = 100\,\mu\text{m}$ ).

computational domain is determined by the film thickness. The number of discretization nodes is 41, and the cell size is uniform. The diffusion of hydrogen is calculated with the fixed liquid composition for each calculation since the overall reaction is very slow as compared to the hydrogen mass transfer, which does not significantly affect the liquid composition during the calculation. In this calculation, $c_{\mathrm{G,H2}}$ which represents the hydrogen concentration in the gas bubble is kept constant during the calculation. Therefore, constant equilibrium concentration can be applied to the boundary condition at the interface. At phase interface ($z = 0$), equilibrium concentration is, therefore, set to a Dirichlet type boundary condition as $c_{\mathrm{G,H2}} H_{\mathrm{H2}}$. The value of $c_{\mathrm{G,H2}}$ ($380\,\mathrm{mol/m^3}$ at $303.15\,\mathrm{K}$) is specified to the total concentration, $c_{\mathrm{t}}$. Since surface reactions are not considered in this study, boundary conditions at the solid wall ($z = d_{\mathrm{f}}$, film thickness) are zero gradient ($\partial c / \partial z = 0$) corresponding to no reactive flux.

As discussed in section 4.1, Reynolds and capillary numbers are the major parameters to determine the hydrodynamic behaviors of Taylor flow. Combination of these two dimensionless numbers comes up with Laplace number which relates viscous forces to inertial and surface tension forces ($La := Re / Ca = \sigma \rho_{\mathrm{L}} L_{\mathrm{ref}} / \mu_{\mathrm{L}}^2$). The reference length is set to the channel height used in the Taylor flow calculations in the previous chapter ($L_{\mathrm{ref}} = h = 100\,\mathrm{\mu m}$). As shown in Fig. 6.6, Laplace number is clearly varied with respect to the liquid composition in two liquid mixtures. This difference Laplace number causes different mass transfer behaviors in the liquid film because liquid properties depend on Laplace number as well. In the following sections, the mass transfer in liquid film region is taken into account in two points of view according to these two dimensionless numbers, namely, fixed capillary number and variable capillary number. Once capillary number is fixed, Reynolds number can be obtained by the relation of Laplace number. After calculation, diffusive mass transfer in two liquid mixtures is analyzed with regard to the liquid composition.

## 6.2.1 Fixed capillary number (*Ca*=0.01)

Capillary number given in Eq. (4.1) is one of the most important dimensionless numbers for the gas-liquid flow in micro fluidic applications. From the definition, this number relates to the surface tension and liquid viscosity, and accounts for the shape of the bubble for gas-liquid Taylor flow. As described in Eq. (4.2), the film thickness of Taylor flow can be estimated by a correlation of capillary number. Fixed capillary number considered in this section results in the

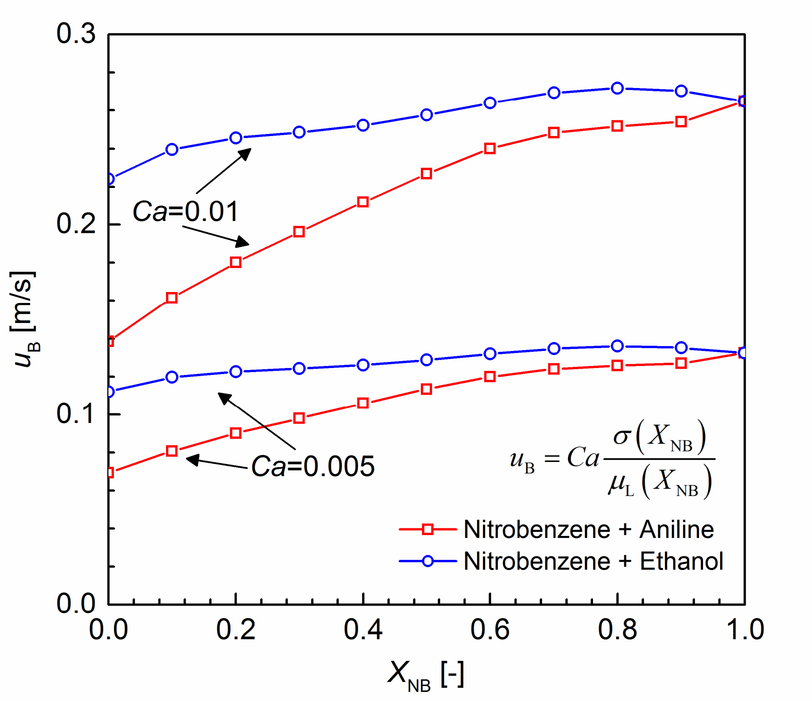

Fig. 6.7: Bubble velocity of nitrobenzene + aniline and nitrobenzene + ethanol mixtures for *Ca* = 0.01 and 0.005 with respect to the liquid composition.

fixed thickness of liquid film where hydrogen undergoes diffusive mass transfer toward the wall. With fixed capillary number, the one-dimensional diffusion is therefore calculated within a fixed distance so that the distance of diffusion path is always identical and independent on the liquid composition. Capillary number is specified to 0.01, and the corresponding film thickness is $3.21\mu\text{m}$ with the channel height of $100\mu\text{m}$. With constant capillary number, bubble velocity $u_B$ is also a variable of liquid composition as the composition-dependent viscosity and surface tension shown in Section 6.1 vary against the composition.

Fig. 6.7 plots the estimated bubble velocity with respect to the mole fraction of nitrobenzene in two mixtures. For mixture of nitrobenzene + aniline, the bubble velocity is monotonically increasing as nitrobenzene mole fraction, while for nitrobenzene + ethanol mixture it increases until $X_{NB} = 0.8$ and decreases again. For half capillary number of this case (*Ca*=0.005), the same trends of velocity appear with half velocity magnitude. The bubble velocity of nitrobenzene + ethanol mixture is turned out to be higher than that of nitrobenzene + aniline mixture. Thus, different combination of mixture can control the bubble velocity with fixed capillary number or vice versa. Moreover, the film thickness is changeable by conversion of nitrobenzene to aniline so that the bubble velocity can be a control parameter to keep the constant film thickness during the reaction process. However, this variation of bubble velocity

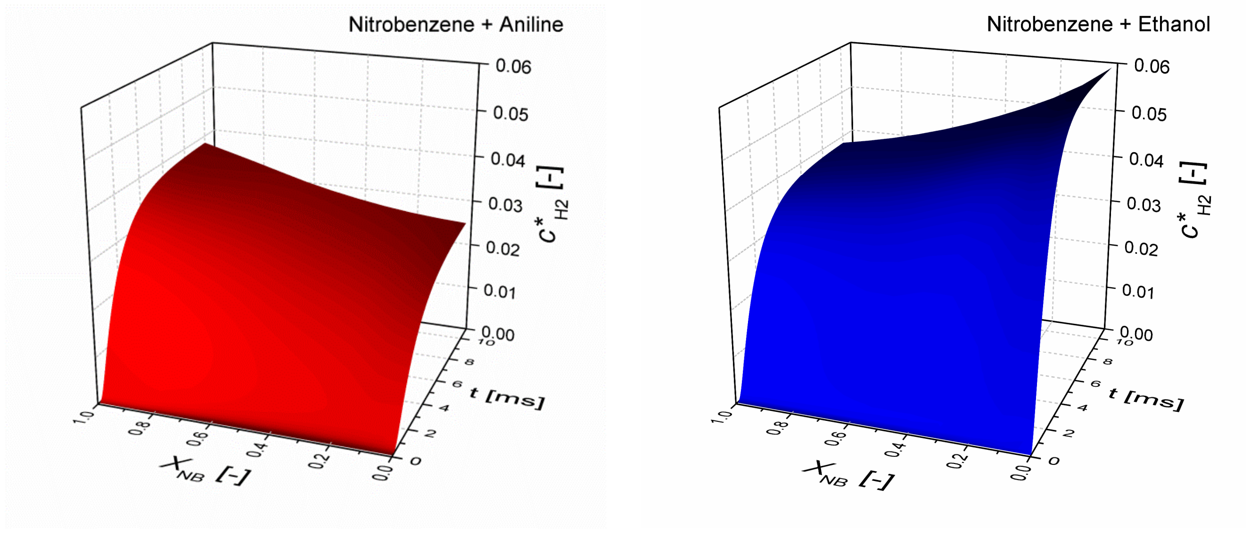

(a) (b)

Fig. 6.8: Time evolution of hydrogen wall concentration ($c^* = c/c_{G,H2}$) for nitrobenzene + aniline (a) and nitrobenzene + ethanol (b) mixtures with respect to the liquid composition (*Ca*=0.01).

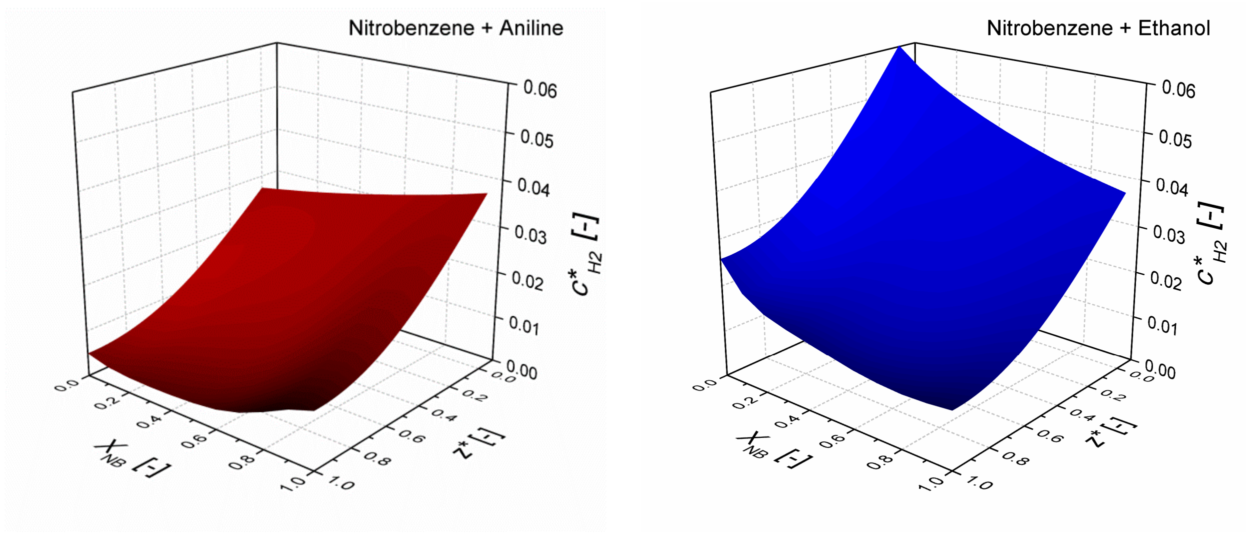

(a) (b)

Fig. 6.9: Instantaneous hydrogen concentration profiles($c^* = c/c_{G,H2}$) along the distance ($z^* = z/d_F$) at 1ms (*Ca*=0.01) as a function of nitrobenzene mole fraction for the mixture of (a) nitrobenzene + aniline and (b) nitrobenzene + ethanol.

does not directly affect the mass transfer due to its orthogonal direction against the wall-normal diffusion.

From the computation results, temporal and spatial behaviors are firstly analyzed with respect to the liquid composition. The main parameters to govern the diffusion rate are the equilibrium concentration and diffusivity since the distance of diffusion is fixed due to the

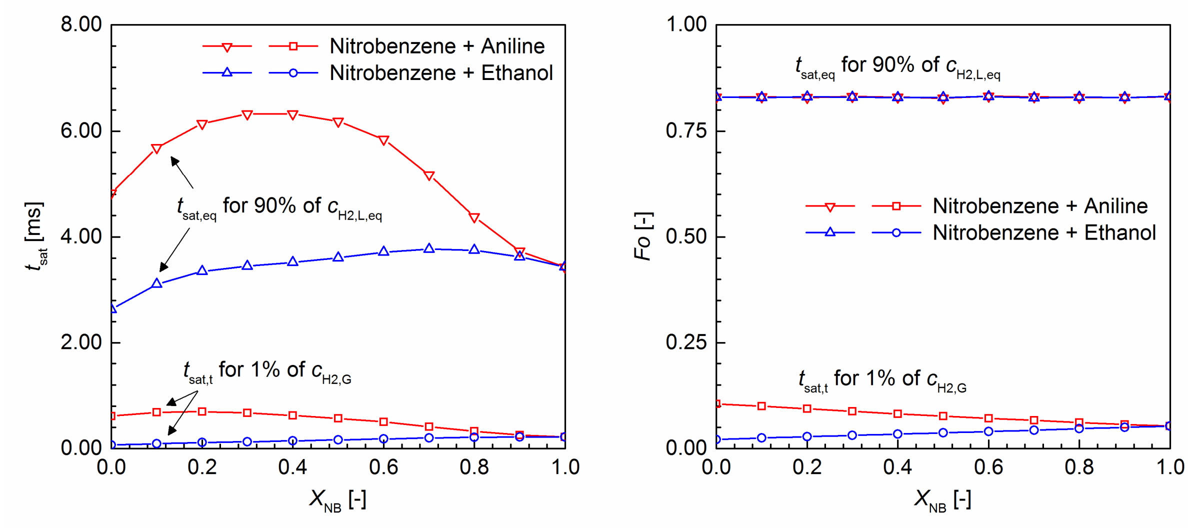

(a) (b)

Fig. 6.10: Hydrogen saturation time for 90% of liquid equilibrium concentration and 1% of gas concentration (a) and corresponding Fourier numbers (b) for the test case with $Ca$=0.01.

constant capillary number. Fig. 6.8 (a) and (b) show the values of wall concentration regarding time and composition. In concentration surfaces of both mixtures, the wall concentration is initially zero and increasing as diffusion takes place. Finally, the values reach to the equilibrium concentrations of each composition. Fig. 6.9 shows the distribution of concentration along the wall-normal coordinate after $1\,\mathrm{ms}$. The concentration at $z^*$=0 is the equilibrium concentration as given by boundary conditions, while the concentration at $z^*$=1 is the wall concentration at the time instant. Here, it is shown that the shape of concentration at a time instant is similar to the shape of the composition-dependent mixture diffusivity shown in Fig. 6.3. This illustratesthat the diffusivity mostly governs the species distributions in this cases, and the influences of the other parameters are minor (e.g. equilibrium concentration).

The saturation times for two mixtures are compared in Fig. 6.10 (a) to analyze the effect of mixture composition on the extent of diffused species. The saturation time accounts for the required time until hydrogen concentration in liquid film reaches to a certain percent of saturation. Here, two saturation times are considered; the saturation time for 90% of equilibrium concentration $t_{\mathrm{sat,eq}}$ and 1% of total hydrogen concentration $t_{\mathrm{sat,t}}$. These values are obtained by

$$\int_0^{d_{\mathrm{F}}} c(t_{\mathrm{sat,eq}})\,\mathrm{d}z = 0.9c_{\mathrm{L,H2,eq}} \tag{6.18}$$

$$\int_0^{d_{\mathrm{F}}} c(t_{\mathrm{sat,t}})\,\mathrm{d}z = 0.01c_{\mathrm{G,H2}} \tag{6.19}$$

The saturation times clearly show the influence of the liquid composition on diffusive mass transfer. The saturation time of 90% equilibrium concentration, $t_{\mathrm{sat,eq}}$ takes only into account the influence of mixture diffusivity since it is relative diffusion time with the composition-dependent equilibrium concentration. For nitrobenzene + aniline mixture, $t_{\mathrm{sat,eq}}$ of mixtures are higher than those for the pure liquids ($X_{\mathrm{NB}}$=0 and 1) in a wide range of composition (0.1<$X_{\mathrm{NB}}$<0.7). The increase of $t_{\mathrm{sat,eq}}$ in mixture is observed in nitrobenzene + ethanol mixture as well. The remarkable point is that the shapes of $t_{\mathrm{sat,eq}}$ profiles for both mixtures are similar to the inversed shape of the diffusivity profiles of respective mixtures shown in Fig. 6.3. This proves that diffusivity is the only factor that influences the saturation time in this case. In contrary, the saturation time for 1% total concentration $t_{\mathrm{sat,t}}$ shows different shape because it contains the influence of composition-dependent equilibrium concentration.

The profiles for both saturation times show a similar tendency for nitrobenzene + aniline mixture. However, the gradient of the curve for $t_{\mathrm{sat,t}}$ is lower as compared to $t_{\mathrm{sat,eq}}$. This decrease of the gradient is caused by increasing solubility as $X_{\mathrm{NB}}$ increases. For nitrobenzene + ethanol mixture, $t_{\mathrm{sat,t}}$ is almost monotonically increasing, while $t_{\mathrm{sat,eq}}$ shows convex shape against mixture composition. This retarding behavior of $t_{\mathrm{sat,t}}$ is also affected by solubility. The decrease of solubility by increasing $X_{\mathrm{NB}}$ results in a remarkable delay of mass transfer in nitrobenzene + ethanol mixture. Fig. 6.10 (b) shows Fourier number for mass transfer defined as

$$Fo := \frac{D_{\mathrm{L,H2}} t_{\mathrm{sat}}}{d_{\mathrm{F}}^2} \tag{6.20}$$

where $D_{\mathrm{L,H2}}$ is the diffusivity of hydrogen in the liquid mixture. For $t_{\mathrm{sat,eq}}$ (saturation time for 90% of liquid equilibrium concentration), Fourier number is almost constant against the liquid composition of both mixtures. In principle, Fourier number is a non-dimensional characteristic time that represents a timescale for dimensionless concentration diffusing into a dimensionless length scale.

In normalized concentration field, the concentration at $t_{\mathrm{sat,eq}}$ is always identical because the normalized $t_{\mathrm{sat,eq}}$ is unity. Since $t_{\mathrm{sat,eq}}$ in Fig. 6.10 (a) forms a function of the inverse of diffusivity, the effect of variable diffusivity is canceled out in the numerator of Eq. (6.20). Therefore, Fourier number $t_{\mathrm{sat,eq}}$ with constant capillary number is independent of the liquid composition. However, Fourier number for $t_{\mathrm{sat,t}}$ (saturation time for 1% of total concentration) is not constant with changing composition, because the results of $t_{\mathrm{sat,t}}$ cannot be identically normalized by the composition-dependent equilibrium concentration. The profile of Fourier number is similar to the inverse of solubility profile against the liquid composition. This investigation turns out that both Fourier numbers does not contain the information of composition-dependent diffusivity and can be used to analyze the mass transfer for liquid mixture excluding the effect of variable diffusivity.

## 6.2.2 Variable capillary number

This section describes the diffusive mass transfer in the liquid film with variable capillary number. Capillary number and Reynolds number are related to Laplace number as shown in Fig. 6.6. In this section, Reynolds number is fixed as 100 for variable capillary number. Bubble velocity is also a variable of composition in case of variable capillary number. Furthermore, film thickness is changed by the composition as well so that the diffusion path is now changeable with respect to the liquid composition. Fig. 6.11 shows the bubble velocity and film thickness of two mixtures for *Re*=100. With composition-dependent density and viscosity, the bubble velocity can be estimated for given Reynolds number. The film thickness is estimated by Halpern and Gaver relationship Eq. (4.2) with variable capillary number. The estimated bubble velocity and film thickness show similar behaviors for both mixtures against the liquid composition because these two parameters are obtained by a respective function of capillary

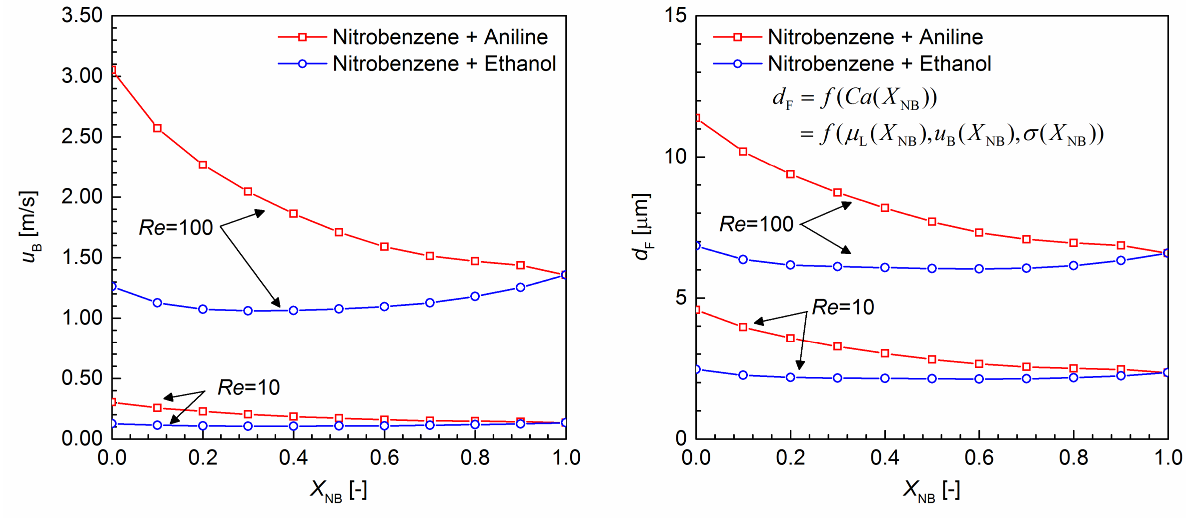

(a) (b)

Fig. 6.11: Bubble velocity (a) and film thickness (b) as a function of nitrobenzene mole fraction for nitrobenzene + aniline and nitrobenzene + ethanol mixtures with variable capillary number ($L_{\text{ref}} = 100\,\mu\text{m}$).

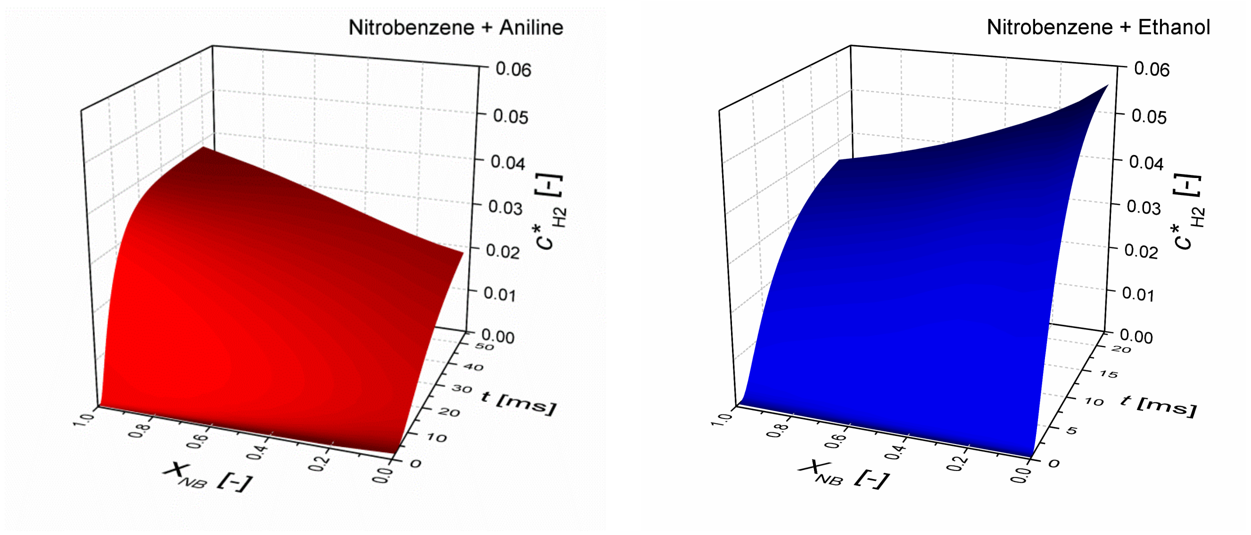

(a) (b)

Fig. 6.12: Time evolution of hydrogen wall concentration ( $c^* = c/c_{G,H2}$ ) for nitrobenzene + aniline (a) and nitrobenzene + ethanol (b) mixtures with respect to the liquid composition (*Re*=100).

number. In this section, the simplified one-dimensional model considers, therefore, variable distances for diffusion depending on the mixture composition. Thus, the film thickness is also a governing parameter for the calculation with variable capillary number in addition to the equilibrium concentration and mixture diffusivity.

Fig. 6.12 shows results of the simplified model for variable capillary number. Generally, the results are similar to those of fixed capillary number, but this case requires more time for diffusion due to the larger film thickness than previous cases ( $d_F = 3.21 \mu m$ for $Ca = 0.01$ ). Fig. 6.12 (a) presents the faster decrease of wall hydrogen concentration by increasing $X_{NB}$ as compared to that of fixed capillary number in Fig. 6.9 (a), because the film thickness, in this case, becomes longer by increasing $X_{NB}$ . However, in Fig. 6.12 (b) the shape of concentration contour is almost the same as Fig. 6.9 (b), because the film thickness of nitrobenzene + ethanol mixture shows minimal change in liquid composition.

To analyze the results of variable capillary number, Fig. 6.13 (a) compares the two saturation times as for the previous section. For both mixtures, the saturation times are monotonically changing by liquid composition. In nitrobenzene + aniline mixture, the saturation time for 90% of equilibrium concentration $t_{sat,eq}$ is mainly governed by the film thickness due to the large deviation of film thickness. However, for nitrobenzene + ethanol mixture $t_{sat,eq}$ is

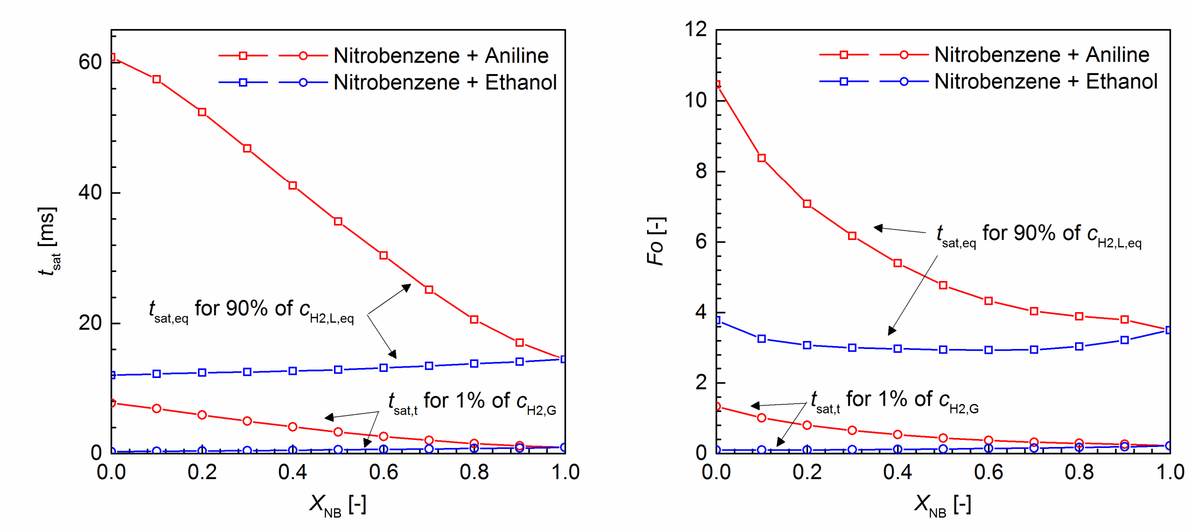

(a) (b)

Fig. 6.13: Hydrogen saturation time for 90% of liquid equilibrium concentration and 1% of gas concentration (a) and corresponding Fourier numbers (b) for the test case with variable capillary number (*Re*=100).

influenced by the combination of mixture diffusivity and variable film thickness. In the curves of 1% of total concentration $t_{sat,t}$ , the gradients of both results are smaller and much linear as compared to $t_{sat,eq}$ . This difference is caused by the influence of the composition-dependent solubility.

Fig. 6.13 (b) shows Fourier number for variable capillary number case. Variable film thickness in both mixtures clearly affects the Fourier number for $t_{sat,eq}$ (90% of equilibrium concentration). Since it is obtained by the relative saturation time of equilibrium concentration, the influence of solubility is immanently excluded. The influence of diffusivity is also not included in Fourier number of relative saturation time as discussed in the previous section. On the other hand, Fourier number for $t_{sat,t}$ (1% of total concentration) shows the combined effect of mixture solubility and film thickness.

From the investigation of mass transfer in liquid mixtures, it is concluded that the mixture properties in terms of liquid composition are a prerequisite for prediction of mass transfer in the liquid mixture. The estimation of diffusion in liquid mixture requires a complex function of the composition-dependent mixture properties. The delay of diffusion caused by the non-ideality effect in liquid mixture leads to another limitation factor which further retards the overall rate of surface reaction. Another interesting point is that the effect of three major factors can be distinguished by different estimation method. The influences of diffusivity, solubility and film thickness are observed in the $t_{sat,eq}$ , Fourier number for $t_{sat,t}$ and Fourier number for $t_{sat,eq}$ , respectively. These parameters can be useful for investigation of mass transfer characteristics in the liquid mixture.

### 6.2.3 Estimation of a favorable bubble length

The analysis of saturation time allows investigation of the relevant bubble length required for a certain percent of saturation in case of different liquid composition. Taylor and Krishna [132] explains the exposure time that the fluid element resides at the interface where mass exchange takes place with the adjoining phase by process of unsteady-state. For a rising bubble, the exposure time is defined by bubble traveling distance divided by bubble velocity. Similarly, the film exposure time $t_{\mathrm{F,ex}}$ is introduced as follow:

$$t_{\mathrm{F,ex}} = L_{\mathrm{B}} / u_{\mathrm{B}} \tag{6.21}$$

where the film length is assumed the same as the bubble length $L_{\mathrm{B,ex}}$ . Thus, $t_{\mathrm{F,ex}}$ represents the time that the film region is exposed for mass transfer while a single bubble travels the length of a bubble. Fig. 6.14 explains the definition of film exposure time of a single Taylor bubble passing through the monitor point.

This section is devoted to the investigation of $t_{\mathrm{F,ex}}$ in liquid mixture to come up with a relation between bubble length and mass transfer. To estimate the film exposure time required for a certain level of saturation, the film exposure time is set equal to the aforementioned saturation time as

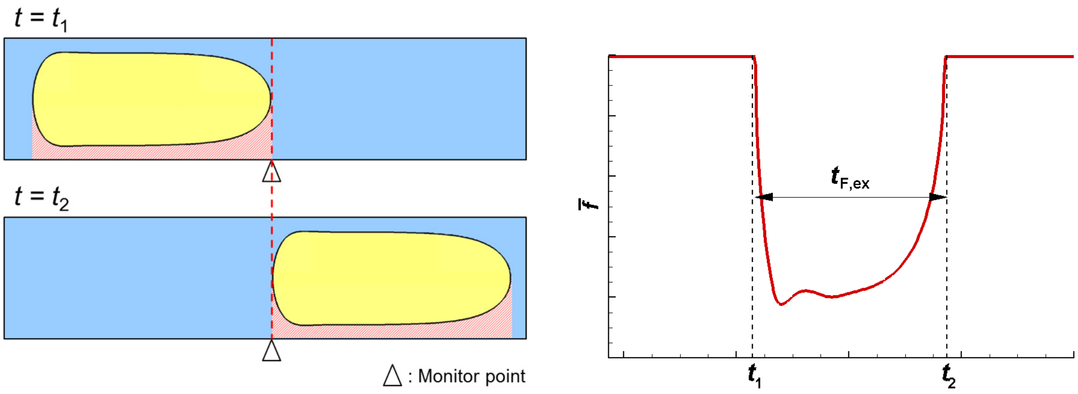

Fig. 6.14: Definition of film exposure time of Taylor flow. Left: a Taylor bubble passing through the monitor point. Right: estimation of film exposure time from the time evolution of mean volume fraction at the monitor point.

$$t_{\mathrm{F,ex}} = t_{\mathrm{sat}} \tag{6.22}$$

Then, the corresponding bubble length which is the minimum required length for such saturationlevel is obtained by Eq. (6.21), which relates to the saturation time and bubble velocity. To generalize this equation, the Eq. (6.21) is substituted by a combination of dimensionless numbers:

$$\frac{L_{\mathrm{B,sat}}}{L_{\mathrm{ref}}} = Fo \cdot Sc \cdot La \cdot Ca \frac{d_{\mathrm{F}}^2}{L_{\mathrm{ref}}^2} \tag{6.23}$$

where $Fo := D_{\mathrm{L}} t_{\mathrm{sat}} / d_{\mathrm{F}}^2$, $Sc := \mu_{\mathrm{L}} / (\rho_{\mathrm{L}} D_{\mathrm{L}})$, $La := \sigma \rho_{\mathrm{L}} L_{\mathrm{ref}} / \mu_{\mathrm{L}}^2$, $Ca := \mu_{\mathrm{L}} u_{\mathrm{B}} / \sigma$ and $L_{\mathrm{ref}}$ represents here the channel height. With the correlation of film thickness shown in Eq. (4.2), the Eq. (6.23) is further substituted with capillary number as

$$\frac{L_{\mathrm{B,sat}}}{L_{\mathrm{ref}}} = 0.0435 Fo \cdot Sc \cdot La \cdot Ca \cdot (1 - \exp(-1.67 Ca^{0.5025}))^2 \tag{6.24}$$

Finally, the non-dimensional bubble length is derived by a combination of dimensionless numbers. Schmidt number purely depends on the liquid properties. Fourier number relates to the diffusion and saturation time within the liquid film so that Fourier number is varying with different extent of saturation. With fixed fluid properties, Laplace number depends on the reference length, while capillary number is a function of bubble velocity.

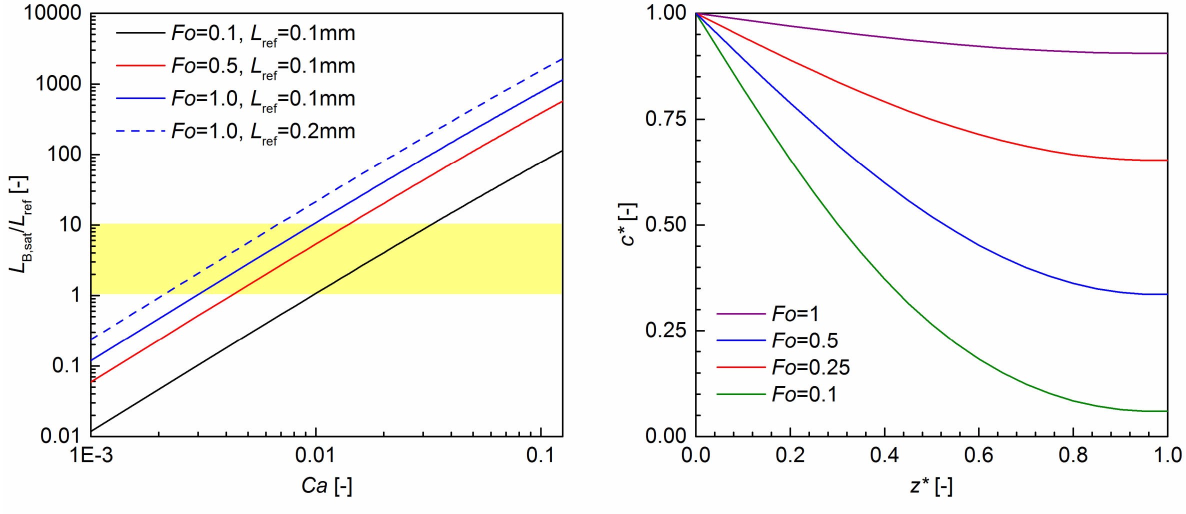

(a) (b)

Fig. 6.15: (a) The non-dimensional bubble length $L_{\mathrm{B,sat}}/L_{\mathrm{ref}}$ as a function of capillary number with different combination of dimensionless numbers ( $Sc = 545$ ) (b) distributions of non-dimensional concentration with respect to the Fourier number.

Fig. 6.15 (a) shows the variation of non-dimensional bubble length for saturation with different Fourier number ( $Fo = 0.1$, 0.5 and 1), reference length ( $L_{\mathrm{ref}} = 100\,\mu\mathrm{m}$ and $200\,\mu\mathrm{m}$ ), and fixed Schmidt number ( $Sc = 545$ ). The results illustrate that higher capillary number requires longer Taylor bubble to reach the same level of saturation by mass transfer. As shown in Eq. (6.23), $L_{\mathrm{B,sat}}/L_{\mathrm{ref}}$ is proportional to the square of film thickness which is also a function of capillary number in Eq. (6.24). Therefore, higher capillary number results in thicker liquid film and it causes a dramatic increase of $L_{\mathrm{B,sat}}$. Since capillary number depends on the bubble velocity, it also represents that increasing bubble velocity leads to a sharp increase of $L_{\mathrm{B,sat}}$. Fig. 6.15 also shows that $L_{\mathrm{B,sat}}$ increases linearly as either Fourier number or Laplace number increases, because $L_{\mathrm{B,sat}}$ in Eq. (6.24) has a linear relation against both $Fo$ and $La$, which corresponds to the degree of saturation and the length scale of the system, respectively. High value of $L_{\mathrm{B,sat}}/L_{\mathrm{ref}}$, for example, $L_{\mathrm{B,sat}}/L_{\mathrm{ref}} = 100$ which requires 100 times longer bubble than the channel height, is not suitable for the real application. The realistic condition is approximately $1 < L_{\mathrm{B,sat}}/L_{\mathrm{ref}} < 10$ (emphasized by yellow shading in Fig. 6.15 (a)). Fig. 6.15 (b) shows the non-dimensional concentration profiles with different Fourier numbers corresponding to the extent of saturation. These profiles provide an idea to choose the relevant Fourier number for a certain level of concentration in the liquid film.

In addition, these dimensionless numbers also change with respect to the liquid

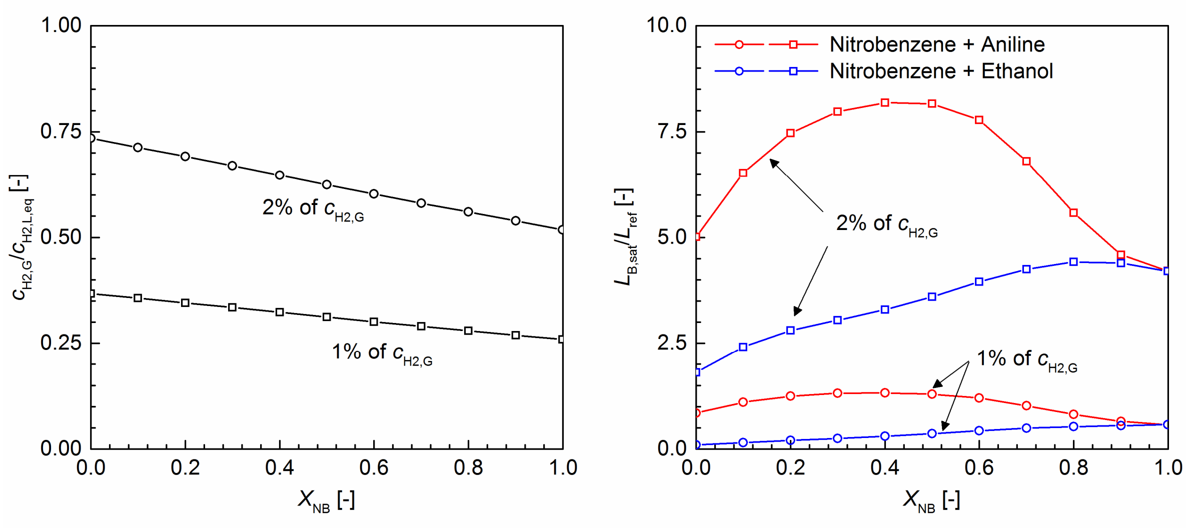

(a) (b)

Fig. 6.16: (a) Non dimensional Henry numbers for 1% and 2% of gas hydrogen concentration (b) non-dimensional bubble length for saturation of 1% and 2% of gas hydrogen concentration both nitrobenzene + aniline and nitrobenzene + ethanol mixtures ($Ca$=0.01).

composition. Fig. 6.16 (a) plots the non-dimensional Henry number according to the 1% and 2%of gas hydrogen concentration. Fig. 6.16 (b) shows the variable non-dimensional bubble length for the mixture of nitrobenzene + aniline and nitrobenzene + ethanol with corresponding gas hydrogen concentration. To estimate the variation of $L_{\mathrm{B,sat}}$ with fixed diffusion path, the $t_{\mathrm{sat,t}}$ for fixed capillary number (section 6.2.1) is chosen for the plot. Thus, $L_{\mathrm{B,sat}}$ in Fig. 6.16 (b) represents the minimum required length for the saturation of 1% of gas hydrogen concentration in the liquid film with respect to the liquid composition. Since the channel height is $100\,\mu\mathrm{m}$ in this study, the value of $1\,L_{\mathrm{ref}}$ means $100\,\mu\mathrm{m}$ as well. Similar to the $t_{\mathrm{sat,t}}$ profiles in Fig. 6.10, $L_{\mathrm{B,sat}}$ of nitrobenzene + aniline mixture has convex shape against the liquid composition, while $L_{\mathrm{B,sat}}$ of nitrobenzene + ethanol mixture show mostly increasing tendency as $X_{\mathrm{NB}}$ grows. In nitrobenzene + aniline mixture, the $L_{\mathrm{B,sat}}$ for 1% $c_{\mathrm{H2,G}}$ is less than $1\,L_{\mathrm{ref}}$ in the range of $X_{\mathrm{NB}} < 0.1$ and $X_{\mathrm{NB}} > 0.8$, which requires shorter bubble than the channel height. This condition gives rise to the flow closer to the bubbly flow. For wide range of liquid composition $0.1 < X_{\mathrm{NB}} < 0.8$, the values of $L_{\mathrm{B,sat}}$ for 1% of $c_{\mathrm{H2,G}}$ are higher than those for both pure nitrobenzene and aniline. The magnitudes of curves for 1% and 2% of gas hydrogen concentrations are obviously different in both mixtures. However, the overall shapes of those curves are similar with respect to the liquid composition. In overall reaction procedure, the required bubble length is almost 1.5 times longer than that of the pure aniline. Meanwhile, $L_{\mathrm{B,sat}}$ for nitrobenzene + ethanol mixture is shorter than that of pure nitrobenzene. Adding ethanol to the nitrobenzene hydrogenation process may reduce the required bubble length for saturation, which leads to having a sufficient time for saturation with shorter Taylor bubble. Thus, ethanol plays not only a role of diluent for the liquid nitrobenzene but also another role for reducing the time for saturation, which shortens the required length of a single Taylor bubble.

# Chapter 7 Summary and conclusions

The present study focuses on the numerical simulation of catalytic hydrogenation of nitrobenzene within a gas-liquid Taylor flow in a single channel of monolith reactor. The simulation covers a range of physical phenomena in a microchannel reactor such as two-phase flow and mass transfer as well as surface chemical reactions. Fickian diffusion assumption allows modeling molecular diffusion by concentration gradients, while chemical reactions on catalysts can be simplified by mean field approximation. With choosing proper approximations, this study treats the scale of problem as a continuum level where the continuous behavior of matters can be modeled by computational fluid dynamics (CFD) comprised of conservation laws.

For this purpose, a computer code has been successfully developed by means of coupling two computer codes, TURBIT-VOF and DETCHEM$^{TM}$. DETCHEM$^{TM}$ subroutines are embedded into TURBIT-VOF where TURBIT-VOF computes hydrodynamic behaviors of two-phase flow and associated mass transfer, while catalytic chemical reactions are handled by DETCHEM$^{TM}$. At the reactive wall where the two codes actually exchange the information, TURBIT-VOF provides the extrapolated wall concentrations of soluble species as input for DETCHEM$^{TM}$ routines. Then, DETCHEM$^{TM}$ calculates the Arrhenius rate equations that come up with a set of surface reaction rates for each elementary step, and delivers them with a form of reactive fluxes. TURBIT-VOF employs the reactive fluxes as Neumann boundary conditions for species transport equations explicitly. Treating the reactive boundary condition is a crucial idea of the coupled solver, which enables it to take into account the interaction between mass transfer and chemical reaction.

For consideration of chemical reactions with coupled solver, the species balance equation that was already implemented for the single species are expanded for the multicomponent mass transfer by diffusion models. Two diffusion models, multicomponent model (MCM) and effective diffusivity model (EDM), are implemented and validated with several one-dimensional non-reactive/reactive ternary cases. It turns out that EDM is sufficiently accurate for the practical calculations in continuum level with associating low computational effort, as already known from many other studies. In diluted condition, for example, the diffusion of gaseous species in the liquid where the concentration of gas species is generally very small as compared to its solvent concentration, the diffusivities in both MCM and EDM are almost identical. Moreover, it has been demonstrated that the values of diffusivity from both models are almost the same as the binary diffusion coefficients. By means of diffusion models, this study finds out the negligible influence of gas composition on composition-dependent diffusivities when gas species diffuse into liquids, and confirms the validity of using composition-independent diffusion coefficients for calculating gaseous species diffusion in liquids, which are generally utilized in many other studies.

TURBIT-VOF using a continuous single-field formulation for two-phase flow employs the continuous concentration diffusion model (CCDM) for mass transfer across the phase interface. In this study, CCDM is reinvestigated to verify its necessity and the influence of interface positions inside the computation cell. Without CCDM numerical solutions slightly deviate from analytical solutions, while with CCDM the difference between numerical and analytical solutions is drastically decreasing. The difference is smallest when the interface is placed in the middle of mesh cell. Also, parametric studies turn out that the results of both numerical and analytical models are in very good compliance for various model parameters, such as diffusivity ratio, reaction rate and Henry coefficient. As a result, the combination of CCDM and EDM is well applicable for simulating mass transfer and chemical reactions, which requires the composition-dependent diffusivity due to the reactions.

Before dealing with practical applications, the flow and mass transfer within a Taylor flow are pre-studied with an artificial fluid system in order to understand the characteristics of those problems numerically and find test conditions for the real-fluid system. The film thicknesses of numerical solutions are firstly validated with the correlation of Bretherton problem. From the results of the artificial fluid system, it has been found that the erroneous numerical oscillations disappear where $0.01<Ca<1.0$ and $Re<100$. Therefore, numerical simulations for the real fluid system utilize these favorable ranges to eliminate any expected numerical difficulties.

In addition, the simulation of mass transfer has also been performed with an artificial fluid system with additional artificial transport properties. At quasi-steady state, the overall shape of the bubble and its velocity are not developing anymore but just moving with a constant terminal velocity of the bubble. Therefore, during the calculation of mass transfer, the velocity field can be frozen with a concept of moving reference frame, which assumes that the computational domain is moving with the same velocity of the bubble. In fixed reference frame approach, the gradient of volume fraction near the front and rear interface is smeared because of the lack of the mesh resolution. The computation of mass transfer in fixed reference frame approach may require much more cells to reduce numerical errors in the vicinity of the interface. The moving reference frame in the present study is advantageous without considering the movement of the interface and saves the computational cost for simulations. Similarly, a recent study by Heckmann and Ehrhard utilizes separated, body-fitted, static computational domains to minimize the numerical diffusion onto the simulation of mass transport [58].

The physical and transport properties of species which take part in the hydrogenation process are estimated by several empirical correlations and models from literature. With these properties and the criteria from the study of the artificial fluid system, the input parameters for the real fluid system such as dimensionless Reynolds and capillary numbers can be determined. The channel height is selected as a 100 μm, and the velocity range is between 0.5 and 1.2 m/s, which complies with the numerically favorable condition of $0.01<Ca<1.0$ and $Re<100$. The numerical solutions of hydrodynamics for the Taylor flow of nitrobenzene and hydrogen are obtained with these test conditions. The film thicknesses of the real fluid system are in good agreement with the correlation of Halpern and Gaver [50] as well.

Based on hydrodynamic solutions of the real fluid system, the mass transfer of hydrogen from Taylor bubble to liquid nitrobenzene is calculated in moving reference frame. The liquid phase is either pure nitrobenzene or nitrobenzene saturated by hydrogen. The converted rate constant from Höller et al. [64] is applied to the channel wall as a Neumann boundary condition. In results of both pure and saturated nitrobenzene, the production of aniline (the product of the reaction) is highest at the rear part of the bubble where the film thickness is thinnest. In pure nitrobenzene, hydrogen from the gas phase moves to the wall by convective and diffusive mass transfer, while the results of saturated nitrobenzene show that the given hydrogen near the wall is consumed due to the reaction. There is a tradeoff relationship between the convective mass transfer caused by recirculating flow and the diffusive mass transfer in the liquid film. The results illustrate that the higher bubble velocity causes the stronger intensity of the convective mass transfer. Meanwhile, the film thickness becomes thicker, which requires a longer time for the diffusive mass transfer in the liquid film. The combination of these two mass transfer mechanisms governs the mass transfer efficiency and apparent reaction rate.

Furthermore, a detailed reaction mechanism is developed for the feasibility test of the coupled solver. Due to the lack of the physical properties in operating temperature, a qualitative analysis has only been carried out with an arbitrary scaled set of reaction rates. The results with detailed kinetic mechanism provide qualitatively acceptable behaviors of bulk species within a Taylor flow, which enables to investigate the surface species behaviors during the hydrogenation process. For more precise and practical prediction, experimental studies of this type of reactor are a prerequisite.

To investigate the influence of liquid composition on the mass transfer in the liquid film, one-dimensional diffusion equation has been computed with variable physical properties as a function of nitrobenzene mole fraction changing by the reaction. The composition-dependent physical properties are represented by correlations from literature. The results of calculation indicate that in a wide range of composition the mass transfer in liquid mixture is slower than that in the pure liquids. This delay caused by the non-ideality effect in liquid mixture leads to another limiting factor which further inhibits the mass transfer during the reaction procedure. The analysis of diffusion time demonstrates that the varying mixture composition plays not only a role for the dilution of reactants, but also affects the mass transfer due to the varying physical properties. Based on the saturation time for liquid mixture, the required bubble length for a certain level of saturation is finally determined by a combination of dimensionless numbers. This may give a guideline for the suitable length of the bubble within a liquid mixture.

Based on the investigations performed on the numerical simulation of gas-liquid Taylor flow with the catalyzed heterogeneous reaction it is concluded that:

1. Development of a computer code for the gas-liquid Taylor flow with catalytic surface reaction has been successfully accomplished by coupling TURBIT-VOF and DETCHEM$^{TM}$.
2. Effective diffusivity model is sufficiently accurate for multispecies gaseous mass transfer into liquid, where gas concentrations insignificantly affect the total concentration. The composition-dependent effective diffusivity becomes almost constant and is even close to the binary diffusion coefficient of gas species.
3. From the parametric study of Taylor flows with the artificial fluid system (gas-liquid density ratio=0.1, gas-liquid viscosity ratio=0.001 and 0.001 m < channel height < 0.1 m), the numerical parameters for the real fluid system have been determined. The suitable numerical solutions of Taylor flows are obtained by TURBIT-VOF, when $Re<100$ and $0.01<Ca<1$.

4. Using moving reference frame approach is advantageous for simulation of mass transfer with keeping realistic flow field, avoiding numerical errors such as smearing concentration gradient near the interface and less computational effort. No feedbacks of mass transfer on hydrodynamics are considered in this study.
5. For reactive mass transfer within a Taylor flow, increasing bubble velocity enhances the convective mass transfer by promoting recirculating flow between bubbles, while it diminishes the diffusive mass transfer in the liquid film by increasing the film thickness.
6. One-step global and own generated detailed kinetic mechanisms are used to simulate qualitative behaviors of reactants and products for catalyzed hydrogenation of nitrobenzene. For quantitatively reasonable prediction, the mechanisms need to be validated with experimental study.
7. Study on the mass transfer with variable liquid composition comes up with guidelines for optimal operation, such as liquid composition and required bubble length for a certain level of saturation. The composition of the liquid mixture is also a control parameter for saturation in the liquid film, in addition to hydrodynamic changes such as film thickness and velocity.

The developed computer code has successfully predicted the mass transport phenomena for two-phase reactive flow. This code can be further used for the other chemically reactive two-phase flow operated in the confined rectangular reactor such as monolith reactor. The moving reference approach and the symmetric boundary condition used in the present study can also be extended to the three-dimensional problems.

# Bibliography

1. *Surface tension values of some common test liquids for surface energy analysis,* http://www.surface-tension.de.
2. Abo-Ghander, N.S., F. Logist, J.R. Grace, J.F.M. Van Impe, S.S.E.H. Elnashaie, and C.J. Lim, *Heterogeneous modeling of an autothermal membrane reactor coupling dehydrogenation of ethylbenzene to styrene with hydrogenation of nitrobenzene to aniline: Fickian diffusion model.* Chemical Engineering and Processing, 2014. **77**: p. 50-65.
3. Akbar, M.K., D.A. Plummer, and S.M. Ghiaasiaan, *On gas–liquid two-phase flow regimes in microchannels.* International Journal of Multiphase Flow, 2003. **29**(5): p. 855-865.
4. Aland, S., S. Boden, A. Hahn, F. Klingbeil, M. Weismann, and S. Weller, *Quantitative comparison of Taylor flow simulations based on sharp-interface and diffuse-interface models.* International Journal for Numerical Methods in Fluids, 2013. **73**(4): p. 344-361.
5. Bird, R.B. and D.J. Klingenberg, *Multicomponent diffusion-A brief review.* Advances in Water Resources, 2013. **62**: p. 238-242.
6. Bird, R.B., W.E. Stewart, and E.N. Lightfoot, *Transport phenomena*. 2nd, Wiley international ed. 2002, New York: J. Wiley. xii, 895 p.
7. Bothe, D. and S. Fleckenstein, *A Volume-of-Fluid-based method for mass transfer processes at fluid particles.* Chemical Engineering Science, 2013. **101**: p. 283-302.
8. Bothe, D., M. Koebe, K. Wielage, J. Prüss, and H.J. Warnecke, *Direct numerical simulation of mass transfer between rising gas bubbles and water*, in *Bubbly flows. Analysis, modelling and calculation*, M. Sommerfeld, Editor. 2004, Springer. p. 159-174.
9. Bothe, D., M. Kröger, A. Alke, and H.J. Warnecke, *VOF-based simulation of reactive mass transfer across deformable interfaces.* Progress in Computational Fluid Dynamics, 2009. **9**(6-7): p. 325-331.
10. Bothe, D., M. Kröger, and H.J. Warnecke, *A VOF-Based Conservative Method for the Simulation of Reactive Mass Transfer from Rising Bubbles.* Fluid Dynamics & Materials Processing 2011. **7**(3): p. 303-316.
11. Burcat, A. and B. Ruscic, *Third Millennium Ideal Gas and Condensed Phase Thermochemical Database for Combustion with Updates from Active Thermochemical Tables*. 2005, Argonne National Laboratory.
12. Burghoff, S. and E.Y. Kenig, *A CFD model for mass transfer and interfacial phenomena on single droplets.* AIChE Journal, 2006. **52**(12): p. 4071-4078.
13. Cai, X., M. Wörner, H. Marschall, and O. Deutschmann, *Numerical study on the wettability dependent interaction of a rising bubble with a periodic open cellular structure.* Catalysis Today, 2016. **273**: p. 151-160.
14. Carty, R. and T. Schrodt, *Concentration Profiles in Ternary Gaseous Diffusion.* Industrial & Engineering Chemistry Fundamentals, 1975. **14**(3): p. 276-278.
15. Chapman, S., *The Kinetic Theory of Simple and Composite Monatomic Gases: Viscosity, Thermal Conduction, and Diffusion.* Proceedings of the Royal Society of London A: Mathematical, Physical and Engineering Sciences, 1916. **93**(646): p. 1-20.
16. Chasanis, P., A. Lautenschleger, and E.Y. Kenig, *Numerical investigation of carbon dioxide absorption in a falling-film micro-contactor.* Chemical Engineering Science, 2010. **65**(3): p. 1125-1133.
17. Chevalier, J.L., P. Petrino, and Y. Gastonbonhomme, *Estimation Method for the Kinematic Viscosity of a Liquid-Phase Mixture.* Chemical Engineering Science, 1988. **43**(6): p. 1303-1309.
18. Crank, J., *The mathematics of diffusion*. 2d ed. 1975, Oxford, Eng: Clarendon Press. viii, 414 p.
19. Crowe, C.T., M. Sommerfeld, and Y. Tsuji, *Multiphase flows with droplets and particles*. 1998, Boca Raton, Fla.; London: CRC Press. 471p.
20. Cui, X., X. Li, H. Sui, and H. Li, *Computational fluid dynamics simulations of direct contact heat and mass transfer of a multicomponent two-phase film flow in an inclined channel at sub-atmospheric pressure.* International Journal of Heat and Mass Transfer, 2012. **55**(21–22): p. 5808-5818.

21. Curtiss, C.F. and R.B. Bird, *Multicomponent diffusion.* Industrial & Engineering Chemistry Research, 1999. **38**(7): p. 2515-2522.
22. Curtiss, C.F. and J.O. Hirschfelder, *Transport Properties of Multicomponent Gas Mixtures.* The Journal of Chemical Physics, 1949. **17**(6): p. 550-555.
23. Cussler, E.L., *Diffusion: mass transfer in fluid systems*. 3rd ed. 2009, Cambridge ; New York: Cambridge University Press. xvii, 631 p.
24. Davidson, M.R. and M. Rudman, *Volume-of-fluid calculation of heat or mass transfer across deforming interfaces in two-fluid flow.* Numerical Heat Transfer Part B-Fundamentals, 2002. **41**(3-4): p. 291-308.
25. Deising, D., H. Marschall, and D. Bothe, *A unified single-field model framework for Volume-Of-Fluid simulations of interfacial species transfer applied to bubbly flows.* Chemical Engineering Science, 2016. **139**: p. 173-195.
26. Desilets, M., P. Proulx, and G. Soucy, *Modeling of multicomponent diffusion in high temperature flows.* International Journal of Heat and Mass Transfer, 1997. **40**(18): p. 4273-4278.
27. Dessimoz, A.L., L. Cavin, A. Renken, and L. Kiwi-Minsker, *Liquid-liquid two-phase flow patterns and mass transfer characteristics in rectangular glass microreactors.* Chemical Engineering Science, 2008. **63**(16): p. 4035-4044.
28. Deutschmann, O., L.I. Maier, U. Riedel, A.H. Stroemman, and R.W. Dibble, *Hydrogen assisted catalytic combustion of methane on platinum.* Catalysis Today, 2000. **59**(1-2): p. 141-150.
29. Deutschmann, O. and L.D. Schmidt, *Modeling the partial oxidation of methane in a short-contact-time reactor.* Aiche Journal, 1998. **44**(11): p. 2465-2477.
30. Deutschmann, O., S. Tischer, C. Correa, D. Chatterjee, S. Kleditzsch, V.M. Janardhanan, N. Mladenov, H.D. Minh, H. Karadeniz, and M. Hettel, *DETCHEM Software package*. 2014: Karlsruhe, Germany.
31. Durán Martínez, F.L., C. Julcour, A.-M. Billet, and F. Larachi, *Modelling and simulations of a monolith reactor for three-phase hydrogenation reactions — Rules and recommendations for mass transfer analysis.* Catalysis Today, 2016. **273**: p. 121-130.
32. Enskog, D., Inaugural Dissertation, Uppsala, Sweden, 1917.
33. Falconi, C.J., C. Lehrenfeld, H. Marschall, C. Meyer, R. Abiev, D. Bothe, A. Reusken, M. Schlüter, and M. Wörner, *Numerical and experimental analysis of local flow phenomena in laminar Taylor flow in a square mini-channel.* Physics of Fluids, 2016. **28**(1): p. 012109.
34. Frikha, N., E. Schaer, and J.L. Houzelot, *Methodology of multiphase reaction kinetics and hydrodynamics identification: Application to catalyzed nitrobenzene hydrogenation.* Chemical Engineering Journal, 2006. **124**(1-3): p. 19-28.
35. Furry, W.H., *On the Elementary Explanation of Diffusion Phenomena in Gases.* American Journal of Physics, 1948. **16**(2): p. 63-78.
36. Gandhi, K.S., *Use of Fick's law and Maxwell–Stefan equations in computation of multicomponent diffusion.* AIChE Journal, 2012. **58**(11): p. 3601-3605.
37. Gelder, E.A., S.D. Jackson, and C.M. Lok, *The hydrogenation of nitrobenzene to aniline: a new mechanism.* Chemical Communications, 2005(4): p. 522-524.
38. GESTIS-Stoffdatenbank, *Institut für Arbeitsschutz der Deutschen Gesetzlichen Unfallversicherung*.
39. Ghidersa, B.E., *Finite volume-based volume-of-fluid method for the simulation of two-phase flows in small rectangular channels*, in *Wissenschaftliche Berichte, FZKA-6889*. 2004, Universität Karlsruhe.
40. Gjaldbaek, J.C., *The Solubility of Hydrogen, Oxygen, and Carbon Monoxide in Some Non-Polar Solvents.* Acta Chemica Scandinavica, 1952. **6**(5): p. 623-633.
41. Gjaldbaek, J.C. and E.K. Andersen, *The Solubility of Carbon Dioxide, Oxygen, Carbon Monoxide and Nitrogen in Polar Solvents.* Acta Chemica Scandinavica, 1954. **8**(8): p. 1398-1413.
42. Govindan, K. and G. Ravichandran, *Excess volumes and viscosities of mixtures of nitrobenzene and certain aromatic bases.* Journal of Solution Chemistry, 1996. **25**(1): p. 75-82.
43. Gracki, J.A., G.P. Flynn, and J. Ross, *Viscosity of nitrogen, helium, hydrogen, and argon from -100º to 25ºC up to 150-250 atmospheres*, in *Project SQUID*. 1969: Purdue university.
44. Gubbins, K.E. and J.D. Moore, *Molecular Modeling of Matter: Impact and Prospects in Engineering.* Industrial & Engineering Chemistry Research, 2010. **49**(7): p. 3026-3046.
45. Gunther, A., M. Jhunjhunwala, M. Thalmann, M.A. Schmidt, and K.F. Jensen, *Micromixing of miscible liquids in segmented gas-liquid flow.* Langmuir, 2005. **21**(4): p. 1547-1555.

46. Guo, Z.Y., D.F. Fletcher, and B.S. Haynes, *Implementation of a height function method to alleviate spurious currents in CFD modelling of annular flow in microchannels.* Applied Mathematical Modelling, 2015. **39**(16): p. 4665-4686.
47. Haase, S. and T. Bauer, *New method for simultaneous measurement of hydrodynamics and reaction rates in a mini-channel with Taylor flow.* Chemical Engineering Journal, 2011. **176–177**(0): p. 65-74.
48. Haase, S., R. Langsch, T. Bauer, and R. Lange, *Impact of Spherical Catalyst Particles on Gas-Liquid Flow Regimes in Minichannels with Square Cross Section.* Chemie Ingenieur Technik, 2014. **86**(4): p. 467-475.
49. Haelssig, J.B., A.Y. Tremblay, J. Thibault, and S.G. Etemad, *Direct numerical simulation of interphase heat and mass transfer in multicomponent vapour–liquid flows.* International Journal of Heat and Mass Transfer, 2010. **53**(19–20): p. 3947-3960.
50. Halpern, D. and D.P. Gaver, *Boundary Element Analysis of the Time-Dependent Motion of a Semi-infinite Bubble in a Channel.* Journal of Computational Physics, 1994. **115**(2): p. 366-375.
51. Hampel, U., R. Dittmeyer, A. Patyk, T. Wetzel, R. Lange, H. Freund, W. Schwieger, M. Grunewald, M. Schluter, and U. Petasch, *The Helmholtz Energy Alliance "Energy Efficient Multiphase Chemical Processes".* Chemie Ingenieur Technik, 2013. **85**(7): p. 992-996.
52. Harkins, W.D., E.C.H. Davies, and G.L. Clark, *The orientation of molecules in the surfaces of liquids, the energy relations at surfaces, solubility, adsorption, emulsification, molecular association, and the effect of acids and bases on interfacial tension.1 (surface energy vi.).* Journal of the American Chemical Society, 1917. **39**(4): p. 541-596.
53. Haroun, Y., D. Legendre, and L. Raynal, *Volume of fluid method for interfacial reactive mass transfer: Application to stable liquid film.* Chemical Engineering Science, 2010. **65**(10): p. 2896-2909.
54. Hatziantoniou, V., B. Andersson, and N.-H. Schöön, Ind. Eng. Chem. Proc. Des. Dev., 1986. **25**: p. 964.
55. Hayashi, K. and A. Tomiyama, *Interface Tracking Simulation of Mass Transfer from a Dissolving Bubble.* The Journal of Computational Multiphase Flows, 2011. **3**(4): p. 247-262.
56. Hayes, R.E. and S.T. Kolaczkowski, *Introduction to Catalytic Combustion*. 1998: Taylor & Francis.
57. Hayes, R.E., B. Liu, R. Moxom, and M. Votsmeier, *The effect of washcoat geometry on mass transfer in monolith reactors.* Chemical Engineering Science, 2004. **59**(15): p. 3169-3181.
58. Heckmann, C. and P. Ehrhard. *Simulation of mass transfer in liquid/liquid slug flow*. in *PAMM Proc. Appl. Math. Mech. 16*. 2016.
59. Hettel, M., C. Diehm, H. Bonart, and O. Deutschmann, *Numerical simulation of a structured catalytic methane reformer by DUO: The new computational interface for OpenFOAM (R) and DETCHEM (TM).* Catalysis Today, 2015. **258**: p. 230-240.
60. Hildebrand, J.H., J.M. Prausnitz, and R.L. Scott, *Regular and related solutions: the solubility of gases, liquids, and solids*. 1970: Van Nostrand Reinhold Co.
61. Hildebrand, J.H. and R.L. Scott, *The solubility of nonelectrolytes*. 1950: Reinhold Pub. Corp.
62. Hirt, C.W. and B.D. Nichols, *Volume of fluid (VOF) method for the dynamics of free boundaries.* Journal of Computational Physics, 1981. **39**(1): p. 201-225.
63. Hoar, T.P. and D.A. Melford, *The surface tension of binary liquid mixtures: lead + tin and lead + indium alloys.* Transactions of the Faraday Society, 1957. **53**(0): p. 315-326.
64. Höller, V., D. Wegricht, I. Yuranov, L. Kiwi-Minsker, and A. Renken, *Three-phase nitrobenzene hydrogenation over supported glass fiber catalysts: Reaction kinetics study.* Chemical Engineering & Technology, 2000. **23**(3): p. 251-255.
65. Irandoust, S. and B. Andersson, *Mass-Transfer and Liquid-Phase Reactions in a Segmented 2-Phase Flow Monolithic Catalyst Reactor.* Chemical Engineering Science, 1988. **43**(8): p. 1983-1988.
66. Irandoust, S. and B. Andersson, *Simulation of Flow and Mass-Transfer in Taylor Flow through a Capillary.* Computers & Chemical Engineering, 1989. **13**(4-5): p. 519-526.
67. Irandoust, S., S. Ertle, and B. Andersson, *Gas-Liquid Mass-Transfer in Taylor Flow through a Capillary.* Canadian Journal of Chemical Engineering, 1992. **70**(1): p. 115-119.

68. Irving, J.B., *Viscosities of Binary Liquid Mixtures: A Survey of Mixture Equations*. 1977: National Engineering Laboratory.
69. Ishii, M. and T. Hibiki, *Thermo-fluid dynamics of two-phase flow*. 2006, New York; London: Springer. xvii, 462 p.
70. Jacobson, B., *Association Numbers in Liquid Systems from Intermolecular Free Length Relationships.* Acta Chemica Scandinavica, 1955. **9**(6): p. 997-1006.
71. Jacqmin, D., *Calculation of two-phase Navier-Stokes flows using phase-field modeling*. Journal of Computational Physics, 1999. **155**(1): p. 96-127.
72. Jasper, J.J., *The Surface Tension of Pure Liquid Compounds.* Journal of Physical and Chemical Reference Data, 1972. **1**(4): p. 841-1010.
73. Kahl, T., K.-W. Schröder, F.R. Lawrence, W.J. Marshall, H. Höke, and R. Jäckh, *Aniline*, in *Ullmann's Encyclopedia of Industrial Chemistry*. 2000, Wiley-VCH Verlag GmbH & Co. KGaA.
74. Karadeniz, H., C. Karakaya, S. Tischer, and O. Deutschmann, *Numerical modeling of stagnation-flows on porous catalytic surfaces: CO oxidation on Rh/Al2O3.* Chemical Engineering Science, 2013. **104**: p. 899-907.
75. Kataoka, S., Y. Takeuchi, A. Harada, T. Takagi, Y. Takenaka, N. Fukaya, H. Yasuda, T. Ohmori, and A. Endo, *Microreactor containing platinum nanoparticles for nitrobenzene hydrogenation.* Applied Catalysis A: General, 2012. **427–428**: p. 119-124.
76. Kataoka, S., Y. Takeuchi, A. Harada, T. Takagi, Y. Takenaka, N. Fukaya, H. Yasuda, T. Ohmori, and A. Endo, *Microreactor containing platinum nanoparticles for nitrobenzene hydrogenation (vol 427, pg 119, 2012).* Applied Catalysis a-General, 2012. **433**: p. 280-280.
77. Katayama, T. and T. Nitta, *Solubilities of Hydrogen and Nitrogen in Alcohols and Normal-Hexane.* Journal of Chemical and Engineering Data, 1976. **21**(2): p. 194-196.
78. Katz, M., P.W. Lobo, A.S. Minano, and H. Solimo, *Viscosities, Densities, and Refractive Indices of Binary Liquid Mixtures.* Canadian Journal of Chemistry, 1971. **49**(15): p. 2605-&.
79. Kececi, S., M. Wörner, A. Onea, and H.S. Soyhan, *Recirculation time and liquid slug mass transfer in co-current upward and downward Taylor flow.* Catalysis Today, 2009. **147**(Supplement 1): p. S125-S131.
80. Kee, R.J., M.E. Coltrin, and P. Glarborg, *Chemically reacting flow: theory and practice*. 2003, Hoboken, N.J.: Wiley-Interscience. xxxiii, 848 p.
81. Kee, R.J., G. Dixon-Lewis, J. Warnatz, M.E. Coltrin, and J.A. Miller, *A FORTRAN computer code package for the evaluation of gas-phase, multicomponent transport properties*, S.N. Laboratories, Editor. 1986.
82. Kenig, E. and A. Gorak, *A Film Model-Based Approach for Simulation of Multicomponent Reactive Separation.* Chemical Engineering and Processing, 1995. **34**(2): p. 97-103.
83. Kenig, E.Y., F. Butzmann, L. Kucka, and A. Gorak, *Comparison of numerical and analytical solutions of a multicomponent reaction-mass-transfer problem in terms of the film model.* Chemical Engineering Science, 2000. **55**(8): p. 1483-1496.
84. Kenig, E.Y., A.A. Ganguli, T. Atmakidis, and P. Chasanis, *A novel method to capture mass transfer phenomena at free fluid-fluid interfaces.* Chemical Engineering and Processing, 2011. **50**(1): p. 68-76.
85. Kenig, E.Y. and L.P. Kholpanov, *Simultaneous Mass and Heat-Transfer with Reactions in a Multicomponent, Laminar, Falling Liquid-Film.* Chemical Engineering Journal and the Biochemical Engineering Journal, 1992. **49**(2): p. 119-126.
86. Kenig, E.Y., R. Schneider, and A. Gorak, *Multicomponent unsteady-state film model: a general analytical solution to the linearized diffusion-reaction problem.* Chemical Engineering Journal, 2001. **83**(2): p. 85-94.
87. Klemm, E., B. Amon, H. Redlingshofer, E. Dieterich, and G. Emig, *Deactivation kinetics in the hydrogenation of nitrobenzene to aniline on the basis of a coke formation kinetics - investigations in an isothermal catalytic wall reactor.* Chemical Engineering Science, 2001. **56**(4): p. 1347-1353.
88. Kreutzer, M.T., *Hydrodynamics of Taylor flow in capillaries and monoliths channels.* 2003, Delft Univ.
89. Kreutzer, M.T., F. Kapteijn, J.A. Moulijn, and J.J. Heiszwolf, *Multiphase monolith reactors: Chemical reaction engineering of segmented flow in microchannels.* Chemical Engineering Science, 2005. **60**(22): p. 5895-5916.
90. Krishnamurthy, R. and R. Taylor, *A Nonequilibrium Stage Model of Multicomponent Separation Processes .1. Model Description and Method of Solution.* Aiche Journal, 1985. **31**(3): p. 449-456.

91. Kumar, A. and S. Mazumder, *Assessment of various diffusion models for the prediction of heterogeneous combustion in monolith tubes.* Computers & Chemical Engineering, 2008. **32**(7): p. 1482-1493.
92. Lam, S.H., *Multicomponent diffusion revisited.* Physics of Fluids, 2006. **18**(7).
93. Lange, R., *Kinetikempfehlungen für die Hydrierung von Nitrobenzol zu Anilin*. 2013, TU Dresden.
94. Leclaire, S., M. Reggio, and J.Y. Trepanier, *Numerical evaluation of two recoloring operators for an immiscible two-phase flow lattice Boltzmann model.* Applied Mathematical Modelling, 2012. **36**(5): p. 2237-2252.
95. Lei, Z.G., Y.Y. Guo, C.N. Dai, L.H. Zi, and B.H. Chen, *Simulation of hydrodynamic and mass transfer performances in monolith channel.* Catalysis Today, 2016. **276**: p. 150-160.
96. Lemcoff, N.O., *Liquid-Phase Catalytic-Hydrogenation of Acetone.* Journal of Catalysis, 1977. **46**(3): p. 356-364.
97. Lühring, P. and A. Schumpe, *Gas Solubilities (H-2, He, N-2, Co, O-2, Ar, Co2) in Organic Liquids at 293.2-K.* Journal of Chemical and Engineering Data, 1989. **34**(2): p. 250-252.
98. Lutz, A.E., R.J. Kee, J.F. Grcar, and F.M. Rupley, *OPPDIF: A Fortran Program for Computing Opposed-Flow Diffusion Flames*. 1997, Report No. SAND 96-8243, Sandia National Laboratories.
99. Machado, R.M., *Fundamentals of Mass Transfer and Kinetics for the Hydrogenation of Nitrobenzene to Aniline*, in *ALR Application Note*. 2007, Mettler-Toledo AutoChem. Inc.
100. Mahata, A., R.K. Rai, I. Choudhuri, S.K. Singh, and B. Pathak, *Direct vs. indirect pathway for nitrobenzene reduction reaction on a Ni catalyst surface: a density functional study.* Physical Chemistry Chemical Physics, 2014. **16**(47): p. 26365-26374.
101. Marschall, H., K. Hinterberger, C. Schuler, F. Habla, and O. Hinrichsen, *Numerical simulation of species transfer across fluid interfaces in free-surface flows using OpenFOAM.* Chemical Engineering Science, 2012. **78**: p. 111-127.
102. Maxwell, J.C., *The Scientific Papers of James Clerk Maxwell*. 1952.
103. Mazumder, S., *Critical assessment of the stability and convergence of the equations of multi-component diffusion.* Journal of Computational Physics, 2006. **212**(2): p. 383-392.
104. Mhetar, V.R. and J.C. Slattery, *The Stefan problem of a binary liquid mixture.* Chemical Engineering Science, 1997. **52**(8): p. 1237-1242.
105. Miller, L.P., H.N. Wachter, and V. Fried, *Densities and molar volumes of binary solutions of nitrobenzene in electron donating solvents.* Journal of Chemical & Engineering Data, 1975. **20**(4): p. 417-419.
106. Muradoglu, M., A. Günther, and H.A. Stone, *A computational study of axial dispersion in segmented gas-liquid flow.* Physics of Fluids, 2007. **19**(7): p. 072109.
107. Muramatsu, K., Y. Youn, Y. Han, Y. Hasegawa, and N. Shikazono, *Numerical study on the effect of initial flow velocity on liquid film thickness of accelerated slug flow in a micro tube.* International Journal of Heat and Fluid Flow, 2015. **54**: p. 77-86.
108. Newman, J., *Stefan-Maxwell mass transport.* Chemical Engineering Science, 2009. **64**(22): p. 4796-4803.
109. Nikam, P.S., M.C. Jadhav, and M. Hasan, *Density and Viscosity of Mixtures of Nitrobenzene with Methanol, Ethanol, Propan-1-Ol, Propan-2-Ol, Butan-1-Ol, 2-Methylpropane-1-Ol, and 2-Methylpropan-2-Ol at 298.15 and 303.15 K.* Journal of Chemical and Engineering Data, 1995. **40**(4): p. 931-934.
110. Onea, A., M. Wörner, and D.G. Cacuci, *A qualitative computational study of mass transfer in upward bubble train flow through square and rectangular mini-channels.* Chemical Engineering Science, 2009. **64**(7): p. 1416-1435.
111. Onsager, L., *Reciprocal Relations in Irreversible Processes. I.* Physical Review, 1931. **37**(4): p. 405-426.
112. Öztaskin, M.C., M. Wörner, and H.S. Soyhan, *Numerical investigation of the stability of bubble train flow in a square minichannel.* Physics of Fluids, 2009. **21**(4): p. 042108-1 - 042108-17.
113. Petera, J. and L.R. Weatherley, *Modelling of mass transfer from falling droplets.* Chemical Engineering Science, 2001. **56**(16): p. 4929-4947.

114. Petrov, L., K. Kumbilieva, and N. Kirkov, *Kinetic-Model of Nitrobenzene Hydrogenation to Aniline over Industrial Copper Catalyst Considering the Effects of Mass-Transfer and Deactivation.* Applied Catalysis, 1990. **59**(1): p. 31-43.

115. Poling, B.E., J.M. Prausnitz, and J.P. O'Connell, *The Properties of Gases and Liquids*. 5th ed. 2004: McGraw-Hill.

116. Powers, M.F., D.J. Vickery, A. Arehole, and R. Taylor, *A Nonequilibrium Stage Model of Multicomponent Separation Processes .5. Computational Methods for Solving the Model-Equations.* Computers & Chemical Engineering, 1988. **12**(12): p. 1229-1241.

117. Prausnitz, J.M. and F.H. Shair, *A Thermodynamic Correlation of Gas Solubilities.* Aiche Journal, 1961. **7**(4): p. 682-687.

118. Purwanto, R.M. Deshpande, R.V. Chaudhari, and H. Delmas, *Solubility of hydrogen, carbon monoxide, and 1-octene in various solvents and solvent mixtures.* Journal of Chemical and Engineering Data, 1996. **41**(6): p. 1414-1417.

119. Radhakrishnan, K., P.A. Ramachandran, P.H. Brahme, and R.V. Chaudhari, *Solubility of Hydrogen in Methanol, Nitrobenzene, and Their Mixtures - Experimental-Data and Correlation.* Journal of Chemical and Engineering Data, 1983. **28**(1): p. 1-4.

120. Raimondi, N.D. and L. Prat, *Numerical Study of the Coupling Between Reaction and Mass Transfer for Liquid-Liquid Slug Flow in Square Microchannels.* Aiche Journal, 2011. **57**(7): p. 1719-1732.

121. Reid, R.C., J.M. Prausnitz, and B.E. Poling, *The Properties of Gases and Liquids*. 1987: McGraw-Hill.

122. Roudet, M., K. Loubiere, C. Gourdon, and M. Cabassud, *Hydrodynamic and mass transfer in inertial gas-liquid flow regimes through straight and meandering millimetric square channels.* Chemical Engineering Science, 2011. **66**(13): p. 2974-2990.

123. Sabisch, W., *Dreidimensionale numerische Simulation der Dynamik von aufsteigenden Einzelblasen und Blasenschwärmen mit einer Volume-of-Fluid-Methode*, in *Forschungszentrum Karlsruhe Wissenschaftliche Berichte, FZKA 6478*. 2000.

124. Salmi, T. and J. Warna, *Modeling of Catalytic Packed-Bed Reactors Comparison of Different Diffusion-Models.* Computers & Chemical Engineering, 1991. **15**(10): p. 715-727.

125. Sander, R., *Compilation of Henry's law constants (version 4.0) for water as solvent.* Atmospheric Chemistry and Physics, 2015. **15**(8): p. 4399-4981.

126. Sobolev, S.L., L.V. Poluyanov, and F. Liu, *An analytical model for solute diffusion in multicomponent alloy solidification.* Journal of Crystal Growth, 2014. **395**: p. 46-54.

127. Stefan, J., *Über das Gleichgewicht und die Bewegung, insbesondere die Diffusion von Gasmengen.* Sitzungsber. Akad. Wiss. Wien, 1871. **63**: p. 63-124.

128. Suri, S.K. and R. .V, *Surface Tension of Some Binary Liquid Mixtures.* Journal of Physical Chemistry, 1968. **72**(9): p. 3073-&.

129. Sussman, M., P. Smereka, and S. Osher, *A Level Set Approach for Computing Solutions to Incompressible Two-Phase Flow.* Journal of Computational Physics, 1994. **114**(1): p. 146-159.

130. Talimi, V., Y.S. Muzychka, and S. Kocabiyik, *Numerical simulation of the pressure drop and heat transfer of two phase slug flows in microtubes using moving frame of reference technique.* International Journal of Heat and Mass Transfer, 2012. **55**(23–24): p. 6463-6472.

131. Taylor, G.I., *Deposition of a Viscous Fluid on the Wall of a Tube.* Journal of Fluid Mechanics, 1961. **10**(2): p. 161-165.

132. Taylor, R. and R. Krishna, *Multicomponent mass transfer*. Wiley series in chemical engineering. 1993, New York: Wiley. xxxiv, 579 p.

133. Thulasidas, T.C., M.A. Abraham, and R.L. Cerro, *Flow patterns in liquid slugs during bubble-train flow inside capillaries.* Chemical Engineering Science, 1997. **52**(17): p. 2947-2962.

134. Tong, S.B., K.F. O'Driscoll, and G.L. Rempel, *Kinetics of nitrobenzene hydrogenation using a gel entrapped palladium catalyst.* The Canadian Journal of Chemical Engineering, 1978. **56**(3): p. 340-345.

135. Turek, F., R. Geike, and R. Lange, *Liquid-phase hydrogenation of nitrobenzene in a slurry reactor.* Chemical Engineering and Processing: Process Intensification, 1986. **20**(4): p. 213-219.

136. Turek, F., R. Geike, and R. Lange, *Liquid-Phase Hydrogenation of Nitrobenzene in a Slurry Reactor.* Chemical Engineering and Processing, 1986. **20**(4): p. 213-219.

137. Unlusu, B. and A.K. Sunol, *Modeling of equilibration times at high pressure for multicomponent vapor-liquid diffusional processes.* Fluid Phase Equilibria, 2004. **226**: p. 15-25.

138. Unverdi, S.O. and G. Tryggvason, *A front-tracking method for viscous, incompressible, multi-fluid flows.* Journal of Computational Physics, 1992. **100**(1): p. 25-37.
139. Warnatz, J., U. Maas, and R.W. Dibble, *Combustion: physical and chemical fundamentals, modeling and simulation, experiments, pollutant formation*. 4th ed. 2006, Berlin ; New York: Springer. xii, 378 p.
140. Weast, R.C., *CRC Handbook of Chemistry and Physics, 50th Edition*. 1969: Taylor & Francis.
141. Wilke, C.R., *Diffusional Properties of Multicomponent Gases.* Chemical Engineering Progress, 1950. **46**(2): p. 95-104.
142. Wilke, C.R. and P. Chang, *Correlation of Diffusion Coefficients in Dilute Solutions.* Aiche Journal, 1955. **1**(2): p. 264-270.
143. Williams, F.A., *Elementary Derivation of the Multicomponent Diffusion Equation.* American Journal of Physics, 1958. **26**(7): p. 467-469.
144. Wisniak, J. and M. Klein, *Reduction of Nitrobenzene to Aniline*. Industrial & Engineering Chemistry Product Research and Development, 1984. **23**(1): p. 44-50.
145. Woo, M., M. Wörner, S. Tischer, and O. Deutschmann, *Validation of a numerical method for interface-resolving simulation of multicomponent gas-liquid mass transfer and evaluation of multicomponent diffusion models.* Heat and Mass Transfer, 2017.
146. Wörner, M., *Taylor bubbles in small channels: a proper guiding measure for validation of numerical methods for interface resolving simulations.* Advances in Mathematical Fluid Mechanics, Editors: D. Bothe, A. Reusken.
147. Wörner, M., *Numerical modeling of multiphase flows in microfluidics and micro process engineering: a review of methods and applications.* Microfluidics and Nanofluidics, 2012. **12**(6): p. 841-886.
148. Yang, C. and Z.-S. Mao, *Numerical simulation of interphase mass transfer with the level set approach.* Chemical Engineering Science, 2005. **60**(10): p. 2643-2660.
149. Yeong, K.K., A. Gavriilidis, R. Zapf, and V. Hessel, *Experimental studies of nitrobenzene hydrogenation in a microstructured falling film reactor.* Chemical Engineering Science, 2004. **59**(16): p. 3491-3494.
150. Yue, J., L.G. Luo, Y. Gonthier, G.W. Chen, and Q. Yuan, *An experimental study of air-water Taylor flow and mass transfer inside square microchannels.* Chemical Engineering Science, 2009. **64**(16): p. 3697-3708.
151. Zhang, L., J. Jiang, W. Shi, S. Xia, Z. Ni, and X. Xiao, *Insights into the hydrogenation mechanism of nitrobenzene to aniline on Pd3/Pt(111): a density functional theory study.* RSC Advances, 2015. **5**(43): p. 34319-34326.

# Publications related to the dissertation

## Journal Article

Woo, M., Wörner, M., Tischer, S., Deutschmann, O., *Validation of a numerical method for interface-resolving simulation of multicomponent gas-liquid mass transfer and evaluation of multicomponent diffusion models*, Heat Mass Transfer (2017). https://doi.org/10.1007/s00231-017-2145-x.

## Conference proceeding

Woo, M., Wörner, M., Tischer, S., Deutschmann, O., *Development of a Computer Code for Numerical Simulation of Reactive and Catalytic Two-phase Flows with Detailed Chemistry*, 2nd Int. Symp. Multiscale Multiphase Process Engineering, Hamburg, Germany, September 24-27, 2014.

## Poster presentations

Woo, M., Wörner, M., Maier, L., Tischer, S., Deutschmann, O., *A Numerical Study on Gas-Liquid Taylor Flow for Catalytic Hydrogenation of Nitrobenzene with Detailed Kinetic Mechanism*, Jahrestreffen ProcessNet Fachgruppe Mehrphasenströmungen, Dresden, Germany, March 14-15, 2017 (awarded poster prize in the multiphase flow section).

Woo, M., Wörner, M., Tischer, S., Deutschmann, O., *Mass transfer and catalytic reaction in Taylor flow: parametric numerical study for frozen hydrodynamics*, International Conference on Structured Catalysts and Reactors (ICOSCAR-5), Donostia - San Sebastian, Spain, June 22-24, 2016.

Woo, M., Wörner, M., Tischer, S., Deutschmann, O., *Detailed Numerical Simulation of Gas-Liquid Taylor Flow with Heterogeneous Chemical Reaction*, European Symposium on Chemical Reaction Engineering (ESCRE), Fürstenfeldbruck, Germany, October 27-30, 2015.

# Nomenclature

| Symbol | Description | Unit |
|---|---|---|
| $a$ | area | m$^2$ |
| $a$ | area | m$^2$ |
| $c$ | concentration | mol/m$^3$ |
| $d$ | distance | m |
| $D$ | Fick's diffusivity | m$^2$/s |
| Đ | Maxwell-Stefan diffusivity | m$^2$/s |
| $E$ | activation energy | J/mol |
| $f$ | volume fraction | - |
| $G$ | gravity | m/s$^2$ |
| $H$ | Henry coefficient | mol/(m$^3$·MPa) |
| $h$ | height | m |
| $j$ | diffusive flux relative to mass-average velocity | mol/(m$^2$s) |
| $J$ | diffusive flux relative to molar-average velocity | mol/(m$^2$s) |
| $K$ | equilibrium constant | (mol/l)$^{-1}$ |
| $k$ | reaction constant | mol/(m$^2$s) |
| $L$ | length | m |
| $m$ | mass | kg |
| $n$ | mass flux | kg/(m$^2$s) |
| $N$ | molar flux | mol/(m$^2$s) |
| $p$ | pressure | Pa |
| $r$ | volumetric reaction rate | mol/(m$^3$s) |
| $\dot{s}$ | surface reaction rate | mol/(m$^2$s) |
| $T$ | temperature | K |
| $t$ | time | s |
| $u$ | mass-average velocity | m/s |
| $U$ | molar-average velocity | m/s |
| $V$ | volume | m$^3$ |
| $X$ | mole fraction | - |
| $x$ | axial distance | m |
| $y$ | mass fraction | - |
| $z$ | wall-normal distance | m |

## Greek symbols

| Symbol | Description | Unit |
|---|---|---|
| $\delta$ | solubility parameter | $J^{0.5}/m^{1.5}$ |
| $\phi$ | liquid volume fraction | - |
| $\Gamma$ | gas to liquid ratio between properties in two phases | - |
| $\kappa$ | curvature | $m^{-1}$ |
| $\mu$ | viscosity | Pa·s |
| $\nu$ | stoichiometric coefficient | - |
| $\rho$ | density | $kg/m^3$ |
| $\sigma$ | surface tension | N/m |
| $\tau$ | characteristic time | s |

## Superscripts

| Symbol | Description |
|---|---|
| * | Non-dimensional parameter |
| 0 | Initial value |
| E | excess properties in liquid mixture |
| T | matrix transposition |
| V | volume average property |

## Subscripts

| Symbol | Description |
|---|---|
| br | breakthrough |
| cat | catalyst |
| eff | effective |
| ex | exposure |
| exp | experimental |
| F | film |
| G | gas |
| int | interface |
| L | liquid |

| | |
|---|---|
| m | mixture |
| NB | nitrobenzene |
| num | numerical |
| ref | reference |
| S | surface |
| sat | saturated |
| vap | vapor |

# List of figures

Fig. 1.1: The objective for the simulation of reactive gas-liquid flow in monolith reactor.

Fig. 2.1: Definition of the cells and those cell-centered indices near the boundary $(z = 0)$.

Fig. 2.2: Schematic diagram of coupling TURBIT-VOF and DETCHEMTM.

Fig. 2.3: Data exchanging procedure between TURBIT-VOF and DETCHEMTM at the reactive wall boundary.

Fig. 3.1: Schematic diagram of the examples for two-phase flow and mass transfer across the interface.

Fig. 3.2: Sketch of the test conditions for layered Poiseuille flow.

Fig. 3.3: Velocity profiles for Γμ=0.01 (a) and 0.001 (b). Comparison between analytic solutions and numerical results with a different number of cells in the z-direction.

Fig. 3.4: Velocity profiles for different interface locations. Comparison of numerical solutions with analytic solution for Γμ=0.01.

Fig. 3.5: Numerical results with 41 non-equidistance cells (shown in right side) and with 101 equidistance cells. Comparison of velocity profiles between numerical results and analytic solution.

Fig. 3.6: Schematic diagram of the Stefan diffusion example.

Fig. 3.7: Comparison of predicted mole fraction by the MCM and EDM with experimental data [14] and numerical solution of the MS equations.

Fig. 3.8: Diffusivities of MCM and EDM for the Stefan diffusion example.

Fig. 3.9: Sketch for the ternary diffusion of $CO$, $O_2$, and $CO_2$ with catalyzed heterogeneous reaction.

Fig. 3.10: Mole fraction profiles for the ternary diffusion with heterogeneous reaction. Comparison of MCM and EDM (with and without assumption $Đ_{1,2}=Đ_{1,3}$) with an analytical solution of the MS equation.

Fig. 3.11: Diffusivity profiles for the ternary diffusion with heterogeneous reaction. Comparison of MCM and EDM (with and without assumption $Đ_{1,2}=Đ_{1,3}$).

Fig. 3.12: Instantaneous concentration profiles for three different values of the diffusivity ratio ($H=1$, $f_{\text{int}}=1$, $t=0.05\,\text{s}$). Comparison of analytical and numerical solution with and without CCDM.

Fig. 3.13: Concentration profiles of analytical and numerical solution with and without CCDM for different interface locations within a mesh cell (a), and differences between analytic and numerical solutions normalized by $c_{\text{ref}}$ (b).

Fig. 3.14: Concentration profiles for steady-state two-phase reactive mass transfer ( $k=10$ m/s ). Comparison between numerical and NESM solution for three different diffusivity ratios and two different Henry number. ($H=1$ (a) and $H=2$ (b)).

Fig. 3.15: Concentration profiles for steady-state two-phase reactive mass transfer ($H=0.5$, $\Gamma_D=1$ (a) and 10 (b)). Comparison between numerical and NESM solution for two different reaction rates.

Fig. 3.16: Concentration profiles for two-phase reactive mass transfer of H2-O2-H2O mixture. (a): entire domain, (b): zoom-in for liquid region.

Fig. 3.17: The elements of the diffusivity matrix in (a) gas phase and (b) liquid phase for H2-O2-H2O mixture. Comparison of EDM (numerical solution) and MCM (by NESM).

Fig. 3.18: Prescribed mole fraction profiles for studying the dilution effect. The inset shows the profile of the respective degree of dilution as defined by Eq. (3.16).

Fig. 3.19: Diffusivities of MCM and EDM with respect to the degree of dilution.

Fig. 3.20: Dependence of differently averaged velocities on the degree of dilution.

Fig. 3.21 Comparison between numerical solutions and experimental results [64].

Fig. 3.22: Comparison of concentration profiles according to the different rate constant $k'$ corresponding to the hydrogen partial pressure.

Fig. 3.23: Conceptual sketch for the semi-batch reactor in Frikha et al. [34].

Fig. 3.24: (a) Temperature profile from the experiment [34] and estimated temperature profile for the computation by curve-fitting from the experimental data. (b) Comparison of predicted and measured values for conversion of nitrobenzene.

Fig. 4.1: The shape of a bubble and surrounding liquid film for Ca < 0.04 at the cross-section of a square channel (adapted from Kreutzer [88]).

Fig. 4.2: The symmetrical computational domain and its boundary condition for 2D Taylor flow.

Fig. 4.3: Results of hydrodynamic test cases (upper half: streamlines and velocity in moving frame of the bubble, lower half: axial velocity ($u_x$) distributions and velocity vectors in fixed frame).

Fig. 4.4: Five flow types of two-phase flow in a circular mini-channel (adapted from Haase et al. [48]).

Fig. 4.5: Results of the artificial fluid system on flow regime map [3] with respect to Weber numbers of gas and liquid phases.

Fig. 4.6: Comparison of film thicknesses of test cases with Halpern and Gaver correlation [50].

Fig. 4.7: Reynolds-capillary diagram for artificial fluid system.

Fig. 4.8: Time evolution of mean velocities of Taylor flows for case B1~B3 (identical gas kinematic viscosity).

Fig. 4.9: Comparison of terminal bubble shapes for case B1~B3 with identical gas kinematic viscosity

Fig. 4.10: Shape of the bubble and axial velocity field for case B1~B3 (upper half: streamlines and velocity in moving frame of the bubble, lower half: axial velocity ($u_x$) distributions and velocity vectors in fixed frame).

Fig. 4.11: Time evolution of mean velocities of Taylor flows with different density ratios (case B3~B5).

Fig. 4.12: Comparison of the terminal bubble shapes with different density ratio (case B3~B5).

Fig. 4.13: The bubble shapes and velocity fields with different density ratio (case B4 and B5).

Fig. 4.14: Time evolution of mean velocities of Taylor flows with different number of mesh cells.

Fig. 4.15: Comparison of terminal bubble shapes computed with different number of mesh cells.

Fig. 4.16: Wall-normal profiles of axial velocity at the position of P1, P2 and P3 with different mesh cells ($t = 0.5\mathrm{s}$).

Fig. 4.17: Concentration distributions computed with difference mesh cells at $t = 0.625\mathrm{s}$ and $0.75\mathrm{s}$.

Fig. 4.18: Axial concentration profiles computed with difference mesh cells at the centerline ($z = 0$) for $t = 0.75\mathrm{s}$.

Fig. 4.19: Wall-normal concentration profiles computed with different number of mesh cells at the position of P2 and P3 ($t = 0.75\mathrm{s}$).

Fig. 4.20: Conceptual diagram of fixed reference frame and moving reference frame approaches.

Fig. 4.21: The concentration distributions computed in the frame of moving bubble at $t = 0.625\mathrm{s}$ and $0.75\mathrm{s}$ ($N_z = 25$).

Fig. 4.22: Concentration profiles at the centerline ( $z = 0$ ) near the gas-liquid interface (rear interface (a) and front interface (b)) after 1000 time steps. Comparison of the results between fixed frame approach (with 25 and 50 cells) and moving frame approach (with 25 cells).

Fig. 4.23: Comparison of the centerline ( $z = 0$ ) velocity profiles of fixed frame approach and moving frame approach at ten different instants of the time.

Fig. 4.24: Mass transfer coefficient obtained from both fixed and moving frame approaches.

Fig. 5.1: Densities of nitrobenzene and aniline as a function of temperature. Estimation by least square method from the experimental data [42, 78, 93, 105, 109].

Fig. 5.2: Viscosities of nitrobenzene and aniline as a function of temperature. Estimation by power law from the experimental data [4, 42, 78, 93].

Fig. 5.3: Diffusivity of hydrogen in nitrobenzene and aniline, and diffusivity of aniline in nitrobenzene as a function of temperature.

Fig. 5.4: Henry coefficients of hydrogen in nitrobenzene, ethanol and aniline. (a) Comparison between correlated and measured values at 101 kPa as a function of temperature [40, 77, 93, 97, 118, 119].

Fig. 5.5: Surface tension of nitrobenzene and aniline with respect to the temperature.

Fig. 5.6: Comparison of steady bubble shape for different cases given in Table 18.

Fig. 5.7: The axial velocity distributions of hydrodynamics for the nitrobenzene/hydrogen Taylor flow (Upper half: streamlines and velocity of moving frame of the bubble, lower half: axial velocity ( $u_x$ ) distributions and velocity vectors of fixed frame).

Fig. 5.8: Distributions of the hydrogen transferring into pure nitrobenzene and the produced aniline at $t = 0.25\,\mathrm{ms}$ ( $c_{\mathrm{ref}} = 380\,\mathrm{mol/m^3}$ ).

Fig. 5.9: Distributions of the hydrogen transferring into pure nitrobenzene and the produced aniline at $t = 1.25\,\mathrm{ms}$ ( $c_{\mathrm{ref}} = 380\,\mathrm{mol/m^3}$ ).

Fig. 5.10: Distributions of the hydrogen transferring into pure nitrobenzene and the produced aniline at $t = 5\,\mathrm{ms}$ ( $c_{\mathrm{ref}} = 380\,\mathrm{mol/m^3}$ ).

Fig. 5.11: Comparison of wall-normal concentration profile of hydrogen and aniline at three axial positions (front cap, recirculation zone and liquid film, $x^* = 1,\ 3,\ 5.6$ ) at $t = 15\,\mathrm{ms}$.

Fig. 5.12: (a) Time evolution of mean concentrations of hydrogen and aniline within the pure nitrobenzene.

Fig. 5.13: Distributions of the hydrogen transferring into nitrobenzene pre-saturated by hydrogen, and the produced aniline for case D2 at different instants of the time $(t = 0.25,\ 1.25 \text{ and } 5\,\mathrm{ms})$.

Fig. 5.14: Time evolution of mean concentrations of pre-saturated hydrogen and aniline in liquid phase.

Fig. 5.15: Sketch of lateral view for Taylor flow. Definition of characteristic velocities and lengths. Fig. adapted from Wörner [146].

Fig. 5.16: Comparison of four different characteristic times (a) and non-dimensional recirculation time (b) for test case D1, D2 and D3.

Fig. 5.17: Comparison of film Fourier number $Fo_{\mathrm{F}}$ and film Peclet number $Pe_{\mathrm{F}}$ with aniline conversions for test case D1, D2 and D3.

Fig. 5.18: (a) Temporal evolution of mean concentration of hydrogen in liquid phase with various scaling factors of reaction rate ( $f_{\mathrm{s}}$ ). Comparison between the mass transfer of hydrogen into pure and pre-saturated nitrobenzene. (side by side), (b) mass transfer coefficient of hydrogen into the pure nitrobenzene with various scaling factors of reaction rate ( $f_{\mathrm{s}}$ ).

Fig. 5.19: Reaction path from NB to AN on the bimetallic catalyst of platinum and palladium (mechanism B of Zhang et al. [151]).

Fig. 5.20: The result of CSTR calculation with detailed reaction mechanism. Temperature and mole fractions of bulk species (a) and site fractions of surface species (b).

Fig. 5.21: Distributions of bulk species and site fractions of surface species at four different time instants (0.25, 1.25, 2.5, 5 ms). Results of mass transfer of hydrogen into pure nitrobenzene by detailed kinetic mechanism.

Fig. 5.22: Time evolutions of bulk species (a) and coverage fraction of surface species (b) for the case starting with pure NB. (Solid line: average site fraction, dashed line: local site fraction at $x^* = 1.74$ ).

Fig. 5.23: Time evolutions of bulk species (a) and site fractions of surface species (b) for the case with pre-saturated NB.

Fig. 6.1: Conceptual diagram for simplified one-dimensional model for analyzing diffusive mass transfer in the liquid film with respect to the liquid composition.

Fig. 6.2: Density and viscosity of nitrobenzene + aniline mixture (a) and nitrobenzene + ethanol mixture (b) by correlation and experimental data at 303.15K ([42, 105] for nitrobenzene + aniline and [109] for nitrobenzene + ethanol). Inset: Excess viscosity and molar volume.

Fig. 6.3: Diffusivity of hydrogen in nitrobenzene + aniline and nitrobenzene + ethanol mixtures estimated by multicomponent model and effective diffusivity model for ideal and non-ideal fluid at 303.15K (inset: distribution of thermodynamic factor for those solutions with respect to composition).

Fig. 6.4: Henry coefficient of hydrogen in the mixture of nitrobenzene + aniline and nitrobenzene + ethanol at 303.15K and 0.7 MPa by two correlations ([117] and [60]).

Fig. 6.5: Surface tension of nitrobenzene + ethanol mixture at 303.15K. Comparison of Hildebrand method [61] and Hoar and Melford method [63]. Inset: $X_1'$ for Hoar and Melfort method.

Fig. 6.6: Laplace number of nitrobenzene + aniline and nitrobenzene + ethanol mixtures with respect to changing liquid composition ( $L_{\mathrm{ref}} = 100\,\mu\mathrm{m}$ ).

Fig. 6.7: Bubble velocity of nitrobenzene + aniline and nitrobenzene + ethanol mixtures for *Ca* = 0.01 and 0.005 with respect to the liquid composition.

Fig. 6.8: Time evolution of hydrogen wall concentration ( $c^* = c/c_{\mathrm{G,H2}}$ ) for nitrobenzene + aniline (a) and nitrobenzene + ethanol (b) mixtures with respect to the liquid composition (*Ca*=0.01).

Fig. 6.9: Instantaneous hydrogen concentration profiles( $c^* = c/c_{\mathrm{G,H2}}$ ) along the distance ( $z^* = z/d_{\mathrm{F}}$ ) at 1ms (*Ca*=0.01) as a function of nitrobenzene mole fraction for the mixture of (a) nitrobenzene + aniline and (b) nitrobenzene + ethanol.

Fig. 6.10: Hydrogen saturation time for 90% of liquid equilibrium concentration and 1% of gas concentration (a) and corresponding Fourier numbers (b) for the test case with Ca=0.01.

Fig. 6.11: Bubble velocity (a) and film thickness (b) as a function of nitrobenzene mole fraction for nitrobenzene + aniline and nitrobenzene + ethanol mixtures with variable capillary number ( $L_{\mathrm{ref}} = 100\,\mu\mathrm{m}$ ).

Fig. 6.12: Time evolution of hydrogen wall concentration ( $c^* = c/c_{\mathrm{G,H2}}$ ) for nitrobenzene + aniline (a) and nitrobenzene + ethanol (b) mixtures with respect to the liquid composition (*Re*=100).

Fig. 6.13: Hydrogen saturation time for 90% of liquid equilibrium concentration and 1% of gas concentration (a) and corresponding Fourier numbers (b) for the test case with variable capillary number (Re=100).

Fig. 6.14: Definition of film exposure time of Taylor flow. Left: a Taylor bubble passing through the monitor point. Right: estimation of film exposure time from the time evolution of mean volume fraction at the monitor point.

Fig. 6.15: (a) The non-dimensional bubble length $L_{B,sat}/L_{ref}$ as a function of capillary number with different combination of dimensionless numbers ( $Sc = 545$ ) (b) distributions of non-dimensional concentration with respect to the Fourier number.

Fig. 6.16: (a) Non dimensional Henry numbers for 1% and 2% of gas hydrogen concentration (b) non-dimensional bubble length for saturation of 1% and 2% of gas hydrogen concentration both nitrobenzene + aniline and nitrobenzene + ethanol mixtures (*Ca*=0.01).

# List of tables

Table 1: Definitions of dimensionless parameters and numbers for non-dimensional governing equations.

Table 2: Notation for parameters in mole, mass and volume reference frame.

Table 3: Maximum velocities and the relative errors of maximum velocities between analytic solutions and numerical results with a different number of mesh cells in the z-direction.

Table 4: Maximum velocities and the relative error of maximum velocities between the analytic and numerical solutions with different locations of interface.

Table 5: Summary of test conditions for the Stefan diffusion example.

Table 6: Summary of test conditions for the ternary diffusion with heterogeneous reaction.

Table 7: Summary of test conditions for $H_2$-$O_2$ ternary reaction diffusion across the phase interface.

Table 8: Summary of test conditions for the validation case of simplified one-step kinetic model.

Table 9: Summary of test conditions for the validation case of reaction kinetics with gas-liquid mass transfer limitation.

Table 10: Physical properties of an artificial fluid system.

Table 11: Test conditions of the parametric study for variable bubble velocity and channel height.

Table 12: Test conditions for numerical parametric study of the gas density and gas viscosity.

Table 13: The number of cells and cell sizes of meshes for the grid independency test.

Table 14: Density and viscosity of hydrogen in high pressure [43].

Table 15: Summary of the estimation parameters of Radhakrishnan correlation for hydrogen solubility in pure liquids.

Table 16: The physical properties of nitrobenzene and hydrogen at 298K and 0.7MPa.

Table 17: Reynolds and capillary numbers for nitrobenzene with respect to the various bubble velocities and channel heights.

Table 18: Test conditions of Taylor flow for hydrodynamic simulations of hydrogenation of nitrobenzene.

Table 19: Estimated characteristic velocities and lengths for case D1, D2 and D3.

Table 20: Polynomial parameters to estimate the excess molar volume and excess viscosity of nitrobenzene + aniline and nitrobenzene + ethanol mixtures at 303.15K.

# Appendix A. Subroutine DEXTEP

As mentioned in Section 2.2, a special procedure is necessary to determine the orientation of interface in EPIRA. The subroutine DEXTEP (Determine the status of Extension for EPIRA) is designed for the determination of the direction of extension when the interface is not defined by two neighboring cells, but additional two adjacent cells are further required. Therefore, the name of subroutine contains the extension which represents the consideration of original two neighboring cells and extended two additional cells in the interface determining procedure. In case of the extension procedure, the code should choose a pair of cells from the six surrounding pairs of cells. The purpose of this subroutine DEXTEP is to determine the direction of extension by conditional variables which are true when the cell face includes the interface. Fig. A.1 displays the face of interest and its neighboring faces which are used in the determination step of the direction of extension. If a cell face contains an interface, the 16 faces in the neighboring cells are checked by a conditional statement. The conditional equation for $z$-direction of extension forms:

$$\begin{aligned}&\overline{(A\cdot B\cdot C\cdot D)}\cdot\left[E+(A\cdot F)+(B\cdot G)\right]\cdot\left[H+(C\cdot I)+(D\cdot J)\right]\\&\cdot\left[K+(A\cdot L)+(B\cdot M)\right]\cdot\left[N+(C\cdot O)+(D\cdot P)\right]\end{aligned}\tag{A.1}$$

where the alphabets represent the conditional variables of face shown in Fig. A.1 and +, ·

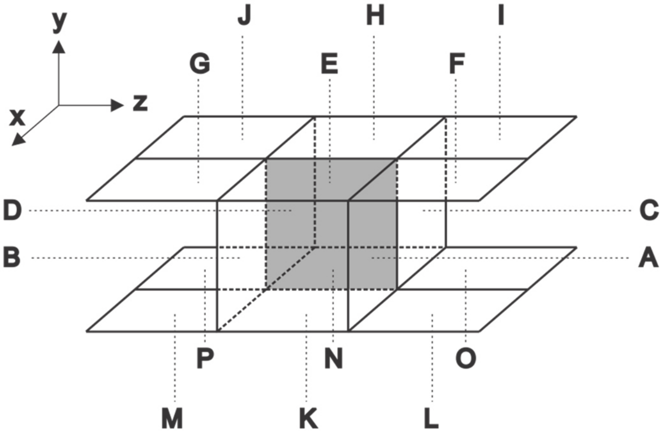

Fig. A.1: A cell face of interest (shading) and 16 faces in the neighboring cells considered in DEXTEP subroutine.

represent the logical operators ‘Or’ and ‘And’, respectively.

For better understanding of the Eq. (A.1), Fig. A.2 gives several examples of the faces cut by interface and the possible orientation of interface plane with those sets of faces. Fig. A.2 (a) represents that the interfacial faces are A, B, C and D. In this case, the direction of normal vector of the interface plane is obviously determined to $y$-direction. Also, Fig. A.2 (b) shows the face E, H, K and N of interface whose normal vector should be oriented to $z$-direction. These two cases have definite orientations of interface without extension of the cells. The Eq. (A.1) starts from these two exact conditions:

$$\overline{(A\cdot B\cdot C\cdot D)}\cdot[E\cdot H\cdot K\cdot N] \tag{A.2}$$

For extension to $z$-direction, the condition shown in Fig. A.2 (a) is inversed and the condition shown in Fig. A.2 (b) is associated as shown in Eq. A.2. In Fig. A.2 (c) and (d) where the face A and F (Fig. A.2 (c)) or B and G (Fig. A.2 (d)) are cut by interface instead of face E, the extension is required in $z$-direction as well. The second parenthesis after $\overline{(A\cdot B\cdot C\cdot D)}$ in Eq. (A.1) means the condition of the case Fig. A.2 (b), (c) and (d) by ‘Or’ operation. For the other faces H, K and N, the similar conditions are described in the next three parentheses of Eq. (A.1).

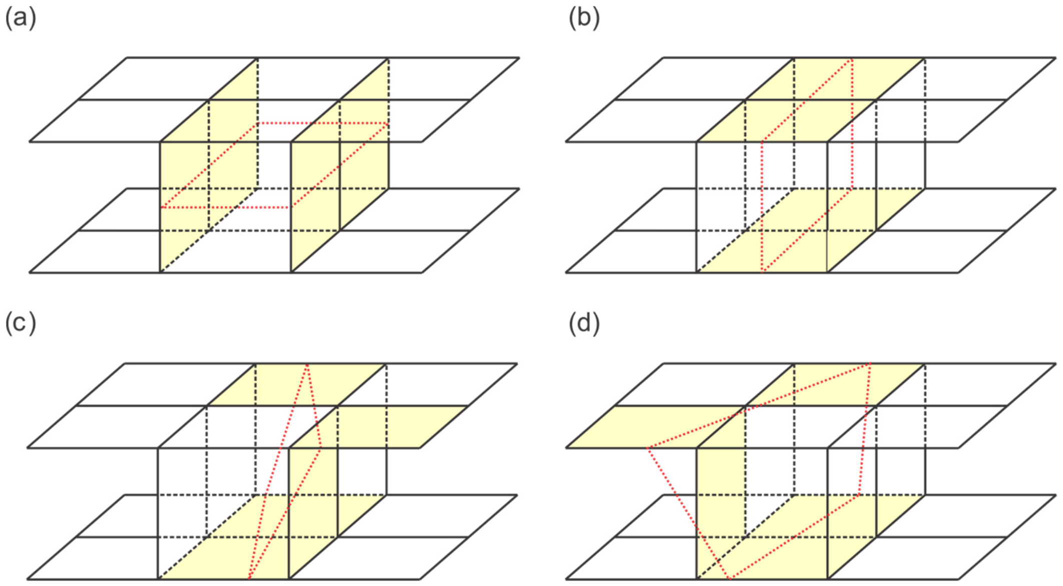

Fig. A.2: The examples of different interfacial faces (yellow shading) and the determined slope of the interface plane (with red line).

# Appendix B. Flotsam treatment

During the computation, the liquid volume fraction of a certain phase becomes rarely non-zero or non-unity due to the numerical error. This numerical artifact called flotsam does not affect $f$ equation itself, but causes an error in the interfacial reconstruction procedure. Fig. B.1 shows the concept of the flotsam error in three-dimensional computational domain where the value of $f$ in a cell is between zero and unity, while those of surrounding cells are either zero or unity. To remove this numerical artifact, the value of volume fraction is set to the same value of a certain adjacent cell. This casual treatment gives rise to another kind of error especially for the interface reconstruction of the cells on the flat interface.

Fig. B.2 displays an example of error caused by wrong flotsam treatment in two-dimensional domain. For two-dimensional domain, flotsam modification is performed for an interfacial cell surrounded with eight non-interfacial cells. Fig. B.2 (a) shows the cell distribution of flat interface where the part emphasized by red dash-line can also be regarded as a flotsam because one interfacial cell are surrounded by eight non-interfacial cells even if the interfacial cell is correctly evolved. If flotsam modification method takes the value of volume fraction from the lower cell, the cell distribution is changed as shown in Fig. B.2 (b), which creates non-physically sharp gradient of interface. This kind of error actually occurred in last version of TURBIT-VOF.

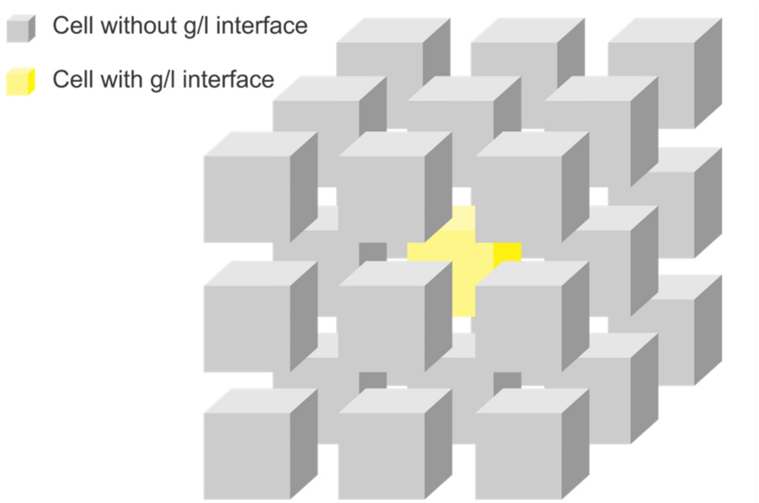

Fig. B.1: The concept of flotsam in three-dimensional domain

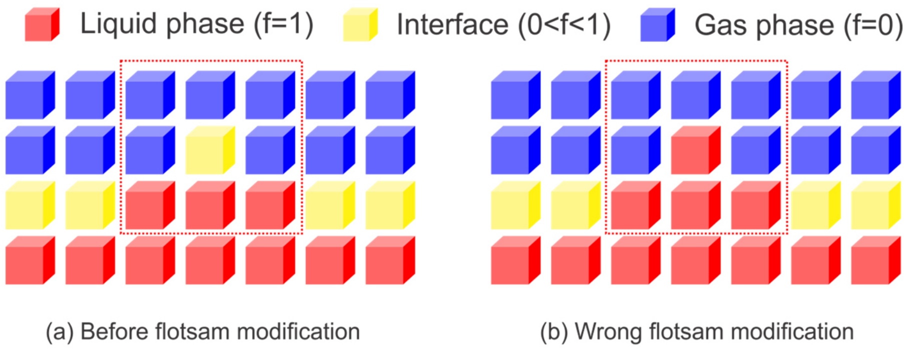

(a) Before flotsam modification

(b) Wrong flotsam modification

Fig. B.2: Example of wrong flotsam modification in two-dimensional domain.

In present study, the flotsam treatment is therefore revised by activating the treatment only when all surrounding cells belong to the same phase. Fig. B.3 shows the results of rear bubble before and after the revision of flotsam treatment. The results clearly illustrate that the problem of wrong flotsam modification is fixed where a non-physical notch shape appears on the middle of the flat surface in Fig. B.3 (a), while it disappears after the revision as shown in Fig. B.3 (b).

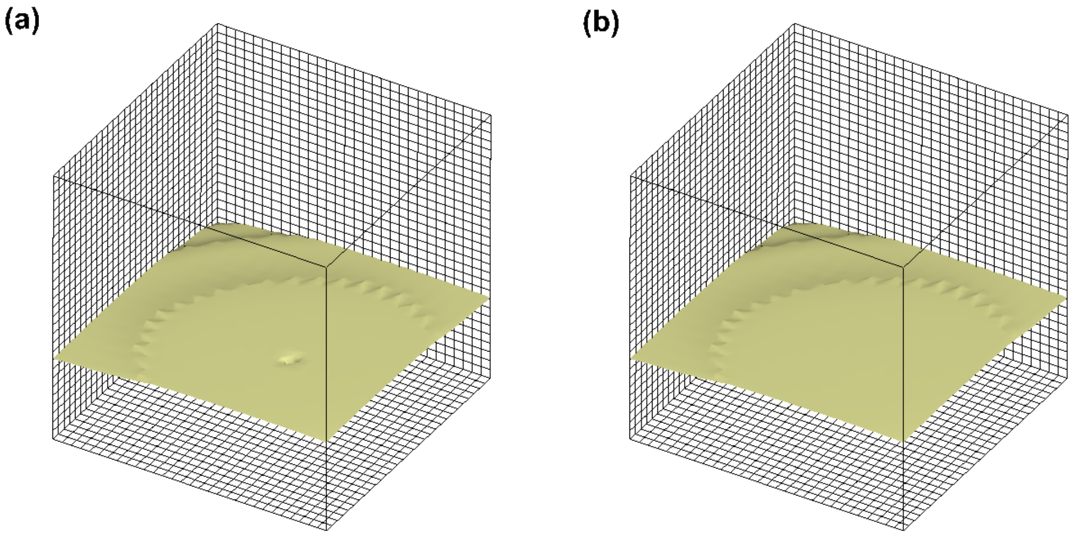

Fig. B.3: Computed rear bubble interface by TURBIT-VOF before (a) and after (b) revision of flotsam treatment.

# Appendix C. Numerical solution of Maxwell-Stefan equation

Maxwell-Stefan equation is one of the classical model for describing constitutive relation between diffusional fluxes and driving forces in multicomponent system, see e.g. [132]. For the ideal fluid where only binary collision of molecules occurs, the Maxwell-Stefan equation is given by

$$F_i = -\sum_{\substack{j=1 \\ j\neq i}}^{n} \frac{(x_i N_j - x_j N_i)}{c_\mathrm{t} Đ_{ij}} \tag{C.1}$$

At constant temperature and pressure, the driving forces of Maxwell-Stefan diffusion $F_i$ are the gradients of mole fractions because the total concentration and the binary diffusion coefficients are constant. For one-dimensional diffusion considered in Section 3.2, the gradient of mole fraction has the form of $dx_i/\mathrm{dz}$. To obtain the numerical solution of Eq. (C.1) in aforementioned conditions, the first order spatial derivative is discretized by a forward finite difference at position $k$ as

$$\frac{x_{i;k+1} - x_{i;k}}{\Delta z} = -\sum_{\substack{j=1 \\ j\neq i}}^{n} \frac{(x_{i;k} N_j - x_{j;k} N_i)}{c_\mathrm{t} Đ_{ij}} \tag{C.2}$$

At $z = 0$, the fixed mole fractions are set as boundary conditions. The information of the boundary is marching to the end of computational domain iteratively in the solution procedure. 40 nodes are used for one-dimensional Stefan-tube problem described in Section 3.2.1.

# Appendix D. Numerical solution of non-equilibrium stage model (NESM)

Non-equilibrium stage model (NESM) is developed for the estimation of two-phase multicomponent distillation process [132]. NESM divides a reactor into several stages. In each stage, there are different kinds of fluxes such as feeding, producing and consuming, and those fluxes are transferred between the stages. In NESM, the characteristics of reactor are, therefore, assessed by a balance of the fluxes among the stages inside the reactor. With NESM, Kenig et al. [82] provided an analytical model for steady-state two-phase mass transfer with heterogeneous reactions. The stage equations of species $i$ in stage $j$ for gas and liquid phase are given by

$$\left(1+r_{\mathrm{G}}\right)\dot{V}_{\mathrm{G},i}^{j}-\dot{V}_{\mathrm{G},i}^{j+1}-\dot{V}_{\mathrm{FG},i}^{j}-J_{\mathrm{G},i}^{V,j}a_{\mathrm{int}}^{j}=0 \tag{D.1}$$

$$\left(1+r_{\mathrm{L}}\right)\dot{V}_{\mathrm{L},i}^{j}-\dot{V}_{\mathrm{L},i}^{j+1}-\dot{V}_{\mathrm{FL},i}^{j}-J_{\mathrm{L},i}^{V,j}a_{\mathrm{int}}^{j}-\dot{S}_{i}^{j}a_{\mathrm{r}}^{j}=0 \tag{D.2}$$

Here, $V_{\mathrm{G},i}^{j}$ and $V_{L,i}^{j}$ denote the molar flow rate to stage $j$ with side stream; $r_{\mathrm{G}}$ and $r_{\mathrm{L}}$ represent the ratio of side stream to inter-stage flow. The second terms in Eq. (D.1) and Eq. (D.2) are the molar flow rates to stage $j+1$. The third terms denote the molar flow rates by additional feed. The fourth terms represent the mass transfer across the gas-liquid interface (with interfacial area $a_{\mathrm{int}}^{j}$). The fifth term, which appears only in the liquid phase equation Eq. (D.2), is the rate of heterogeneous reaction at the surface (with surface area $a_{\mathrm{r}}^{j}$).

For the test cases in Section 3.3, side streams and additional feeds to the stages are not taken into account so that $r_{\mathrm{G}}=r_{\mathrm{L}}=0$ and $V_{\mathrm{FG},i}^{j}=V_{\mathrm{FL},i}^{j}=0$. Also, the interfacial mass transfer occurs only in the single stage which contains interface, while the other stages are filled with either gas or liquid phase. Therefore, Eq. (D.1) and Eq. (D.2) further simplify to three types of equations. For stages containing one phase only, it is

$$\dot{V}_{\mathrm{G},i}^{j}=\dot{V}_{\mathrm{G},i}^{j+1} \text{ or } \dot{V}_{\mathrm{L},i}^{j}=\dot{V}_{\mathrm{L},i}^{j+1}, \tag{D.3}$$

for the stage with the gas-liquid interface, it is

$$\dot{V}_{\mathrm{G},i}^{j}=J_{\mathrm{G},i}^{V,j}a_{\mathrm{int}}^{j} \text{ and } \dot{V}_{\mathrm{L},i}^{j}=J_{\mathrm{L},i}^{V,j}a_{\mathrm{int}}^{j}, \tag{D.4}$$

and for the stage with the surface reaction, it is

$$\dot{V}_{\mathrm{L},i}^{j} = \dot{S}_i^j a_\mathrm{r}^j \tag{D.5}$$

For one-dimensional problems, the interfacial area ($a_\mathrm{int}^j$) and surface area of reaction ($a_\mathrm{r}^j$) are assumed to be identical so that the latter equations simplify to

$$J_{\mathrm{G},i}^{V,j} = J_{\mathrm{G},i}^{V,j+1},\; J_{\mathrm{L},i}^{V,j} = J_{\mathrm{L},i}^{V,j+1} \tag{D.6}$$

and for the stage at the reactive surface

$$J_{\mathrm{L},i}^{V,j} = \dot{S}_i^j \tag{D.7}$$

Finally, the equations Eq. (D.6) and Eq. (D.7) become the same as the flux balance equation. Therefore, the solution procedure of NESM is similar as for the flux balance equation by finite difference method. After discretization, this elliptic problem is solved by an iterative method with 21 stages including one stage at the middle of domain ($z^* = 0.5$) with the gas-liquid interface, and one stage at the right wall ($z^* = 1$) for surface reaction.

# Appendix E. DETCHEM$^{\text{EVAPORATOR}}$

DETCHEM$^{\text{EVAPORATOR}}$ is a numerical code designed for the batch reactor wherein both gas and liquid phases exist. Based on the DETCHEM$^{\text{BATCH}}$, the liquid phase species are additionally solved for homogeneous reactions in both phases and heterogeneous surface reactions. Reactions between species from different phases are not taken into account in the current version of the code. The governing equations of the code for species $i$ are

$$\frac{dn_{\mathrm{G},i}}{dt} = V_{\mathrm{G}} \dot{r}_{\mathrm{G},i} + A\dot{s}_i \text{ (gas-phase species)} \tag{E.1}$$

$$\frac{dn_{\mathrm{L},i}}{dt} = V_{\mathrm{L}} \dot{r}_{\mathrm{L},i} + A\dot{s}_i \text{ (liquid-phase species)} \tag{E.2}$$

$$\frac{d\theta_i}{dt} = \frac{\dot{s}_i}{\Gamma_{\mathrm{S}}} \text{ (surface coverage)} \tag{E.3}$$

where volumes of each phase are

$$V_{\mathrm{G}} = \sum_{i=1}^{N} n_{\mathrm{G},i} \frac{RT}{p}, \quad V_{\mathrm{L}} = \sum_{i=1}^{N} \frac{n_{\mathrm{L},i} m_{\mathrm{L},i}}{\rho_{\mathrm{L},i}} \tag{E.4}$$

respectively. Adiabatic and isentropic conditions can be applied when the reactor temperature is unknown. With these equations, DETCHEHM$^{\text{EVAPORATOR}}$ can predict the time evolution of gaseous, liquid and surface species.

In the example case shown in section 3.6, liquid phase is only considered for the validation. The Langmuir-Hinshelwood type reaction rate of pellet catalyst is modeled by an user-defined subroutine as a volumetric reaction rate in liquid phase ($\mathrm{mol/(m^3s)}$).

# Appendix F. Influence of numerical schemes for spatial derivatives

Due to the high viscosity and density ratio, the numerical solutions of nitrobenzene-hydrogen Taylor flow are sensitively controlled by its test conditions. To avoid any factors which possibly arouse the numerical errors, the numerical schemes for spatial derivatives are examined in this appendix. For spatial derivative, TURBIT-VOF offers two alternative schemes, central difference scheme (CDM) and upwind scheme. To verify the numerical solutions with different spatial derivatives, some relevant test cases in Chapter 4 and Chapter 5 are revisited with both numerical schemes.

Fig. F.1 shows the time evolutions of the mean velocity by developing Taylor flow from the initial condition. Two test cases are chosen for the comparison; i.e. one case of artificial fluid system (case A2 in section 4.1) and one case of real fluid system (case D2 in section 5.3.1). In case A2, the mean velocity profiles of both schemes are almost exactly the same, while those for the real fluid system shown in case D2 show slight deviation after $t^* = 5$. The test conditions of artificial fluid system are more favorable for numerical simulation with lower Morton number as described in Section 4.1. This may be the reason why the test cases with artificial fluid system do not significantly depend on the numerical schemes for spatial derivatives. Although the solutions

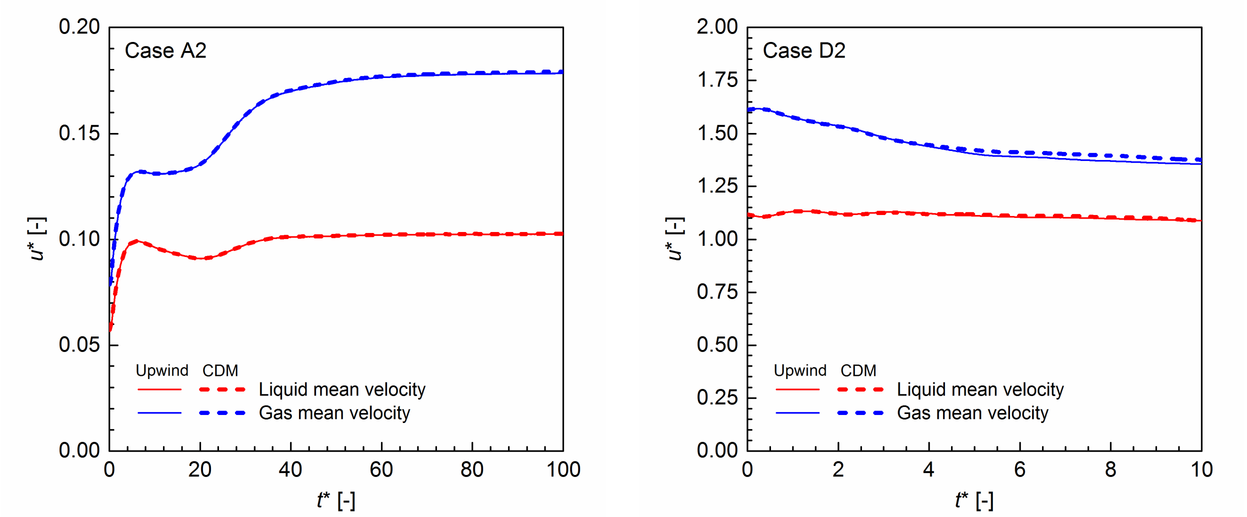

Fig. F.1: Time evolution of the mean velocities of Taylor flow computed by upwind and central difference schemes for case A2 in section 4.1 (left) and case D2 in section 5.3.1 (right).

of case D2 for real fluid system deviate by using different schemes, the difference of mean velocity is very small. Meanwhile, in most of the test cases with artificial fluid system which are not displayed here, there are almost no differences between the results from both schemes as well. Only in case A6 which is in churn flow regime, there is a notable difference of the mean velocities between two schemes. The calculation with central difference scheme is even diverged in the condition of case A6. Except for this extreme case, most cases have no significant difference by using both schemes and the upwind scheme is turned out to be numerically more stable than the central difference scheme.

In addition, the axial velocity fields obtained by both schemes are depicted in Fig. F.2. For case A2, the velocity fields from both schemes are very similar and look numerically stable. The solutions slightly differ only in the area of high velocity inside the bubble. In both results, the unphysical velocity perturbation appears at front and rear part of the bubble. Nevertheless, both results can be acceptable with having no significant difference of velocity fields. However, the velocity fields of case D2 show obvious difference of using both spatial schemes. The result of central difference scheme has large problematic and spurious velocity in front and rear part of the bubble. This erroneous velocity affects the velocity inside the bubble so that the velocity field inside the bubble is unstable. Even though the problematic velocity appears in the result with upwind scheme as well, it does not significantly influence the velocity field inside the bubble. Moreover, the time step for the central difference scheme is half of that used for the upwind

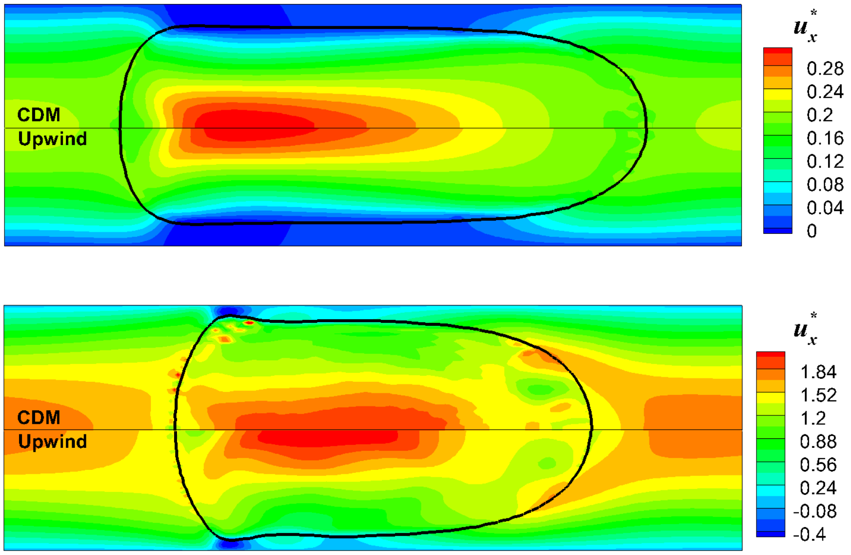

Fig. F.2: Axial velocity distributions computed by both spatial schemes for case A2 in section 4.1 (upper) and case D2 in section 5.3.1 (lower).

scheme. These facts represent that the central difference scheme results in the numerically unstable solution with harsh test conditions such as that of case D2 in real fluid system, while the upwind scheme is numerically more stable in wide range of the test condition. Since the overall velocity fields of both results do not differ noticeably, the upwind scheme is chosen for the hydrodynamic simulation in the present study, although central difference scheme is known as more suitable method for the capturing accurate interface in literature.

In addition to the velocity field, both schemes are also examined for the simulation of mass transfer. The flow field of this test case is based on the case A2 whose velocity field is stable for both schemes. The diffusivity for both gas and liquid phases are arbitrary set to $1\times10^{-9}\ \mathrm{m^2/s}$ and $1\times10^{-4}\ \mathrm{m^2/s}$, respectively. Henry number is 0.1 and the dimensionless time step is specified as $1\times10^{-4}$. Fig. F.3 compares the concentration profiles obtained by both schemes at the two instants of time. The results from both schemes are very different. In the results of central difference scheme oscillation of concentration is created from the front part of the bubble and propagating into the concentration field inside the bubble. This erroneous oscillation of concentration makes high fictitious concentration in the front part of the bubble. The concentration in some part is even bigger than one, which is physically wrong. However, the solution of upwind scheme contains no such problematic oscillations of concentration. Based on the results of both schemes, the upwind scheme is turned out to be more stable for calculation of mass transfer as well. In case calculation using much smaller time step or finer mesh resolution,

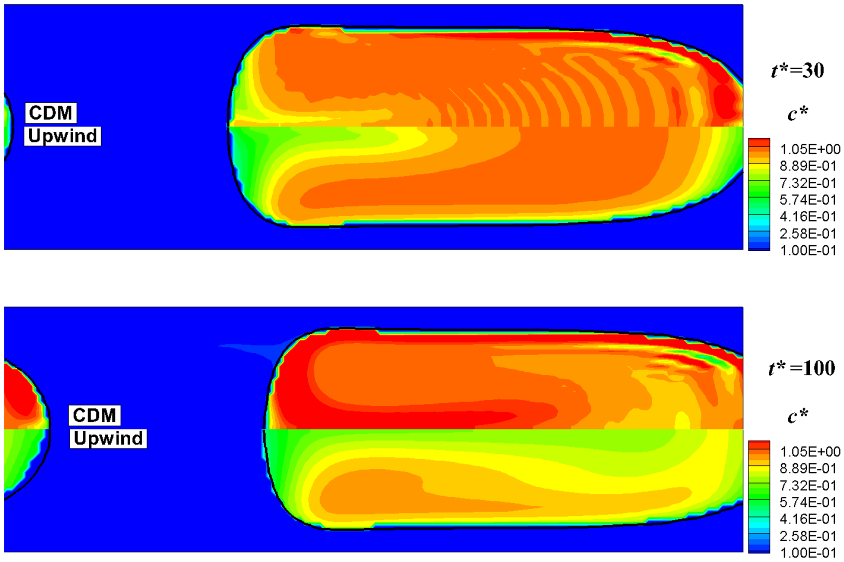

Fig. F.3: The concentration profiles computed by both spatial schemes at $t^* = 30$ and 100 (case A2).

the central difference scheme may also be stable. Nevertheless, this study employs the upwind scheme for calculation of both hydrodynamic and mass transfer to prevent any possible numerical errors.

# Appendix G. Kinetic theory

The transport properties for monatomic gaseous species at low density are predictable with the kinetic theory proposed by Chapman [15] and Enskog [32]. For the collision of rigid spherical molecules, the mean molecular speed and mean free path are given by

$$\bar{u} := \sqrt{\frac{8\kappa T}{\pi m}}\,,\ \lambda = \frac{1}{\sqrt{2}\pi d^2 n} \tag{G.1}$$

where $\kappa$ is the Boltzmann constant, and $m$ is the molecular mass and $n$ is the number density. With these definitions, the transport properties are derived by Bird et al. [6]

$$\mu = \frac{1}{3}\rho\bar{u}\lambda\,,\ D_{ii} = \frac{1}{3}\bar{u}\lambda \tag{G.2}$$

For rigorous and accurate prediction, Chapman-Enskog theory employs the intermolecular potential energy which can be estimated by an empirical correlation of Lennard-Jones (6-12) potential. Then, the viscosity and diffusivity in Eq. (G.1) are rewritten as

$$\mu = \frac{5}{16}\frac{\sqrt{\pi m\kappa T}}{\pi\sigma^2\Omega_\mu}\,,\ D = \frac{3}{8}\frac{\sqrt{\pi m\kappa T}}{\pi\sigma^2\Omega_D}\frac{1}{\rho} \tag{G.3}$$

where $\sigma$ is the characteristic diameter of the molecules and $\Omega_\mu, \Omega_D$ are the collision integral of viscosity and diffusivity, respectively. The Lennard-Jones parameters for various species are listed in Bird et al. [6]. The viscosity and diffusivity is further simplified by substituting constants. The simplification procedure is described in Bird et al. [6] as well. Finally, the viscosity in unit of $\mathrm{g/(cm \cdot s)}$ and the diffusivity in unit of $\mathrm{cm^2/s}$ are

$$\mu = 2.6693\times 10^{-5}\frac{\sqrt{mT}}{\sigma^2\Omega_\mu}\,, \tag{G.4}$$

$$D_{i,j} = 0.0018583\sqrt{T^3\left(\frac{1}{m_i}+\frac{1}{m_j}\right)}\frac{1}{p\sigma_{ij}^2\Omega_{D,ij}} \tag{G.5}$$

# Appendix H. Reaction mechanism for hydrogenation of nitrobenzene

```
SURFACE MECHANISM OF THE HYDROGENATION OF NITROBENZEN ON PD
***********************************************************************
****                                                                  *
****     HYDROGENATION OF C6H5NO2 ON PD - SURFACE MECHANISM           *
****                                                                  *
****     Version 1.0, L.Maier, August  2015                           *
****     DFT data from L. Zhang, RSC Adv., 2015, 5, 34319-34326       *
****                                                                  *
****                                                                  *
****     Kinetic data:                                                *
****      k = A * T**b * exp (-Ea/RT)         A          b       Ea   *
****                                       (cm,mol,s)    -     kJ/mol *
****                                                                  *
****     STICK: A in next reaction is initial sticking coefficient    *
****                                                                  *
****     $..  : additional coverage dependence of Ea (3rd column)     *
****               or changed reaction order (2nd column)             *
****                                                                  *
****     (DETCHEM format)                                             *
****                                                                  *
***********************************************************************
***********************************************************************
**** 1.  ADSORPTION
***********************************************************************
STICK
H2      +(Pd)    +(Pd)    >H(Pd)   +H(Pd)     5.00E-04   0.0       0.0
STICK
C6H5NO2 +(Pd)    >NB(Pd)                      1.00E-05   0.0       0.0
STICK
C6H5NH2 +(Pd)    >AN(Pd)                      1.00E-05   0.0       0.0
STICK
H2O     +(Pd)    >H2O(Pd)                     2.000E-01  0.0       0.0
***********************************************************************
**** 2. DESORPTION
***********************************************************************
H(Pd)   +H(Pd)   >(Pd)    +(Pd)    +H2        3.000E+21  0.0      82.8
H2O(Pd)          >H2O     +(Pd)               3.000E+13  0.0      41.8
NB(Pd)           >C6H5NO2 +(Pd)               3.500E+13  0.0      88.8
AN(Pd)           >C6H5NH2 +(Pd)               1.000E+14  0.0      64.0
***********************************************************************
**** 3.  SURFACE REACTIONS
***********************************************************************
NB(Pd)  +H(Pd)   >NBH(Pd) +(Pd)               3.000E+24  0.0      55.9
NBH(Pd) +(Pd)    >NB(Pd)  +H(Pd)              3.000E+19  0.0      20.2
NBH(Pd) +H(Pd)   >NBH2(Pd)+(Pd)               3.000E+25  0.0     112.9
$NBH(Pd)                                      0.0        0.0      22.0
NBH2(Pd)+(Pd)    >NBH(Pd) +H(Pd)              3.000E+20  0.0     135.1
NBH2(Pd)+H(Pd)   >PHG(Pd) +H2O(Pd)            3.000E+25  0.0     120.6
$NBH2(Pd)                                     0.0        0.0     118.0
PHG(Pd) +H2O(Pd) >NBH2(Pd)+H(Pd)              3.000E+20  0.0     250.9
PHG(Pd) +H(Pd)   >PHA(Pd) +(Pd)               3.000E+24  0.0      99.4
```

```
$PHG(Pd)                                      0.0        0.0       60.0
PHA(Pd) +(Pd)     >PHG(Pd) +H(Pd)             3.000E+20  0.0      159.2
PHA(Pd) +H(Pd)    >PHNH(Pd)+H2O(Pd)           5.000E+26  0.0      166.9
$PHA(Pd)                                      0.0        0.0      104.0
PHNH(Pd)+H2O(Pd)  >PHA(Pd) +H(Pd)             3.000E+20  0.0      272.1
PHNH(Pd)+H(Pd)    >AN(Pd)  +(Pd)              3.000E+26  0.0      153.4
$PHNH(Pd)                                     0.0        0.0      147.0
AN(Pd)  +(Pd)     >PHNH(Pd)+H(Pd)             3.000E+20  0.0      200.7
**********************************************************************
END
```

# Curriculum Vitae

## Personal Details

| | |
|---|---|
| Name | Woo, Mino |
| E-Mail | mino.woo@kit.edu |
| Nationality | Republic of Korea |
| Sex | Male |
| Languages | Korean (mother tongue), English (independent user), German (basic user) |

## Education

| | |
|---|---|
| 03/2003~02/2007 | Bachelor of mechanical engineering<br>Hanyang University, Rep. Korea |
| 03/2007~02/2009 | Master of mechanical engineering<br>Combustion Analysis and Virtual Engine Lab. (CAVEL)<br>Hanyang University, Rep. Korea |
| 03/2013~07/2017 | PhD-student<br>Institute of Catalysis Research and Technology (IKFT)<br>Karlsruhe Institute of Technology (KIT), Germany |

## Work experience

| | |
|---|---|
| 03/2009~02/2013 | Research engineer<br>Kyungwon Engineering and Communication (KWEnC), Rep. Korea |
| 12/2016~02/2017 | Research engineer<br>Automotive Simulation Center Stuttgart e. V., Germany |